THE UNIVERSITY of ADELAIDE

Deutsches Zentrum für Luft- und Raumfahrt
DLR

EXPERIMENTAL INVESTIGATION OF HIGH FREQUENCY COMBUSTION INSTABILITY IN CRYOGENIC OXYGEN-HYDROGEN ROCKET ENGINES

Justin S. Hardi

Experimental Investigation of High Frequency Combustion Instability in Cryogenic Oxygen-Hydrogen Rocket Engines

Justin S. Hardi

School of Mechanical Engineering
The University of Adelaide
South Australia 5005
Australia

A thesis submitted in fulfilment of the requirements
for the degree of Ph.D in Aerospace Engineering
in June 2012

Contents

List of figures

List of tables

Glossary

Nomenclature

A	Area
β^*	Reduced acoustic admittance
c	Sound speed
c^*	Characteristic exhaust velocity
c_p	Specific heat capacity
CH_4	Methane
D	Diameter
η_{c^*}	Characteristic exhaust velocity efficiency
f	Frequency
F	Thrust
g_0	Standard gravitational acceleration, 9.8 m/s^2
GH_2	Gaseous hydrogen
GN_2	Gaseous nitrogen
GOx	Gaseous oxygen
γ	Ratio of specific heats
H_2	Hydrogen
I	OH* emission intensity
I_{sp}	Specific impulse
J	Momentum flux ratio
L	Length
LH_2	Cryogenic ('liquid') hydrogen
LN_2	Liquid nitrogen
LOx	Liquid oxygen
$\dot{m}$	Mass flow rate
M	Molecular mass, g/mol
M_{bulk}	Bulk flow Mach number
n	Mode index
N	Response factor
N_2	Nitrogen
O_2	Oxygen
p	Pressure
p'	Acoustic pressure
P_{cc}	Combustion chamber pressure
$\dot{q}$	Heat release rate
ρ	Density
R_p	Rayleigh index based on acoustic pressure
R_u	Rayleigh index based on acoustic velocity
ROF	Oxidiser-to-fuel mixture ratio
t	Time
T	Temperature
u	Velocity
u'	Acoustic particle velocity
VR	Inner-to-outer-propellant injection velocity ratio

Subscripts

bulk	Bulk, total
cc	combustion chamber
crit	Critical therophysical property
d	Droplet (of LOx)
H	Hydrogen (fuel)
MN	Main (exhaust) nozzle
O	Oxygen (oxidiser)
SN	Secondary (exhaust) nozzle
x	x-axis direction
y	y-axis direction
z	z-axis direction

Acronyms

CFD	Computational Fluid Dynamics
CNRS	National Scientific Research Centre (France)
DLR	German Aerospace Center
FEA	Finite Element Analysis
IRPHE	Research Institute for Equilibrium Systems (France)
ONERA	National Aerospace Lab (France)
NASA	National Aeronautics and Space Administration

Abstract

Self-sustaining pressure oscillations in the combustion chamber, or combustion instability, is a commonly encountered and potentially damaging phenomenon in liquid propellant rocket engines (LPREs). In the high-frequency variety of combustion instability, the pressure oscillations in the combustion chamber take on the form and frequency of an acoustic resonance mode of the combustion chamber volume. The most common mode in naturally occurring instability, and also the most destructive, is the first tangential mode, with acoustic gas oscillations oriented transversally to the direction of propellant injection. The instability is driven by the coupling between acoustic oscillations and unsteady energy release from combustion. The mechanisms through which injection and combustion firstly respond to the acoustic field, and secondly feed energy back into the acoustic field have not yet been fully characterised.

Shear coaxial-type injectors are common in LPREs. Past experimental and numerical research efforts have investigated the interaction between this type of injector and transverse acoustic fields. Some experimental efforts have successfully forced transverse acoustic modes and studied their influence on shear coaxial injection under LPRE-like conditions. Acoustic forcing of coaxially injected LOx/H_2 has previously been conducted only at low pressures and injection performance levels. This work addresses the lack of experimental data available for the interaction of shear coaxial injection of LOx/H_2 with acoustics under conditions representative of industrial engines.

A new experimental rocket combustor, designated 'BKH', was developed for investigating the response of a reacting spray of coaxially injected LOx/H_2 to an acoustic field. For characterising the response, simultaneous high-speed recordings of both backlit shadowgraph and hydroxyl radical (OH*) chemiluminescence imaging have been captured through optical access windows. The operating conditions of BKH extend to conditions more representative of actual LPREs than has previously been achieved with LOx/H_2 in studies of flame-acoustic interaction. BKH was run at pressures of 40 or 60 bar, which correspond to subcritical and supercritical thermo-physical regimes for oxygen. Hydrogen injection temperature was ambient, around 290 K, or cryogenic, around 50 K. An array of multiple injectors was used to better represent real engines. A system for modulating the nozzle exhaust flow was used to induce acoustic perturbations inside the combustion chamber. Two types of perturbation were applied to the near-injection region; oscillating acoustic pressure, and oscillating transverse acoustic velocity.

BKH was used to investigate how subcritical or supercritical pressure level and ambient or cryogenic hydrogen injection temperature influence the interaction of acoustic pressure or velocity with injection and combustion processes. Shadowgraph imaging reveals up to 70% reduction in the length of the oxygen jet when subjected to acoustic velocity of amplitude approaching that of the hydrogen injection velocity. Furthermore, the mode of jet breakup changes from its natural growth-and-detachment behaviour to a 'transverse stripping' mechanism. OH* imaging reveals a corresponding decrease in the extent of the flame, and increase in emission intensity. When subjected to acoustic pressure, OH* emission from the flame was observed to fluctuate in phase with pressure. Thus, responses to both acoustic pressure and velocity have been observed in BKH, which together may form the basis of a coupling mechanism for driving natural combustion instability in LPREs.

Declaration of originality

I certify that this work contains no material which has been accepted for the award of any other degree or diploma in any university or other tertiary institution and, to the best of my knowledge and belief, contains no material previously published or written by another person, except where due reference has been made in the text. In addition, I certify that no part of this work will, in the future, be used in a submission for any other degree or diploma in any university or other tertiary institution without the prior approval of the University of Adelaide and where applicable, any partner institution responsible for the joint-award of this degree.

I give consent to this copy of my thesis, when deposited in the University Library, being made available for loan and photocopying, subject to the provisions of the Copyright Act 1968.

I also give permission for the digital version of my thesis to be made available on the web, via the University's digital research repository, the Library catalogue and also through web search engines, unless permission has been granted by the University to restrict access for a period of time.

Justin S. Hardi

June 2012

Acknowledgements and disclaimer

First and foremost I would like to thank my supervisors, A/Prof Bassam Dally and Prof Michael Oschwald. Their guidance was invaluable, and their expertise and patience were an endless source of inspiration. A special mention must also be made of Dr Gerald Schneider who made it possible for me to leave little old Adelaide for the exciting world of aerospace in Europe.

I am indebted to Dimitry Suslov and Bernhard Knapp for their additional valued guidance.

For their collaboration in development of the BKH combustor, I would like to thank Gerhard Krühsel and the Engineering department, especially David Hladik. Thanks also to all personnel of the M10 and M29 workshops, to M3 technicians Michael Zepmeisel and Markus Dengler, and to Andreas Märklen for their expertise in hardware preparation. Philipp Groß and the P8 Test Facility team are acknowledged for their professional efforts in test operations. Thanks to Walter Clauß for the design and operation of optical diagnostics.

I wish to express my gratitude to my fellow students who assisted me over the course of the project; Samuel Webster, Scott Beinke, Harvey Camilo Gomez Martinez, Jannis Schücker, Maike Neuland and Filip Dimoski. I hope you learned as much from me as I did from all of you.

To my colleagues and good friends Michele Negri, Stefan Gröning, and all the Wohnheimers who made coming to work so enjoyable, as well as life in Möckmühl, cheers!

Finally, I owe my deepest gratitude to my family and to Katharina Wirth for their love and support.

Research undertaken for this report has been assisted with a grant from the Smith Fund (www.smithfund.org.au). The support is acknowledged and greatly appreciated.

The Smith Fund by providing funding for this project does not verify the accuracy of any findings or any representations contained in it. Any reliance on the findings in any written report or information provided to you should be based solely on your own assessment and conclusions. The Smith Fund does not accept any responsibility or liability from any person, company or entity that may have relied on any written report or representations contained in this report if that person, company or entity suffers any loss (financial or otherwise) as a result.

1. INTRODUCTION

Liquid propellant rocket engines (LPREs) are at the heart of all vehicles used for launching large payloads into orbital or interplanetary space, and will continue to be for the foreseeable future. There is a need for continuous improvement in the performance and reliability of existing LPREs, as well as the development of new engines to keep up with the ever growing payload mass demands placed on launch vehicles.

Combustion instability is one of the foremost technical challenges for development of current and future LPREs. Combustion instability manifests as self-sustaining oscillations in the pressure inside LPRE thrust chambers. Unstable combustion can cause extreme pressure fluctuations and excessive heat transfer which can damage engine parts or even destroy an engine and launch vehicle. Substantial effort has been expended in the past to try to understand and control the combustion process in the hopes of minimising the occurrence of combustion instability. However, the mechanisms which cause unstable combustion are still not fully understood and therefore design methodologies lack proper refinement to be able to guarantee safe engine operation.

It would be beneficial to the field of LPRE design if instability could be predicted from such basic design parameters as propellant combination, engine geometry and injector design. It is hoped that the combustion instability problem can be solved by understanding in sufficient detail the transitional processes through which an element of propellant goes from the moment of injection to exhaust through the nozzle. With this understanding, quantitative connections between instability phenomena and the basic physiochemical and geometrical properties of an engine design could be made. A quantitative grasp of combustion instability, applied in modelling and simulation, would promote continual performance and reliability improvement in existing and future LPREs by substantially reducing the financial burden which full scale testing places on development programs.

The objective of this project is to contribute to the efforts of the research community to better understand the mechanisms which drive combustion instability. An experimental approach was used to investigate the interaction of simulated combustion instability with injected propellants under conditions representative of real engines. The investigation has attempted to characterise the interaction and, where possible, quantify the behaviour.

The project was undertaken as part of the ongoing HF combustion instability research program at the German Aerospace Center (Deutsches Zentrum für Luft- und Raumfahrt, or DLR), Institute for Space Propulsion. The DLR Institute for Space Propulsion operates the

largest LPRE test facility in Western Europe. The institute is located in the area of Hardthausen, southern Germany, and includes a high pressure test facility primarily designed for studying high pressure combustion of oxygen and hydrogen. This test facility, designated ‘P8’, can provide oxygen and hydrogen at thermo-physical conditions representative of cryogenic rocket engine operating conditions.

A new experimental combustor was developed to integrate with the P8 facility and to artificially force pressure oscillations inside the combustion chamber to simulate HF instability. The experimental setup was used to conduct testing under realistic rocket engine conditions, especially supercritical pressure, and higher mass flow rates and energy densities than have previously been attempted. This combination of conditions was intended to address shortcomings of previous research as were identified by a survey of current literature.

Conventional sensors as well as high-speed optical diagnostics were used to capture combustor behaviour during testing. Observations were aimed at characterising how the jet mixing and combustion process are influenced by acoustic pressure and/or velocity fluctuations of the type typical of HF instability. From such observations it was hoped to gain more detailed insight into the mechanisms by which chamber pressure oscillations couple with combustion leading to self-sustaining instability.

This thesis begins with background on LPREs, and on the oxygen-hydrogen propellant combination, which was the focus of this work. The phenomenon of combustion instability is also introduced, before a more detailed survey of literature on instabilities is presented in chapter 3. Chapter 4 describes the development of the new experimental combustor for this work, known as ‘BKH’. Chapter 5 describes the techniques used in experimentation with BKH. Acoustic characterisation of BKH from initial testing is presented in chapter 6. Studies of temporal and spatial response of the flame in BKH are presented in chapter 7, followed by studies of oxygen jet behaviour in chapter 8. Finally, findings of these studies are summarised in chapter 9.

2. BACKGROUND

This chapter provides background on the field of liquid propellant rocket engines, and on the topic of this research project; high frequency combustion instability in liquid rocket engines. Different types of rocket engines and their applications are described, with a focus on engines powered by the oxygen-hydrogen propellant combination. Finally, background on the topic of high frequency combustion instability is provided, including a summary of strategies used to address the problem in industrial engines.

2.1 Launch vehicles

A launch vehicle is a flight vehicle capable of carrying a payload above the earth's atmosphere. The term launch vehicle, or 'booster', is commonly associated with the large, rocket propelled vehicles used to place manned or unmanned satellites into earth orbit or space probes into interplanetary trajectories. Four examples of launch vehicles are pictured in Figure 2.1.

Earth orbiting satellites are the mainstay of the space industry. Among their many and varied applications, satellites provide unique earth observation capabilities, allow detailed exploration of the universe, facilitate world-wide military and commercial communication, enhance global navigation and enrich the everyday lives of the public with luxuries such as reliable weather forecasting, entertainment broadcasting and personal communication. The space industry contributes to the world economy through the production, launch and operation of satellites, as well as the development of new technology which can be exploited in countless other fields of industry.

Manned and unmanned space exploration has resulted in significant scientific discoveries and continues to produce a wealth of information which helps scientists to better understand the history of the universe, our solar system, and the origins of life on earth.

The space industry and scientific community rely on launch vehicles to safely place their payloads into orbit or send probes on their way. The structure of a launch vehicle is determined by the need to accommodate a large volume of fuel, and to provide a platform for the propulsion system. The propulsion system is the heart of any launch vehicle and consists of multiple rocket engines, either clustered in parallel or staged in series. Rocket engines produce the thrust required to lift the launch vehicle and its payload above the atmosphere and

accelerate it to orbital velocity. Rocket engines must perform reliably to ensure safe delivery of the payload.

Figure 2.1: Heavy launch vehicles using LPREs; (from left to right) Ariane 5 (Arianespace 2012), Space Shuttle (NASA 2007), Soyuz (Arianespace 2012), and Delta IV (Boeing 2007).

2.2 Rocket propulsion

Rockets produce thrust by expelling stored propellants at high velocity in the opposite direction to the intended motion. By virtue of conservation of momentum, the rocket gains momentum equal in magnitude and opposite in direction to that of the expelled propellant. The thrust force imparted on the vehicle due to the change in momentum of the propellants is given by

$$F = \frac{dm}{dt} u_2 = \dot{m} u_2 \ , \tag{1}$$

where u_2 is the constant and uniform velocity of the ejected propellant, and the mass flow rate through the nozzle is denoted by $\dot{m}$.

There are various means by which propellant can be accelerated and ejected from a rocket engine. For example, the propellant could be stored under pressure and simply allowed to escape, or it can be heated and forced to expand and accelerate through a nozzle. Thermal energy can be provided by chemical reaction, electrical heating, or concentrating solar radiation. Alternatively, propellant could be accelerated by electric or magnetic fields, with batteries, a nuclear reactor, or photovoltaic cells generating the required electrical energy. By far the most practical means of energising large amounts of propellant quickly is through chemical reaction. Chemical reaction of a propellant itself quickly produces very high temperature gaseous products whose internal energy can be converted to kinetic energy via thermodynamic expansion through a nozzle.

There are four main categories of chemical rocket propulsion systems based on the type of propellant combination used; bipropellant, solid propellant, hybrid, and monopropellant. Bipropellant propulsion systems pump separate streams of fuel and oxidiser to a thrust chamber where they react and produce thrust. Since the fuel and oxidiser are usually in liquid form, bipropellant rockets are often termed liquid propellant rocket engines (LPREs). Solid propellant consists of a pre-mixed charge of solidified fuel and oxidiser, called a 'grain', which supports combustion on its exposed surfaces. Hybrid rockets are a cross between liquid and solid rockets, employing both solid and liquid propellants. A typical hybrid rocket works by burning an inert solid fuel grain in the presence of a gaseous or liquid oxidiser. Hybrids have promising operational advantages, mainly in the area of safety; however remain largely in a developmental state due to performance limitations. Figure 2.2 shows basic schematics of these first three types of propulsion system. Finally, monopropellants contain pre-mixed fuel and oxidising species in a stable, liquid state. The monopropellant will sustain self-combustion following ignition or when properly catalysed.

Figure 2.2: Schematics of liquid, solid and hybrid rocket propulsion systems (Image credit: Andrew Sysouphat 2005).

Currently, rockets are the only form of propulsion capable of propelling a vehicle to orbital velocities or to escape the earth's gravitational field to achieve interplanetary trajectories. All launch vehicles to date incorporate either LPREs, solid rocket motors, or both. LPREs provide high levels of thrust for sustained periods and are typically used for the main 'core' stage of heavy launch vehicles. Solid rockets produce very high levels of thrust for relatively short periods of time and are often staged in parallel with a LPRE core stage as 'strap-on' solid rocket boosters (SRBs), providing additional thrust in the early stage of flight. The European Ariane 5, pictured in Figure 2.3, is an example of a launch vehicle utilising this parallel staging arrangement.

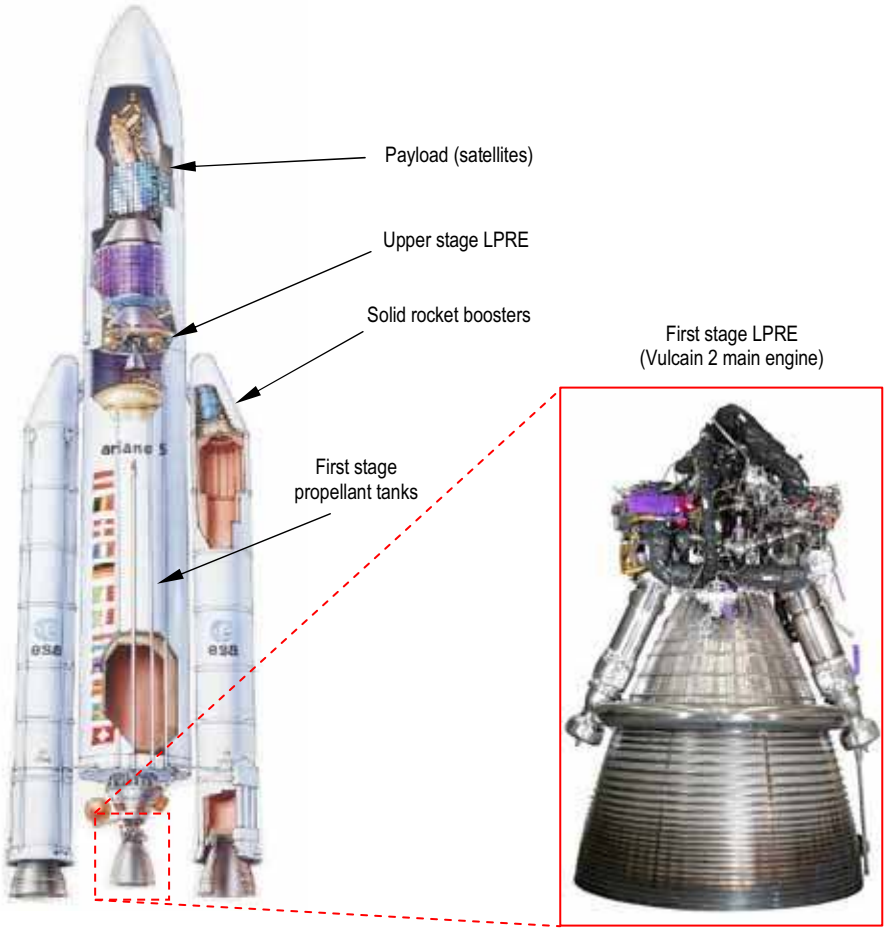

Figure 2.3: Ariane 5 launch vehicle highlighting the main components (modified from DKimages 2007).

2.3 Liquid propellant rocket engines

Rocket engines which burn propellants stored in the liquid state are characterised by high performance and versatility. They are usually used as the main core stage in heavy launch vehicles, but also as main upper stage engines or for in-space propulsion. Various propellant combinations are suited to different applications and engine performance will also depend heavily on the method of injection prior to combustion.

LPREs are not as simple in design as solid rockets, requiring complicated propellant storage, delivery, injection, and ignition systems. The main components of a liquid rocket are shown schematically in Figure 2.4. The propellants, a reactive combination of a fuel and an oxidiser, are stored separately in tanks which usually occupy the majority of the vehicle's overall volume. A delivery system transports the liquid propellants to the injector via various pipes, control valves, pumps and manifolds. A pressurising gas may be used to force one or both of the propellants through the delivery system. However, pumps powered by turbines which consume a small percentage of the main propellants are a more efficient way to provide the high flow rates required in large engines. Propellants are injected into the head of the thrust chamber via the injector, the purpose of which is to ensure the propellants are properly inter-mixed and combust efficiently so that the highest possible percentage of chemical energy content is extracted. The thrust chamber contains the combusting propellants under high pressure and temperature and usually requires active thermal management to withstand the

heat. The nozzle causes the high energy combustion products to accelerate to hypersonic velocities as they leave the chamber, vastly increasing the amount of propulsive energy produced.

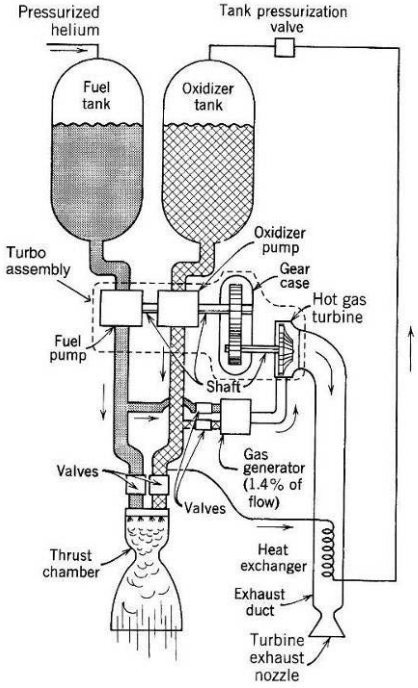

Figure 2.4: Schematic diagram of the main components of a liquid rocket (Sutton & Biblarz 2001, p.8).

2.3.1 Liquid propellant rocket engine performance

Liquid rocket propulsion is the most efficient of the chemical rocket systems, achieving the highest values of specific impulse. Specific impulse is a figure of merit commonly used to describe the efficiency of a rocket engine and can be used to compare dissimilar rocket systems. Specific impulse I_s is defined as the total impulse (or amount of useful extractable propulsive energy) per unit weight of propellant. The equation

$$I_s = \frac{\int_0^t F\, dt}{g_0 \int_0^t \dot{m}\, dt} \tag{2}$$

gives a time-averaged value of I_s, where F and $\dot{m}$ are the instantaneous thrust and propellant mass flow rate, respectively (Sutton & Biblarz 2001, p.28). For constant thrust and flow rate, and neglecting start-up and shut-down transients, the equation could be simplified to become

$$I_s = \frac{F}{\dot{m} g_0} \ . \tag{3}$$

Higher values of specific impulse imply higher efficiency of the overall rocket propulsion system, including propellant properties and effectiveness of propellant utilisation. Table 1

compares the typical range of values for specific impulse which have been achieved with different types of chemical rocket propulsion systems. Liquid bipropellant is clearly the highest performer.

Besides high performance, liquid bipropellant systems have a further advantage of controllability. By controlling the flow rate of propellants through the injector, the engine can be throttled or shut down on command, and sometimes restarted during flight. For example, the Lunar Module Descent Engine on the Apollo Lunar Excursion Module could vary its thrust over a wide range from 4448 to 44,480 N (Hurlbert, Sun & Zhang 1995, p.126). Liquid monopropellant and hybrid systems share this capability, but solid propellant rockets do not.

Table 1: Typical specific impulse for chemical rocket types.

Type of chemical rocket engine	Typical range of specific impulse*
Liquid bipropellant	250 – 450 s
Solid propellant	190 – 270 s
Hybrid	230 – 380 s
Liquid monopropellant	180 – 233 s

*Values sourced from (Sutton & Biblarz 2001)

2.3.2 Liquid propellants

Propellant combinations for liquid bipropellant engines are classified broadly by physical state at standard atmospheric temperature and pressure (STP) conditions. Earth storable propellants are stable liquids at STP, for example kerosene or nitrogen tetroxide. Cryogenic propellants are liquids produced by chilling and compression, and must be kept under pressure in insulated containers. In practice it is impossible to prevent some wastage of cryogenic propellants from fuelled vehicles awaiting launch. Heat will invariably be transmitted through tank insulation into the propellants during this time, causing some evaporation, or 'boil-off'. An advantage of storable propellants is that vehicles can remain on standby, fully fuelled, almost indefinitely. Combinations of one storable propellant and one cryogenic have also been used.

One of the most common combinations of storable propellants is nitrogen tetroxide (N_2O_2) as an oxidiser and a 50-50 blend of hydrazine with unsymmetrical dimethylhydrazine (UDMH) for fuel (otherwise known as A-50 fuel). This combination of substances is hypergolic, meaning they react spontaneously when brought into contact. Hypergolic combinations permit multiple engine restarts and have been used in engines which perform several burns per mission, for example the AJ-10 engine of the Apollo Service Module. N_2O_2 is also commonly combined with monomethylhydrazine (MMH) for in-space reaction control of spacecraft and satellites.

The most common combination of cryogenic propellants is liquid oxygen as oxidiser and liquid hydrogen for fuel (LOx/H_2). This combination has very high performance, but is not hypergolic and therefore requires an ignition source to start the engine. It is commonly used for boost stages with long duration, continuous burns such as the Vulcain engine on the Ariane 5 vehicle. Upper stage engines using LOx/H_2 may also have re-start capability, for example the J-2 engine on the second and third stages of the Saturn V vehicle, or the VINCI engine currently in development for the upper stage of Ariane 5 ME (Mid-life Evolution).

A common cryogenic-storable propellant combination is liquid oxygen oxidiser with highly refined kerosene, called RP-1 (rocket propellant 1), for fuel. This combination was used by the F-1 engines of the Saturn V first stage.

2.3.3 Injector types

The manner in which propellants are injected into the thrust chamber is the primary controlling factor for combustion efficiency and stability. The combustion process is controlled by the design of the injection elements and their number and distribution on the injector face. Various injector element designs tend to be well suited to a particular propellant combination.

Some common injector designs are shown in Figure 2.5. The showerhead injector is the simplest design, where propellants are simply injected from multiple orifices in parallel streams into the thrust chamber where they mix and burn. Mixing of injected liquid propellants can be improved by injecting adjacent streams at an angle such that they impinge on one another at some short distance downstream of the injector face. Impinging doublet or even triplet streams may be unlike (i.e. fuel and oxidiser streams) or like-on-like (i.e. streams of the same propellant impinge).

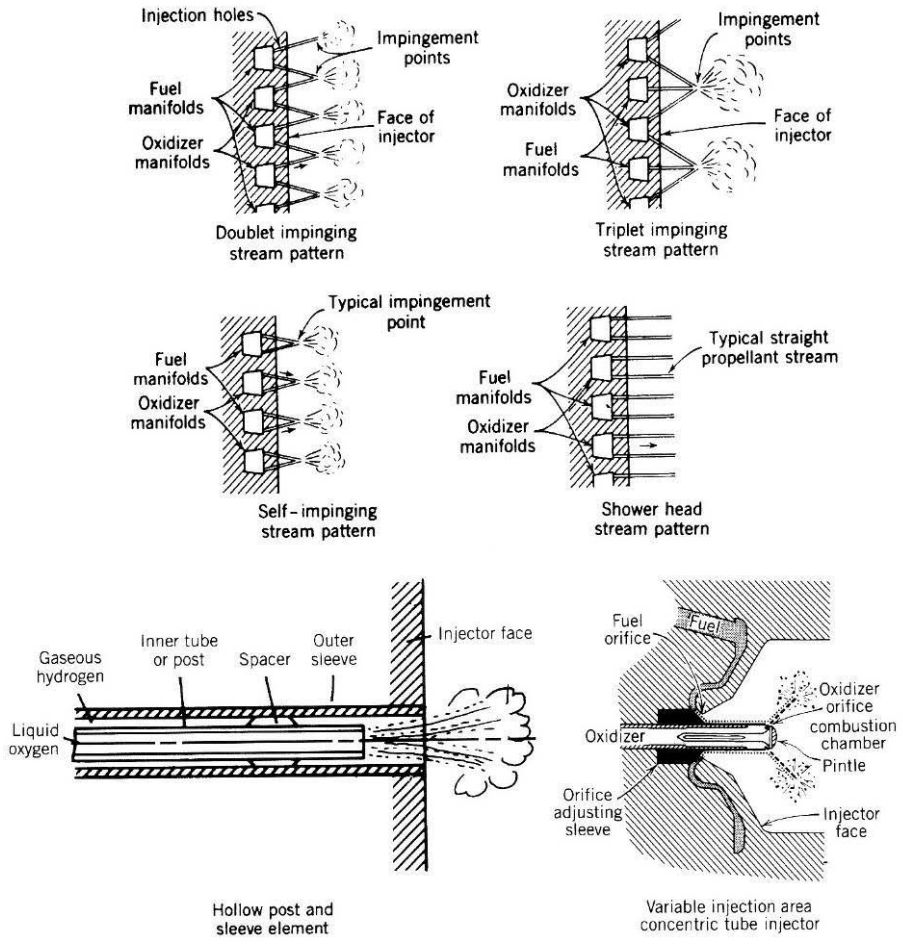

Figure 2.5: Schematic diagrams of several liquid rocket injector types (Sutton & Biblarz 2001, p.274).

Coaxial injectors, depicted in Figure 2.6, have one propellant injected through a circular, central orifice and the second through an annular orifice surrounding the first. Coaxial injectors may be termed swirl coaxial, where either the inner or outer flow is injected with an angular velocity component, or shear coaxial, where the injected flow vector for both streams is purely axial. Shear coaxial injectors are most commonly implemented with the LOx/H_2 propellant combination, mainly because they are so effective at mixing a liquid propellant stream (LOx) with a gaseous stream (GH_2). The difference in velocity between the liquid core jet and the gaseous annulus results in effective atomisation of the LOx jet and mixing of the propellants. For LOx/H_2, shear coaxial injection results in high efficiency and relatively stable combustion.

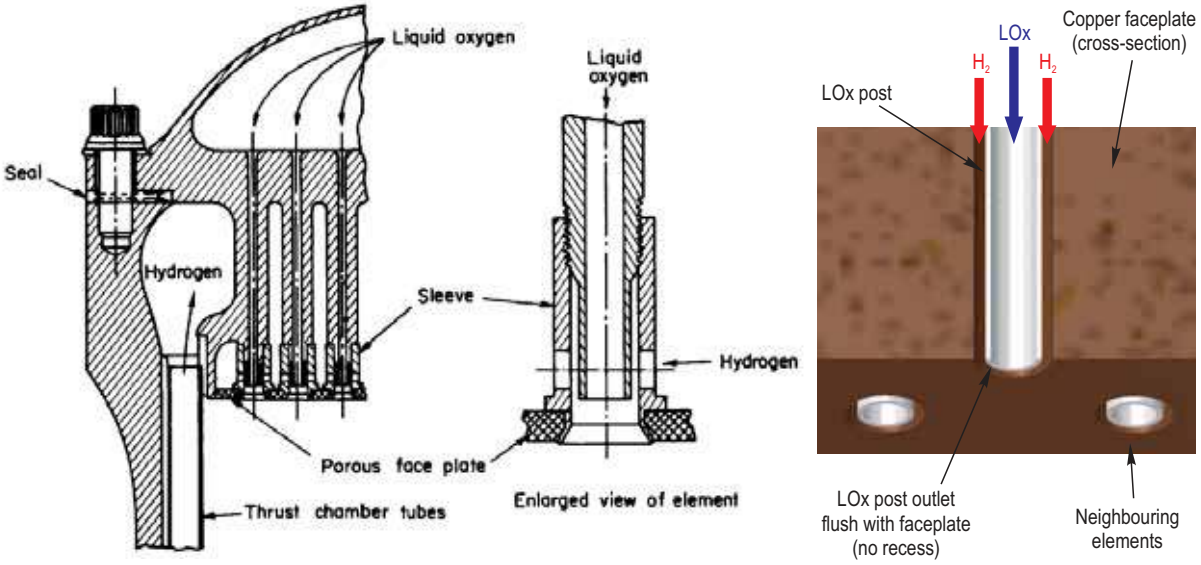

Figure 2.6: The injector assembly of the J-2 engine (left) (Dykema 1972, p.360), and an illustration of a simple shear coaxial injector with no recess (right).

2.3.4 Propellants

The selection of propellants for a liquid bipropellant system is made on the basis of required performance (specific impulse), physical properties, cost and availability, storability and handling characteristics, and to a lesser extent combustion stability. LOx/H_2 is a prominent propellant combination because it has mostly positive attributes in these areas. Table 2 compares theoretical values of specific impulse for several common liquid bipropellant combinations. The LOx/H_2 combination provides very high performance, and its chemical formulation is simple compared to other combinations. While fluorine-hydrogen has the highest theoretical specific impulse, fluorine is toxic and expensive to produce and handle.

The oxygen-hydrogen combination is likely to remain a popular selection in the future because it is environmentally friendly and abundantly available. The propellants are non-toxic and the combustion product is harmless water vapour. They could be produced from water via electrolysis making their availability virtually unlimited. Electrolysis could potentially utilise electricity generated from renewable energy sources, which would further minimise the environmental impact of propellant production. The availability of oxygen and hydrogen also extends beyond planet earth. Deposits of water throughout the solar system could be used for in-situ production of oxygen and hydrogen propellants to facilitate exploration. According to

Curreri (2006), in-situ production of propellants from water ice deposits on the moon or mars has been identified as essential to fully realising the potential of human exploration. Since the oxygen-hydrogen propellant combination is likely to remain important into the foreseeable future, it is imperative that the technology of engines utilising these propellants continues to be improved.

Table 2: Specific impulse for bipropellant combinations.

Type of chemical rocket engine	Typical range of specific impulse[a]
Fluorine - hydrogen	410 s
Oxygen - hydrogen	390 s
Fluorine - hydrazine	334 s
Hydrogen peroxide - RP-1[b]	297 s
Nitrogen tetroxide - A-50[c]	289 s
Oxygen - RP-1	285 s
Red fuming nitric acid - RP-1	269 s

[a] Values are maximum theoretical specific impulse for 6895 kPa chamber pressure in an ideal rocket – i.e. stoichiometric mixture ratio, adiabatic combustion, and isentropic, optimum expansion of ideal gas in the nozzle. Source: values are taken from Table 5-5 in (Sutton & Biblarz 2001).

[b] RP-1 = Rocket propellant 1, high grade kerosene

[c] A-50 = (Aerozine 50) 50-50 blend of hydrazine (N_2H_4) and unsymmetrical dimethyl hydrazine (UDMH)

2.4 Oxygen-hydrogen propellant combination

As the LOx/H_2 propellant combination is the focus of this project, further information is given here on the thermo-physical properties of hydrogen and oxygen, as well as the conditions they experience in LPREs.

2.4.1 Hydrogen fuel

Hydrogen has very high performance when burned with liquid oxygen, as shown in Table 2. It also has a very low density, which can be a disadvantage for launch vehicles. Low liquid density means larger tank sizes are required, resulting in a weight penalty and higher atmospheric drag on the launch vehicle.

With a boiling point of 20.4 K, liquid hydrogen is the coldest of all cryogenic propellants. Hydrogen tanks in a launch vehicle must be properly insulated to minimise boil-off wastage of the fuel while sitting on the launch pad. Furthermore, tank and piping materials must be specially selected to withstand the extremely low temperature. Gaseous hydrogen is highly flammable and explosive when mixed with air, thus safety dictates strict control of leak detection and management. These handling requirements and safety risks raise the operational costs of hydrogen as a fuel.

While stored as a cryogenic liquid in the tanks, hydrogen is injected into the rocket engine as a gas. Cold, liquid hydrogen from the tank is first passed through cooling channels in the wall

of the thrust chamber and sometimes also the nozzle, known as ‘regenerative cooling’. This process preheats the hydrogen so that by the time it reaches the injector it is usually between 80 K and 220 K. The hydrogen then enters the thrust chamber in a gaseous state (GH_2), most commonly through the annular port of a shear coaxial injector element.

2.4.2 Liquid oxygen oxidiser

Oxygen is an oxidiser that is widely used in large rocket engine applications due to its high attainable performance levels. Oxygen was used with RP-1 fuel in the Atlas, Thor, Jupiter, Titan I, and Saturn launch vehicles, with alcohol in the V-2 and Redstone, and is currently used with hydrogen in the Space Shuttle, Centaur upper stage, and Ariane 5. Despite relatively high performance, the use of liquid oxygen has disadvantages in the areas of storage, delivery system complexity and safety.

At standard atmospheric pressure, liquid oxygen (LOx) is a cryogen with a boiling point of 90 K. It is non-corrosive and non-toxic, but must be stored in a properly insulated tank to minimise waste from boil-off venting. Pressure relief valves must be fitted to storage tanks to prevent explosion from over-pressurisation. Although stable in its pure form, liquid oxygen may detonate if suddenly pressurised with organic matter or a fuel, and can accelerate the combustion of other materials. Hence, strict handling procedures and servicing schedules must be adhered to in order to reduce the risks associated with using LOx, which also raises the cost of production and handling. However, these procedures are well established making LOx a relatively inexpensive propellant for rocket propulsion.

LOx is pumped from the tank to the injector in its liquid state. It is injected into the thrust chamber at temperatures typically around 100 K, still in a liquid state, usually through the central port of a shear coaxial injector element.

2.4.3 Supercritical conditions

In Section 2.2, it was explained that thrust is the result of the change in momentum of the propellants as they are accelerated in the thrust chamber. The origin of thrust may also be understood by regarding the force balance on a thrust chamber. Figure 2.7 illustrates the pressure distribution on typical thrust chamber geometry. The axial pressure at the top of the chamber is unbalanced at the nozzle entrance at the opposing end of the chamber, the resultant of which constitutes the thrust force. From this it is obvious that higher pressure in the chamber will result in higher thrust. A simple thermodynamic analysis of an ideal rocket engine can also show that higher chamber pressure results in higher thrust as well as higher specific impulse. This fundamental property has motivated a historical trend towards higher chamber pressures for rocket engines.

As a result of the relationship between chamber pressure and thrust output, modern LOx/H_2 thrust chambers are often operated at conditions above the critical pressure of both hydrogen and oxygen. The critical properties of hydrogen and oxygen are included in Table 3. LOx/H_2 thrust chambers typically operate at pressures between 30 bar and 200 bar. It is therefore important to consider supercritical fluid properties when investigating injection and combustion processes in LOx/H_2 rocket engines.

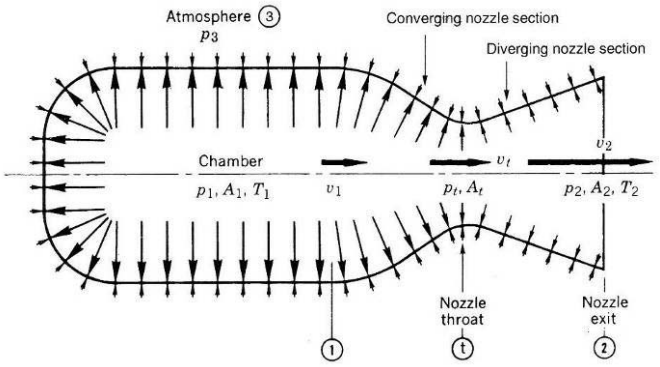

Figure 2.7: Pressure balance on a typical thrust chamber (Sutton & Biblarz 2001, p.33).

Table 3: Critical properties of oxygen and hydrogen.

Property	Oxygen	Hydrogen
Critical temperature, T_{crit}	154.59 K	32.97 K
Critical pressure, P_{crit}	50.43 bar	12.93 bar

In a qualitative sense, the critical point for any substance is where the liquid and vapour phases become indistinguishable. The latent heat of vaporisation and surface tension both decrease to zero approaching the critical pressure. Above the critical point the substance state is known as 'supercritical fluid', as indicated on the phase diagram for oxygen in Figure 2.8, which is overlayed on a surface of specific heat capacity c_p. The behaviour of a supercritical substance can only be referred to as fluid, rather than existing in a distinguishable liquid or gaseous phase. Near the critical point itself, small increases in temperature cause large increases in specific volume. Heat capacity of the fluid also varies drastically (Spalding 1959), as seen in Figure 2.8. These changes in fluid properties have been shown to greatly influence the behaviour of rocket propellants injected under such conditions, including oxygen and hydrogen.

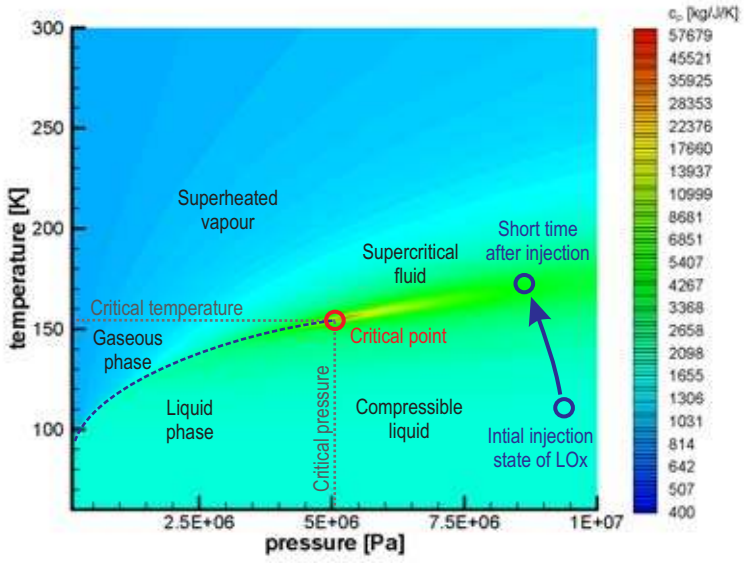

Figure 2.8: Phase diagram indicating transcritical injection of oxygen, c_p values from Younglove (1982).

In modern LOx/H_2 engines, hydrogen is injected at temperatures and pressures above its critical point, and strictly speaking is therefore in a supercritical state. It is common for the LOx to be injected with a temperature initially below its critical temperature into a thrust chamber with supercritical pressure. The intense heat in the chamber will quickly raise the LOx temperature above the critical point, resulting in the LOx entering a completely supercritical state as it mixes and burns with the already supercritical hydrogen. This situation, with initially subcritical temperature but supercritical pressure, is often referred to as "transcritical" injection, and is indicated schematically on the phase diagram in Figure 2.8.

A great deal of effort has been expended internationally on understanding high pressure injection, atomisation and mixing processes. One important finding is that the critical point has been found to shift for multi-component systems, such as for injection of binary propellant combinations like LOx/H_2. The range of conditions where the mixture can be considered supercritical is defined by the critical *mixture* region, the boundaries of which depend on the relative concentrations of injected species. For a given pressure and relative concentration, there exists a critical mixture temperature below which there exists equilibrium with liquid and gaseous phases. Above this temperature the phase boundary disappears and the mixture is considered a supercritical fluid. The dependence of critical mixing temperature on pressure is shown for three different binary systems in Figure 2.9. It follows a general decrease in critical temperature with increasing pressure (Mayer & Smith 2004). Further discussion of research into supercritical injection can be found in Section 3.3.

Figure 2.9: Critical mixing lines for three binary systems (Mayer & Smith 2004, p.8).

2.5 Combustion chamber processes

Before combustion instability can be addressed, it is essential to have an understanding of the processes the propellants undergo inside the thrust chamber of a LOx/H_2 engine. Propellants need to be gasified, mixed and reacted to produce the high energy exhaust gases for acceleration through the nozzle. Broadly, the processes which need to occur before exhaust gases are produced can be termed injection, atomisation, vaporisation, mixing and combustion. The processes may differ for subcritical or supercritical chamber conditions.

2.5.1 Propellant injection

At the exit plane of a shear coaxial injector element, a liquid oxygen core flow with a diameter of 2 to 6 mm enters the chamber with a velocity of around 10 to 30 m/s. This core flow is surrounded by an annulus of supercritical hydrogen gas around 0.5 to 2 mm thick travelling approximately 10 times faster. Injection velocity of the inner or outer propellant flows is determined by the supply flow rate and injector orifice size.

This coaxial propellant jet, with a temperature around 100 K, is injected into the thrust chamber where the operating pressure is the order of 100 bar. While the temperature of the oxygen core at injection may be below the oxygen critical temperature of 154.59 K, the operating pressure of the thrust chamber is above the critical pressure of 50.4 bar. Heat transfer from combustion to the surface of the LOx jet will quickly bring it to a supercritical condition. This injection situation has been termed transcritical, as defined previously in Section 2.4.3.

2.5.2 Atomisation of liquid propellants

For injection into subcritical environments, the initial breakup of a liquid jet is termed ‘atomisation’. Shortly after entering the combustion chamber, a jet of liquid oxygen will begin to break up and ‘atomise’, or form a spray of fine droplets. Breakup is caused by aerodynamic shear and capillary forces on the liquid core jet surface due to the velocity difference of the inner and outer injectant flows. Firstly, these forces will perturb the core surface causing wave-like irregularities to form. Ligaments will grow from the surface irregularities, eventually detaching to form droplets which in turn may break up into smaller droplets. The rate at which atomisation occurs and the size of the droplets in the resulting spray depend heavily on the injector design, chamber pressure, and relative velocities of the injected propellants, but typically droplets will contain the order of 10^{15} oxygen atoms (Harrje & Reardon 1972, p.74).

Figure 2.10: Comparison of coaxial injection at subcritical and supercritical pressures (Mayer & Tamura 1996, p.1146).

For injection into near-critical and supercritical chamber pressures, otherwise known as the transcritical injection regime, the lack of appreciable surface tension precludes the formation of droplets, and the term ‘atomisation’ no longer applies. Convective transport of hot gases from the reaction zone to the surface of the oxygen core will increase the jet temperature

above the critical mixing temperature, rendering supercritical conditions. Figure 2.10 attempts to illustrate the differences in the jet breakup process between subcritical and supercritical injection. For supercritical injection, there is no longer spray formation produced by a recognisable atomisation process. The absence of a well-defined boundary between the liquid core and annular gas flows results in a flow regime more accurately described by turbulent, diffusive mixing between a dense and a light fluid in the shear layer.

2.5.3 Secondary atomisation

The initial atomisation of a LOx jet in subcritical conditions is followed by secondary atomisation, whereby the initially formed droplets break up further into smaller droplets. Secondary atomisation occurs because the newly formed droplets find themselves still under the influence of strong shear forces from the coaxial H_2 flow. Droplet breakup occurs on time scales far shorter than vaporisation of primary droplets under the same conditions (Gökalp et al. 2000), thus secondary atomisation accelerates the overall gasification process.

Under near- and supercritical pressure conditions, the surface tension of droplets may be so low that shear forces cause stripping of fluid from the droplet surface rather than breakup into smaller droplets. The Combustion and Reactive Systems Laboratory (LCSR) in France has produced a large body of experimental work on characterising droplet breakup regimes and vaporisation rates (Gökalp et al. 2000).

2.5.4 Vaporisation

For subcritical conditions, the process following atomisation is vaporisation. After atomising, the propellants must still mix at the molecular level before combustion can occur. However, the diffusion rate of gaseous hydrogen into liquid oxygen droplets is prohibitively slow for the high volumetric combustion rates required. Therefore the atomised droplets must subsequently vaporise rapidly enough to facilitate fast mixing of gas phase hydrogen and oxygen, and allow efficient combustion.

Vaporisation is a term which no longer applies in the supercritical regime since the clear distinction between liquid and gas phases does not exist. As described earlier, droplets will not form during atomisation of a LOx/H_2 coaxial jet under supercritical conditions. Stringy, threadlike structures form, but without surface tension to hold them together they readily dissolve and mix in the annular H_2 flow. This makes the propellant mixing process significantly more efficient for supercritical chamber pressures compared to subcritical pressures.

2.5.5 Combustion

Combustion will occur in regions where sufficient mixing of the propellant species has occurred such that the oxidiser-to-fuel ratio will support chemical reaction. At pressures and temperatures found in LPREs, the time for a reacting O_2/H_2 mixture to reach equilibrium is on the order of 1 μs (Ivancic & Mayer 2002). For a shear coaxial injection scheme the flame is anchored by a small recirculation zone attached to the end of the oxygen injection post. Fuel-rich combustion products are recirculated into this zone, which acts as a flame-holding mechanism, providing the heat to sustain ignition and to begin vaporisation of the incoming

LOx. The reaction zone extends downstream from this LOx-post wake in the shear layer between the oxygen core and annular hydrogen flow. Turbulent length scales in the shear layer span three orders of magnitude up to around 2 mm (this is the range of length scales, from the Kolmogorov to the integral length scale, determined by Ivancic and Mayer (2002)). The shear layer thickness and turbulent length scale increase with downstream distance, but directly after injection the smallest turbulent mixing time, the Kolmogorov timescale, may be on the order of the reaction time, around 1 μs.

In shear coaxial injection, the shear layer tends to separate the propellants, acting as a barrier between the oxygen and hydrogen streams. Extremely low gas density in the reaction zone reduces the aerodynamic forces which drive mixing in the shear layer, thereby leading to a diffusion rate-limiting mode of combustion (Mayer & Smith 2004; Oefelein 2006). Despite this separation effect, shear coaxial injectors achieve combustion efficiencies very close to 100% in LOx/H_2 engines.

2.6 Combustion instability

Combustion instabilities are periodic oscillations of the combustion process in a liquid rocket thrust chamber, manifest as periodic oscillations in the chamber pressure. They are heavily dependent on the geometry of the thrust chamber, and are often the result of excitations of the chamber acoustic modes. There may also be coupling of chamber pressure oscillations with the propellant feed system.

High energy release rates and low loss conditions in thrust chambers favour the excitation of instabilities. Only a tiny fraction of the energy released by combustion is required to sustain the oscillations. Thrust chambers are designed primarily for high combustion efficiency and natural damping mechanisms are usually inadequate to prevent the growth of oscillations once initiated.

With the potential to reduce engine life or even cause catastrophic failure, combustion instability is one of the most important issues faced by liquid rocket engine designers. It must be properly understood and controlled to ensure the success of any liquid rocket engine design.

2.6.1 Characterising combustion instability

The combustion process in liquid rocket engines is never perfectly smooth. Ideally, engine design can keep fluctuations in pressure, temperature and flow velocity in the thrust chamber to a minimum. Combustion is considered to be ‘smooth’ when peak-to-peak fluctuations in chamber pressure during steady state operation remain below 5% of the mean chamber pressure (Sutton & Biblarz 2001). When pressure fluctuations exceed 5%, but occur randomly with no discernable periodicity, the engine is considered to experience ‘rough combustion’, as illustrated by Figure 2.11. Occasionally the pressure fluctuations may interact with natural frequencies in the propellant feed system, engine structure, or acoustic modes of the chamber, resulting in periodic oscillations in the combustion process and possibly amplification of the fluctuations. Periodic pressure oscillations which are discernable from the random-noise fluctuations are designated as combustion instability.

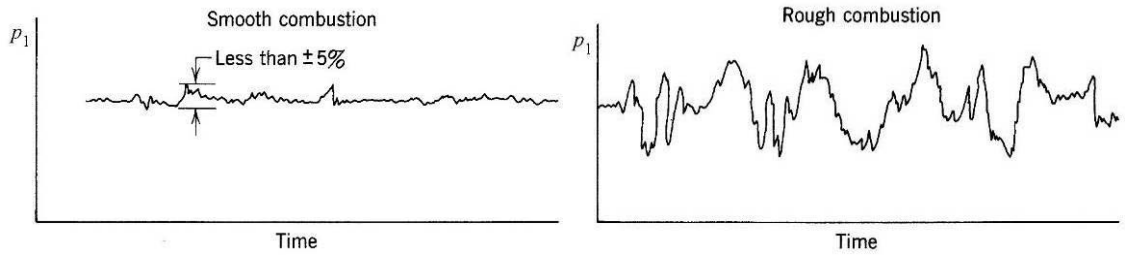

Figure 2.11: Typical traces of chamber pressure with time for smooth and rough combustion (Sutton & Biblarz 2001, p.349).

Instabilities in rocket engines have been loosely categorised by their frequency ranges. Low Frequency (LF) instability, sometimes called 'chugging', is generally associated with periodic fluctuation in the injected propellant flow rate. Pressure fluctuations in the thrust chamber couple with the propellant feed system, or even the entire launch vehicle structure, and result in oscillations commonly in the 10 to 400 Hz range. Intermediate Frequency (IF) instability, classed as being in the 400 to 1000 Hz range, is thought to be largely the result of mechanical vibration of the engine structure. Vibrations in this frequency range may also be caused by fluctuations in the combustion process resulting from flow eddies, pressure coupling with the injector manifold, or propellant mass flux ratio fluctuation. High Frequency (HF) instability, otherwise known as acoustic instability or 'screeching', is generally the result of excitation of combustion chamber acoustic resonances causing oscillations above 1000 Hz. HF instability tends to be the most damaging and the most difficult to solve.

2.6.2 High frequency combustion instability

High frequency, or acoustic, excitation occurs only at discrete frequencies. The walls of the thrust chamber, nozzle entrance and injector face are physical constraints on acoustic wave motion inside the chamber. These constraints prescribe boundary conditions on the oscillatory system which only allow certain modes (frequencies and wave patterns) of oscillation.

Three main classes of HF instability modes have been observed in liquid rocket thrust chambers; longitudinal, transverse, or combined modes. Longitudinal modes are standing waves with the direction of wave propagation along the chamber axis, as illustrated in Figure 2.12a. They are analogous to acoustic standing waves in organ pipes. The injector head at the top acts as a closed end to the cylindrical chamber, and the converging section of the nozzle acts as a semi-closed end at the bottom. Transverse modes are oriented perpendicularly to the chamber axis and can be further classified as radial or tangential. Figure 2.12b shows the acoustic pressure distributions and corresponding gas velocity motion for the first tangential (1T), second tangential (2T), and first radial (1R) modes. If the chamber is viewed axially (in cross-section), radial modes could be thought of as analogous to ripples on a circular pond, with standing waves emanating from the chamber axis. Tangential modes could be thought of as pressure amplitude fluctuations bouncing backwards and forwards across the chamber. The tangential modes could be standing waves with a fixed orientation, but can also rotate as a single vibratory system, called spinning tangential modes, as illustrated in Figure 2.12c. Finally, combinations of these various longitudinal or transverse modes may superimpose, producing complex, three-dimensional modes of oscillation.

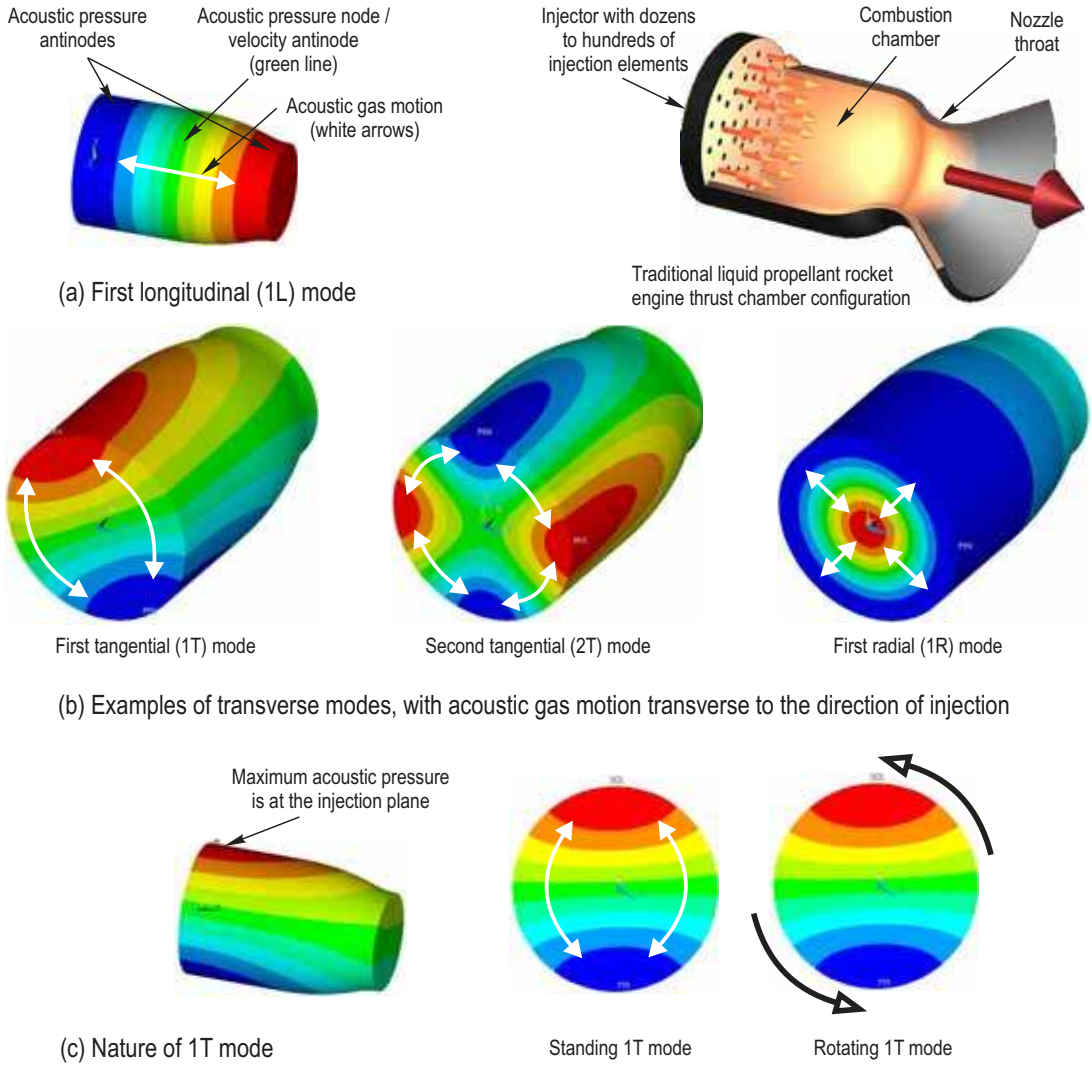

Figure 2.12: Characteristics of transverse modes.

Transverse modes are considered to be the most damaging of combustion instabilities. An established transverse mode can cause spikes in chamber pressure and disrupts the protective boundary layer on the chamber walls, resulting in increased heat transfer rates. In some cases the heat transfer rate has been increased by a factor of 10, melting the chamber walls (Sutton & Biblarz 2001). As can be seen in the pressure distribution of the 1T mode in Figure 2.12c, the pressure amplitude is greatest near the injection plane. This results in the damage caused by 1T-mode instability to be concentrated at the injector; on the injection faceplate itself, and on the chamber walls near the injection plane. Pressure spikes from HF instability can peak at up to twice the mean chamber pressure, causing components to fail. Resulting mechanical vibration levels can be greater than 1000 g, accelerating structural component fatigue or impairing the operation of sensitive on-board equipment. It is imperative to the safe operation of launch vehicles that HF instabilities be properly understood and minimised.

2.6.3 Driving mechanisms of instabilities

In a general sense it has been understood for some time that oscillations in gaseous media may be driven in one of two fundamental ways; by periodic input of mass (gas pulses) or periodic addition of heat energy. Lord Rayleigh (1878; 1945) investigated this second energy

source, heat input, and found a connection between the frequency and amplitude of oscillations in a gaseous system and periodic heat addition to the system. Rayleigh found that if heat was added to a system at the point in a cycle where pressure is at its peak, it would encourage the oscillation (amplitude increased), but if heat is extracted at this point then the oscillation is discouraged (amplitude decreased). Alternatively, oscillations can be promoted by extracting heat at the low pressure point in a cycle, or dampened by adding heat. This principle is commonly known as the Rayleigh Criterion. If, over the course of an oscillatory cycle, fluctuating pressure p' and fluctuating heat addition $\dot{q}'$ are mostly in phase, then their integrated product will be greater than zero. This describes the condition required for amplification of the pressure oscillation, and may be expressed mathematically as

$$\int_0^{2\pi} p' \, \dot{q}' \, d\varphi > 0 \ . \tag{4}$$

Lord Rayleigh further described the influence of the phase of this relationship on frequency. A communication of heat at the point of mean pressure, a quarter-period before or after a pressure peak, will change the frequency of the oscillation. For example, adding heat a quarter-period before a pressure peak will increase the oscillation frequency, whereas adding heat a quarter-period after a pressure peak will decrease the frequency. Heat addition with any other phase will cause a combination of amplitude and frequency change on the oscillating system.

LF instability is driven by an injection-coupled mechanism. Cyclic variations in back pressure cause cyclic variations in propellant flow rate through the feed system which results in cyclic combustion intensity. If the combustion intensity variation is in phase with the back pressure variation then, according to the Rayleigh Criterion, the oscillation will be fed and sustained. While rare, injection coupling is occasionally responsible for HF instability as well. One such example is in the J-2S engine where a 4400 Hz HF instability accompanied LF chugging, and both were attributed to coupling between LOx injector flow and acoustic pressure oscillations (Hutt & Rocker 1995). Increasing the pressure drop of flow through the LOx post was effective in controlling the LF chugging instability, however did not influence HF stability (Hulka & Hutt 1995).

The driving mechanism for HF instability is understood to be intrinsic, meaning the mechanism relates to some process which occurs after the propellant has been injected into the thrust chamber. The acoustic field of HF instability comprises structured, oscillating pressure and velocity perturbations in the medium into which propellants are injected. Pressure or velocity oscillations in the medium somehow affect the combustion of injected propellants, resulting in oscillations in the heat release rate. If the amplitude of the resulting combustion perturbations is sufficient and has the right timing, it is possible to overcome the damping effects on the system and the acoustic–heat release feedback loop results in a self-sustaining instability. Research seems to suggest that the coupling is direct between HF oscillations and the responsible intrinsic mechanisms (Harrje & Reardon 1972), meaning that additional energy release from the combustion process caused by an acoustic oscillation is added to the same half-cycle of oscillation. However, exactly what processes are involved and how energy is transferred to the acoustic field is not fully understood and certainly is yet to be quantified.

Following injection into a thrust chamber, LOx/H_2 propellants undergo a range of processes, some of which are sensitive to local pressure perturbations and some to velocity perturbations.

Pressure sensitive processes which might facilitate coupling with HF pressure oscillations include chemical reaction rates, injection rate, and evaporation rate. Probably the most intuitive pressure-coupling mechanism would be pressure sensitive chemical kinetics. As Putnam (1971) explains, the heat release rate in any combustion process will increase with an increase in pressure. An acoustic pressure oscillation in a rocket combustion chamber will therefore produce localised oscillations in heat release rate. Since the effect of pressure on reaction rate is more or less instantaneous, the heat release rate oscillation would be in phase with the pressure oscillation which, according to the Rayleigh criterion, is the condition necessary for it to promote the instability. Early in the investigation of HF instability, models by Crocco (1952) showed how this type of direct pressure coupling is the most probable driving mechanism. Flame response observations by Knapp and Oschwald (2006) seem to support this mechanism. On the other hand, velocity sensitive processes which might facilitate coupling with HF velocity oscillations include atomisation, mixing, and evaporation rate. General velocity coupling mechanisms suppose the transverse component of acoustic gas motion due to the HF instability promotes mixing of the propellants which in turn results in accelerated combustion and an oscillating heat release rate. These velocity driven heat release rate oscillations may sustain the instability if their amplitude and timing satisfy the Rayleigh criterion. Wieber and Mickelsen (1960) identified coupling of velocity perturbations with droplet vaporisation rate as the most promising candidate, championed again later by Sirignano et al. (1995). Other proposed coupling processes include travelling entropy waves, loss of ignition, detonation and shockwave processes, exploding supercritical droplets, and shattering of liquid streams or drops by gas motion (Harrje & Reardon 1972). Thus researchers have found competing evidence of both pressure and velocity coupling mechanisms, but precise details of which processes are involved, their relative importance, and how they might interact, are not properly understood. Further investigation is required, especially experimental data from representative thrust chamber conditions, to resolve even this more fundamental driving mechanism quandary.

A deeper review of research to address these aspects of HF instability is presented later in Section 3.

2.6.4 Controlling combustion instability

Rocket engine designers have applied various treatments in the past to try to minimise excitation of combustion instability. Low and intermediate frequency (LF and IF) instabilities have been controlled successfully using design modifications based on engineering analysis and simulation. However, LF and IF do not pose as high a risk as high frequency (HF) instability, for which engineering approaches have had only limited success.

LF and IF instabilities are, for the most part, controllable from the design stage of a new launch vehicle. A large enough pressure drop across the injector is usually sufficient to prevent the feed system coupling which causes some LF instability. Oscillation of feed system components, such as a flexible pipe or propellant accumulation cavity, may be prevented simply by changing its resonance frequency to prevent coupling with other components or thrust chamber modes. Sometimes longitudinal LF oscillations in the engine or feed system can couple with the stored propellant in the tanks and entire vehicle structure. Analytical techniques using simplified spring-mass models of the overall launch vehicle are available to avoid this coupling or to determine the appropriate placement of damping measures. Good feed system, pump matching, and engine structural design can minimise the occurrence of IF

instability, which rarely produces oscillations of threatening amplitude anyway (Sutton & Biblarz 2001).

Design methods for preventing HF instability are not well established. Designers usually rely on personal experience with older systems of similar design and test results from experimental engines. Longitudinal mode HF oscillations are usually well damped by the converging nozzle section. Designers of the Vulcain HM-60 engine were able to effectively eliminate longitudinal modes by gently tapering the length of the combustion chamber instead of having a distinct converging nozzle section, according to Sutton and Biblarz (2001). However, Zinn (1972) notes that theoretical and experimental investigations show that nozzle geometry could also act to amplify certain transverse modes.

Axial and transverse combustion distribution directly affects combustion stability for both longitudinal and transverse modes (see Bracco & Harrje 1972; Osborn 1972). Tailoring the distribution of energy release in the chamber can reduce the tendency of pressure and velocity disturbances to couple with the combustion process in regions which support mode propagation. Essentially this principle takes advantage of the Rayleigh criterion by attempting to concentrate energy release away from regions corresponding to antinodes for probable modes of oscillation. A drawback to this method is that distributions promoting stability may be detrimental to heat transfer requirements or combustion efficiency and therefore engine performance and lifetime.

Early in combustion instability research, diagnostic instrumentation limited the effectiveness of fundamental research. Hence many experimental programs tested full-scale engines, aiming simply to develop design trends which would promote stability. Summarised below are some such design trends found to affect engine stability to HF modes, each of which is discussed in considerable detail by Harrje and Reardon (1972).

- Droplet size
  - Larger droplet size results in longer vaporisation time which has a stabilising effect.
- Injection velocity
  - Increasing the axial velocity ratio between the injected liquid propellant stream and surrounding combustion gases has a stabilising effect due to drag forces.
  - However, higher injection velocity leads to smaller droplet sizes, which is destabilising.
- Combustion distribution
  - Tailoring the axial and transverse energy release to areas which do not promote HF oscillations.
- Coaxial injector design features
  - Increasing hydrogen injection angle is stabilising.
  - Optimising oxidiser tube base thickness can be stabilising.
  - Recessing the oxidiser tube is stabilising.
  - Increasing thrust per element in is stabilising.

- Nozzle
  - Nozzle contraction ratio strongly affects longitudinal mode instability. Smaller contraction ratio improves stability.
  - The nozzle can be destabilising to transverse modes.

Such design rules may be helpful in guiding the development of stable engines. However, there are noted exceptions to virtually all of these trends mentioned above. Because the complex interaction of all aspects of engine design influences instability, adhering to any number of these design trends will not guarantee stable operation.

Passive countermeasures have been developed to remove energy from HF instabilities and prevent them from reaching damaging amplitudes. To address the more damaging transverse modes, features such as injector face baffles, injector modifications, acoustic absorption cavities and damping geometry on chamber walls have been applied to combat HF instability with limited success. The A-6 engine on the Redstone rocket managed to avoid triggering HF instability with careful start sequencing. The same approach was attempted for the RS-58 engines for the Atlas booster, but two test launch failures caused by HF instability proved this approach to be unreliable. Atlas development was then delayed by a 14 month program to develop a baffled injector face to prevent HF mode triggering. Figure 2.13 shows a typical injector face baffle configuration for a thrust chamber. The baffles are intended to destroy the symmetry of favoured acoustic modes of the chamber by acting as physical boundaries to transverse fluid motion across the injector face. Vortex generation and viscous damping from the baffle tips also contribute to dissipation of acoustic energy. The RS-58 became the first production engine to use baffles, although the expense of such major modification so late in development of the system was enormous (Monteil & Dykema 1972).

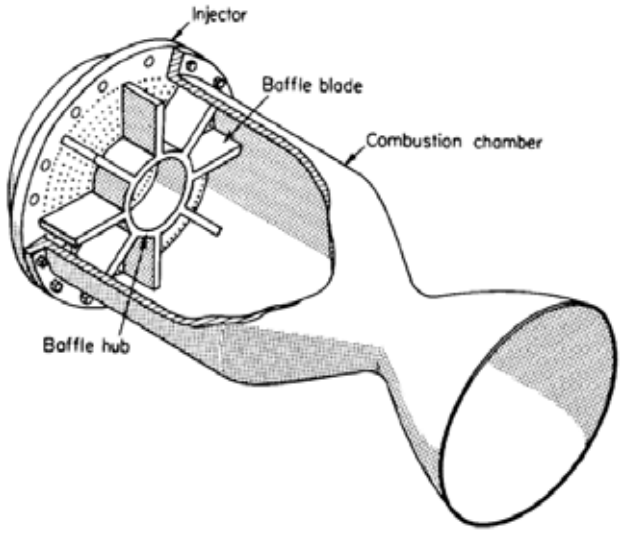

Figure 2.13: Cutaway sketch of a thrust chamber showing the injector-face baffle (Harrje & Reardon 1972, p.157).

Development of the F-1 engine for the Saturn V launch vehicle was another program which suffered at the hands of HF instability. An intensive, and expensive, program to render the engine stable ran for nearly seven years and included more than 2000 full-scale engine tests (Oefelein & Yang 1993). Injector face baffles were eventually developed as a fix for the problem. However, because the fix was determined through trial and error, it required mammoth effort to ensure that it would be effective over all regimes of flight. Ultimately the

baffle development work would only benefit a single engine, the F-1, since these efforts also failed to generate definitive baffle design criteria for optimising baffle numbers, lengths or arrangements in other engines. Applying a similar baffle design during development of the M-1 did nothing to change the stability margins, although it did reduce the amplitude of pressure oscillations when HF instability was triggered (Tomazic, Conrad & Godwin 1968).

A further drawback to baffles is that their addition complicates the oscillation patterns in the chamber and the precise effect is still not fully understood. For example, as part of the Gemini Stability Improvement Program, Anon (1965, cited in Reardon 1972) reported a case where installing baffles produced a new mode which interacted with an existing chamber mode, promoting instability. Thus baffles, and indeed other HF damping devices, usually complicate the instability situation rather than eliminate the problem. Furthermore, damping devices and excessive margins built into the system to stave off instability usually degrade propulsive performance. Nevertheless this typifies the approach for achieving acceptable stability in large LPRE development programs.

Historically the only way to acceptably demonstrate stability in all regimes of engine operation is through costly, time consuming, full-scale testing. Testing full scale motors by inducing sinusoidal transverse oscillations was beyond the capability of any driving device. Instead, short duration pulses of high amplitude were used to try to trigger natural modes of instability. Arranging non-directional explosive charges on the inside of the chamber, or incorporating a pulse gun that blasts inwards from the chamber wall are two techniques used as triggers for stability rating tests. The Chemical Propulsion Information Agency (CPIA) in the U.S. has released guidelines for administering such testing procedures, and criteria for rating the stability of an engine based on testing results (Fry & Klem 1997). During a stability rating test, the induced pressure pulse must damp out within a specified period for the engine to be considered stable. If the engine suffers sustained, organised oscillations with peak-to-peak amplitude greater than 10% of chamber pressure, the engine is classified as unstable. The effectiveness of this procedure is limited by how representative of actual instability initiation the triggers can be and how many tests can be performed for statistical certainty. The procedure is also very expensive, with a great number of tests required over a suitable range of operating conditions and always with the risk of damaging the test engine.

A preferable way to assess engine stability would be through modelling and simulation. Attempts have been made in the past to model combustion instability in the hopes of predicting and hence preventing its occurrence. Combustion instability is a fundamentally complicated problem to model owing to the multitude of dynamic processes occurring simultaneously. Injection, atomisation, vaporisation and mixing processes are continuously occurring and usually overlapping to varying degrees. Mass is added to the system by injection, and heat by combustion. Mean flow in the chamber needs to be taken into account, as well as turbulent fluctuations and instability oscillations. To further impose fluctuations on these processes arising from combustion instability is a demanding prospect. Furthermore, the boundary conditions are complicated due to the distribution pattern of injection elements in the injector face, film cooling flow on chamber walls, and accelerating flow in the nozzle, which partially reflects energy back into the chamber. Priem and Guentert (1962) and Crocco et al. (1960) are examples of researchers who in the past have attempted to develop models to predict instability. However, the success of their models, and those of others, has been limited in practice due to the assumptions and simplifications which are necessary to obtain solutions.

Full-fidelity numerical simulation of rocket engines could provide valuable insight into the complex interactions between dynamical processes, and serve as a tool for engine stability

validation. However, the computational time and resources required to model such a complex system are still prohibitive. Hence the application of computational methods is currently limited to subcriticalsystems and smaller regions of the combustion chamber. For example, modelling of the recessed region of coaxial injectors has revealed behaviour which could potentially be involved in driving instabilities (Zong & Yang 2006). Recent efforts have also made advances in modelling transcritical injection of cryogenic propellants using a large-eddy simulation (LES) approach (Schmitt et al. 2011). Worth noting is that high-fidelity experimental data are still required in order to validate the numerical methods and raise the level of trust in their ability to capture the dynamics of the system.

Ideally, the problem of HF instability should be addressed at the design stage with a sure knowledge of the physics involved. However, the methods currently in use to counter the problem were developed largely by trial and error, and efforts to properly understand HF instability phenomena remain limited. The next chapter contains a review of the literature on HF instability in LPREs.

3. LITERATURE SURVEY

Combating HF instability in a new rocket engine design by trial and error is an extremely expensive exercise and is yet to provide a comprehensive solution. Hence there is a need to understand the mechanisms driving instability so that the problem can be addressed in the design stage before expensive prototyping or testing is conducted. The mechanisms driving instability need to be quantified so that effective modelling and design methodologies can be developed.

This section contains a historical survey of combustion instability research leading up to current efforts. The survey focuses mainly on experimental research relating to HF transverse mode instability, shear coaxial injectors, and LOx/H_2 propellants. Earlier efforts leading up to landmark review publications in 1972 and 1995 are examined first. The trend towards higher operating pressures and the consequences for HF instability research is then explored. Finally, the current state-of-the-art in experimental research from leading agencies in the field is surveyed.

3.1 Investigations up to 1972

Researching combustion processes in rocket engines is in general a difficult task because one is attempting to observe a variety of physical and chemical processes occurring simultaneously at high speed in a high pressure and temperature environment. For this reason progress in the field of combustion instability has been slow since it was first recognised as being a cause of rocket failures in the early 1950s. The most damaging type of instability, HF transverse modes, are almost never observed in industrial combustion processes, so the entire research effort in this area has fallen to the aerospace industry in supporting rocket and turbojet combustor development.

Combustion instability in LPREs was first recognised in the early 1940s, but could only be detected using the most advanced and expensive pressure transducers. The initial drive for research into combustion instability came in the 1950s with the development of intercontinental ballistic missiles. Progress was slow until pressure sensor resolution matured to a level where the oscillations could be detected affordably. Some theoretical work had also begun to address the problem.

Crocco (1951) made the first attempt to theoretically explain the cause for HF instability. Crocco postulated that a pressure fluctuation in the combustion chamber must affect the rates

of various physio-chemical processes involved in propellant combustion. This would in turn cause intensification or weakening of gasification or heat release. Under the appropriate conditions, these fluctuations in heat release could feedback to the pressure fluctuation, reinforcing it. In this manner a high frequency, periodic pressure fluctuation could be self-sustaining. Crocco (1952) built a simple theoretical model which essentially reduced all injection and combustion processes down to two parameters; an amplification factor 'n', and a time delay 'tau'. This 'n-tau' model was a simple way of relating fluctuation of heat release from combustion to the pressure oscillation in the combustion chamber, without having to deal with the physical details of each subcriticalprocess. The n-tau model showed that, if combustion rates were indeed sensitive enough to high frequency pressure oscillations, then organ-pipe modes of instability (longitudinal modes) could be sustained (Crocco & Cheng 1953). Crocco's 1956 publication (cited in Sirignano 1972) refined his original ideas from 1951 and developed the well known 'sensitive time-lag theory'. The theory was later verified experimentally using a variable length chamber to measure the boundaries of operating conditions where HF instability was probable. By comparison with these results, Crocco, Grey and Harrje (1960) showed the time-lag theory to be relatively accurate in predicting the behaviour of longitudinal HF instability. Later, Crocco, Harrje and Reardon (1962) extended the application of sensitive time lag theory to transverse modes. This version of the theory was verified with experimental data using a sector motor, shown in Figure 3.1 to characterise the transverse mode stability limits. The theory predicts several transverse mode phenomena, namely that aerodynamic drag from the presence of liquid droplets has a stabilising effect, whereas increasing the chamber Mach number, concentrating combustion near the injector face, and the acoustic properties of the nozzle are all destabilising influences (i.e. promote transverse instability) (see Crocco 1972).

Figure 3.1: Cutaway sketch of the variable-angle sector motor (Crocco, Harrje & Reardon 1962, p.368).

Purportedly, the first investigation of fluid injection behaviour under external acoustic forcing was conducted by Miesse in the mid 1950s. Miesse (1955) applied high intensity oscillating pressure waves transversely to injected streams of water into ambient air in order to determine the nature and extent of acoustic field effects on free jet break up. As seen in Figure 3.2 for injection of three parallel streams, Miesse showed that free jets certainly will respond to pressure waves. Miesse then subjected the jets to the three main modes of chamber resonance, longitudinal, radial and tangential, by various arrangements of the forcing loudspeakers. Most noticeably for the tangential mode, acoustic resonance affected the dispersion patterns and decreased the solid stream length of the jets. Furthermore, mixing of parallel streams was vastly improved by transverse pressure waves. Considering the observations in Miesse's experiments, it is conceivable that transverse acoustic waves applied to combusting streams

would most likely alter the distribution, intensity, and possibly periodic variation in energy release, somehow resulting in a means for coupling with the pressure oscillation.

Figure 3.2: Droplet stream response to external acoustic forcing for three parallel jets (images of better quality unavailable) (Miesse 1955, p.527).

A literature survey by Harrje (1972) reported that windowed combustion chambers were first used for experimental investigation in 1952 by research groups at the Aerojet and General Electric companies. These chambers made it possible to observe combustion processes occurring inside a firing rocket, albeit in relatively low and unrepresentative chamber pressure conditions. Such work included that of Berman and Cheney (1955), who successfully recorded streak film of longitudinal mode HF instability through the plexiglass slot windows of their lab-scale combustor burning alcohol. From this observation they postulated a coupling mechanism involving entropy wave propagation. Essentially, the mechanism describes a discontinuity in entropy, arising for example from an inhomogeneous oxidiser-to-fuel ratio (*ROF*) distribution at the injector, travelling the length of the chamber and interacting with the sonic shock plane in the nozzle. By conservation laws, they show that the interaction of the disturbance in the nozzle may be reflected back up the chamber in the form of an acoustic wave, which when incident on the injector results in another *ROF* inhomogeneity, or entropy discontinuity, and so closes the cycle. Such a mechanism would, however, operate independently of chamber acoustics, and has lower relevance to transverse mode instabilities.

Another group at Rocketdyne extended the idea to a 2-D ‘slice’ motor in which an entire cross section of the chamber could be observed (Harrje & Reardon 1972). Visualising the inside of combusting engines is an important technique which has been used extensively since these first successful attempts, and is still used currently to provide both qualitative and quantitative insight into processes pertaining to combustion instability.

Some early combustion instability studies conducted at Purdue in 1958 (see Putnam 1971, p.91) used small scale lab motors at relatively low pressures and premixed gaseous propellants. Although transverse modes were observed, the diagnostic techniques were not sophisticated enough to observe heat-release and flame effects, so only very basic hypotheses for explaining the observed phenomena were forwarded. These experiments were not able to realise high pressures or use cryogenic liquid propellants.

Baker and Steffen (1958) claim to be the first to conduct experimental investigation of HF instability in a LOx/H_2 engine. Various injector types and configurations were tested in a small, laboratory scale, low thrust motor with variable chamber length. The group could only confirm the observation of longitudinal modes, although some unidentified high frequency modes occurred for the shortest chamber lengths. A general observation from the tests was that the tendency for spontaneous HF instability with LOx/H_2 was not as prevalent as with other liquid propellant combinations, particularly when using coaxial injectors for which no instability whatsoever was observed. Thus coaxial injectors using the LOx/H_2 combination were established early as having good HF stability properties. Baker and Steffen also noticed from the results of various injector configurations that the driving force for oscillations appeared to be supplied by regions of high heat release per unit volume; implying instability is somehow linked to the combustion process.

Hornstein (1965) set out to test the feasibility of using spectroscopy to investigate HF instability in a lab-scale motor. He used optical probes to guide combustion light via fibres to three photomuliplier tubes; one for detecting hydroxyl radical (OH*) emission, one for methylidyne radical (CH*) emission, and one unfiltered for total luminosity. The simple, cylindrical motor was operated at pressures of 3.4, 6.9 and 10.3 bar. It was powered by a premixed methane-air propellant combination, sonically decoupled from the injection manifold, chosen intentionally to allow the observation of acoustic influence on chemical kinetics as isolated from injection and atomisation/vaporisation processes. Pressure oscillations of the 1L mode near 1100 Hz were accompanied by intensity oscillations of the same frequency and nature in all three optical detectors. For the two lower pressure operating conditions, a time lag of approximately 0.2 ms in the OH* and CH* emission was detected, while at 10.3 bar the lag was no longer detectable and light emission fluctuated in phase with acoustic pressure. The emission fluctuations were interpreted as observation of a pressure-coupled mechanism, where the early chain-branching phase of the methane combustion reaction was responding to pressure, accelerating and decelerating radical production. It was noted that thermal excitation could also account for the OH* fluctuations, noting that "OH* emission, although primarily chemiluminescent in hydrocarbon flames, is also thermally excited and therefore the excited population can be somewhat increased purely by adiabatic heating due to the pressure wave itself." However, analysis of emission response indices suggested the kinetic mechanism to be more likely. The experiments were later repeated by Hornstein, Budnik and Courtney (1966) using liquid pentane and air as propellants. The same general observations were made, although the pressure traces were notably noisier than for methane-air, and emission time lags of 0.3 to 0.4 ms were measured, the longer lag time presumably due to atomisation and vaporisation processes.

Besides pressure waves affecting the combustion process during HF instability, the gas motion associated with the oscillation was also considered to be a possible coupling mechanism. In the 1950s, propellant vaporisation had been identified as a likely candidate process for coupling gas velocity oscillations with the combustion process. A large number of studies concentrated on better fundamental understanding of the vaporisation process so its link to HF instability could be explored. Levine and Bambanek (1956) and Reardon (1961)

(both cited in Reardon 1972) showed through experimentation that transverse velocity components of transverse modes of oscillation have a strong influence on the combustion process, especially in the near-injector region.

Wieber and Mickelsen (1960) provided evidence of a link between the vaporisation process and HF instability. They created a theoretical model for a fuel droplet vaporising in a transverse standing acoustic field. According to the model, the droplet acquired a transverse velocity component and fluctuating vaporisation rate in the presence of the acoustic field. The droplet vaporisation time decreased for higher frequency and amplitude instability. Wieber and Mickelsen offered this result as an explanation for the improved performance of initially low efficiency chambers while experiencing instability. Furthermore, they noted that larger drop sizes may be more likely to amplify fluctuations in a vaporisation-controlled process than small drops.

The results of these and various other experimental efforts conducted between 1954 and 1965 to observe droplet vaporisation and combustion, reviewed by Rosner (1972), provided detailed insight into these fundamental processes. However, Rosner also noted that it was simply too difficult to apply this knowledge directly to full scale rocket thrust chamber design.

The Apollo program in the 1960s was a strong motivator for combustion instability research in the United States. Experimental research with cryogenic propellants began and the sophistication of diagnostic techniques continued to improve. Heidmann and colleagues at the NASA Lewis centre were important contributors to the field at this time.

Heidmann (1965a; 1965b) conducted an experimental study of a liquid oxygen jet combusting in a gaseous hydrogen atmosphere at a time when there had been very little previous experimentation with cryogenic propellants. Heidmann's aim was to get a general physical description of a stable combusting liquid oxygen jet for comparison with studies of other propellants and to identify aspects requiring further investigation. Further to this goal was that of observing HF instability to determine if cyclic variation in atomisation and other phenomena, which had been predicted from non-combusting and theoretical studies, could be detected. Using a two-dimensional, 'pancake' shaped chamber, jets of liquid oxygen were injected radially into a diffuse, gaseous hydrogen atmosphere. Heidmann could induce a HF spinning transverse mode of around 3500 to 5000 Hz by injecting gaseous nitrogen tangentially into the chamber. During instability the oxygen jet length was observed to decrease and the jet breakup process appeared to respond to the oscillations. Reduction in the length of the LOx jet for various amplitudes of instability can be seen in Figure 3.3. Similar behaviour would later be observed in experiments with more conventional chamber configurations.

The behaviour of the oxygen jet during oscillations led Heidmann to believe that the driving mechanism involved velocity sensitivity of the energy addition processes. A velocity perturbation seemed to increase the jet breakup and/or atomisation process, accelerating the release of combustion energy. The velocity cycle peaks twice per pressure cycle so, ordinarily, in-phase and out-of-phase energy additions tended to cancel out. However, the steady tangential flow induced by tangentially injecting N_2 into the pancake chamber increased the component of in-phase energy addition, allowing transverse oscillations to become self sustaining.

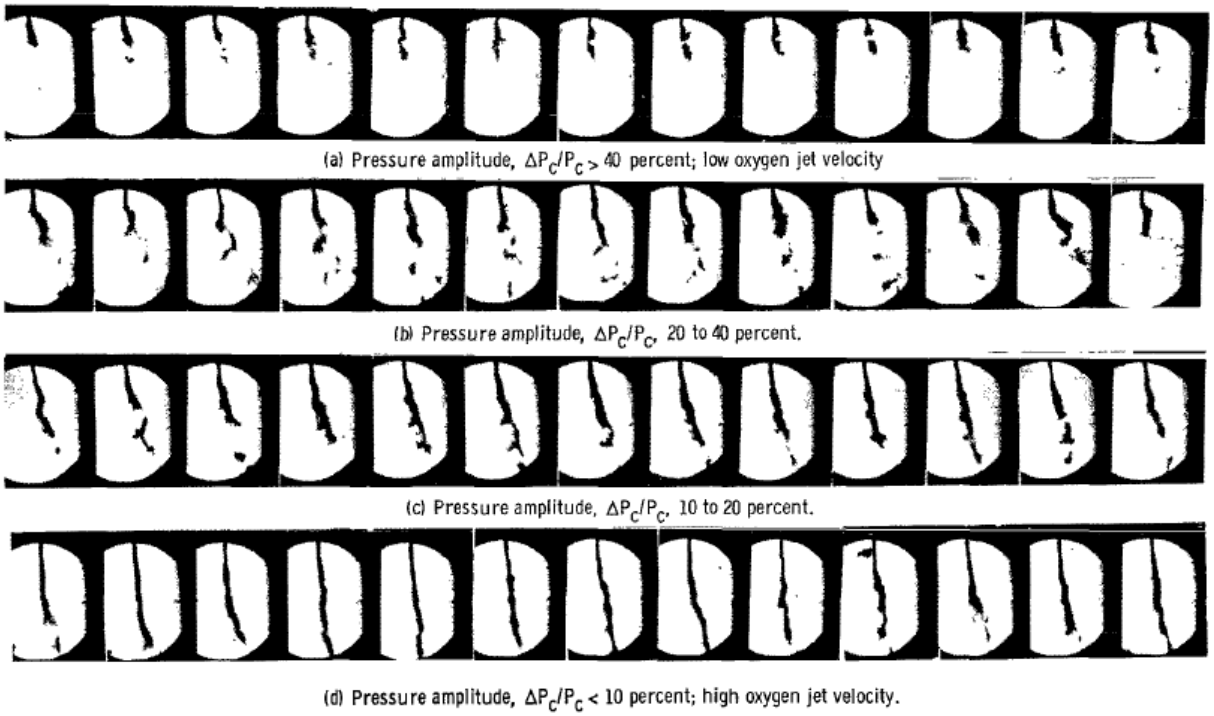

Figure 3.3: Oxygen jet length reduction during transverse mode acoustic instability (Heidmann 1965b, p.10).

The indication of a connection with the atomisation/vaporisation processes from his experimental work led Heidmann and colleagues to conduct a theoretical analysis of droplet vaporisation in a combustor with superimposed transverse pressure oscillations (reported in Heidmann & Wieber 1966a; 1966b). The model did not include combustion, just droplet vaporisation in combustion products at representative combustion temperatures. In general, the response to transverse acoustic oscillation was a decrease in vaporisation time of the propellant. Another important observation was that the oscillation in vaporisation rate of the propellant occurred at twice the frequency of the acoustic pressure oscillations. This is due to the vaporisation model's sensitivity to the velocity difference between droplet and combustion gases, which changes direction twice per acoustic pressure cycle, supporting the explanation forwarded in the previous experimental work.

The vaporisation rate response was determined to be made up of harmonic components of the basic sinusoidal pressure oscillation frequency. It did not simply follow the sinusoidal form of the pressure oscillation and hence could not be described by a gain and phase angle alone. To circumvent this complication, Heidmann and Wieber (1966b) developed a response factor which could be thought of as an effective gain. The response factor is essentially the degree of driving or damping which the vaporisation process feeds back to the oscillation. It takes positive values when the vaporisation rate and chamber pressure are both above or both below their mean values, which according to the Rayleigh criterion (see Expression 4, Section 2.6.3) should induce amplification. Similarly, when the vaporisation rate and pressure are on opposite sides of their respective means the response factor is negative. The response factor N takes the form:

$$N = \sum \frac{w'/\overline{w}}{p'/\overline{p}} \ , \tag{5}$$

where w' and $\overline{w}$ are the fluctuating and mean mass source terms (containing the vaporisation rate), respectively, and p' and $\overline{p}$ are the fluctuating and mean pressure. Summing the response factor for singular droplets over an array of droplets representing the combustion chamber volume is intended to indicate whether the particular operating condition will support the HF instability. In the same year, Heidmann and Wieber (1966a) also presented a simplified, linear formulation of their model. This version used a form of the Rayleigh criterion to express the response factor as:

$$N = \sum \frac{\int_0^{2\pi} \frac{w'}{\overline{w}} \frac{p'}{\overline{p}} d\varphi}{\int_0^{2\pi} \left(\frac{p'}{\overline{p}} \right)^2 d\varphi} \quad . \tag{6}$$

Overall combustor response obtained by summing over an array of response factor results is intended to provide a more relevant design tool for thrust chamber design. Figure 3.4 is a plot of the response curve for n-heptane calculated numerically using the original, nonlinear model formulation. It indicates combustion response initially increasing to a peak, positive value where driving of instability would be strongest. Following this peak the response then decreases eventually to negative values at higher frequencies, indicating that instability of higher frequencies is less likely to be sustained. As pointed out by Heidmann and Wieber (1966b), the form of the response curve is characteristic of a damped resonant system, with a peak response and then negative feedback at higher frequencies. This is an important observation for engine designers because it implies that it may be possible to somehow detune the vaporisation process from the acoustic frequencies of the thrust chamber, thereby preventing instability coupling. However, according to Putnam (1971), the value of a response factor analysis to the designer is highly dependent on how accurately the controlling processes are parameterised and weighted.

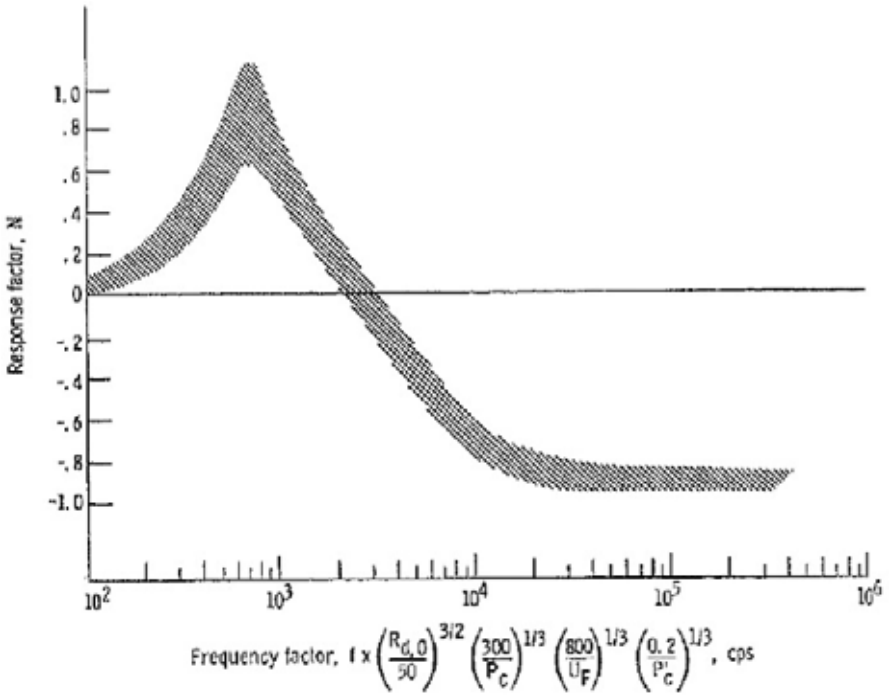

Figure 3.4: Response factor curve for n-heptane based on vaporisation parameters (Heidmann & Wieber 1966a, p.8).

A response curve for oxygen droplets vaporising in LOx/H_2 combustion products was produced for comparison with other propellant combinations. As can be seen in Figure 3.5, this result showed no negative response factor region (i.e. no region of negative gain). The significance of this could be that LOx/H_2 engines may not enjoy an operating range immune to HF instability as predicted for other propellants. However, this result for oxygen should be considered with caution, since the two versions of the model are contradictory on this matter. When calculated with the linear, analytical version of the model, the oxygen response curve always had the same form as for n-heptane, which ends in negative response values in the higher frequency range.

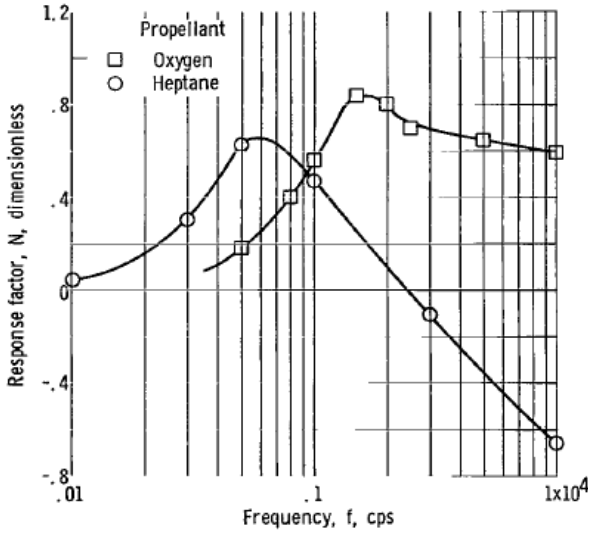

Figure 3.5: Response curves for heptane and oxygen (Heidmann & Wieber 1966b, p.17).

In the 1960s several researchers, for example Jones (1964) and Dahlberg (1965) (both cited in Dykema 1972), discovered an important link between the stability of thrust chambers using coaxial injection of LOx/H_2 and the temperature of the injected hydrogen. Experimentally, it was found that for a given LOx/H_2 engine configuration, there exists a hydrogen injection temperature below which spontaneous HF instability will occur. Later this effect was explained as the result of hydrogen temperature affecting its injection dynamics in the following manner. Decreasing the H_2 temperature increases its density which, for a constant mass flux, decreases injection velocity in turn. Lower injection velocity makes the H_2 stream more responsive to chamber pressure fluctuations and may consequently develop an oscillation. Oscillating injection rate causes oscillation in the combustion rate which promotes the initial pressure oscillation, thus sustaining the instability. A theoretical model by Feiler (1967) supported this hypothesis, showing that for low H_2 temperatures injection coupling becomes important for driving HF instability just as it is for LF instability.

This hydrogen temperature stability threshold could be used by researchers as a way of rating engine stability. The hydrogen injection temperature was gradually decreased to find at what point a particular configuration became unstable. For example, it was used in the early 1960s in the development of the J-2 engine, the upper stage engine for the Apollo program. Initial prototype versions of the J-2, tested at full scale, used simple showerhead injectors. During start up this type of injector always experienced spontaneous HF instability. Baffles were installed to control these instabilities, although bomb testing could still induce instabilities at higher H_2 temperatures than were found for the temperature ramping stability margins (Hulka

& Hutt 1995). This indicates that while H_2 temperature is an important parameter in HF instability, the coupling mechanism may not be solely dependent on some H_2 transition temperature.

J-2 engine development then shifted to the use of shear coaxial elements, which immediately improved H_2 ramping stability margins over those of the simple orifice injectors; highlighting the inherent stability of coaxial injectors. Initially, the central LOx post of the coaxial elements was flush mounted with the injector face. Recessing the post was found to lower H_2 ramping stability temperature further (more stable), while at the same time improving combustion efficiency (Tomazic, Conrad & Godwin 1968). Thus the H_2 ramping technique was useful in establishing design rules-of-thumb for engine stability.

In the late 1960s a research group lead by Wanhainen at NASA's Lewis Research Centre used hydrogen temperature ramping in a generalised, systematic investigation of transverse mode combustion instability in coaxial injector, LOx/H_2 engines (at subcritical pressures). In Wanhainen's studies, correlation of experimental results revealed stability trends for various engine design parameters. Wanhainen, Parish and Conrad (1966) reported that the combustor was stable for hydrogen-to-oxygen injection velocity ratios *VR* greater than 6.5 and unstable for less than 6.5. Hydrogen-to-oxygen injection area ratios less than 1 improved stability, without decreasing engine performance. Tapering the oxidiser tube gives a higher pressure drop for lower exit velocity, allowing higher *VR* while retaining a higher injection pressure drop for LF stability. Recessing the oxidiser tube also improved stability. Wanhainen, Feiler and Morgan (1968) reported that decreasing the contraction ratio (increasing nozzle throat size) improved stability. Decreasing the oxygen injection temperature (increasing density) improved stability. Increasing the oxygen jet diameter improved stability. Changing the chamber pressure by throttling the propellant injection flow rate did not affect stability. Changing the contraction ratio while keeping either the chamber pressure or injection flow rate constant did not affect the amplitude or mode frequency of any instability experienced. Wanhainen and Morgan (1969) reported that leaving an annulus void of injector elements at the injector perimeter, by not extending the radial element distribution all the way to the chamber wall, was detrimental to tangential mode stability. Injector element spacing did not affect combustion performance.

Physical explanations for the trends described in Wanhainen's studies were not offered. However, the goal was to produce empirical correlations useful to designers of shear-coaxial injection elements, rather than advancing understanding of the fundamental processes. The fuel temperature stability effect has yet to be explained, as there are conflicting theories as to whether the controlling mechanism is intrinsic or injection-coupled (see Hutt & Rocker 1995). While the empirically derived rules-of-thumb have been useful to designers, there are almost always exceptions to these rules observed during operation of full-scale engines or sub-scale experiments. For example, while Wanhainen found LOx-post recess to improve stability, Tamura (2005, cited in Nunome et al. 2009) observed worsening HF fluctuations with increasing recess depth.

All early work in the field of liquid propellant rocket engine combustion instability culminated in 1972 in a landmark publication labelled NASA SP-194, *Liquid propellant rocket combustion instability,* edited by Harrje and Reardon. By this time there was enough evidence to suggest that HF instability is most likely controlled by the vaporisation and combustion processes. Droplet size parameters and observed oscillation frequencies were observed to be related. This suggests that the droplet burning process is the controlling

mechanism and instability will be able to be predicted with a model that looks at the droplet processes in sufficient detail (Harrje & Reardon 1972).

Harrje and Reardon (1972) present a review of theoretical models produced by various authors for unsteady combustion of a liquid droplet in ambient gas (with $P < P_{crit}$) undergoing small amplitude oscillations. The models showed coupling of the oscillations with various stages of the droplet vaporisation and combustion processes whenever the frequency became commensurate with the characteristic time of each particular process. Particularly promising was the fact that the predicted ranges of coupling frequencies for each process were consistent with frequencies where HF instability was known to occur, however no study had combined the effects of all processes in a single model so this outcome was never verified. Nevertheless, one outcome which was confirmed by practically all studies was that at high enough frequencies coupling of the combustion and oscillations will no longer occur.

3.2 Investigations from 1972 to 1995

For a time it was felt that the knowledge contained in NASA SP-194 would cover virtually all engineering requirements for future LPRE development programs. Development of the space shuttle main engine (SSME) in the 1970s drew on this knowledge and by the late 1970s HF instability was receiving very little attention. Then, in 1980, the second flight (L02) of the European Ariane 4 rocket was destroyed in flight due to combustion instability in one of its first-stage Viking engines (Yang & Anderson 1995). This incident served as a reminder to the LPRE research fraternity that HF combustion instability was far from being conquered and more work should be done to properly comprehend the fundamental processes at work. The storable-propellant upper stage Aestus engine for Ariane achieved stability with acoustic absorbers. Nevertheless, the engine suffered an episode of HF instability during Ariane 5 flight V510, resulting in the failure of the stage to reach its planned orbit. While never having experienced HF instability in flight, the two cryogenic LOx/H_2 engines for Ariane, HM7/HM7B and Vulcain/Vulcain2, were able to be made unstable during development testing with very low H_2 injection temperatures of below 30 and 50 K, respectively (Preclik & Spagna 1989). The Ariane program motivated continued research in Europe since the 1980s, while the advanced launch system (ALS) program (later cancelled) was the driver in the US.

Initially, research efforts returned to trying to characterise the injected flow. Simulants were often used in place of combustible propellants to study injection and mixing phenomena. Improvements in diagnostics allowed more detailed examination of such phenomena. Computational tools improved rapidly allowing more sophisticated modelling and simulation to complement experimental work. There was also renewed interest in production of systematic experimental data for use in refining models and verifying computational tools.

Another landmark publication was produced in the US in 1995, entitled *Liquid rocket engine combustion instability,* edited by Yang and Anderson (1995). This book was designed as an extension of NASA SP-194, drawing together the work done since 1972.

3.3 High pressure research

Higher chamber pressure results in a higher value of specific impulse; hence by the late 1960s it was becoming more common to have thrust chambers operating above the critical pressure of the propellants. Wieber (1963, cited in Rosner 1972) showed that, when injected into an

environment above the critical pressure P_{crit}, it was possible for propellant droplets to be heated above their critical temperature T_{crit} before vaporisation is complete, hence subjecting the propellant to supercritical conditions.

Under supercritical conditions, atomisation and vaporisation processes cannot be described in the same way as for subcritical conditions since surface tension, latent heat of vaporisation, and the clear distinction between liquid and gas phases no longer exist. It was recognised quickly that conventional subcritical combustion concepts were invalidated at supercritical chamber pressures and that this would drastically impact rocket engine combustion instability analysis. Effectively it was the turbojet and rocket engine industries alone that encouraged special effort into understanding combustion at high pressures.

Spalding in 1959 had already noticed the trend towards higher pressure in turbojet and rocket combustors and addressed the shortcomings of older droplet combustion theory at near-critical pressure. For subcritical conditions, the pressure dependence of vaporisation-combustion rate arose from the pressure dependence of latent heat of vaporisation; however, heat of vaporisation tends to zero approaching the critical pressure. Hence older theory gave droplet combustion times tending to zero as the critical pressure was approached. Spalding (1959) took into account transient effects in the droplet and surrounding gas and created a new theory valid at and around the critical point. Both Spalding and later Rosner (1967) showed that for supercritical pressures fuel droplet burning time actually increases with pressure (with $P^{1/3}$ dependence), in contrast to subcritical droplet combustion time which decreases for higher pressures.

Newman and Brzustowski (1971) claim to be the first to have done experiments on fluid injection into a supercritical environment. A single jet of liquid carbon dioxide (CO_2) was injected into a gaseous nitrogen (N_2) environment with the intent of investigating jet disintegration and spray droplets. The flow was visualised using the backlit shadowgraph technique to record still images. With the N_2 above the critical pressure of CO_2 but initially below its critical temperature, Newman and Brzustowski observed droplets from the injected CO_2 stream become finer as the temperature approached critical. Eventually, for supercritical pressure and temperature, the surface heating of liquid jet and subsequent reduction in surface tension caused the jet breakup to appear more like a continuum flow rather than heterogeneous liquid-gas mixture. In other words, the jet appears to gasify directly without first vaporising.

Aerojet ran an experimental program throughout the 1960s called Hi-Pc which specifically investigated high pressure combustion stability phenomena in LOx/H_2 engines. One of the main objectives of the program was to investigate the effect of injector pattern on stability. Hefner, Reardon and Smith (1967, cited in Dykema 1972) collected results from experimental stability studies ranging from subcritical to supercritical pressures. Correlated results indicated that the characteristic combustion time decreased with increasing chamber pressure for $P < P_{crit}$, however for $P > P_{crit}$ the chamber pressure dependence disappeared. It was postulated that the absence of heat of vaporisation above the critical point is responsible since vaporisation plays a critical role in combustion time for subcritical pressures. Shear coaxial injectors proved to have the best stability in the widest range of conditions. A more general conclusion from Aerojet's experimentation was that there was no apparent difference in the manifestation of HF instability between subcritical and supercritical chamber pressures (Dykema 1972). That means combustion instability still results in potentially damaging oscillations in chamber pressure for supercritical conditions just as it does for subcritical pressure.

The ONERA operated 'Mascotte' test bench, the P8 test bench at DLR Lampoldshausen, and sub-scale combustors at Pennsylvania State University in the U.S. have been used extensively for investigations of cryogenic spray flames from shear coaxial injectors at high pressures. The application of optical diagnostics in particular has provided wealth of information about the basic structure of LOx/H_2 and LOx/CH_4 flames. Optical diagnostic techniques include OH* and CH* emission detection using photomultipliers or high-speed imaging, backlit shadowgraph imaging, laser diagnostic techniques such as planar laser induced florescence, and CARS temperature measurements. Such efforts are well summarised in review papers by Candel et al. (1998; 2003; 2006), Mayer et al. (1998b), Yeralan, Pal and Santoro (2001), and Grisch et al. (2004). A recurring finding from investigations with imaging is that the behaviour of spray flames rarely conforms to that predicted by phenomenological models. Primary breakup mechanisms under reacting conditions rarely coincide with those observed under cold-flow conditions.

Parallel numerical simulation efforts complement the experimental work at the Mascotte test bench. Schmitt (2011) presented results of large-eddy simulation (LES) of LOx/CH_4 flames which capture well the flame structure observed in Mascotte tests. Similar simulation of LOx/H_2 flames are reported to be currently underway. Oefelein (2006), at Sandia National Laboratories in the U.S., has also had success in modelling LOx/H_2 flames at both subcritical and supercritical pressures. Oefelein used both LES and direct-numerical simulation (DNS) techniques to study flames from shear coaxial injectors. For supercritical flames, the mode of combustion is dominated by diffusion mixing of LOx and H_2.

In the mid 1990s, the U.S. Air Force Research Laboratory (AFRL), The Pennsylvania State University, and the German Aerospace Centre (DLR) began parallel experimental research efforts to gain better understanding of injection, atomisation, mixing and combustion processes under high pressure conditions. Major outcomes of the efforts are reviewed by Oschwald et al. (2006). Initially, the simplest case of a single, round jet of liquid nitrogen injected into a supercritical gaseous nitrogen environment was studied, for example by Oschwald and Schik (1999), Oschwald and Micci (2002), and Chehroudi et al. (2003). The data from these tests was used to produce a model of the nitrogen jet breakup process. While showing that improved experimental data would help produce more accurate models, the single nitrogen jet data were not applicable to coaxial injectors or injection into environments of other species.

The agencies then moved on to investigate non-reacting coaxial injection. Glogowski et al. (1994), and Puissant, Glogowski and Micci (1994, cited in Mayer & Tamura 1996) were reportedly the first to study supercritical coaxial injection using liquid and gaseous nitrogen simulants. Their experiments were designed to simulate injection conditions in the pre-burner of the space shuttle main engine (SSME). Imaging showed the spray contracting with chamber pressure increasing up to the critical pressure, then longer liquid breakup lengths at supercritical pressures. Oschwald et al. (1999) used spontaneous Raman scattering to investigate coaxial jets of liquid nitrogen and hydrogen. These studies, as well as others reviewed by Mayer and Smith (2004), revealed much about the thermodynamic property variations and mixing behaviour in binary propellant coaxial injection under both subcritical and supercritical pressures.

At the AFRL, the facility previously used to apply an acoustic field to a single nitrogen jet was used to excite a cold-flow liquid nitrogen-gaseous nitrogen (LN/GN_2) coaxial jet (discussed later). Meanwhile, the DLR worked on combusting coaxially injected LOx/H_2 jets. Mayer and Tamura (1996) observed LOx/H_2 jets combusting under subcritical and

supercritical pressures which provided important insight into atomisation and combustion processes taking place in real rocket thrust chambers. Shadowgraph images in Figure 3.6 from near-critical combusting experiments by Mayer et al. (1996) show the absence of a well-defined boundary between liquid core and annular gas flows as exists for subcritical conditions. Rather, turbulent gas phase mixing between a dense and a light fluid in the shear layer seems to more accurately describe the flow regime. Figure 3.7 provides a comparison of shadowgraph imaging for subcritical and supercritical chamber pressures. At supercritical pressure, stringy, threadlike structures develop from the oxygen core in place of droplet formation, but these structures rapidly dissolve before being given the opportunity to detach. Mayer and Smith (2004) also noted that drastic expansion of the fluid with small increases in temperature occur near the critical point, thus heat transfer also influences the jet breakup process. Observed behaviour was markedly different to that in cold-flow experiments, highlighting the importance of measurements under combusting conditions to complement cold-flow results.

Figure 3.6: Flame and flow field imaging of the near injector region of a reacting flow of LOx/H_2 at 45 bar chamber pressure (modified from Mayer et al. 1996).

Figure 3.7: Comparison of back-lit shadowgraph imaging of the flow field for (a) subcritical and (b) supercritical chamber pressures (modified from Mayer et al. 1996).

One of the significant findings from the 1996 Mayer and Tamura study regarded the influence of various injection conditions on propellant mixing. Chamber pressure was found to have the strongest influence, with mixing performance improving with increasing pressure. The relative velocities of injected propellants and their densities also influenced mixing in the shear layer between coaxial flows. Since density is a factor, it was suspected that hydrogen injection temperature may influence mixing. However, results showed that the effect of combustion heat on species density in the shear layer far overshadowed any influence of the initial H_2 temperature.

Woodward et al. (2006) at Pennsylvania State University attempted to improve correlations between liquid oxygen core length and momentum flux ratio (J) by conducting experimental observations of reacting, coaxially injected LOx/H_2 at a range of pressures from subcritical to supercritical. The researchers also chose extreme flux ratio values from $J = 22$ to 50, higher than any production coaxial injectors, in order to evaluate the behaviour of existing models just outside the normal operating range of existing engines. In the classical, phenomenological, core-stripping spray model, the dense core quickly breaks up into a drop cloud and core length decreases in proportion to J. Woodward et al. did not observe this trend. Rather, a long, sinuous oxygen core was still present even for very large values of J, with the core eventually breaking up into large structures which vaporised/dissolved in the core wake. A new correlation based on density ratio, Reynolds number and Weber number predicted the behaviour more accurately than older inverse-J scaling correlations. Woodward further suggested that, because the observed oxygen cores were so long, their residence time provides chamber bulk flow and other dynamical influences the opportunity to affect breakup and mixing. Therefore, injection parameters alone may be insufficient to completely characterise the breakup and mixing process, as many researchers have previously hoped (see Yang & Anderson 1995).

For supercritical chamber pressures, Woodward et al. (2006) did not observe oxygen droplets around the oxygen core at supercritical chamber pressures and suggested that the reason may not simply be because the oxygen was in a supercritical state, as claimed in DLR papers such as by Mayer and Tamura (1996). Instead it was supposed that atomised droplets in high shear regions of the jets are too fine-scaled to resolve in these experiments and are accelerated by the shear flow and consumed quickly by combustion. In essence, Woodward et al. were suggesting that droplet dynamics may still play a role in injection processes even at supercritical chamber pressures.

Smith et al. (2007) and Chehroudi et al. (2003) noted that stability limits had been presented previously for use in designing LOx/H_2 engines, for example by Heidmann and Wieber (1966a) and Wanhainen et al. (1966), but only for subcritical pressure conditions. Smith and colleagues at DLR addressed the lack of data available for stability rating at supercritical pressures in LOx/H_2 combustors by conducting a systematic experimental investigation of coaxial injection for a wide range of representative thrust chamber conditions. Two of the major findings from this work concerned the influence of propellant injection velocity ratio and temperature on combustion efficiency. Combustion efficiency was found to diminish and the intense part of the flame shifted axially downstream with decreasing velocity ratio. This was true for all pressure regimes, but the effect was more dramatic for near- and supercritical pressures. A further observation was that higher hydrogen injection temperatures gave consistently better combustion efficiency for supercritical pressures, whereas for near- and subcritical pressures there was no discernable effect. Because these injection conditions were observed to have such strong influence on combustion efficiency and flame location, it is expected that they will also influence combustion instability coupling mechanisms.

Although most of the findings from high pressure experimentation described in this section do not relate directly to observations of HF instability, they should be considered during the conduct of any HF instability research under high pressure conditions.

3.4 Recent HF instability research

The remainder of this chapter focuses on the advances in HF instability research since the landmark publication by Yang and Anderson in 1995. Much of this content was also covered in the thorough review volume by Culick (2006), but is also reviewed here in detail for its relevance to the current project. A further important publication by Dranovsky (2007) is noted for its review of the major history of combustion instabilities in the former Soviet Union. The content of this volume is not addressed directly in the current work because Soviet combustor heritage is focussed largely on kerosene-based propellants and gas-centred, swirl coaxial type injection elements.

Experimental research in the field of HF instability has reached the point where externally forced oscillations are being imposed on rocket-like injection conditions, either cold-flow or combusting, in order to study injection and combustion processes under simulated conditions of instability. Currently, the leading research institutions in the field include the Air Force Research Laboratory (AFRL), Pennsylvania State University, Purdue University and Georgia Institute of Technology in the U.S., the DLR in Germany, the National Centre for Scientific Research (CNRS), the National Aerospace Laboratory (ONERA) and École Centrale Paris in France, and the Japanese Aerospace Exploration Agency (JAXA) in Japan. The following is a summary of various controlled experimental studies investigating the effects of acoustic fields on injected jets, both cold-flow and reacting, under a variety of rocket-like conditions.

3.4.1 Non-reacting flows

Recent efforts at the AFRL concentrate on detailed investigation of non-reacting injection conditions. Chehroudi and Talley (2002, cited in Chehroudi et al. 2003) applied a loudspeaker-forced transverse acoustic wave to a stream of liquid nitrogen injected into gaseous nitrogen at subcritical and supercritical pressures. From the back-lit shadowgraph images in Figure 3.8, it can be seen that in the plane parallel to wave propagation the jet was

constricted, or narrowed, whereas perpendicular to the direction of wave travel it was broadened. The effect on the jet was greatest for low nitrogen flow rates and pressures up to near-critical. Interestingly, when the chamber pressure equalled the nitrogen critical pressure the researchers detected no significant impact of the acoustic waves on the jet.

Chehroudi, Davis and Talley (2003) then modified this experiment so the acoustic field could be applied to a liquid nitrogen-gaseous nitrogen (LN_2/GN_2) coaxial jet. Imaging such as that shown in Figure 3.9 revealed the jet taking on a sinusoidal shape under the influence of the transverse wave. The group then systematically investigated the jet under subcritical, near- and supercritical chamber pressures (Davis & Chehroudi 2006). Previous work by Heidmann (1965b) reported definite decrease in the observed length of the dense, inner oxygen jet during transverse instability, and therefore attention was paid to this aspect also. Backlit images in the Davis and Chehroudi experiments showed the dense core length decreasing for higher chamber pressure, higher *VR*, and higher outer jet temperature. This result implies faster mixing for these conditions, and conforms to results from numerous other studies. With acoustic driving, the core length fluctuates, and the level of fluctuation was observed to decrease for higher *VR*. Later, Davis and Chehroudi (2007) hypothesised that the dense core fluctuation could somehow serve as a feedback mechanism for the instability driving process and that higher *VR* improves stability by weakening this fluctuation.

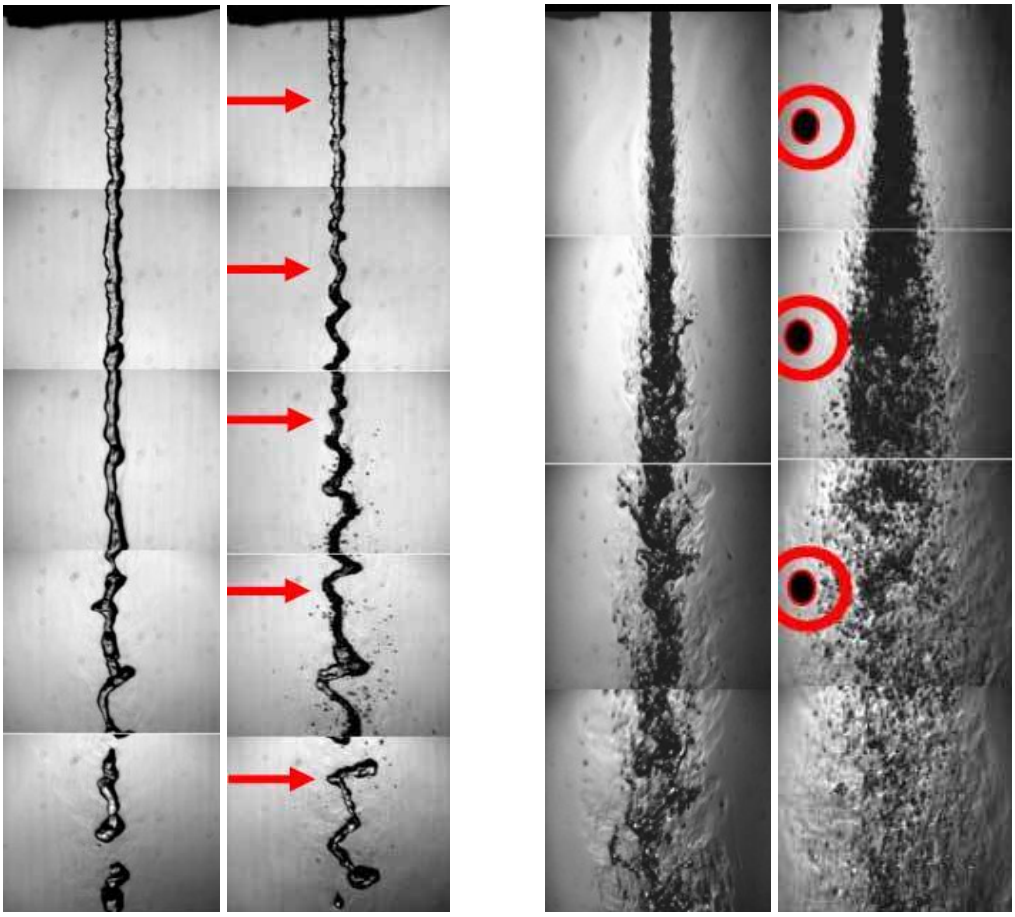

Figure 3.8: Interaction of acoustic waves with a single LN_2 jet injected into GN_2 under subcritical conditions (Chehroudi et al. 2003, p.19).

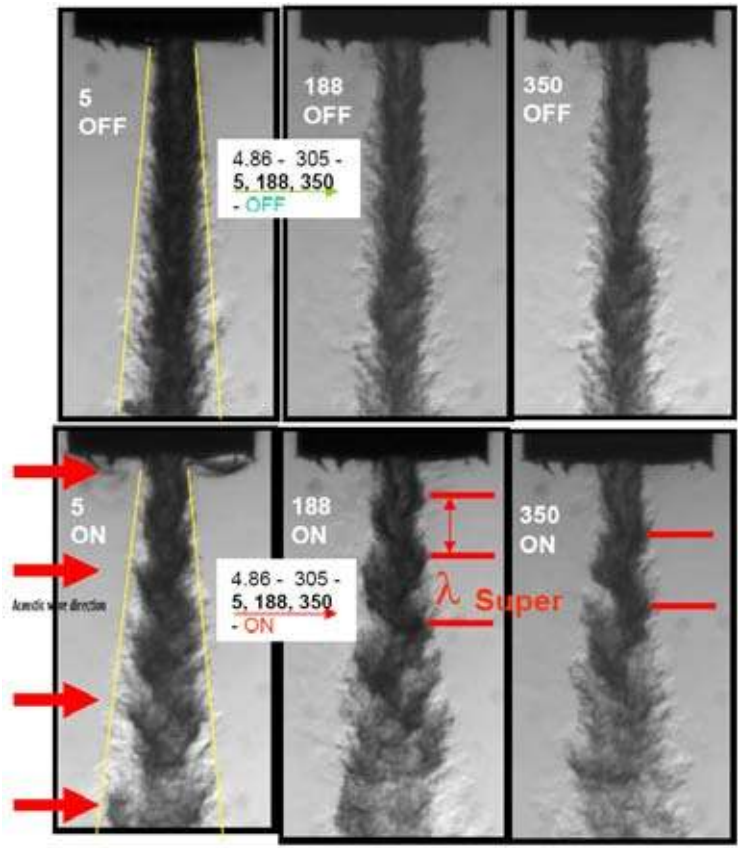

Figure 3.9: Interaction of acoustic waves with a coaxial jet of LN_2/GN_2 under supercritical conditions (Chehroudi et al. 2003, p.26).

A further achievement of this study was the use of high speed cinematography to confirm that transverse jet oscillation under acoustic excitation is still present for near- and supercritical pressure conditions, although the observed effect is less pronounced than for subcritical pressures. Figure 3.10 shows some of these results. Previous efforts had not succeeded in directly observing jet oscillation due to acoustic forcing at supercritical pressures.

Liu et al. (2006) simulated the experimental conditions of Davis and Chehroudi's 2006 investigation using CFD methods. In their results, Liu et al. observed trends consistent with the experimental observations and demonstrated that acoustic excitation had a substantial influence on the flow dynamics. Even small amplitude forcing caused noticeable wave structures on the jet.

It is important to note from the studies by Davis and Chehroudi (2006) and Liu et al. (2006) that the jet was located at a velocity antinode (pressure node) of the induced acoustic field. Hence acoustic velocity perturbations undoubtedly have an important influence in the acoustic coupling process. The visible influence of velocity perturbations was seen by Davis and Chehroudi to diminish as chamber pressure approached the critical pressure. The influence of pressure perturbations was detected by Knapp and Oschwald (2006) in a reacting experiment for subcritical pressures, but is yet to be examined at supercritical pressures. Perhaps the relative importance of pressure coupling comes to outweigh that of velocity coupling for near- and supercritical chamber pressure conditions. Thus the fundamental driving mechanism for HF combustion instability changes to a different mode as the propellant critical pressure is approached and exceeded. Clearly further research is needed to investigate the relative

importance of the pressure and velocity coupling mechanisms on coaxial LOx/H_2 flames at subcritical through supercritical chamber pressure conditions.

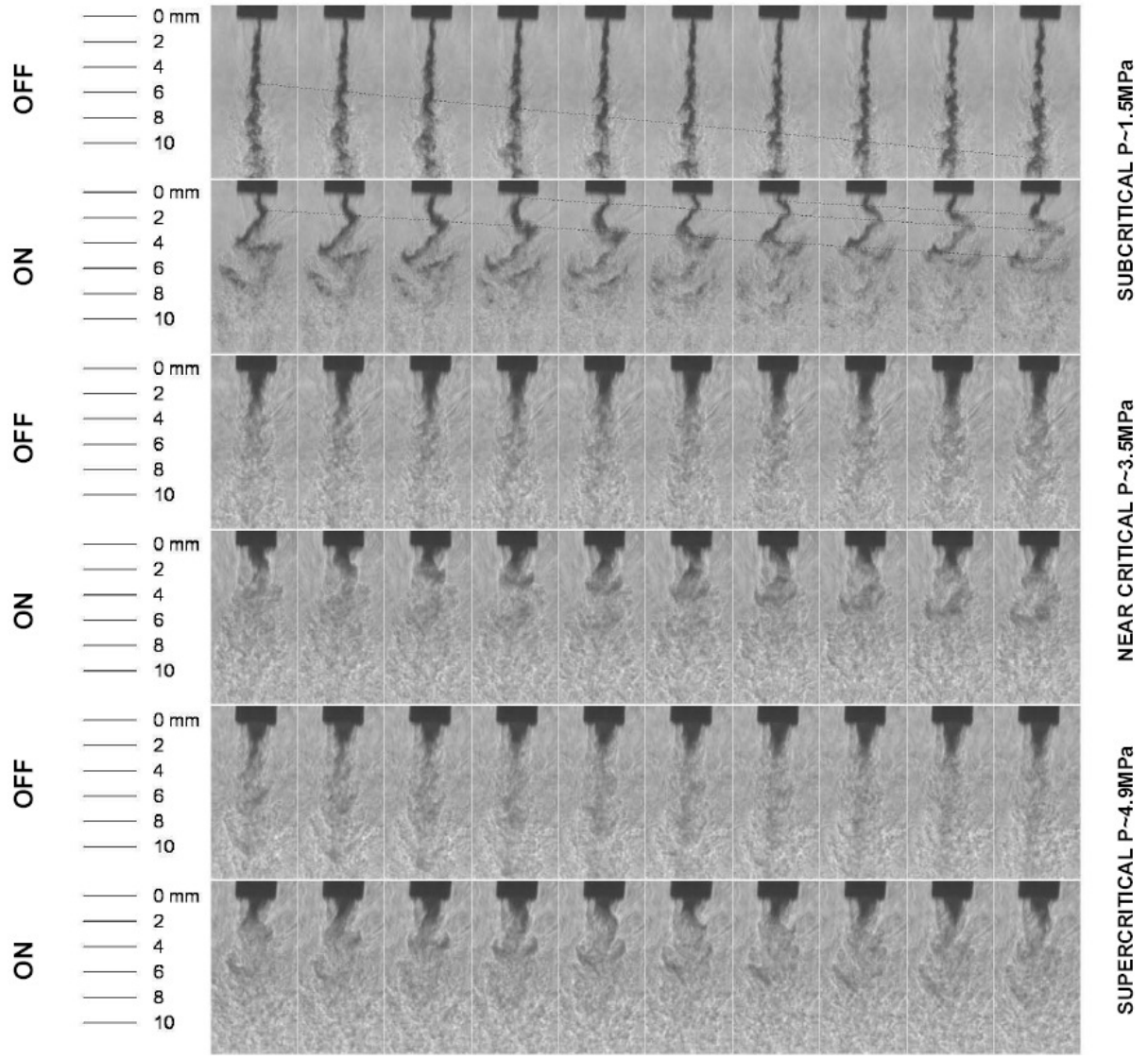

Figure 3.10: Consecutive frames from high-speed shadowgraph imaging of acoustic forcing of a coaxial nitrogen jet under subcritical, near-, and supercritical conditions (Davis & Chehroudi 2006, p.5).

Baillot et al. (2009) conducted similar experiments, exposing coaxially injected water and air simulants under atmospheric conditions to an acoustic field forced by loudspeakers. The study revealed coaxial jet responses to both acoustic pressure and velocity. Acoustic pressure was observed to modulate the injection flow of the gas annulus, which in turn modulated the shear forces exerted on the liquid jet, causing surface instabilities and leading to enhanced atomisation. When the jet was positioned at a velocity antinode the liquid jet was observed to flatten into a sheet in the plane perpendicular to the direction of acoustic particle velocity. The jet flattening was similarly observed by Chehroudi et al. (2003). The liquid sheet was then efficiently atomised by the usual mechanisms of intrinsic sheet instabilities, Faraday instability and membrane breakup. The flattening was explained by local nonlinear radiation pressure effects, or ‘acoustic streaming’, which causes a net gas flow from the pressure antinodes inwards towards the velocity antinodes of the field. Baillot et al. concluded that this effect may lead to an HF instability coupling mechanism in real engines, since the jet

flattening and altered atomisation pattern result in increased droplet concentration near velocity antinodes and therefore an inhomogeneous combustion distribution.

3.4.2 Reacting flows

Woschnak, Suslov and Oschwald (2003) investigated the heat transfer properties in a LOx/H_2 combustion chamber experiencing longitudinal mode HF instability. During this campaign it was noted that the relative intensity of individual eigenmodes in the observed oscillation spectrum changed dramatically when chamber pressure was raised above critical. These observations demonstrated that injection into a supercritical environment strongly affects acoustic wave interaction with the atomisation and combustion process.

Supporting this notion were the observations made by Smith et al. (2004) when conducting a systematic investigation of injection conditions in a lab scale combustor at DLR named 'combustor C' (BKC). Under subcritical conditions, a hydrogen injection pressure drop ΔP_H less than 20% of chamber pressure P_{cc} allowed various modes of unstable combustion to develop. Specifically, an injection coupled LF mode, a vortex shedding mode from the film cooling inlet, and the first longitudinal (1L) acoustic (HF) mode of the chamber were observed. However, under no circumstances was any instability observed when operating near or above the critical pressure of oxygen. Figure 3.11 shows Smith's 'V-profile' pressure ramping test where the instability clearly begins as pressure is lowered below critical. Lal and Oljaca (2004, cited in Smith 2007) independently observed the same effect above the critical pressure in a heptane gas turbine combustor. A similar LOx/H_2 combustor tested by Breisacher (1993) was also stable at supercritical pressure (69 bar) while unstable in the 1L mode at subcritical (20 bar). These observations suggest that the coupling mechanisms for instability may differ for supercritical conditions and that this is an area which requires further research.

Figure 3.11: V-profile pressure ramping test (Smith et al. 2004, p.11).

In the DLR testing, a flickering frequency in the flame was consistently observed at around 7800 Hz. This fluctuation could not be associated with an acoustic mode of the chamber, and was thought to be the result of vortex-shedding from the injector (Smith et al. 2004). Kim, Heister and Collicott (2005) later offered an explanation for this instability from the results of their three-dimensional numerical simulations of the recessed region of SSME injectors. They

were investigating naturally occurring hydrodynamic instabilities arising from the shear forces between the fast H_2 and slow LOx streams of the coaxial injector. This type of instability is known as Kelvin-Helmholz instability, and is considered a possible driving mechanism for HF instability in combustion chambers. In their simulation, the inlet flow conditions to the recessed region (outlet of the LOx post) were kept steady, yet fluctuations in the total mass flow of up to 39% developed in the short distance to the injection plane. The mass flow pulsations had a dominant frequency of 7400 Hz, very similar to the 7800 Hz seen in the DLR combustor. For this reason, as well as the similarity in injection conditions for the SSME and DLR combustor, Kim, Heister and Collicott concluded that hydrodynamic instability in the injector could be responsible for downstream combustion pulsations. Lux and Haidn (2009) later repeated the BKC testing using LOx/CH_4 and compared OH* emission images for operation with and without recess and for subcritical and supercritical chamber pressure. They found that fluctuations in the form of the jet and emission intensity just after injection were visible during operation with a recessed injector, and stronger at supercritical pressure than for subcritical, while no such fluctuations were observed with a non-recessed injector, which seems to support the conclusion of Kim, Heister and Collicott.

A unique suggestion of a possible driving mechanism for instability has been forwarded by a group from the University of Maryland. Ghosh et al. (2006) conducted combustion experiments with an optically accessible, planar model of a coaxial injector. The injector ran with gaseous O_2/H_2 and the flame was subjected to transverse acoustic forcing. It was reported that the orientation of the wrinkling of a combusting flame depended on the direction of the density gradient – that is, which propellant was used for the annular flow and which for the core flow. Ghosh et al. claim that the wrinkling orientation dependence on density gradient vector suggests Rayleigh-Taylor instability may be a contributing factor in acoustic coupling. Rayleigh-Taylor instability describes the perturbed boundary between fluids of different density, and had not previously been put forward as a possible driving mechanism for instability. Several factors call into question the relevance of these results to actual rocket engines, including the use of gaseous propellants, relatively low injection velocities, and intermediate frequency forcing (200 to 1500 Hz). In a later publication (Ghosh, Diao & Yu 2007), the group acknowledges such baroclinic interactions would be negligible during full scale combustion instability, however during the initial onset of instability acoustic pressure amplitude may still be low enough for the effect to dominate and initiate amplification of the flame-acoustic interaction. Thus the action of Rayleigh-Taylor instability is offered by Ghosh et al. primarily as an instability triggering mechanism.

A Japanese research group used the temperature ramping technique of Wanhainen (see Section 3.1) in an attempt to characterise the stability limits of their single-element lab-scale combustor while operating at the supercritical chamber pressure of 80 bar. As with the Wanhainen tests, the onset of instability occurred whenever the H_2 fuel dropped below a certain cryogenic temperature; 62 K for a straight-bore LOx-post, 50 K for a post with taper (Nunome et al. 2008). The lower onset temperature for a tapered post implies better stability, which is in accordance with Wanhainen's results. Dynamic pressure data indicated fluctuations originating in the injectors rather than the chamber, and high-speed imaging of the injector area revealed the flame retreating into the LOx-posst recess region during the transition to unstable combustion. The researchers speculated that instability in the shear layer behind the LOx post tip caused injection fluctuations which resulted in "flame bursts" producing the chamber pressure oscillations; a straight forward injection coupling mechanism, but with unknown origins in the injector recess region. Spontaneous instabilities observed by Kawashima et al. (2010) in both single- and multi-element sub-scale combustors running LOx/CH_4 were attributed to this mechanism. Nunome et al. (2011) supposed that these

pressure oscillations in the LOx-post recess region were coupling with LOx post resonance frequencies. This was supported by results from an accompanying injection-coupled stability model by Kobayashi et al. (2011), based on Crocco's classical n-tau method. A further experimental observation was that decreasing the LOx post diameter improved stability, which is *inconsistent* with Wanhainen's results. Although Nunome et al. do not identify the possible reasons in their study, one may speculate that other dependent parameters such as pressure drop, injection velocity or velocity ratio are responsible, as they were previously identified by Wanhainen to be important. Regardless of the mechanism behind these observations, with improved diagnostics applied to an old investigation technique, injector related phenomena were shown to still be a leading contender in HF instability mechanisms, even at supercritical pressures.

Davis and Chehroudi (2006) and Chehroudi (2009) attempted to explain the temperature ramping instability mechanism based on observations from their non-combusting injection experiments. Essentially, they lay responsibility on the dense oxygen core, or more specifically the stability of its length. Lower velocity ratios were accompanied by an increased RMS fluctuation in the length of the intact core. Davis and Chehroudi theorise that by lowering the H_2 temperature and thereby the injection velocity ratio, the LOx core becomes more susceptible to fluctuations. Fluctuating breakup of the core may become coupled with pressure oscillations, eventually establishing and maintaining a full-blown case of combustion instability. While the observation of "flame bursts" by Nunome et al. seems to be consistent with this mechanism, it is yet to be verified by tests under reacting conditions.

A French group from Ecole Centrale Paris and CNRS are currently exploring the idea that interaction between flames from neighbouring injectors may be a fundamental mechanism for sustaining combustion instability. A laboratory scale chamber with three or five coaxial injectors which allows forced excitation of chamber acoustic modes, known as the Multi Injector Combustor (MIC), is operated at the Mascotte test bench at ONERA. Initially, the propellant combination LOx/H_2 was used (Rey et al. 2003), but later changed to liquid oxygen and methane (LOx/CH_4) (Richecoeur et al. 2006a) in favour of lower injection velocities and therefore flames which are more receptive to acoustic perturbation. Images from the MIC show the flame structure significantly affected by external transverse modulation, with an increase in spreading angle and turbulence (Figure 3.12). Shear regions of adjacent flames collided and interacted, which was presumed to increase the rate of atomisation and mixing, subsequently resulting in the observed increase in combustion intensity and chamber temperature. The MIC experiments indicated that injector-injector interaction may play a significant role in the instability driving mechanism. To date, MIC testing with LOx/CH_4 has been conducted at chamber pressures up to 60 bar (supercritical), but only up to 9 bar with LOx/H_2 (subcritical). Atomisation and combustion behaviour depend heavily on the fuel, as demonstrated for example by Yang, Cuoco and Oschwald (2007) or Oschwald et al. (2008b). After comparing the atomisation and combustion performance of LOx/H_2 and LOx/CH_4 in a sub-scale combustor, these researchers concluded that injection Weber and Reynolds numbers are insufficient to scale coaxial injector performance from one fuel to another. It is therefore important to study the LOx/H_2 combination in parallel to others such as LOx/CH_4. Understanding of real engine instability phenomena in LOx/H_2 systems would benefit from similar experiments to those at ONERA with forced acoustic excitation at supercritical pressures.

Rey et al. (2004) proposed a mechanism and accompanying analytical model for HF instability based on observations from the MIC. Essentially, the model suggests that transverse displacement of the injection jets with the transverse acoustic velocity field results

in higher intensity combustion in the region of, and in phase with, the pressure antinodes of the chamber 1T mode. This is essentially a velocity coupling mechanism driven by large global displacements of the injection jet facilitated by the acoustic velocity field. The concept is simple and does not implicate any vaporisation or combustion subcriticalprocesses in the coupling mechanism, which may make it viable across all injection regimes, subcritical to supercritical. It would be important to compare the effectiveness of the velocity-displacement driver under supercritical conditions, and under injection conditions more representative of real engines.

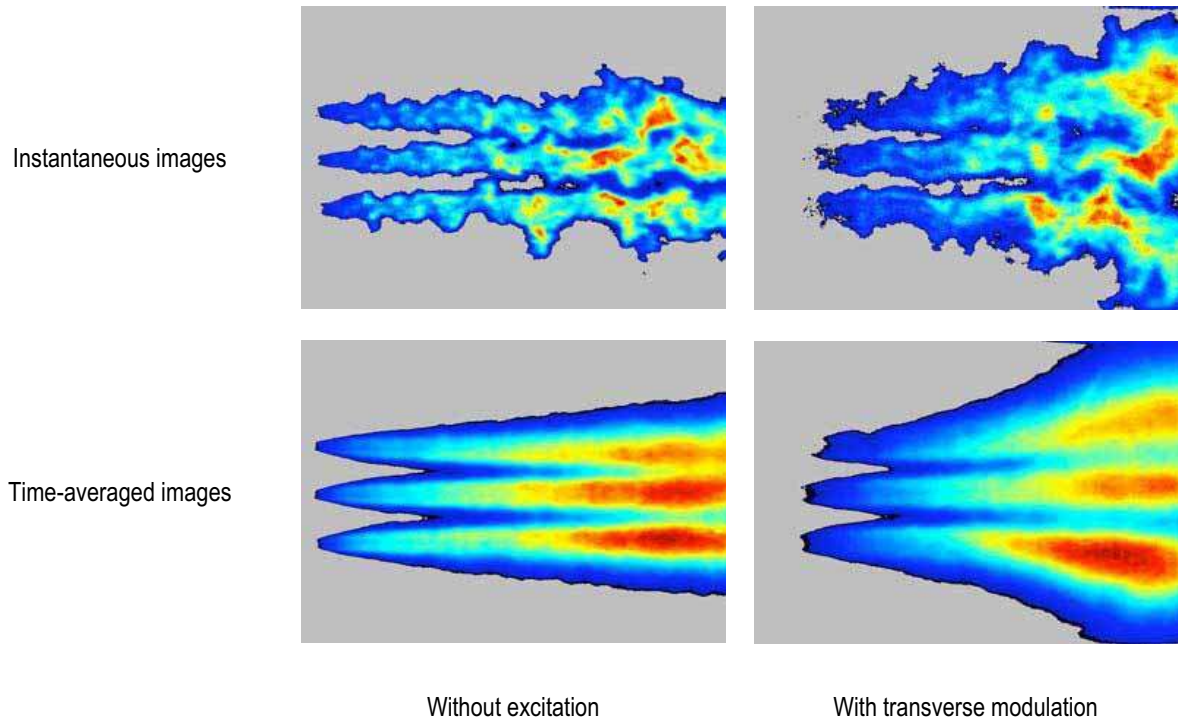

Figure 3.12: Instantaneous and time- averaged OH* emission images (in false colour) from the MIC, without (left column) and with (right column) 1T mode excitation (Richecoeur 2006, p.78).

Pennsylvania State and Purdue Universities undertook a combined experimental, computational study of HF transverse modes. The experimental side of the effort uses a laboratory scale, wide rectangular chamber, shown schematically in Figure 3.13, intended to encourage natural transverse oscillations across multiple swirl coaxial injector elements with combusting LOx/CH_4. The computational effort, in parallel, attempts to predict the behaviour of the experimental chamber using numerical simulations. The ultimate goal of the program is to validate numerical modelling of transverse instability phenomena. Preliminary results for initial tests at subcritical chamber pressures (17 bar) were reported by Marshall et al. (2006a). Although a very low magnitude chamber pressure oscillation was observed (only 4% of chamber pressure, P_{cc}), the results indicated a correlation between acoustic response amplitude and the number and location of injector elements used. In general, the response conformed to the Rayleigh criterion insofar as higher amplitudes were observed when injector flames were aligned with pressure antinodes. Later testing (Marshall et al. 2006b) introduced an additional flow of nitrogen between two of the coaxial elements. This flow increased the amplitude of pressure oscillations, theorised to be the result of simultaneous disruption of atomisation in the neighbouring elements, allowing them to couple more readily with chamber acoustics.

Figure 3.13: Configuration of the multi-element rectangular combustor (top, cross-sectional view) with the first and second mode shapes superimposed (Marshall et al. 2006a, p.3).

Current research at the German Aerospace Center (DLR) concentrates on HF instability in coaxial LOx/H_2 flames. Knapp and Oschwald (2006) at the DLR argue in favour of the pressure coupling mechanism based on experimental results from a laboratory combustor known as the Common Research Combustor (CRC). The CRC is specially designed to excite HF transverse oscillations in the presence of a burning LOx/H_2 spray under subcritical pressure conditions (see Section 4.1.2 for more detail about the combustor). The combustor design allowed the alignment of either pressure oscillation nodes or antinodes with the injection flame, facilitating the investigation of both acoustic pressure and acoustic velocity interactions with combustion. High-speed hydroxyl radical (OH*) imaging of the entire combustor volume was used as a time-resolved indicator of heat release distribution. Knapp and Oschwald observed that heat release intensity fluctuations during instability were strongest at the location of pressure fluctuation antinodes and could determine no phase difference between the heat release and pressure fluctuations. They concluded that they had observed coupling of combustion with acoustic pressure, which supports Putnam's theory of a pressure coupled instability driving mechanism described in Section 2.6.3.

Another method of studying instabilities at the laboratory scale is the use of historically unstable elements to excite resonance modes of a combustor, as employed at Purdue University in the U.S. Miller et al. (2005) describe the setup of a simple, cylindrical combustor with a single, gas-centred swirl coaxial element of Russian heritage running decomposed hydrogen peroxide (H_2O_2) and kerosene. The length of the central gaseous oxygen injector could be varied continuously during a hot-fire test. As the length of oxygen injector was decreased, a longitudinal resonance mode of the combustion chamber would be excited (Sisco et al. 2006; Yu et al. 2008; Yu et al. 2009). Parallel computational simulations by Xia et al. (2011) were able to reproduce spontaneous instability, subject to the chemical kinetic model and grid resolution used. The simulation will be used to further study sensitivity of stability to various system parameters. Harvazinski, Anderson and Merkle (2011) used a numerical simulation of the system to study the spatial and temporal response of combustion to the instability. The approach used was analogous to many of the experimental investigations described in this chapter.

With experience in intentionally de-tuning this type of element to be naturally unstable, they were subsequently applied to a rectangular combustor to study transverse mode instability. These de-tuned 'driving elements' are arranged towards the outside of the faceplate, near the

walls, in order to excite the transverse resonance mode. A ‘study element’ is located in the centre of the faceplate where the acoustic velocity antinode is located (Pomeroy, Morgan & Anderson 2011). A liquid-centred swirl coaxial element injecting cryogenic oxygen and methane was studied using the combustor configuration in Figure 3.14. Dynamic pressure measurements showed that the element had a damping influence compared to when the combustor was run with only driving elements (Wierman, Nugent & Anderson 2011), presumably an observation of the drag force imparted on the acoustic gas oscillation by the injected liquid spray. While this observation in itself says nothing of the stability of the coaxial injector, it does demonstrate that the interaction between acoustic velocity and spray combustion is significant.

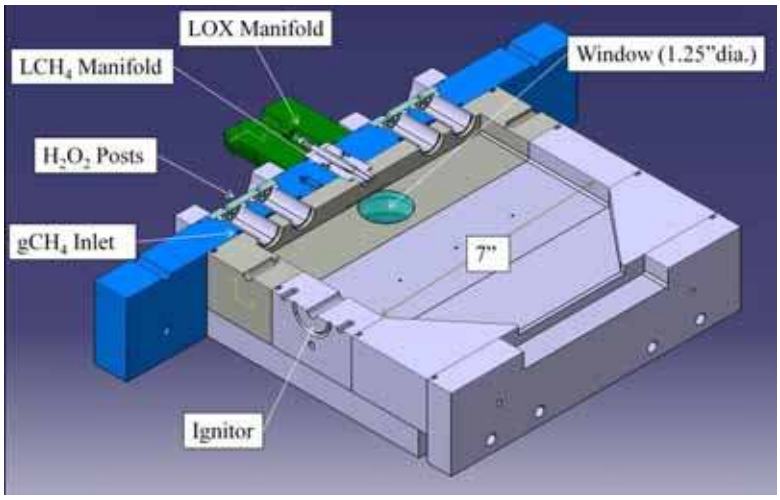

Figure 3.14: Purdue University rectangular combustor with central swirl coaxial study element (Wierman, Nugent & Anderson 2011, p.3).

A further example of the application of unstable, gaseous oxidiser-centred swirl coaxial injectors is the LPRE combustor simulator at the Georgia Institute of Technology in the U.S. While the sub-scale combustor only operates at atmospheric pressure, its cylindrical cross-section allows the spontaneous development of a 5 kHz, spinning 1T mode instability. The 1T mode was observed using high-speed chemiluminescence imaging. Stability of the system was determined to be dependent on the equivalence ratio of injected air and kerosene propellants, and on the ratio of counter-rotating swirl introduced into the air or fuel (Bibik et al. 2008). The damping influence of a single baffle on the system was also investigated. As the baffle was progressively inserted into the combustor the spinning mode first damped out, then reappeared as a stationary 1T mode, having adjusted its form and frequency to suit the new acoustic configuration dictated by the baffle (Lubarsky et al. 2008). Experience with the CRC at DLR has also revealed the importance of acoustic conditions on the development on unstable modes. Recent tests with LOx/CH_4 have better characterised the tendency for the 1T mode to manifest as a spinning mode. It was found that the behaviour of the mode could be theoretically described as a superposition of counter-rotating 1T modes. Extensive deployment of pressure sensors around the perimeter of the combustion chamber allowed the acoustic mode to be reconstructed from hot-fire measurements. The mode was observed to transition randomly from spinning to stationary then back to spinning, switching rotational direction in the process (Sliphorst, Gröning & Oschwald 2011). From the observations in these and other experimental system, it is supposed that spinning behaviour of the 1T mode may play a role in naturally occurring HF instability.

3.5 Summary

Despite significant research efforts over several decades, the ability to quantitatively predict HF transverse mode combustion instability based on propellant physiochemical properties and engine design and operating conditions has not yet eventuated. The main reason is the lack of understanding of the fundamental mechanisms which sustain HF oscillations in an operating engine. Unresolved fundamental questions facing LPRE combustion instability researchers are: which coupling mechanism, pressure or velocity, dominates during HF instability; could they each dominate under different operating conditions or for different engines and propellants; and, which pressure or velocity sensitive processes facilitate the coupling and how? Before effective models of HF instability can be produced, further research is required to positively identify and characterise the driving mechanism or combination of mechanisms.

While studying non-reacting flows of simulants has provided some insight into acoustic interaction with injection jets, past research has highlighted the importance of observing reacting flows with injection properties and chamber pressure representative of real engine operating conditions. Acoustic interaction with the injection jet which is characteristic of HF transverse mode combustion instability should be examined since the literature clearly identifies the understanding of this interaction as deficient. Based on the survey of literature presented here, it is determined that, to date, a reacting flow of coaxially injected LOx/H_2 influenced by an externally applied transverse acoustic field has not been observed under high pressure conditions. 'High pressure' in this context is more specifically defined as pressure conditions above the critical point of the propellants and at levels representative of real engine operating conditions. It has been established that acoustic wave interaction with the atomisation and combustion process differs for LOx/H_2 injected into subcritical or supercritical conditions. Therefore it is important to conduct experiments with acoustic forcing under high pressure conditions.

Hydrogen fuel injection temperature has also been identified as important to stability in LOx/H_2 systems and warrants further investigation. Varying H_2 temperature in an experimental study, and observing any change in sensitivity to the applied acoustic field, may reveal dependent physical processes which are involved in the coupling mechanisms.

All state-of-the-art sub-scale experimental combustors discussed in this chapter are equipped with windows to provide optical access to the flame. The application of high-speed optical measurements of combustion emission in such forced-excitation experiments provides a means to compare the spatial and temporal distribution of heat release to the acoustic field distribution. While the principle was attempted in the mid to late 2000s, it is only very recently that results with useful spatial and temporal resolution have begun to emerge. Such results have demonstrated the ability to detect in-phase combustion response to acoustic pressure, as well as detect phase delayed combustion response to acoustic velocity. Definitive answers on the dominant process evoking response from the flame, and how the observed responses help to explain naturally occurring instability, have not yet been developed.

An added benefit of conducting experimental research is to generate high fidelity data, which is missing in the literature at high pressures. These data will be valuable for the development and validation of numerical models.

4. COMBUSTOR DEVELOPMENT

Based on the conclusions drawn from a review of past research efforts in the field of HF combustion instability, it was decided an experimental approach would be used to investigate instability coupling mechanisms under realistic LOx/H_2 rocket conditions. Using a laboratory combustor capable of operating at representative engine operating conditions, in particular supercritical pressure, the interaction of an externally applied acoustic field with a reacting injection jet of LOx/H_2 would be investigated. More specifically, observations would be aimed at characterising how the jet mixing and combustion process are influenced by acoustic pressure and/or velocity fluctuations. From such observations it is hoped to gain more detailed insight into the mechanisms by which chamber pressure oscillations couple with combustion leading to self-sustaining instability. An approach which addresses some of the shortcomings of previous experimental apparatus was called for. This chapter details the development of a new experimental combustor in order to carry out the research objectives of the project.

Firstly, previous experimental combustors targeted at studying high frequency combustion instabilities are reviewed, with five more recent, state-of-the-art combustors presented as case studies. Following the review, requirements for the new system for the current work are laid out and several concepts which were considered to meet these requirements are assessed. For a description of the final hardware configuration, the reader may skip directly to Section 4.4.

4.1 Experimental combustor review

4.1.1 Historical overview

Early experimental research into combustion instability was conducted using full-scale engine tests. Detonating bombs or firing gas cannons in an operating, full scale combustion chamber were common methods of triggering combustion instabilities in order to characterise the engine behaviour and its ability to suppress the instability. Such tests are costly and make the application of specialist diagnostic techniques difficult.

Researches began to investigate the problem in the 1950s using sub-scale engines and experimental combustors. For example, Berman and Cheney (1955) successfully recorded streak film of longitudinal mode HF instability through the plexiglass slot windows of their lab-scale combustor. Tischler and Male (1956) presented streak film of a spinning 1T mode later captured in the same combustor with a transverse slot window, shown in Figure 4.1.

While convenient and affordable to operate in a laboratory setting, a troublesome trait of sub-scale combustors is that they appear very rarely to develop spontaneous transverse-mode HF instabilities. Several reasons are thought to be responsible. Smaller dimensions of a sub-scale combustion chamber dictate natural frequencies much higher than in full scale engines. Higher frequency acoustic modes interact with the flame on shorter time scales, which may not be compatible with the mechanisms which reinforce spontaneous instabilities in real engines. Lab-scale experiments which do have representative dimensions and therefore mode frequencies suffer from low energy density since they are fed by smaller or fewer injectors. High surface area to volume ratios of sub-scale chambers probably leads to viscous damping at the chamber walls outstripping the energy available to drive an unstable mode.

Figure 4.1: Streak photography of a rotating 1T mode instability (Tischler & Male 1956).

Researchers sought to overcome the inherent stability of sub-scale combustors by using apparatus designed to assist or trigger natural combustion instabilities. For example, Heidmann (1965a) used tangentially injected nitrogen gas in his flat, cylindrical combustor to increase in-phase energy addition and allow transverse modes to become self-sustaining. Techniques were also developed to artificially create and sustain conditions representative of real combustion instabilities, essentially entailing continuous forcing of pressure oscillations at high frequencies. While a loud speaker may be used effectively in small scale cold flow experiments such as those by Davis and Chehroudi (Section 3.4.1), this approach faces difficulties for larger-scale experiments with combustion. Breisacher (1993) used a discharge from a bomb grain, guided through a tube to the combustion chamber, in an attempt to trigger the 1L mode of a small, cylindrical, single-element, LOx/H_2 combustor. This technique was deemed unsuccessful in the lab-scale combustor, neither triggering nor affecting the behaviour of existing 1L mode instability. While bombing is not expected to be an effective approach for producing sustained oscillations in a sub-scale combustor, it would provide information on system damping.

One technique for acoustic forcing of hot-fire experiments is the use of nozzle modulation. A spinning wheel with teeth at its perimeter is used to periodically open and close the outlet of the combustion chamber exhaust nozzle. Alternatively, a secondary nozzle joined to the main combustion chamber may be modulated. This action introduces pressure fluctuations into the combustion chamber at a frequency depending on the speed at which the toothed wheel is driven. When applied at the appropriate frequency, the pressure fluctuations can be amplified through excitation of the natural resonances of the combustion chamber volume. This technique enables sustained, well-defined acoustic conditions to be applied. Diagnostics can then be used to observe the effect of acoustics on injection processes for extended durations, under quasi-steady conditions.

The nozzle modulation technique was originally developed for studying combustion instability in solid-fuelled rocket motors. Lecourt and Foucaud (1987) were the first to apply the technique to the study of liquid propellant systems. They excited the first longitudinal mode of a lab-scale combustor burning liquid propellants by modulating the exhaust nozzle with a toothed wheel. The injector could be installed at the head of the chamber with axial injection to investigate the influence of the pressure antinode of the first longitudinal (1L)

mode, or in the centre of the chamber with radial injection for interaction with the velocity antinode. Not only did the nozzle modulation technique provide good control over the frequency of excitation, but also allowed the acoustic losses of the system to be measured. By using a modified wheel with only a small number of teeth concentrated over a small sector of the wheel, as illustrated in Figure 4.2, the excitation took place over a small part of the rotational period and normal chamber operation over the remainder. During the remaining part of the period, the time over which the excited pressure disturbances dampen out can be determined. Modern experimental systems employing the nozzle modulation technique of forced excitation include the Common Research Combustor (CRC) operated by CNRS and DLR, the Multi-Injector Combustor (MIC) and the Very High Amplitude Modulator (VHAM), both operated by ONERA and CNRS. Each of these, as well as two other experimental combustors used for the study of transverse mode HF instability will be reviewed in greater detail in the following paragraphs.

Figure 4.2: Working principle of small rocket combustor with intermittant nozzle modulation (Lecourt & Foucaud 1987, p.2).

4.1.2 CRC

Since 2002, researchers at the Research Institute for Equilibrium Systems (IRPHE) in Marseilles (Cheuret 2005) and in parallel at DLR Lampoldshausen (Knapp, Farago & Oschwald 2007; Sliphorst 2011) have operated identical experimental combustors called the Common Research Combustor (CRC). The CRC was born of the research logic proposed by a newly formed German-French working group designed to jointly tackle the problem of HF combustion instabilities. The first report of the working group (Fortunier 1999) called for a versatile experiment, with acoustic forcing using modulated exhaust, dedicated to the study of flame-acoustic interaction. The CRC, illustrated in Figure 4.3, has a flat cylindrical geometry with a diameter of 200 mm and length of 40 mm. Acoustically, the principle is essentially that of the Heidmann pancake combustor, whereby the extremely short chamber length shifts the frequencies of the longitudinal modes above those of the transverse modes, thus minimising their influence during excitation of representative transverse modes. The diameter of 200 mm is typical of upper stage engines and results in a first tangential (1T) mode frequency of approximately 4 kHz when operating with LOx/H_2. Also similar to the Heidmann combustor, the primary nozzle is located centrally in the end wall of the chamber and propellant is injected radially from the side of the chamber through a single injector. The injector is approximately $1/10^{th}$ scale of those found in industrial engines. Optical access to the chamber is provided by two 6 cm diameter windows or one full diameter window for access to the entire chamber volume. The application of both high-speed shadography and OH*

chemiluminescence imaging has allowed the interaction of the spray flame with forced acoustics to be studied in great detail. The modular design of the chamber periphery allows other diagnostic instruments to be installed in a variety of orientations around the chamber.

Figure 4.3: CRC combustor for HF research (Knapp, Farago & Oschwald 2007, p.3).

Forcing of HF oscillations is achieved through modulation of a cavity which joins the main chamber periphery and terminates in a sonic nozzle. Modulation of this 'secondary nozzle' establishes a tangential oscillation of the pressure field inside the chamber, exciting the 1T mode. Various secondary nozzle throat areas allow the excitation amplitude to be altered, with larger throat diameters resulting in greater excitation amplitudes. Amplitudes of up to 5% of the mean chamber pressure ($p'/P_{cc} \approx 5\%$) have been achieved during LOx/H_2 operation. The angular position of the secondary nozzle relative to the injection element is adjustable, allowing the orientation of excited modes to be changed. This important capability allows the radial injection jet to be positioned either in a pressure node or antinode of the excited mode, as illustrated in Figure 4.4, facilitating study of either velocity or pressure interaction, respectively. The advantage of this feature is that velocity or pressure interaction can be studied using the same 1T mode frequency and therefore the same time scales of acoustic and injection process interactions.

Figure 4.4: Pressure fields in the DLR combustor with the secondary nozzle in the 180° position (left) and the 90° position (right) (Knapp, Farago & Oschwald 2007, p.3).

Also evident in Figure 4.4 is how the secondary nozzle influences the acoustic modes of the chamber. The presence of the secondary nozzle cavity has changed the pressure distribution

of the otherwise symmetrical 1T mode of a pure cylinder. As a result the pressure nodal line is somewhat offset from the centreline of the chamber and the injection jet is not subjected to a uniform velocity interaction, nor is the velocity interaction of the maximum amplitude present in the system. Such distortion to the acoustic mode structure is a drawback of introducing pressure modulation to the system via a secondary nozzle.

The existing CRC combustor is capable of operating at chamber pressures up to 10 bar, and its injector has relatively low performance, which are limitations with regards to investigating representative rocket engine conditions. Furthermore, the radially injected propellants must return to the centre of the chamber and turn 90 degrees in order to exit through the axial main nozzle. This unconventional flow field limits the applicability of results to real engines, and may influence the interaction of the acoustic field with the flame.

4.1.3 MIC and VHAM

The Multi Injector Combustor (MIC) is a lab-scale experimental combustor, developed especially for HF combustion instability research, operated on the Mascotte test bench at ONERA in Paris (Richecoeur 2006). There are three and five injector versions of the MIC, both with the elements arranged linearly with a spacing of 17 mm as can be seen in Figure 4.5. A secondary nozzle in the upper wall aligned perpendicularly to the chamber axial direction is modulated using a toothed-wheel in the same manner as the CRC. The frequency of excitation can be changed simply by changing the rotational speed of the electric motor driving the wheel. Usually the frequency was ramped up through a range containing the first few fundamental modes of the chamber, exciting resonance of each one as it passed through. Excitation of the 1T mode of the chamber is used to study the influence of a transverse acoustic field on the flames and the interaction of neighbouring flames in the linear array. Windows allow optical access to the near injector region and OH* emission imaging is used to capture the flame structure while photomultipliers record temporal fluctuation in OH* emission. While the MIC is designed for operating pressures up to 75 bar, reported operation with liquid LOx/H_2 propellants by Rey et al. (2004) extends only to 9 bar.

Rey et al. made a simple comparison of the excited acoustic energy and combustion energy in the MIC. By assuming linear acoustic, ideal gas conditions, acoustic energy density can be written as

$$\varepsilon = \frac{1}{2}\frac{p'^2}{\rho_{bulk} c^2} + \frac{1}{2}\rho_{bulk} u'^2 \ , \tag{7}$$

where p' and u' are the fluctuating acoustic pressure and velocity amplitudes, respectively, ρ_{bulk} is the bulk equilibrium mixture density in the combustion chamber, and c is the corresponding sound speed. By assuming $u' \approx p'/(\rho_{bulk} c)$ and averaging over one acoustic cycle, the period-averaged energy density can be estimated using

$$E = \frac{1}{2}\frac{p'^2}{\rho_{bulk} c^2} \ . \tag{8}$$

MIC operating conditions with LOx/H_2 gave a value of $E \approx 40$ J/m^3. This was then compared to the enthalpy of the reacted propellants, given by

$$H = \rho_{bulk} c_p T_{bulk} \ , \tag{9}$$

where c_p is the bulk mixture heat capacity and T_{bulk} the adiabatic temperature. The estimated energy density from combustion is therefore $H \approx 4.5$ MJ/m^3. Because the acoustic energy density is so small in comparison, Rey et al. concluded that the driving mechanism for combustion instabilities must arise from the transverse modulation of the flames, rather than energy addition from the acoustic field.

This simple calculation may also be used to illustrate the sensitivity of full-scale LPRE engines to HF instabilities. Taking an engine operating at $P_{cc} = 60$ bar with $ROF = 6$, and estimating bulk equilibrium mixture properties using the CEA2 software by Gordon and McBride (1994), the enthalpy of combustion products would be approximately $H \approx (2.72 \text{ kg/m}^3)(9.776 \text{ J/kg.K})(3534 \text{ K}) = 94 \text{ MJ/m}^3$. Even if an instance of HF instability were to reach an amplitude of 50% of P_{cc}, the acoustic energy density would only be $E \approx 0.5(30\times10^5 \text{ Pa})^2/[(2.72 \text{ kg/m}^3)(1585 \text{ m/s})^2] = 0.7 \text{ MJ/m}^3$, or less than 1% of the enthalpy of combustion. Therefore, a full-scale instability also represents an extremely small portion of the total energy released in a rocket engine.

Spreading of the flames observed during modulation at 1T resonance lead the neighbouring flames to overlap, despite the relatively large spacing between the injection elements. This implies that in a real engine, where the element spacing is even smaller (typically 1.7 – 2.0 D_{LOx}), interaction of neighbouring flames may play an important role in the instability coupling mechanisms. Although the use of multiple injectors and application of optical diagnostics allowed this important observation of flame-flame interaction to be made, the injector distribution employed in the MIC is not ideal. The extent of flame spreading observed in the vertical direction would not be accommodated by the horizontal dimension of the chamber, therefore horizontal flame spread may be somewhat constrained by the chamber side walls. This chamber boundary interaction is likely to influence the vertical flame spread and therefore also interaction between neighbouring flames and with the acoustic field.

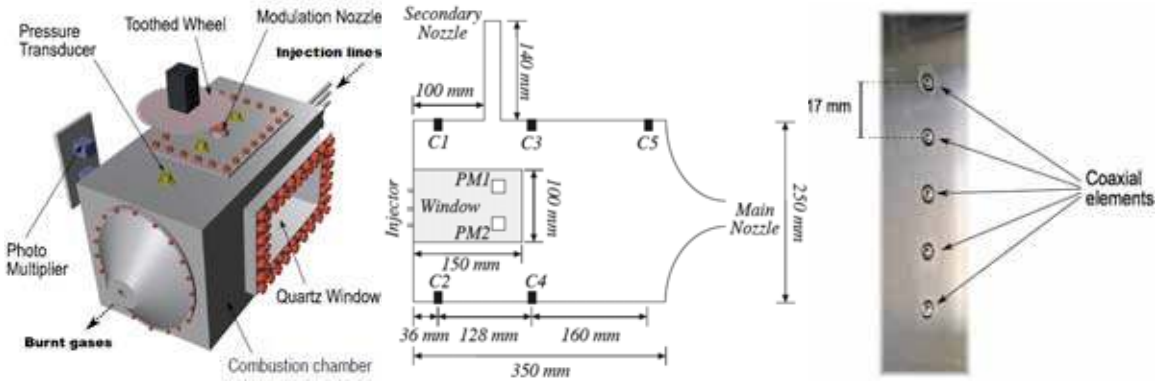

Figure 4.5: Illustration of the MIC configuration with three injection elements (left, middle), and a photograph of the five-element version of the injector (right) (modified from Richecoeur 2006).

The Very High Amplitude Modulator (VHAM) is a later addition to the MIC. Rather than a perpendicular secondary nozzle for excitation, the VHAM configuration uses twin primary axial nozzles, both subject to modulation. By modulating the primary nozzles rather than a smaller secondary nozzle, the VHAM is intended to achieve greater excitation amplitudes, expected to reach up to 20% of P_{cc}. This was considered an important development since excitation amplitudes in the MIC were often too low for any significant flame response to be

detected, especially with LOx/H_2 propellants (Rey et al. 2003). Only results of cold flow tests have been published to date (Méry et al. 2008).

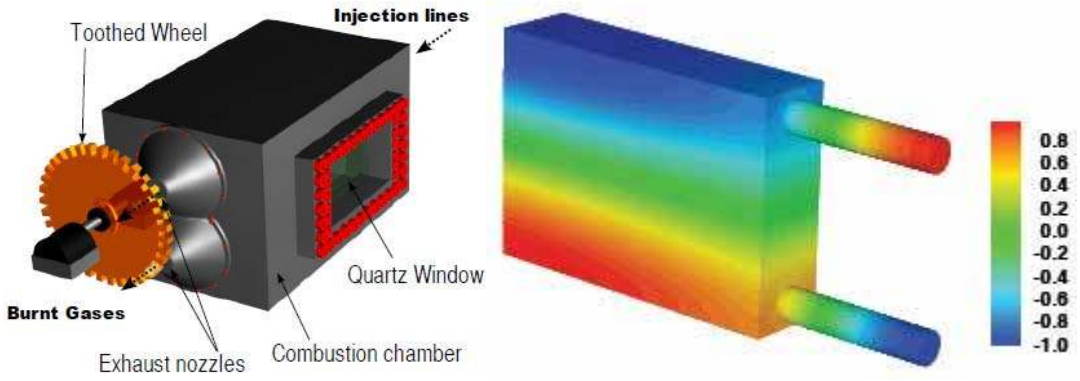

Figure 4.6: Illustration of the MIC equipped with the VHAM (left) (Méry et al. 2008), and a numerically calculated 1T mode pressure distribution (right) (Richecoeur 2006, p.246).

4.1.4 Pennsylvania State University rectangular combustor

A rectangular combustor from Pennsylvania State University in the U.S. for the study of transverse-mode HF instability was described previously in Section 3.4.2. It has multiple elements and multiple exhaust nozzles and is intended for the study of spontaneous HF instability. As many lab-scale combustors do, it suffered from low amplitudes of naturally oscillating combustion. Later testing attempted to increase the amplitude of oscillations by artificially modulating the supply flow of LOx or methane to the injectors. The pulsating supply flow rate, however, failed to manifest as pressure fluctuations in the combustion chamber (Marshall et al. 2006b). This suggests that supply flow modulation may be an ineffective means of forcing HF oscillations in an experimental combustor. Furthermore, the approach may not be appropriate when the research goal is to investigate intrinsic, rather than injection-coupled, driving mechanisms.

Various combinations of injectors and exhaust nozzles at different positions along the inlet and outlet walls of the combustor would also result in varying flow fields, affecting the comparison of results from test to test. In many configurations the injected flow must turn dramatically to exit through the nozzles, reducing the degree to which the experiment may be considered representative of real engines. This unconventional flow field is considered somewhat of a drawback to this combustor configuration.

4.1.5 Purdue University rectangular combustor

Also described in Section 3.4.2 is a rectangular combustor from Purdue University in the U.S. which uses deliberately de-tuned, unstable injectors to drive the combustion chamber 1T mode (Pomeroy et al. 2008). This method appears to be highly effective in reliably exciting high amplitude instability. The system has the added advantage of simplicity, with no electro-mechanical system required for modulation. However, chamber modes cannot be selectively excited, as there is no means to control the modulation frequency or amplitude. Furthermore, a damping study using the sector-wheel excitation technique of Lecourt and Foucaud is not possible. Finally, the driving elements seem to depend on the use of kerosene fuel for unstable

behaviour. Mixing these propellants in the same chamber with those of the intended subject of study, LOx/H_2, would result in a complicated acoustic environment and possibly further unknown outcomes.

4.1.6 Summary

Based on this review, the following aspects of existing experimental systems were considered in the design of a new combustor to address the objectives of the current work:

- The nozzle modulation method is a proven way to excite the chamber acoustic modes during hot-fire operation. It allows good control over excitation frequency and amplitude, and the duration of forced interaction. Modified 'sector-wheels' also provide a way to measure the system damping.
- It is considered important to have mode frequencies representative HF instability in real engines so that the time scales for the processes involved are also similar. Using a characteristic dimension of the combustion chamber in a sub-scale combustor which is representative of full-scale engines facilitates this requirement.
- An important aspect of the versatility of modern experimental systems is the ability to allow separate investigation of pressure or velocity field interaction with the injection jet. This is fundamental to the question of which coupling mechanisms are at work during self-sustaining combustion instabilities.
- Modern systems developed to study high frequency combustion instabilities have contributed greatly to the understanding of processes occurring within combustion chambers through the application of sophisticated optical diagnostic techniques.
- The energy density of the system should be as high as possible in order to combat the high inherent stability of sub-scale combustors which may normally impede the effectiveness of forced excitation.
- Injector-injector interaction is thought to potentially play an important role in the coupling mechanism, and therefore combustors with multiple injectors are considered to provide improved research value.

4.2 New combustor specifications

The decision to develop a new HF research combustor was taken early in the project in order to meet the research objectives by overcoming some of the limitations of the systems reviewed in Section 4.1. Specifying operating conditions which address these limitations was the first step taken in the development of the new system. A test facility at DLR which could provide these conditions was identified. A critical aspect of the experiment, the injector, was also specified at this early stage of the project.

4.2.1 Operating conditions

One of the primary project research objectives being investigation of flame-acoustic interaction at supercritical pressures, a new combustor capable of operating pressures above

the critical pressure of oxygen (50.4 bar) was required. Operation below the critical pressure to facilitate comparison of flame response in the two different regimes is logically also required. From previous experimental studies, such as Smith et al. (2007) and Davis and Chehroudi (2007), a separation of 10 bar above and below the critical pressure is found to place the injection conditions firmly in the supercritical or subcritical regimes, respectively. Combustion chamber pressures of 40, 50 and 60 bar were therefore chosen as target operating pressures for the new system.

The mixture ratio of oxidiser to fuel is also an important parameter in defining rocket engine performance. For the propellant mixture LOx/H_2 at the specified chamber pressure range, a mixture ratio of approximately $ROF = 4.5$ provides theoretically the optimal vacuum specific impulse. Real engines operate in the range $ROF = 4.5$ to 7.2, making values of 4 and 6 reasonable choices for representative conditions. Extending the range down further provides a wider range of injection velocity ratios for a given injector element dimensioning. Theoretical specific impulse drops sharply below $ROF = 3$, so a value of 2 was taken as an appropriate lower limit.

Resonance mode frequencies of the combustion chamber were to be close to those which may occur in an upper stage rocket engine, typically between 1 and 6 kHz. Using representative mode frequencies ensures the interaction of the acoustic field with injection, atomisation, vaporisation, mixing and combustion processes will occur on time scales which are representative of real, self-sustaining combustion instabilities. Using representative time scales is considered to be important since Heidmann and Wieber (1966a) established sensitivity of such processes to frequency. Considering the diameter of the CRC of 200 mm, which is a typical size for upper stage engines, the typical frequency of a 1T mode was estimated. Operation with LOx/H_2 could give sound speeds in the chamber which vary between that of combusting gases and ambient gaseous hydrogen, so an approximate mean value of 1500 m/s was chosen. This results in a 1T mode frequency of around 4 kHz, which was hence selected as a design specification for the new combustor. Results would also be comparable to those from the CRC.

Increasing the energy density of the system is also considered important to the representation of realistic rocket engine conditions. Per-element mass flow rates on the order of 100 to 400 g/s would therefore be sought.

A further research objective is the effect of hydrogen injection temperature on flame acoustic interaction. Supply of both cryogenic oxygen and hydrogen was therefore required.

4.2.2 Test facility

The desired operating pressures, mass flow rates, and cryogenic H_2 injection temperatures are offered by the P8 test facility at DLR Lampoldshausen. The Lampoldshausen site of the German Aerospace Center (DLR), located in the area of Hardthausen, southern Germany, is home to the Institute of Space Propulsion. The institute operates the largest LPRE test facilities in Western Europe, including test facility ‘P8’, which is primarily designed for studying high pressure LOx/H_2 LPRE combustion. This test facility can provide LOx and H_2 at thermo-physical conditions representative of cryogenic rocket operating conditions. Propellant mass flow rates of up to 8 kg/s for LOx and 1.5 kg/s for H_2 are achievable, with specimen interface pressures up to 360 bar. Test durations of 15 s have been achieved with maximum propellant mass flow rate, or 7 min tests at lower mass flow rates. De-ionised

cooling water is available at a maximum supply pressure of 160 bar and mass flow rate of 50 kg/s. Liquid or gaseous nitrogen or gaseous helium is available for cooling or purging purposes.

The available range of temperatures for the supply of hydrogen is of particular interest. P8 can supply gaseous H_2 either at ambient temperatures, around 280 to 300 K, or cryogenic hydrogen at temperatures around 100 K, or around 50 K. Supply of both ambient and low temperature hydrogen allows the influence of H_2 injection temperature to be investigated, which is known to have an impact on engine stability (Section 3.1). When supplying H_2 at ambient temperatures, operation is said to be with gaseous hydrogen (GH_2). When supplying cryogenic H_2, operation is said to be with liquid hydrogen (LH_2), although strictly speaking hydrogen is a supercritical fluid at the temperatures and pressures it experiences throughout the system, up to and including injection into the combustion chamber. The terminology of GH_2 for ambient temperature hydrogen and LH_2 for $T_H \sim 50$ K will be adopted throughout this work.

Experimental combustors with modular configurations have been developed for use in the test bench, allowing a variety of injection elements, chamber geometries, and chamber pressures to be investigated. Past experimental combustors have also been designed to allow optical access to the chamber for effective use of non-intrusive optical diagnostic techniques including shadowgraph imaging, spectral analysis, and laser thermometry.

The propellant supply capabilities of P8, and its history of hosting subscale experimental combustors and diagnostic techniques lead to its selection for use with the new HF research combustor.

4.2.3 Injector

The injector for the new combustor was defined early in the project as it is a driver for many other design factors. Coaxial injection elements would be used as they are the most common style for LOx/H_2 engines. Recess and taper would not be applied to the LOx post as these are identified as stabilising features (see Section 2.6.4) which may hinder efforts to excite the system to significant acoustic amplitudes and complicate study of the flame. The ability to adjust the outer diameter of the fuel outlet annulus was specified. A minimum of two different outlet dimensions would allow comparison of high and low injection velocity ratios while holding all other injection parameters constant.

The requirement for a multi-element injector to allow investigation of injector-injector interaction was given high priority. It was decided to use an injector pattern with five elements (penta-injector) arranged with one central element and four evenly spaced surrounding elements as illustrated in Figure 4.7. This ‘matrix’ arrangement provides an environment for the central jet which is representative of real, multi-element injector distributions where each element, excepting those next to the chamber wall, is completely surrounded by others in the pattern. It was hypothesised that this ‘matrix’ style arrangement may provide more realistic injector-injector interaction conditions than a linear arrangement such as that used in the MIC where jets are bound by the chamber wall on both sides. Spacing between the elements should be as tight as possible for realistic injector interaction, while still maintaining sufficient spacing to afford an unobscured view to the central element, which would be the subject of study with optical diagnostics.

The penta-injector may also facilitate a simple study of different injector patterns. The acoustic field interaction with two effectively different injector patterns can be tested by aligning the penta-injector at 0 or 45 degrees relative to the chamber acoustic field, as illustrated in Figure 4.7.

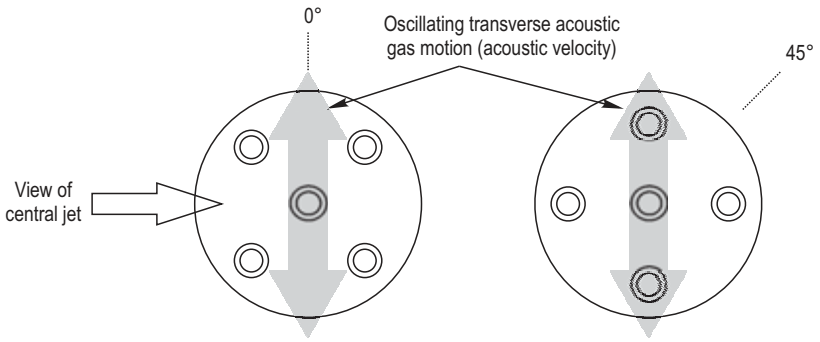

Figure 4.7: Penta-injector pattern and relative acoustic field orientation.

4.3 Conceptual design

Following establishment of the desired experimental conditions, a design study was conducted to assess various concepts capable of achieving those conditions. The acoustic and practical characteristics of the following five new design concepts were explored. Readers interested only in the final combustor design are directed to skip to Section 4.4.

4.3.1 Concept 1: High pressure CRC

Initially it was envisaged that the existing CRC design could simply be upgraded to operate at high pressures and incorporate multiple injectors. Figure 4.8 illustrates the internal geometry of this concept. However, it was quickly realised that the radial injection configuration of the CRC would be poorly suited to higher injection mass flow rates and velocities produced by a representative injector. Firstly the flow is constrained tightly in the direction of injection, quickly meeting the opposite wall and being forced to turn and fill the semi-circular spaces above and below the injector. The flow must then return to the chamber axis and exit perpendicularly to the original direction of injection through the central main nozzle. This irregular flow field is unrepresentative of the purely axial flow fields in real engines.

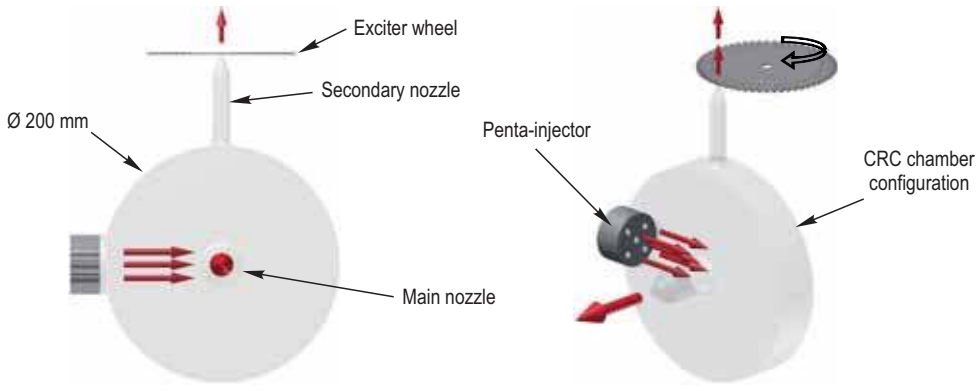

Figure 4.8 High pressure CRC concept (internal geometry).

The existing CRC is uncooled and is therefore limited to very short test durations. The higher heat loads accompanied by higher operating pressures, energy densities, and longer test durations dictate the need for active cooling of combustor walls and nozzles. Actively cooling the CRC configuration would be prohibitively difficult.

4.3.2 Concept 2: Rectangular chamber

A rectangular cross-section chamber design, similar to the MIC described in Section 4.1.3, was considered. The matrix penta-injector would be located centrally at the head of the chamber, as shown in Figure 4.9. Studies of flame-flame interaction would therefore complement those of the MIC with a linear arrangement of injectors. The primary advantages of such a configuration are the simplicity of the acoustic mode shapes and orientations, and the ease of optical access.

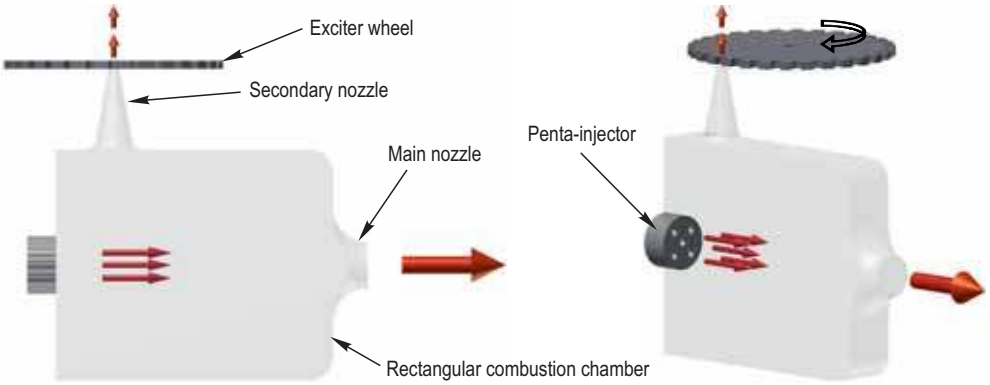

Figure 4.9: Rectangular combustor concept (internal geometry).

The rectangular geometry results in highly uniform acoustic field distributions across the injector face, which is important when attempting to assess the interaction of the field with multiple injectors as is the case with the MIC. However, this advantage is to a certain degree negated by the excitation system, since the cavity of the secondary nozzle destroys the symmetry of the acoustic field distributions compared to a purely rectangular chamber. This influence of the secondary nozzle on the acoustic field symmetry is evidenced in the numerically calculated mode shapes for the MIC in Figure 4.10.

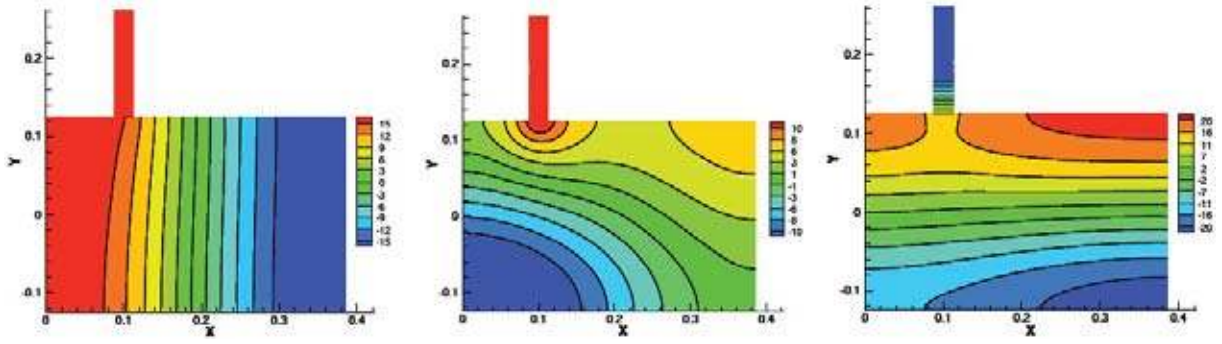

Figure 4.10: First three acoustic mode shapes for the MIC illustrating the influence of the secondary nozzle on mode symmetry (Richecoeur 2006, p.57).

A further drawback of this configuration is the unrepresentative flow field in the chamber. Large recirculation zones outside the main injection stream likely influence the primary injection stream and result in a highly non-uniform sound speed distribution, adversely affecting the acoustic mode shape. While such strong recirculation zones are to a degree unrepresentative of the purely axial flow fields in real engines, the situation is not as extreme as in the CRC.

4.3.3 Concept 3: Excitation segment for BKB

DLR operates a number of experimental sub-scale combustors with modular design at the P8 test facility. The approach of developing a new HF segment which integrates with existing hardware was considered in the hopes of reducing development time and costs. Design concepts which involve the integration of an HF segment and excitation system with an existing modular combustor were explored, thus taking advantage of existing test bench interfaces and expensive injector and nozzle components.

The modular combustor BKB, illustrated in Figure 4.11, was identified as a suitable candidate for a new HF segment since it has standard interfaces between all modular segments. BKH can operate at the conditions specified for this project and already has a matrix penta-injector. A concept requiring minimal development effort is a new BKB segment with a secondary nozzle and toothed-wheel modulation system, as depicted in Figure 4.12. However, this concept does not comply with the goal of achieving transverse mode frequencies representative of real engines. BKB has an internal diameter of 50 mm resulting in a 1T mode frequency of around 18 kHz, far greater than the target of 4 kHz.

Figure 4.11: Experimental combustor BKB (Suslov et al. 2005, p.3).

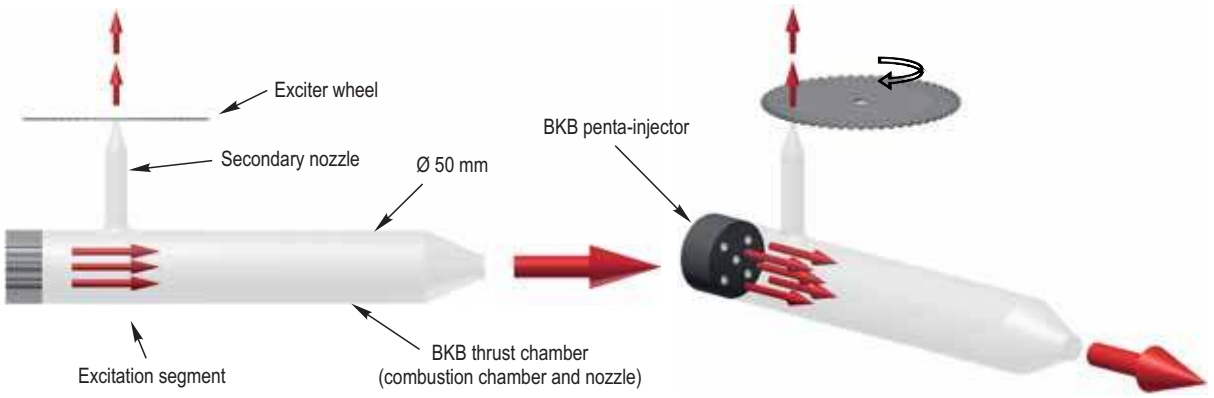

Figure 4.12: BKB with excitation segment concept (internal geometry).

4.3.4 Concept 4: Ring resonator segment for BKB

A further concept for BKB with dimensions resulting in a 4 kHz 1T mode was considered. The 'ring resonator' concept, depicted in Figure 4.13, is essentially a segment with the same dimensions and excitation system as the CRC, integrated between the injector and main chamber segments of BKB. Propellant injection occurs axially through the ring resonator segment rather than radially from the side as in the CRC.

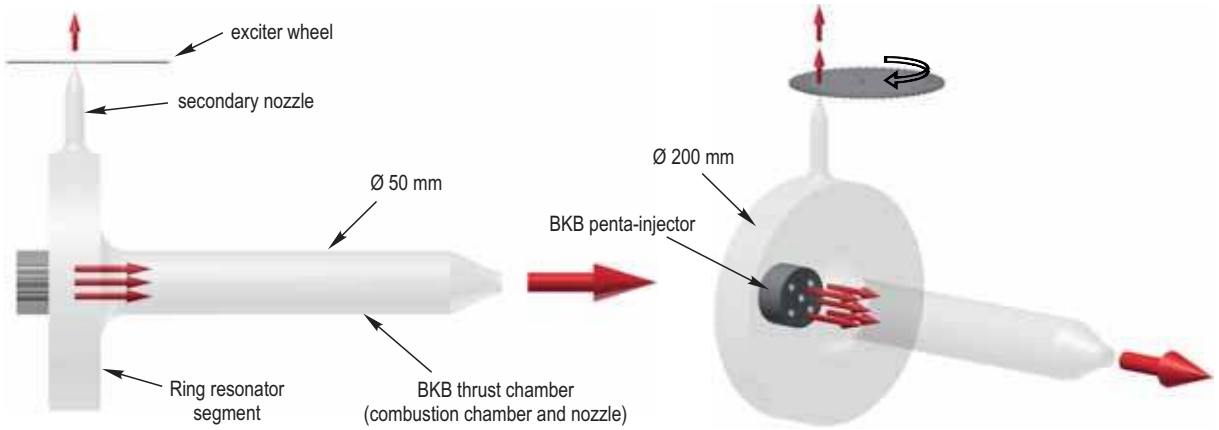

Figure 4.13: BKB with ring resonator concept (internal geometry).

An acoustic mode study was conducted to better understand the behaviour of the three dimensional acoustic modes of the BKB with ring resonator configuration. The finite element software package ANSYS 11.0 (ANSYS Inc 2011), was used to create a basic three dimensional model of the resonator and chamber geometry and solve the acoustic wave equation to determine the pressure distribution and frequencies of the acoustic modes. Acoustic mode shapes and frequencies are calculated using linear acoustic theory. Linear acoustic theory is based on the assumptions that viscosity can be neglected, the velocities of the acoustic wave motion are much smaller than the sound speed, c, and there is no mean flow over which the acoustic motions are superimposed. Using these assumptions the acoustic pressure distribution $p' = p'(x,y,z,t)$ of an acoustic field can be described by the differential equation:

$$\frac{\partial p'}{\partial t^2} + c^2 \nabla p' = 0 \ . \tag{10}$$

Assuming a solution for the pressure variation with harmonic time dependence of the form $p'(t) \propto \sin(\omega t)$, the pressure field equation can be reduced to an eigenvalue problem of the form:

$$\nabla p' + \frac{\omega^2}{c^2} p' = 0 \ , \tag{11}$$

where $\omega = 2\pi f$ is the acoustic resonance frequency.

For some simple geometries, such as a cylindrical resonator, the pressure distribution and mode frequencies are relatively simple to calculate analytically. However, for more complicated three-dimensional geometries there exists no analytical solution and so the pressure field equation must be solved numerically using a finite element approach. This approach has also been used by Cheuret (2005) to predict the resonance modes of the CRC and is able to fairly closely predict the measured resonance frequencies despite the non-uniform sound speed conditions and flow field present during operation of the real combustor.

For simplicity, gas conditions inside the combustion chamber are assumed to be homogeneous with a single value of sound speed. The sound speed value can be estimated using the well-known NASA-Glenn 'Chemical Equilibrium with Applications' program (CEA2) (Gordon & McBride 1994). For the intended operating condition with P_{cc} = 60 bar and oxidiser-to-fuel mixture ratio of ROF = 6, CEA2 estimates an adiabatic, equilibrium mixture temperature of T_{bulk} = 3534 K, molar mass of M = 13.31 g/mol, and specific heat ratio of γ = 1.14, giving a theoretical sound speed of c_{th} = 1585 m/s.

Figure 4.14 shows the numerically calculated acoustic pressure distributions and frequencies for the first few resonance modes of the ring resonator geometry. The colour scale indicates the distribution of fluctuating acoustic pressure, with red and blue indicating locations of pressure antinodes, and green indicating the location of a pressure nodal line. The 1T mode frequency is much the same as for the CRC, as would be expected, however suffers from the same nodal line asymmetry due to the presence of the secondary nozzle. The 1L mode of the chamber at 1557 Hz could be used to study pressure interaction with injection. The next mode with an appreciably uniform pressure antinode at the injector location is the 1R3L (Figure 4.14c), which has a natural frequency of 8830 Hz. This is too far from the target frequency of 4 kHz to be of interest.

Practical drawbacks to this configuration are the large surface area to volume ratio and the expected difficulty in applying active cooling to the segment as well as optical access. Optical access would be especially limited since a window could not be longer than the thickness of the ring resonator segment itself and the large volume of gas in the space between the injector and the window at the resonator wall would degrade the quality of shadowgraph imaging of the injection streams.

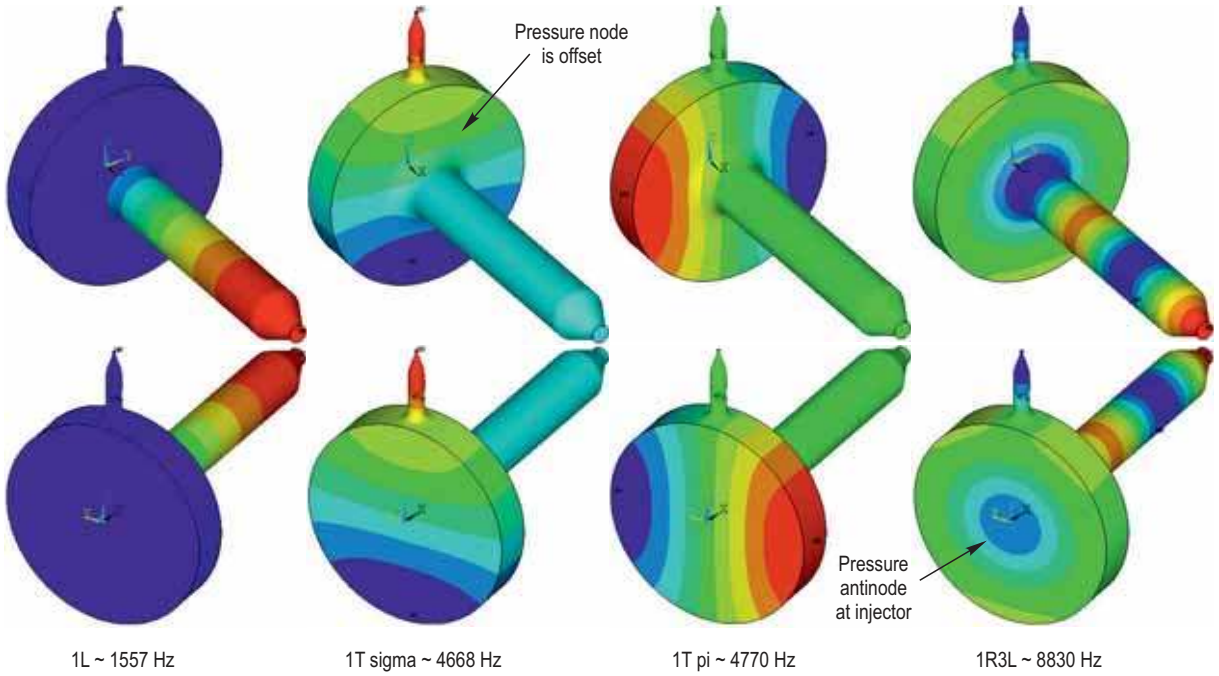

Figure 4.14: Numerically calculated BKB-ring resonator chamber resonance modes.

4.3.5 Concept 5: Twin resonator segment for BKB

In addressing the aforementioned practical drawbacks, the ring resonator evolved into the so called 'twin resonator segment' (TRS) concept, illustrated in Figure 4.15. The TRS essentially consists of two resonator cavities of the same cross section as the main BKB combustion chamber extending perpendicularly from either side of the chamber. The upper resonator cavity tapers to a secondary nozzle where modulation of the exhaust flow is applied.

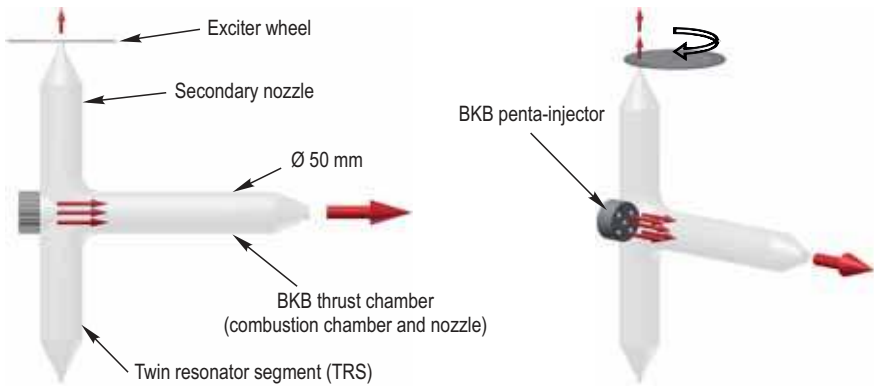

Figure 4.15: Twin resonator segment concept (internal geometry).

ANSYS was again used to conduct a study of the three-dimensional acoustic modes of the twin resonator concept in the same way as for the ring resonator concept. The length of the main chamber and depth of the resonator cavities was varied so the behaviour of the 3D mode frequencies could be better understood. It was discovered that for a practical range of chamber and resonator dimensions there are three adjacent chamber modes of interest. The pressure distributions for these three modes, calculated using ANSYS for a uniform sound speed of

1585 m/s, are shown in Figure 4.16 (note that a cutting plane is taken through the centreline of the chamber). The first mode, designated $1L_z$ (the first longitudinal mode of the resonator, which is aligned with the z-axis) and pictured in Figure 4.16a, has a velocity antinode at the location of the injector, so it provides the opportunity to study transverse mode velocity interaction with the injection stream. The second mode, designated $2L_z$ $1L_x$ (second longitudinal mode of the resonator, first longitudinal mode of the main chamber), has a pressure antinode at the injector, providing the opportunity to study pressure interaction. The third mode, designated $2L_z$ $2L_x$, also has a pressure antinode at the injector, however the relative amplitude of the pressure antinode is higher and its spatial distribution seems to be more uniform in the injector region, so it may result in more effective interaction with the injection stream than the $2L_z$ $1L_x$ mode and should therefore be considered as well.

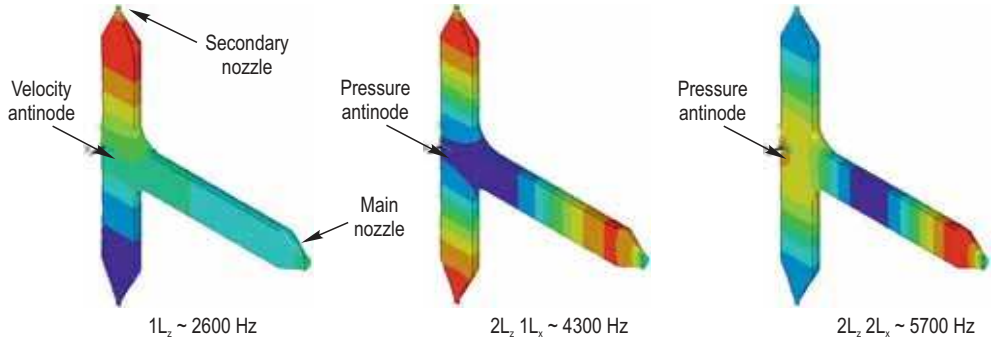

Figure 4.16: Twin resonator segment resonance modes of interest.

These three modes lie within a relatively small frequency range around the target frequency of 4 kHz, so they can be considered representative of real HF combustion instability. Thus velocity or pressure interaction can be studied simply by exciting a different one of these three modes. Alternatively, the resonator length could be adjusted, perhaps by inserting an extension segment between tests, placing the $1L_z$ mode at the same frequency as the $2L_z$ $1L_x$, allowing investigation of pressure and velocity interaction at the same resonance frequency.

Further advantages of this configuration are that the secondary nozzle for the excitation system does not interfere with the shape of the acoustic modes, as it does not break the symmetry of the chamber geometry, and the length of an optical access window would not be hindered by the resonator size in the axial direction.

4.3.6 Concept selection

For its apparent design simplicity, favourable acoustic mode properties and the potential for application of optical access, the twin resonator concept was initially selected for further development over the other concepts described previously. Following more extensive design study, which is summarised in Appendix A, it was decided to abandon the TRS concept in favour of the rectangular combustor concept (see Section 4.3.2). A new rectangular combustor was developed through to implementation. The new combustor, used to conduct the experimental work for this project, is described in the remainder of this chapter.

4.4 New rectangular combustor: BKH

With the abandonment of the TRS concept, the opportunity to design a completely new combustor led to the re-assessment of the rectangular combustor concept. The rectangular combustor concept, introduced previously in Section 4.3.2, is a proven experimental system for HF investigation (see Section 4.1.3). The configuration allows the inclusion of optical access with relative ease and could be developed to integrate with the P8 test facility. This concept was therefore selected as it satisfies the project objectives.

4.4.1 BKH concept overview

The new combustor was dubbed ‘combustor H’, or ‘BKH’; ‘BK’ being an abbreviation of the German word ‘Brennkammer’, meaning combustion chamber, and ‘H’ being the next letter available for naming an experimental combustor developed by DLR for the P8 test facility. Illustrated conceptually in Figure 4.17, the BKH configuration is similar to the rectangular cross-sectioned MIC combustor (Section 4.1.3). At one end of the chamber is the injector which injects hydrogen and oxygen through multiple shear coaxial injection elements. At the opposite end is the main nozzle ensuring mean flow in the (axial) x-direction through the chamber. Located in the upper wall, a short distance downstream of the injection plane, is the secondary nozzle for the excitation system. Flow through the secondary nozzle is periodically blocked by a toothed ‘exciter wheel’ which spins over the exit to the nozzle, as for the excitation system of the CRC. When the excitation system is not installed, the secondary nozzle is replaced with a plug which blocks the cavity and gives a ‘clean’ combustor configuration. Windows in both side walls provide optical access to the near-injector region. The windows are protected from the flame by a film of ambient temperature gaseous hydrogen. Above and below the primary injector are arrays of simple, circular elements for the injection of secondary hydrogen, also of ambient temperature. The combustion chamber and nozzles are actively cooled using water flowing through a series of channels distributed inside the walls of the chamber segments. Water cooling allows the combustor to withstand very high combustion temperatures and operate for long test durations.

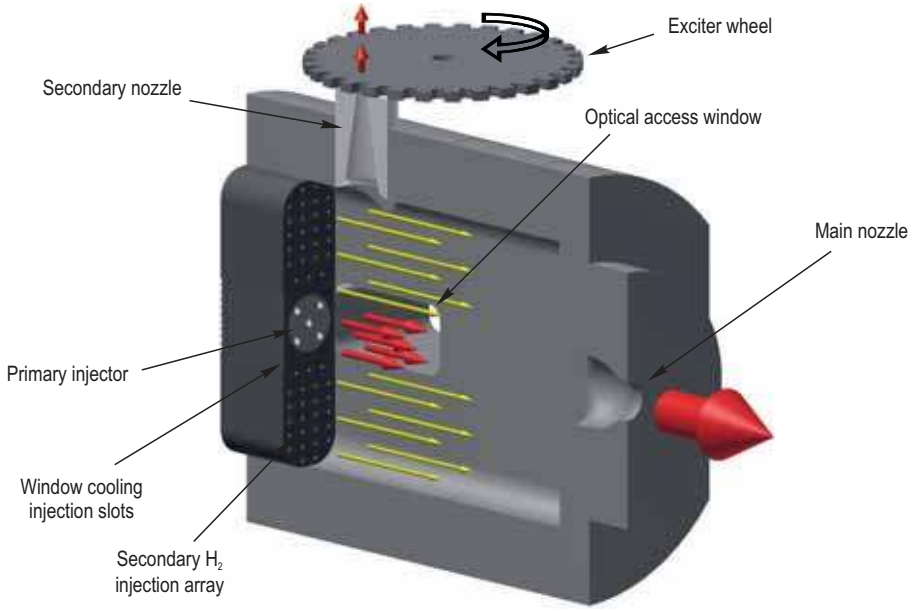

Figure 4.17: BKH combustor concept.

4.4.2 Combustion chamber acoustics

The internal volume of the BKH combustion chamber is sketched in Figure 4.18. Detailed dimensions of the internal volume of the combustor and injection system are given in Appendix B. The basic dimensions of the combustion chamber; length L_x = 305 mm, width L_y = 50 mm, and height L_z = 200 mm, were selected so as to result in acoustic modes which satisfy the design specifications and experimental objectives.

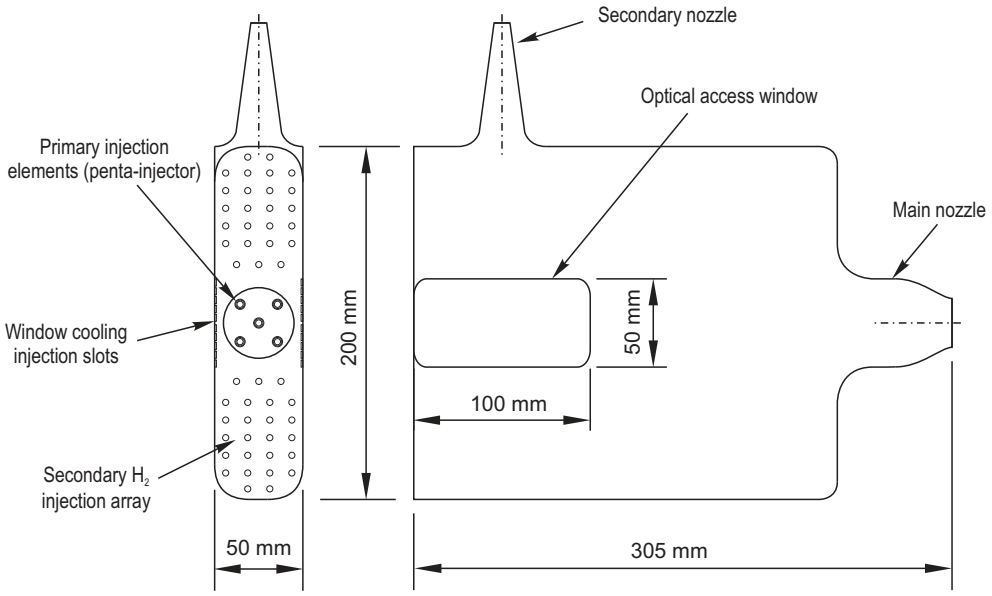

Figure 4.18: Internal volume of the BKH combustion chamber.

The acoustic mode frequencies of BKH may be estimated using the following analytical approach. Firstly the model geometry is greatly simplified, taking the combustion chamber as a closed rectangular volume with no nozzles, injectors or any other cavities. The conditions inside the volume will be assumed to satisfy linear acoustics, namely uniformly distributed ideal gas properties, small amplitude oscillations, and no mean flow. The mode frequencies can be calculated using

$$f(n_x, n_y, n_z) = \frac{c}{2}\sqrt{\left(\frac{n_x}{L_x}\right)^2 + \left(\frac{n_y}{L_y}\right)^2 + \left(\frac{n_z}{L_z}\right)^2} \quad , \tag{12}$$

where $c = [\gamma(R/M)T_{bulk}]^{1/2}$ is the sound speed, L_x, L_y, and L_z are the length, width and height, respectively, and n_x, n_y, and n_z are the mode indices. For illustrative purposes an intended operating condition of BKH with P_{cc} = 60 bar and oxidiser to fuel mixture ratio of ROF = 6 is considered. The overall oxygen-hydrogen mixture ratio is ROF_{bulk} = 0.49, which takes into account the primary injector ROF of 6 as well as the secondary and window cooling H_2 injection (see Section 4.4.4). For these conditions the CEA2 program estimates an adiabatic, equilibrium mixture temperature of T_{bulk} = 774 K, molar mass of M = 3.004 g/mol, and specific heat ratio of γ = 1.38, giving a theoretical sound speed of c_{th} = 1712 m/s. The first few mode frequencies of BKH then take the values listed in Table 4. The three-dimensional acoustic wave equation (Equation 10) can be solved analytically for the rectangular volume to give the corresponding mode pressure distributions shown in Figure 4.19.

The first two fundamental modes, the first longitudinal (1L) and first transverse (1T), as well as the first combined mode (1L1T), lie within the frequency range of interest, 1 to 6 kHz. These are considered to be the primary modes of interest for use in the study of flame-acoustic interaction in BKH. The 1L mode has a uniform pressure antinode covering the entire injector face and can therefore be used to study the interaction of acoustic pressure with the flames. Both the 1T and 1L1T modes have a pressure node at the primary injection region which results in acoustic gas motion, or 'acoustic velocity', transversally across the primary injection jets. The 1T and 1L1T modes are therefore important for the study of the interaction of acoustic velocity with the flames. In this way, excitation of the 1L, 1T, or 1L1T modes affords similar functionality to the CRC with its adjustable secondary nozzle positioning. The CRC internal dimension of 200 mm was used in BKH to give a 1T mode frequency near 4 kHz, satisfying the design specification. The length of 305 mm gives good separation of the 1L mode frequency from the 1T. Finally, the narrow width of the combustion chamber shifts modes in the horizontal y-orientation well above the frequency range of interest, so there are only longitudinal, transverse and combined modes in the vertical xz-plane to deal with.

Table 4: Theoretical mode frequencies for basic chamber dimensions of BKH.

Mode name	Label	n_x	n_y	n_z	Frequency (Hz)
First longitudinal	1L	1	0	0	2802
First transverse	1T	0	0	1	4280
First combined	1L1T	1	0	1	5116
Second longitudinal	2L	2	0	0	5604
First horizontal	$1L_y$	0	1	0	17,120

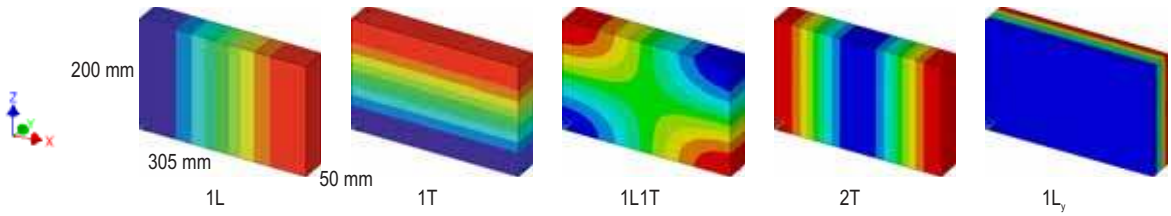

Figure 4.19: Pressure distributions for the resonance modes of a simple rectangular volume as listed in Table 4.

4.4.3 Primary injector

BKH has a primary injector with five shear coaxial injection elements (penta-injector), arranged in a matrix pattern as illustrated in Figure 4.20. While it is conceded that the outer four elements will be affected by the boundary conditions, namely window cooling film injection at the sides, and secondary H_2 injection above and below the primary injector, the matrix pattern shields the central jet from these influences. The central jet environment is thus intended to be representative of real multi-element injector distributions. Study of the central jet will therefore be the focus of optical investigations.

Injection element orifice sizes and pattern spacing were selected based on typical values of real injectors. Table 5 summarises these typical values and lists those chosen for BKH. The LOx outlet diameter D_O and fuel annulus dimensions result in injection velocities which fall

within the range of typical values. By virtue of realistic element dimensions, the values of similarity parameters, such as velocity ratio *VR* and momentum flux ratio *J*, are also representative. Subsequently, atomisation and mixing processes, which are controlled by such parameters, will also be representative of conditions found in operational engines. The LOx post has no recess or taper, since these are known to be stabilising features. The injection pressure drops for LOx and H_2 are representative of typical design rule-of-thumb values, intended to provide sufficient de-coupling between injection manifolds and the combustion chamber. The spacing between elements S_O is very slightly outside the normal range identified for real engines; $S_O = 2.6\ D_O$, compared to $S_O \sim 1.7$ to $2.0\ D_O$ for real engines. This slightly greater spacing was chosen intentionally to maximise clarity of optical access to the central jet, while maintaining a value closely representative of real engines, and a tighter spacing than previous systems such as the MIC.

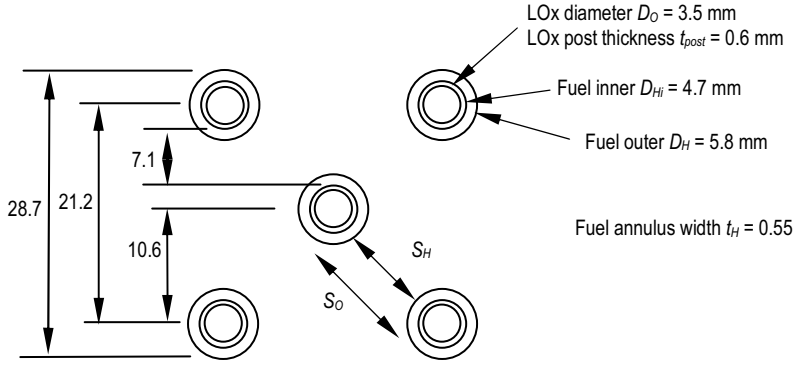

Figure 4.20: BKH Penta-injector pattern dimensions.

Table 5: BKH injector design parameters.

Injector parameter		Typical values	BKH injector
LOx injector diameter	D_O	2–6 mm	3.5 mm
H_2 outer diameter	D_H	5–10 mm	5.8 mm
H_2 annulus width	t_H	0.5–1.0 mm	0.55 mm
Injector spacing	S_O	1.7–2.0 D_O	2.6 D_O
	S_H	1.1–1.3 D_H	1.6 D_H
LOx injection velocity	u_O	10–30 m/s	7–30 m/s
H_2 injection velocity	u_F	180–360 m/s	100–400 m/s
Oxidiser-to-fuel ratio	*ROF*	4.4–7.2	2–6
Injection velocity ratio	$VR = u_H / u_O$	9–17	6–100
Momentum flux ratio	$J = \rho_H u_H^2 / \rho_O u_O^2$	10–20	2–55

4.4.4 Secondary injection

An important feature of BKH is the extensive use of secondary injection. Gaseous hydrogen at ambient temperature is injected as a parallel co-flow through simple orifices into the spaces above and below the primary injector. The arrays of secondary H_2 injector elements have a

simple, square distribution pattern with spacing similar to that of the primary elements. The mass flow of secondary H_2 can be controlled independently of the primary injector.

Large recirculation zones above and below the primary injector were previously identified as drawbacks to the rectangular combustor configuration (see Section 4.3.2), as they result in disturbances to the flow field of the injection streams. In BKH it was decided to use a secondary flow parallel to that from the primary penta-injector in order to combat the formation of large recirculating flow fields which would otherwise develop with only the centralised primary injector. This situation is illustrated in Figure 4.21.

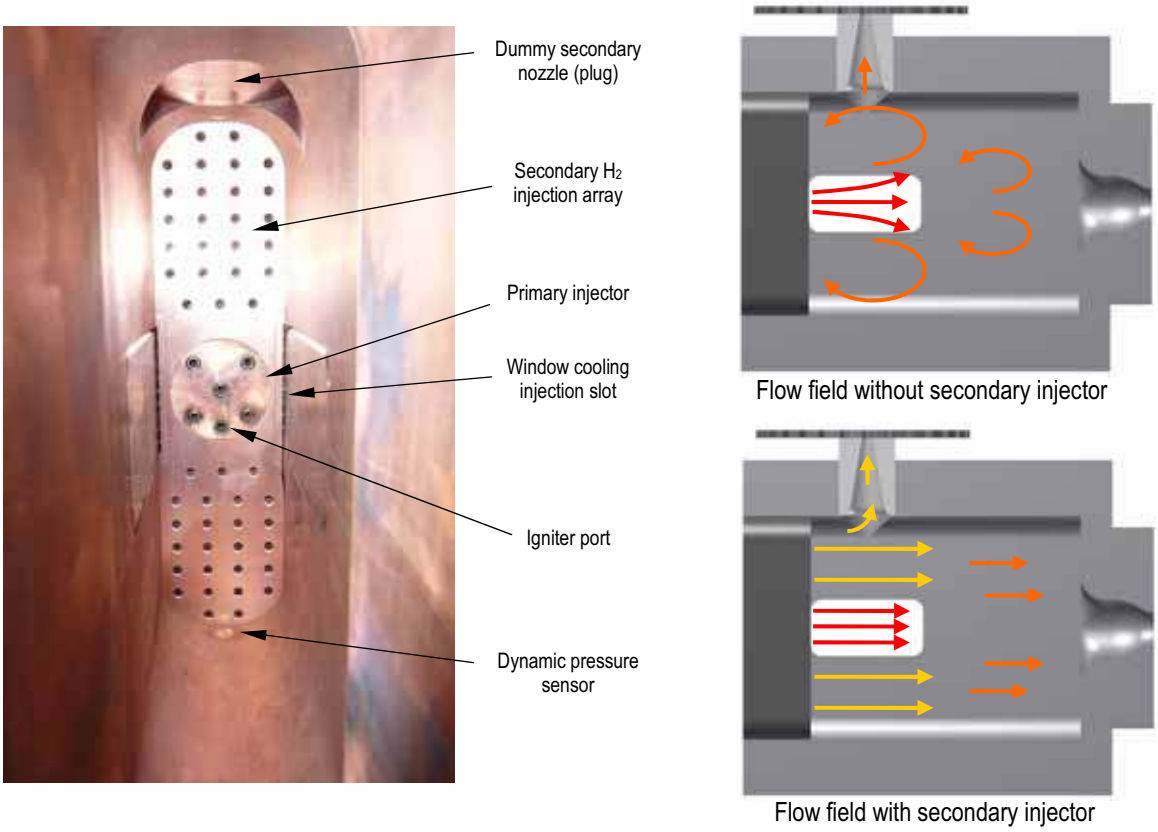

Figure 4.21: Injector faceplate showing secondary hydrogen injection arrays, and the desired influence on the flow field.

A further motivation for using secondary H_2 injection in this manner is the desire to create a uniform acoustic environment. With the primary injectors clustered in the centre of the chamber, the dead spaces above and below would otherwise be filled with recirculating combustion products. An acoustic wave travelling down along the vertical (z-axis) direction from the cooling combustion products in the dead space through the flame zone would experience extreme gradients in temperature and therefore in sound speed. This would result in distortion to the acoustic resonance mode structures and unpredictable frequency effects. The use of secondary H_2 injection is expected to minimise such effects since the difference in sound speed between the flame zone and ambient temperature H_2 is small.

4.4.5 Diagnostics

BKH has a suite of integrated pressure, temperature and vibration sensors, as well as access windows for the application of optical diagnostics.

Dynamic pressure sensors are used to record high frequency, acoustic pressure oscillations in both the combustion chamber and the injection manifolds. There are three sensors flush mounted along both the upper and lower walls of the combustion chamber, labelled *PCCdyn1* through *PCCdyn6*. Their distribution allows detection and identification of the primary acoustic modes of interest. Dynamic pressure sensors are also installed in each of the three injection manifolds; LOx (*PIOdyn*), primary H_2 (*PIFdyn*), and secondary H_2 (*PIHdyn*). These should assist in the identification of any injection coupling with combustion chamber acoustics. Placement of the dynamic pressure sensors is shown in Figure 4.22.

The dynamic pressure sensors are of the piezo-electric type. A combination of Kistler and PCB brand sensors are used as indicated in Figure 4.22. All sensors have a natural frequency well outside the range of interest. Signals are sampled at 100 kHz and an anti-aliasing filter is implemented with a cut-off frequency of 40 kHz.

Static pressure sensors are applied to the combustion chamber and all injection manifolds via short capillary tubes to protect them from extreme temperatures. Static pressure readings are used to define operating conditions and determine the pressure drop across injectors.

Thermocouples protruding a small distance from the wall are used to measure the temperature of injectants in their respective manifolds prior to injection. Combustion chamber wall temperature and main nozzle throat temperature are monitored using thermocouples inside the wall with approximately 1 mm depth. The chamber wall temperature sensors are located a short distance downstream of the optical windows, offset slightly from the chamber centreline, such that they may detect variation in heat load on the chamber walls as a result of any response to excitation.

Accelerometers mounted on the outside of the combustor record structural vibration, which can be used to supplement dynamic pressure data in the determination of resonant frequencies.

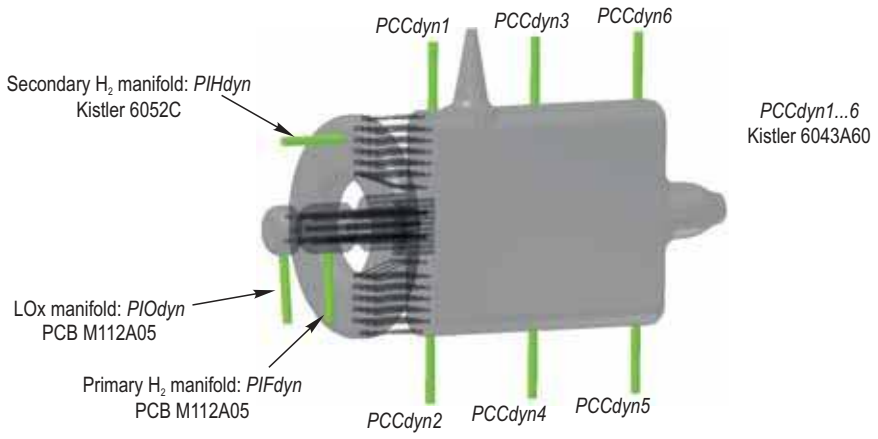

Figure 4.22: Dynamic pressure sensor locations and model names in BKH.

4.4.6 Optical access

Windows on the side walls of the chamber provide optical access to the near-injector region. The windows are made from quartz glass which is transparent to wavelengths from infra-red through to near ultra-violet. This allows the application of shadowgraph imaging techniques using infra-red and visible wavelengths, as well as imaging of hydroxyl radical (OH*) emission which occurs in the vicinity of 307 nm.

The window height of 50 mm was chosen to provide a view of all five primary injection elements. The length of 100 mm was a compromise between maximising the downstream view of the injection streams, and engineering considerations such as the structural integrity and cooling of the quartz window. Dummy versions of the windows made from steel can be used when optical access is not required. These dummy windows are instrumented with nine flush-mounted thermocouples for measurement of the gas temperature in contact with the combustion chamber walls. Photos of the quartz windows and the steel dummy windows installed in BKH are shown in Figure 4.23.

The windows require protection from direct contact with the combustion zone since large thermal gradients can cause quartz to crack. Injection of ambient temperature H_2 through slots either side of the primary injector provides film cooling of these windows. The mass flow rate of window cooling H_2 can be controlled independently of the primary injector or secondary H_2 injector.

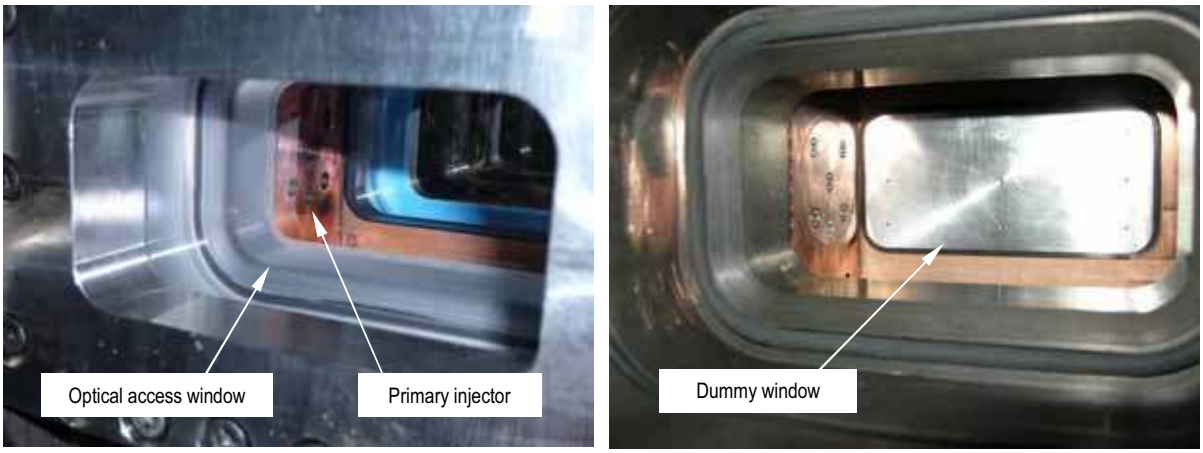

Figure 4.23: Optical access windows and dummy windows.

4.4.7 Excitation system

The excitation system employed on BKH is essentially a scaled up version of the CRC or MIC nozzle modulation systems. While no pattern for scaling such a system currently exists, functional principles learned from experience with the CRC at DLR were applied in developing the system. The exciter wheel should spin freely yet pass as close as possible to the outlet plane of the secondary nozzle throat to effectively block the flow and maximise pressure build up during each blockage phase. Excitation amplitude in the CRC is found to be strongly dependent on the spacing between secondary nozzle exit and the surface of the exciter wheel tooth (Sliphorst 2011). The vertical positioning of the BKH exciter wheel can

be finely adjusted so as to determine the spacing between the secondary nozzle outlet and the exciter wheel teeth.

Excitation amplitude is also dependent on secondary nozzle exit area. The secondary nozzle of BKH was made as large as possible to maximise excitation amplitude while ensuring that the exciter wheel would withstand the force exerted by the exhaust jet with minimal deflection, and minimising the rotational inertia of the wheel to allow the use of a conveniently sized servomotor drive system. The diameter of the nozzle D_{SN} was also chosen to conform to the same criteria used in the CRC, namely the ratio between secondary nozzle diameter and main nozzle diameter D_{MN};

$$D_{SN} = D_{MN} / \sqrt{10} \ . \tag{13}$$

The entrance diameter is as large as possible, and smoothed, to maximise acoustic coupling with the combustion chamber volume. The depth of the secondary nozzle was chosen to be as short as practically possible, minimising the opportunity for viscous damping to reduce the amplitude of acoustic excitation. A short nozzle length is also important to minimise the impact of the cavity on the structure of the 1T acoustic mode. Ideally, the nodal line of the 1T pressure distribution should be aligned with the centre of the faceplate to ensure uniform acoustic velocity interaction with the injection streams. This is the case for a simple rectangular volume, whereas in BKH the addition of the secondary nozzle cavity in the upper wall causes the nodal line to move upwards, resulting in an asymmetrical 1T mode pressure distribution. This influence of secondary nozzle length is illustrated by the series of two-dimensional, FlexPDE numerical modal analysis results shown in Figure 4.24. The nodal line is deflected upwards by 12 mm from the chamber centre line for the chosen secondary nozzle length of 70 mm.

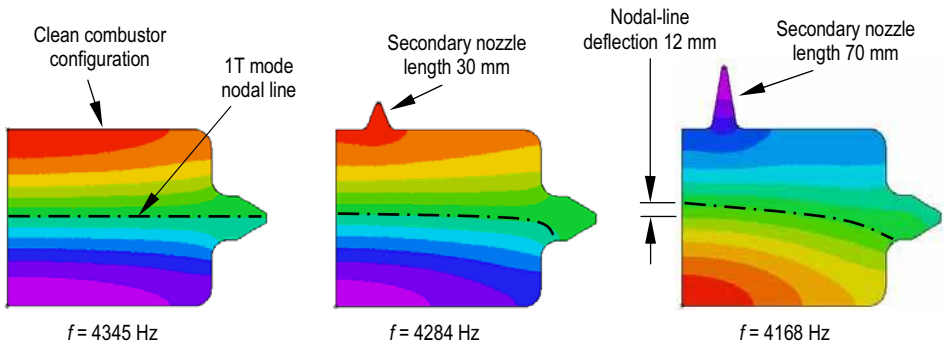

Figure 4.24: Modal analysis results showing the influence of secondary nozzle length on the 1T mode structure. The numerical mode calculations were conducted in FlexPDE using a sound speed of 1712 m/s. The primary and secondary nozzle exit sizes have been scaled for two-dimensionality.

Excitation of transverse acoustic oscillations at the injection plane is strongest when the secondary nozzle is positioned at the injection plane. This is considered to be important to the experimental goal of reproducing conditions of transverse mode HF instability because the 1T mode is known to be strongest at the faceplate (Section 2.6.2). The secondary nozzle was therefore positioned as near to the injection plane as possible, while accommodating a dynamic pressure sensor directly adjacent to the injector plane.

The secondary H_2 injection (Section 4.4.4) results in a mostly cool, hydrogen-rich flow through the secondary nozzle. This ensures that thermal loads on the exciter wheel from the secondary nozzle exhaust are minimal. The exciter wheel is driven by an electric servomotor. The electric servomotor can be programmed to execute a desired excitation profile during a test. Excitation frequencies up to 6 kHz are possible in order to excite the 1L, 1T and 1L1T modes of interest. Photographs of the system installed on the combustor are shown in Figure 4.25.

The entire system is enclosed in a sealed pressure housing to prevent the free discharge of combustible hydrogen into the test facility. Gaseous nitrogen (GN_2) is used to continuously purge this housing to ensure a combustible mixture does not exist inside the housing. A photograph with the housing installed is shown in Figure 4.26. Nitrogen flow is also directed onto the upper surface of the exciter wheel for cooling. An exhaust pipe directs the secondary exhaust gases and nitrogen mixture out from the housing to be burned harmlessly in the exhaust plume from the primary nozzle.

When the excitation system is not in use, the secondary nozzle is replaced with a plug which fills the cavity and results in a ‘clean’ configuration of the combustion chamber.

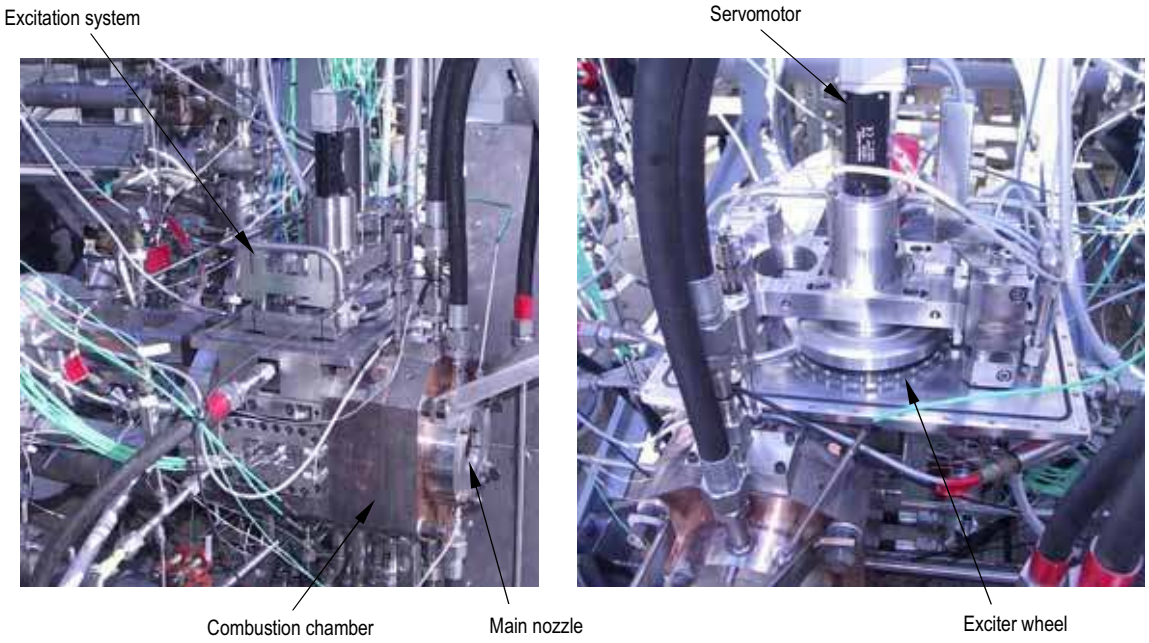

Figure 4.25: Photographs of the excitation system installed on BKH.

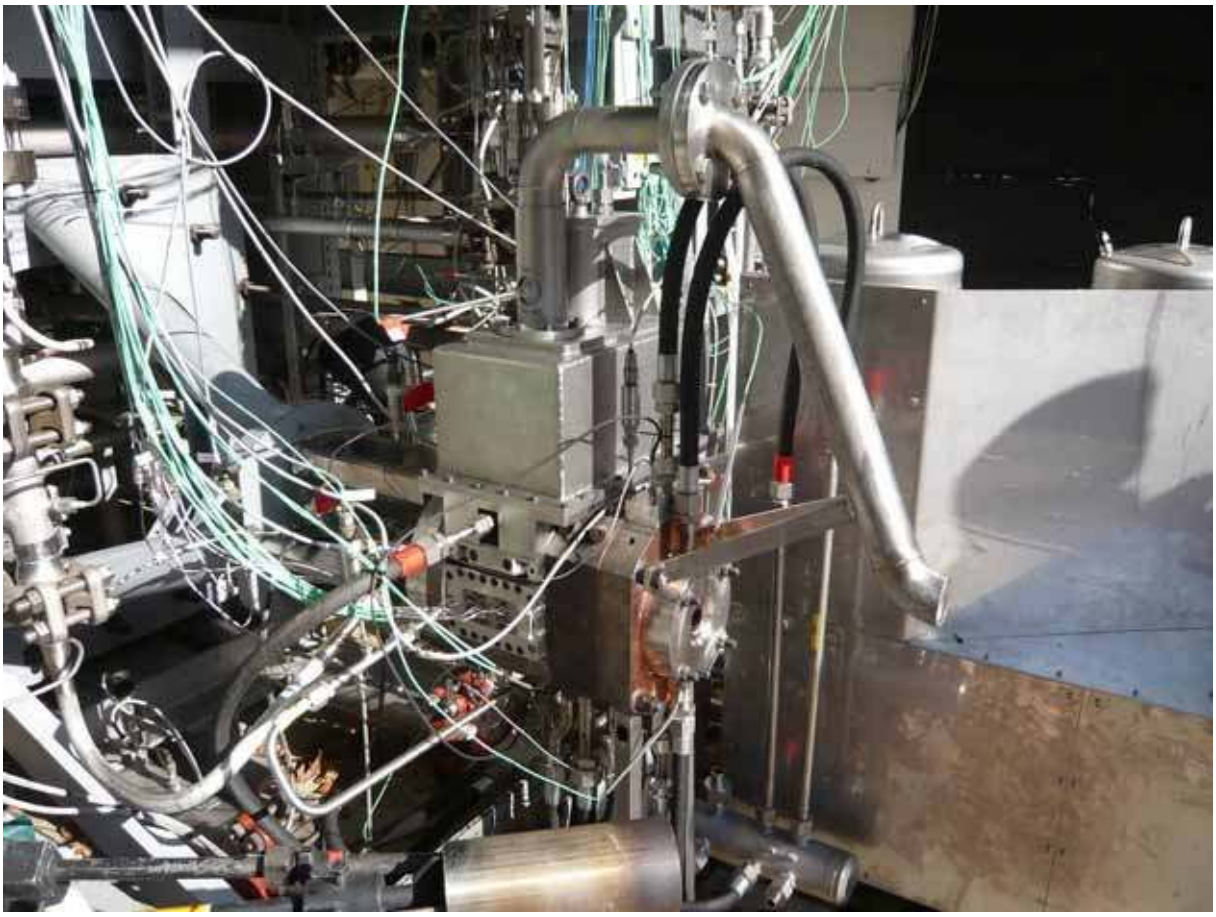

Figure 4.26: The excitation system on BKH with housing installed.

5. EXPERIMENTAL TECHNIQUES

The experimental results presented in this work were obtained from tests conducted at the German Aerospace Centre (DLR), Institute of Space Propulsion located near the town of Lampoldshausen in the district of Hardthausen, southern Germany. Tests were conducted using the BKH combustor, described in detail in the previous chapter, in the context of five separate test campaigns on the P8 test facility at DLR Lampoldshausen.

This chapter begins with a general overview of the test facility and test operation, followed by more detailed descriptions of each of the test campaigns, covering hardware and diagnostic configurations, and the achieved test conditions.

5.1 Test operations

5.1.1 Test facility

Tests with the BKH combustor were conducted at the European Test Facility for Cryogenic Rocket Propulsion 'P8', as was one of the defining specifications of the project. The P8 test facility, pictured in Figure 5.1, is operated in a partnership between CNES, DLR, EADS Astrium, and SNECMA (Haberzettl 2000).

The facility provides cryogenic propellants at pressures which allow tests to be run at conditions fully reflecting those of current, upper stage-scale engines. Propellant supply flow rates and conditions can be regulated to a high degree of accuracy. Tests are controlled by the fully automated measurement, command and control (MCC) system which runs pre-programmed test sequences providing precise control of supplied media mass flow rates, pressures and temperatures and recording sensor signals obtained from the test facility and specimen diagnostic systems. Further details on the capabilities of the P8 facility were presented in Section 4.2.2.

5.1.2 Test campaigns

For this work, five test campaigns with the BKH combustor were carried out on the P8 test facility. The first two were designated as initial hardware testing campaigns for the newly developed combustor. The third ended prematurely when a sequencing error resulted in

critical hardware damage during the first test run. The final two were designed to achieve the test conditions required for completion of this work. More detail on the execution and outcomes of each of these campaigns is given later in this chapter.

Figure 5.1: European Test Facility 'P8' for cryogenic rocket engine research.

5.1.3 Hardware integration

The combustor BKH is integrated with the test facility as pictured in Figure 5.2. The assembled chamber is mounted to the thrust frame inside the test cell (pictured from the outside in Figure 5.1). The media supply system of BKH is connected to the test facility supply interfaces. The supply system for BKH is relatively complex compared to most test specimens operated at P8 due to the separate feed systems for window cooling and secondary GH_2 injection. The additional flow meters and regulation valves for this warm GH_2 supply system were installed in a specially built support frame to ease integration in the test cell and to provide shielding for the system components from the main nozzle exhaust plume.

5.1.4 Test runs

On a designated test day during a P8 campaign, the test facility is brought to an operational state in order to conduct testing. Once the experimental combustor has been configured as required, a test run is performed by the test facility team. The run is defined as beginning approximately 20 minutes before the start of a test sequence, when the test facility is made live, to the end of the sequence when the test specimen and facility are shut down and returned to a safe, inactive state. Test runs are controlled remotely from inside control building D68, situated more than 100 m away from the test cell. Figure 5.3 shows photographs of the test cell during a BKH test run, taken from the control building, D68. The number of tests which can be performed in a single test day depends on the capabilities of the test specimen itself and the turnaround time between tests, which depends on such factors as run-tank filling and whether inspection or adjustment of the test specimen is required. In the case of the BKH combustor, the number of test runs achievable within one test day is two or three. Repetition of test sequences for the sake of statistical repeatability was therefore prohibitively expensive. A total of 59 test runs were executed over the course of the project.

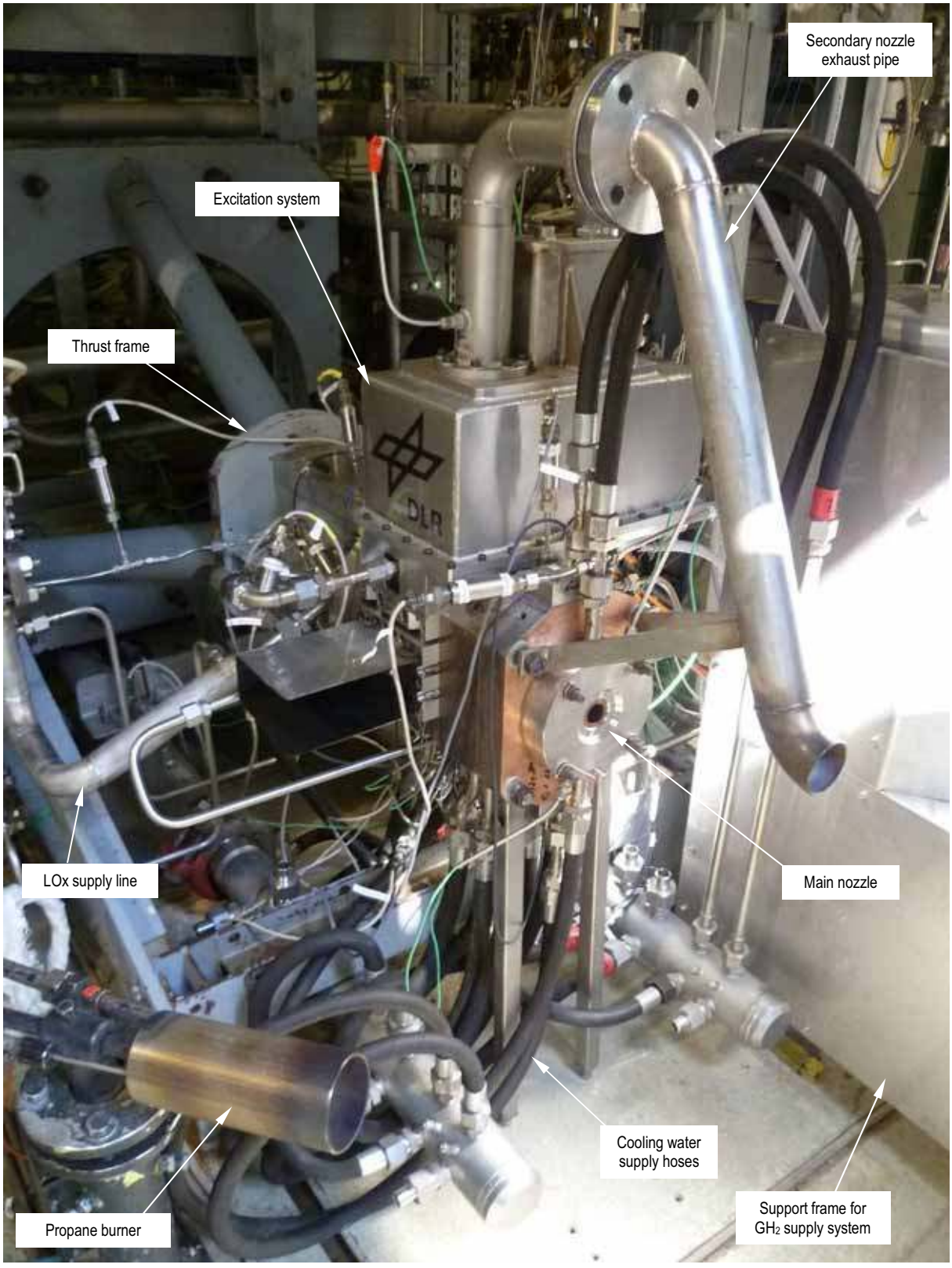

Figure 5.2 BKH integration with the P8 test facility.

Figure 5.3: Photographs of the test cell during a BKH test run, taken from the D68 control building.

5.1.5 Test sequences

Test sequences are pre-programmed into the MCC system by experienced test facility personnel. Sequences are written so as to achieve the desired pre-test conditions, ignition transient, steady state operating conditions, stage transitions, and shut down and purge sequences. Pre-test purge is used to prepare the test specimen for a test, involving pre-

warming or pre-cooling and removing build up of explosive mixtures where they may be dangerous. The ignition sequence introduces the primary media and ignition source to the combustion chamber with such precise timing as to provide reliable ignition and a specified mechanical and thermal load transient. Ignition sequences, as well as shut down sequences, are particularly critical for operation with optical windows, which are sensitive to spatial and temporal temperature and pressure gradients. During the steady state phase of a sequence, mass flow rates and pressures of media supplied from the test facility are actively regulated so as to achieve the desired combustion chamber pressure and oxidiser-to-fuel mixture ratios.

Test sequences may also be staged, with more than one steady state phase separated by transition periods where combustion chamber pressure, mixture ratio, media temperatures, or any combination of these parameters are changed to the next stage. Finally, shut down sequences ensure the test is ended safely and the specimen is returned to a stable, approachable state. Shut down sequences may also be activated before the end of a planned test run if an automated safety protocol is enforced. These safety protocol, known as 'Redlines', are specified ranges of allowable sensor output values which trigger the shut down sequence if violated, in order to avoid damage to the specimen or test facility.

5.2 Diagnostics and data acquisition

The full suite of static and dynamic pressure transducers and thermocouples, as specified in the system design, were installed in the BKH system and operated throughout both campaigns. Sensors in operation for any given test varied slightly between hardware configurations where instrumented modular hardware was installed or removed, for example dummy windows or the excitation system. The P8 test facility is also fully instrumented, monitoring such parameters as tank, feed line, and interface pressures and temperatures, flow rates and valve control inputs and feedback. All sensors, both those belonging to the test facility and specific to BKH, are connected either to a low-frequency or high-frequency channel of the MCC system. All channels are therefore recorded to the MCC databanks and receive the same time stamp, ensuring temporal accuracy.

The conventional diagnostics in the BKH system, namely temperature, static pressure and flow rate measurements are recorded on low-frequency channels with a sample rate of 1 kHz. The thermocouples used for warmer temperature measurement have a published uncertainty of ±1.5 K for temperatures between 233 and 648 K, and ±0.004 K for 648 to 1273 K. Those for cryogenic temperatures have an uncertainty of ±2.5 K between 106 and 313 K, and $\pm 0.015|T - 273|$ K below 106 K. The P8 MCC introduces a further ±0.5 K of noise into the signal. The static pressure sensors are of the strain gauge type and measure absolute pressure. They have a published uncertainty of ±0.2%, and MCC system noise brings the total measurement chain uncertainty to ±1%. Flow rate measurements are performed using turbine type flow meters. Volumetric flow rate measurements are converted to mass flow rate measurements in real time in the MCC computer. Fluid density values are determined from lookup tables using temperature and pressure measurements. The uncertainty in the entire measurement chain, including determination of density values from temperature and pressure measurements, is ±3%.

Dynamic pressure sensors for measurement of acoustic activity in the combustion chamber and injector head, and accelerometers for structural vibration were recorded on high-frequency channels at a rate of 100 kHz. Dynamic pressure transducer signals pass through a series of amplifying and filtering stages before they are recorded to the MCC data bank.

Firstly they pass through a charge amplifier, amplifying and inverting the polarity of the voltage from the piezoelectric sensing element in the transducer. A low-pass filter function, built in to the charge amplifier, was utilised with a cut-off frequency setting of 30 kHz. A further low-pass filter, built in to the acquisition cards of the MCC system, was utilised with a 40 kHz setting. The 30 and 40 kHz filters provide an anti-aliasing function, preventing the introduction of aliased signals into the lower range of effective measurement between 0 and 30 kHz. This measurement chain is designed to provide a signal optimised for analysing acoustic activity in the frequency range of interest for BKH. Measurement chain uncertainty, including sensor and amplifier sensitivity, is ±0.04 bar.

5.3 Optical diagnostics

The details of the setup of optical diagnostics varied from campaign to campaign, and sometimes test to test. Generally, the setup of optical equipment made use of the diagnostic rooms either side of the test cell, as well as space around the combustor inside the test cell. One high-speed camera for Shadowgraph imaging, the back-lighting source, and related optics were setup in the diagnostic rooms either side of the test cell. The setup provides a perpendicularly aligned line-of-sight through the chamber windows. A second high-speed camera with built-in intensifier for OH* chemiluminescence imaging was installed in a protective housing inside the test cell. Optical imaging is recorded to on-board memory of the high-speed cameras themselves, not to the MCC. The cameras could however be triggered to begin recording by signals from the MCC, programmed at specific time points in the test sequence. Trigger output signals from the cameras were also recorded on MCC high-frequency channels, providing a reference for synchronisation with the MCC timeline. Camera synchronisation is conservatively considered with an uncertainty of ±5 μs (one-half sample at 100 kHz), which equates to approximately ±7° of phase at the 1T mode frequency of 4 kHz. The following is a brief discussion of each of the applied optical diagnostic techniques.

5.3.1 OH* chemiluminescence imaging

Imaging of chemiluminescence is often used to study the reaction zone of flames. Chemiluminescence is photon emission from electronically excited species, for example the hydroxyl radical (OH*), which are not in thermal equilibrium during chemical reaction (Docquier & Candel 2002). OH* may be formed in O_2/H_2 combustion by the following reactions:

$$O + H \rightarrow OH^* \tag{14}$$

$$O_2 + H \rightarrow OH + H_2O \tag{15}$$

Radical concentration is greatest for lean to stoichiometric conditions, and the excited species are very short lived before they return to an unexcited state by spontaneously emitting a photon (chemiluminescence). These properties make chemiluminescence a good indicator of the reaction zone of a flame. OH* emission bands are well separated from those of other species in the emission spectrum of O_2/H_2 flames, making it convenient to isolate with narrow-band interference filters. Figure 5.4 shows the O_2/H_2 emission spectrum as measured in another subscale LOx/H_2 combustor operated at the P8 test facility. The combustor, called ‘BKD’, has 42 shear coaxial injection elements, and optical access to the near-injector region

is provided by fibre-optic probes. The spectrum in Figure 5.4 was recorded at an operating condition of P_{cc} = 80 bar with ROF = 6. It should be noted that the spectrum has not been calibrated to compensate for the influence of the optical measurement chain on relative intensity. The frequency content of the spectrum is consistent with O_2/H_2 spectra published by Gaydon (1974), and also with those measured by Mayer and Tamura (1996) in a single injector, sub-scale combustor. The strong peak between 305 and 310 nm is identified as originating from OH* chemiluminescence. According to de Izarra (2000), the strongest emission from OH* is from two peaks at 306.4 and 309.2 nm, but these are not distinguishable by the measurement resolution used here. In the current project an optical filter with a wavelength pass-band of 305 ± 5 nm was used. This filter allows the primary peaks of OH* chemiluminescence emission to pass but excludes all other spectral content.

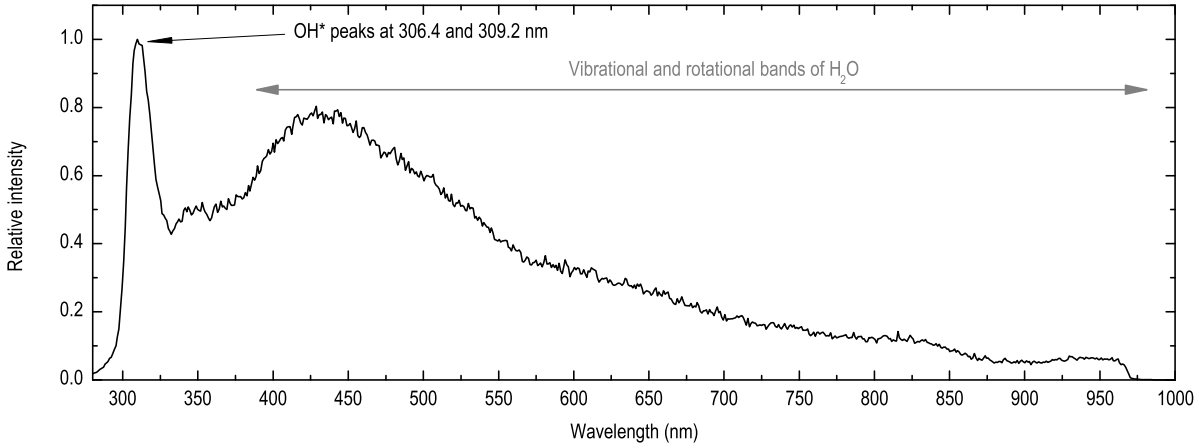

Figure 5.4: Emission spectrum from a LOx/H_2 sub-scale combustor.

Care must be exercised in interpreting imaging of OH* chemiluminescence. OH (ground state) is not uniquely associated with the reaction zone as is, for example, CH in hydrocarbon combustion. OH is an equilibrium species in the combustion products, and the reaction

$$H_2O + O \rightarrow 2OH \tag{16}$$

contributes to observed OH* intensity. Furthermore, absorption of OH* by major species in combusting LOx/H_2 mixtures is low (Gaydon & Wolfhard 1978), so images consist of integrated measurements of OH* emission along the line of sight. In studies of combustion instability, it is often a goal to measure fluctuations in heat release rate. Chemiluminescence intensity has often been used as an indirect measure of heat release rate under the assumption that the two are directly related. There are also known limitations to this assumption. The ground-state OH species may be excited either in the reaction zone or by thermal collisions. OH* may return to an unexcited state by either chemiluminescence, or by collisional quenching. Thermal excitation and collisional quenching of OH* are not yet well understood, especially under LPRE-like conditions. Bellows (2004), for example, studied OH* emission in a premixed methane combustor, simulating gas turbine conditions with forced acoustics. OH* emission intensity was observed to respond proportionally to the acoustic field amplitude, up to high amplitudes where saturation was reached. The saturation limit was found to be a function of equivalence ratio, and hysteresis in the flame response was observed depending on the ramping direction (positive or negative) of acoustic forcing. This example illustrates the difficulties in relating a measurement of emission intensity to a quantitative value of heat release rate. Despite known limitations of chemiluminescence imaging as a

diagnostic technique, numerous experimental combustion instability studies have used it to contribute to the understanding of flame response to acoustics (Section 3.4.2, Section 7.1). Its practicality in testing under LPRE-like conditions led the method being selected for the current work.

5.3.2 Shadowgraph imaging

Shadowgraph imaging is a technique used to visualise a flow field in two-dimensions. Light passing through a media containing differing refractive indices is diffracted to differing degrees, resulting in an image on the other side of the media which can be recorded, for example digitally with a charge-coupled device (CCD). In media with only weak differences in refractive indices, a knife edge may be used to further diffract light exiting the media and thereby enhance contrast in the image, known as a Schlieren setup. In experiments under LPRE-like conditions, the knife edge is not necessary because the large gradients in fluid density, particularly between liquid oxygen jets and the surrounding gas, result in strong differences in refractive index. A back-lighting source is required, placed behind the flow being investigated, and a filter to suppress combustion light may also be required.

The majority of shadowgraph studies in LPRE combustion experiments to date have used flash-lamp backlighting. Flash backlighting is powerful enough to overcome combustion light and produce a clear image of the dense, liquid oxygen jets. Flash-type backlighting is, however, limited to low imaging frequencies. In current project, the dynamic response of injection is under investigation. To realise high-speed shadowgraph imaging, a high-power Xenon gas-discharge lamp was used as a continuous backlighting source. An RG850 long-pass filter was used to suppress combustion light. The filter allows wavelengths longer than 850 nm to pass, so the powerful near-infrared content of the Xenon lamp is not blocked.

5.3.3 OH* chemiluminescence recording with photomultipliers

Photomultipliers (PMs) for OH* detection were also installed inside the test cell. These sensors are connected directly to the MCC acquisition system. Signals from the PMs were sampled at 100 kHz, also with the MCC-integrated 40 kHz anti-aliasing filter active. With the higher sampling rate, these sensors provide higher temporal resolution of OH* emission. They also have a higher dynamic range than the high-speed cameras, with the signals sampled in 16 bit compared to the 8-bit camera CCDs. The PM signals were not calibrated for measurements of absolute OH* concentration, however their response is linear to OH* emission intensity and so measurements of relative intensity will be presented in this work.

5.4 Campaigns 1 and 2: initial hardware testing

The first and second BKH test campaigns were for initial hardware testing, with the primary goal of bringing the new experimental combustor into operation. The operational performance of the new hardware was to be characterised by testing the operational domain of the BKH combustor, and in doing so collect baseline data for future analysis. Further goals included development of the optical diagnostics system for reliable flow field and flame visualisation, and to demonstrate operation of the excitation system.

5.4.1 Test type 1; clean configuration

Initial configuration of the BKH combustor was for basic operation with LOx and GH_2 (GH_2 is hydrogen with $T_H \sim 290$ K, as defined previously in Section 4.2.2). The configuration is shown in Figure 5.5, with dummy windows and dummy secondary nozzle installed. This 'clean' configuration is essentially the same as a standard rocket engine, with a single main nozzle, and was the simplest and safest way to bring the combustion chamber into operation for the first time. This configuration also provides baseline data on the acoustic properties of the system without a secondary nozzle cavity in the upper wall.

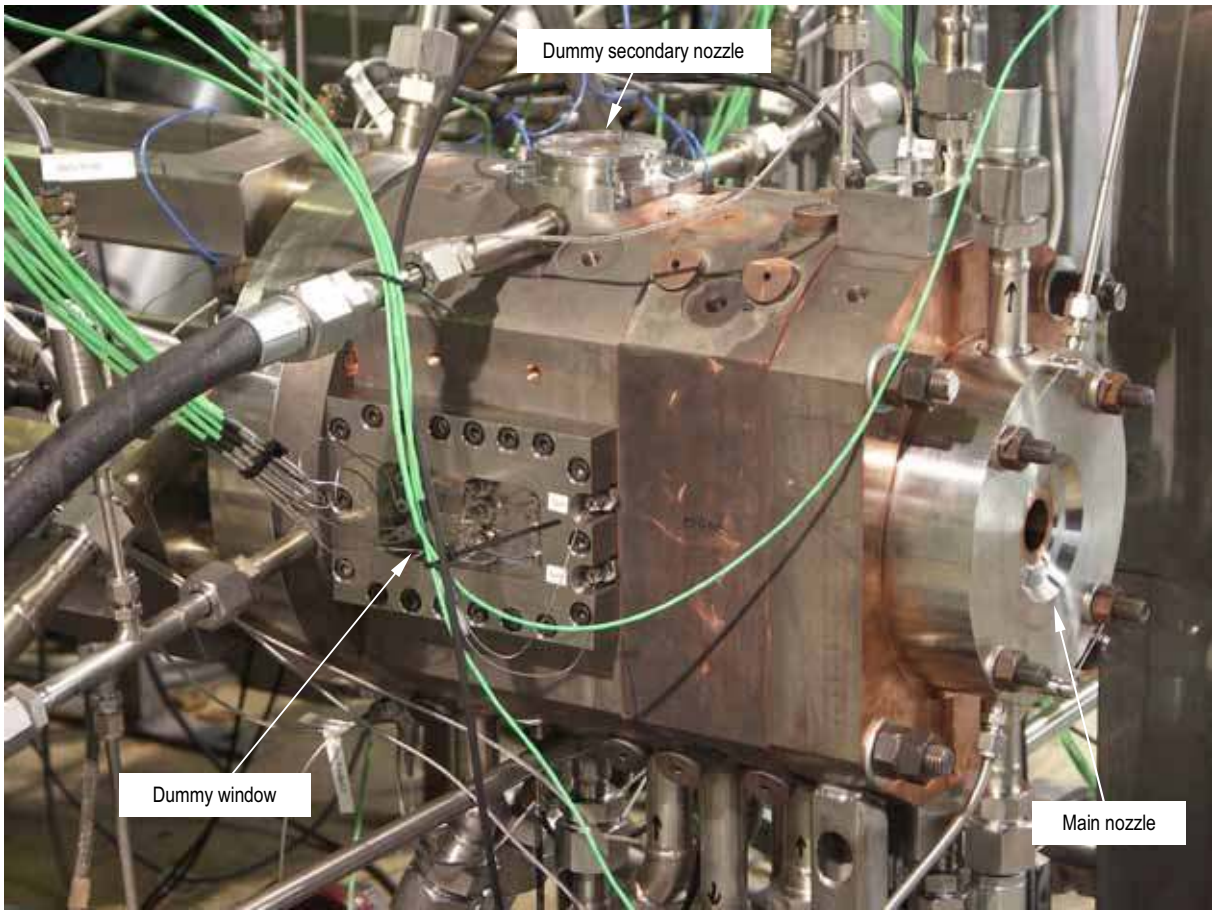

Figure 5.5: BKH configuration for test type 1; clean configuration.

The test sequences to be run were designed in order to systematically explore the design operational envelope of the hardware. The objective was to achieve the full range of design operating conditions, namely chamber pressures of P_{cc} = 40, 50 and 60 bar with mixture ratios of ROF = 2, 4 and 6. The example test sequence shown in Figure 5.6 is a typical hardware test sequence with chamber pressure P_{cc} = 40 bar held constant and three stages of mixture ratio values stepping progressively from ROF = 2 to 4 to 6. The stages are made long enough to allow flow rate, temperature and pressure transients to stabilise and provide the desired duration of steady state operation. Note that, being an early test, the transition from the first to the second stage (at t = +15 s) was not yet optimal. This staged approach is designed to make full use of the long test duration capabilities of the test facility and BKH combustor, allowing several different operating conditions to be achieved within a single test run, which is important when the number of test runs available is so limited.

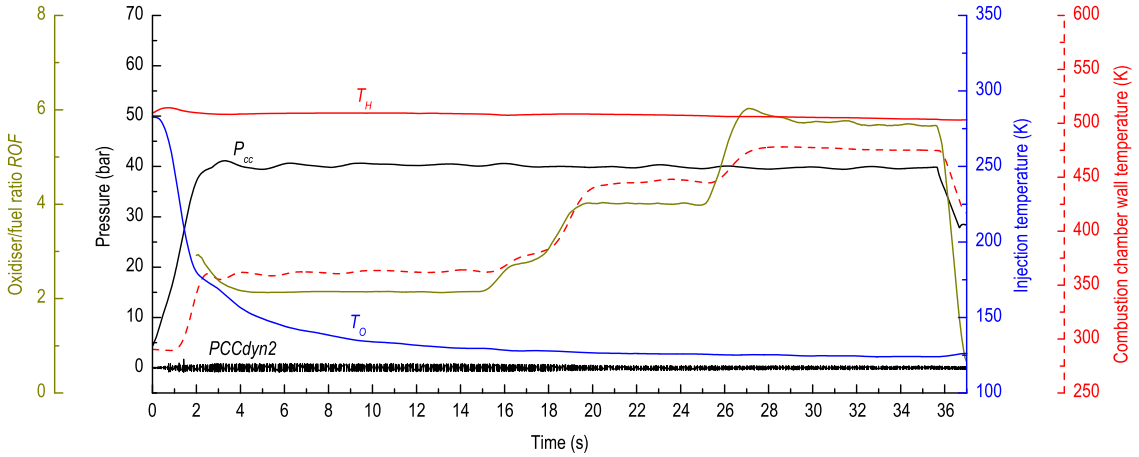

Figure 5.6: Example test sequence for test type 1; staged *ROF*.

5.4.2 Test type 2; clean configuration with optics

The 'clean' combustor configuration was also used to test optical diagnostics, with the optical windows replacing the dummy windows, as shown in Figure 5.7. A vapour shield extends from the window frame, deflecting water vapour originating from cryogenic fluid supply lines around the line-of-sight to the window and minimising its impact on imaging. The windows were installed only after thermal conditions for the expected range of operating conditions were known with confidence.

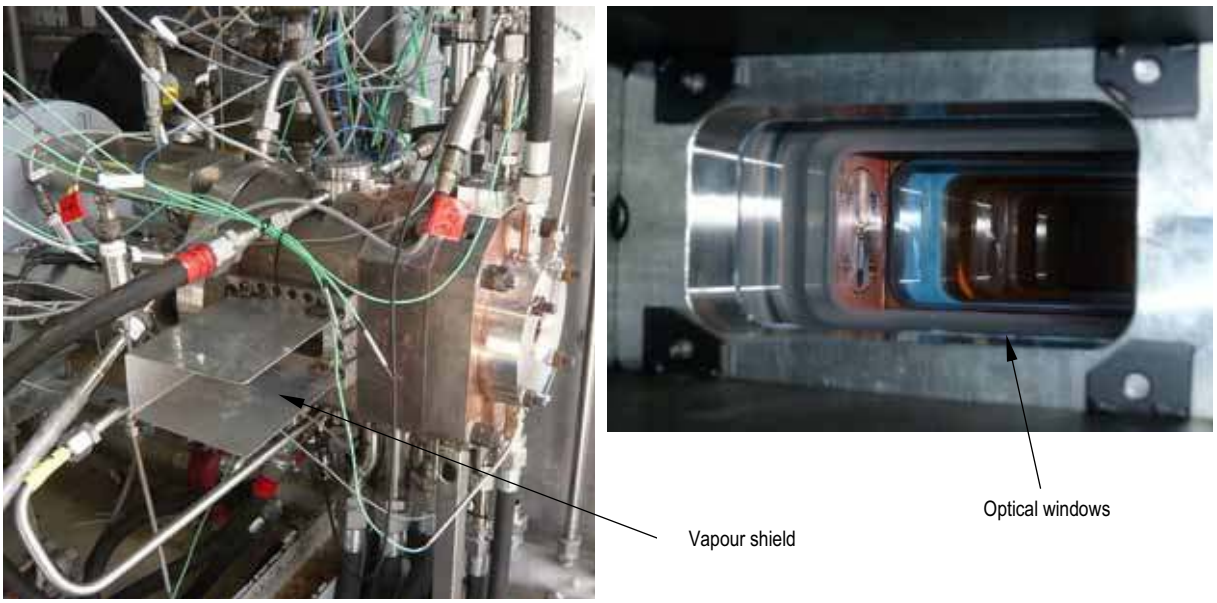

Figure 5.7: BKH configuration for test type 2; clean configuration with optics.

Optical diagnostics were applied using the setup in the simplified schematic illustration in Figure 5.8. The backlighting source with 100 W of power for shadowgraph imaging was passed through a series of spatial filters and mirrors to create a parallel beam which was also aligned with the optical axis. The optical axis is defined as a line parallel to the y-axis of BKH which passes through the centre of the windows. After passing through the combustor, the

beam was refocussed down to an image sized for entering the high-speed camera. This image is passed through a Schott UG11 long-pass filter for suppressing combustion light, then onto the CCD sensing element of the Photron FASTCAM 1024PCI camera where it is recorded in 8-bit greyscale. A second, Photron FASTCAM APX-i^2 intensified high-speed camera was setup for OH* imaging. This camera was directed at the optical window at a slight angle to the optical axis. An OH*-pass filter was installed directly in front of the lens of the camera. Camera settings with an intensifier potential of 3.5 V and gating time of 2 µs were found to produce a good image for the range of luminosity in the flame.

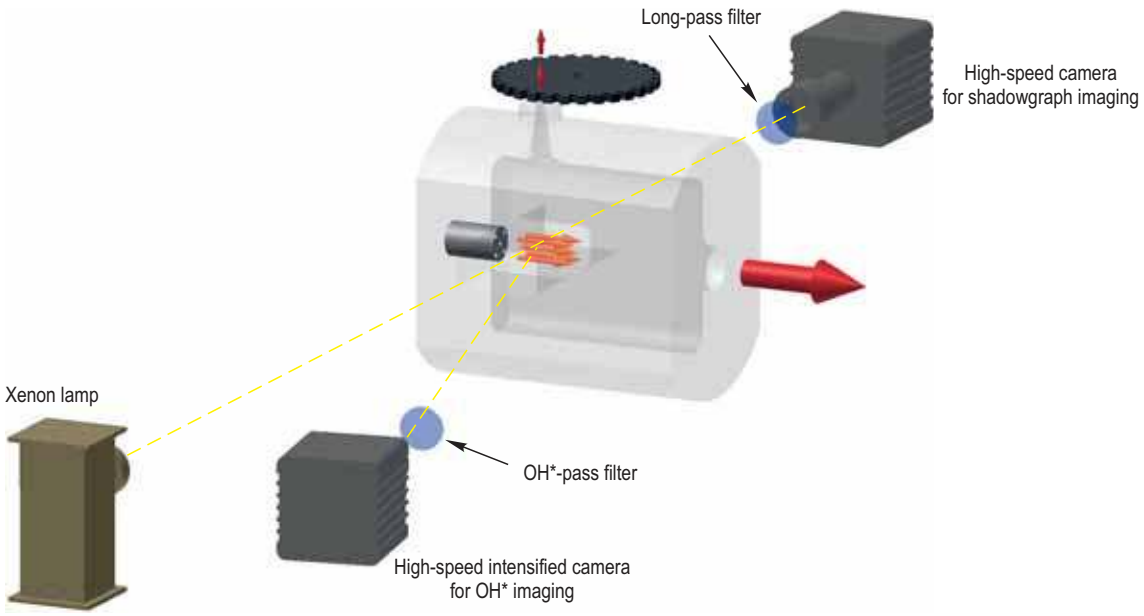

Figure 5.8: Initial optical setup for campaigns 1 and 2.

The staged *ROF* sequencing approach was also applied with optical windows installed, as the high speed cameras are able to be triggered with precise timing using a command programmed into the test sequence. Three triggers were used to capture a short period of video from each of the three stages of the sequence. Figure 5.9 is an example test sequence showing the trigger times for the high-speed cameras.

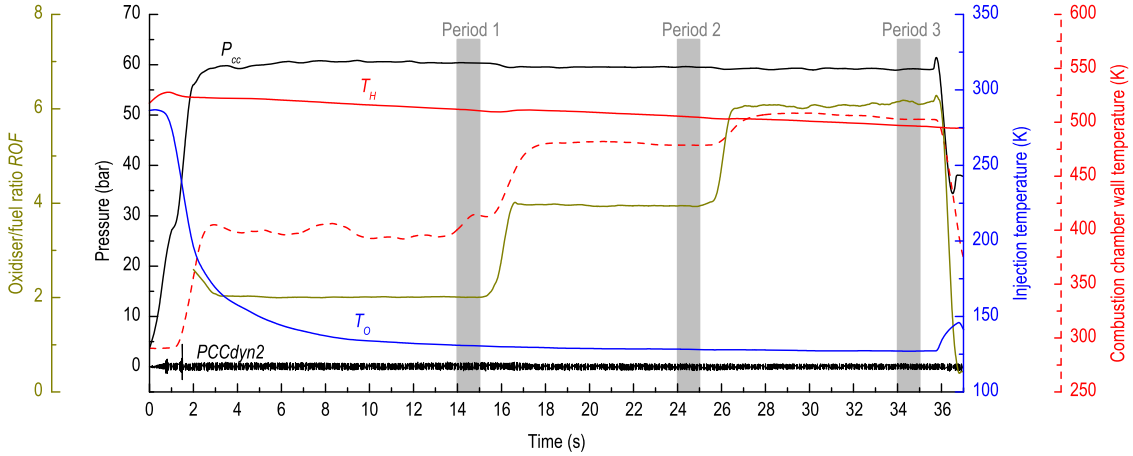

Figure 5.9: Example test sequence for test type 2; staged *ROF* with optics.

Little usable data was obtained from shadowgraph or OH* imaging systems as the need for trial-and-error adjustment of optical systems quickly consumed available test runs. Applying optical diagnostics at representative LPRE-like conditions is very challenging. High density gradients and flame luminosity make it difficult to anticipate required optical settings. The shadowgraph system only provided usable images from three runs, and of those the image was not optimal. Due to inadequate back-lighting intensity, the dense phase of the LOx injection jet was not resolved; rather an image of infrared emission from the flame was captured. Example images from a test at 40 bar are shown in Figure 5.10. Such images will yield only qualitative information on the flame and flow field and not the intact dense core length as intended.

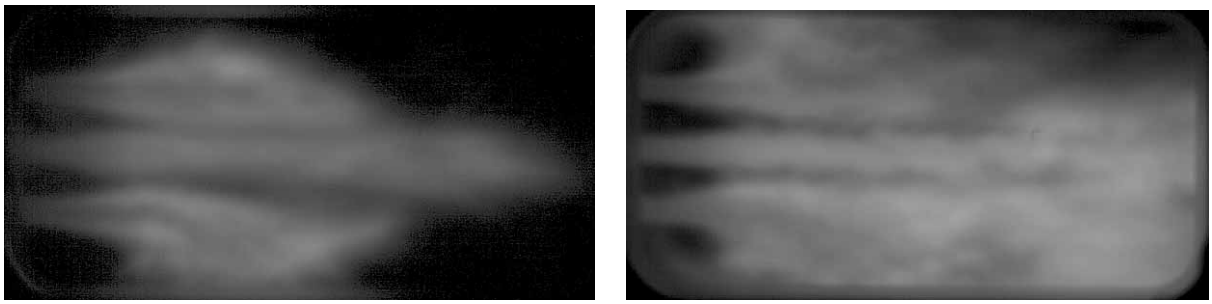

Figure 5.10: Example shadowgraph images from test type 2, for a 40 bar operating condition with *ROF* = 2 (left), and with *ROF* = 6 (right).

5.4.3 Test type 3; with excitation and optics

In a final set of tests for the initial test campaigns, the excitation system was introduced, as shown in Figure 5.11. Primary injector operation with LH_2 was also tested. The operating condition sequence consisted simply of a single, continuous chamber pressure and *ROF* value to provide steady state acoustic conditions in the combustion chamber. Optical imaging was also performed.

The excitation system did not perform according to expectations during the initial test campaign. It was discovered during flow checks that the nitrogen cooling flow, injected as small jets directed onto the exciter wheel at the base of the teeth, has a powerful braking effect on the exciter wheel. Upon introduction of the cooling flow, the servomotor was overpowered and the exciter wheel decelerated to low speed, rendering it useless for the intended test profile. Shutting off the nitrogen cooling during the course of test sequences did not provide a solution since the exciter wheel met with similar aerodynamic resistance from the secondary nozzle flow and the servomotor was unable to regain sufficient influence.

An exciter wheel was modified such that the upper surface of the teeth was machined down to a diagonal ramp, as seen in Figure 5.12. This so-called ‘bladed’ exciter wheel was intended to utilise the nitrogen cooling jets impinging on the upper surface of the teeth to provide a tangential thrust, and thereby drive-assisting torque on the wheel. The angle of the tooth blades was chosen to provide an assisting torque which would counter balance the resistance from the secondary nozzle flow, allowing the servomotor to retain command of the exciter wheel. The system did not, however, function as expected. The nitrogen cooling continued to provide only resistance, whereas the secondary nozzle flow produced a powerful thrust in the opposite rotational direction as was intended for the nitrogen cooling thrust assistance.

This secondary nozzle thrust completely overpowered the servomotor, causing it to be disabled, and driving the exciter wheel ever faster to speeds greater than the capabilities of the servomotor itself. With the nitrogen cooling disabled, the exciter wheel was driven with a high rate of acceleration, resulting in an excitation frequency ramp faster than planned, which passed through all chamber mode frequencies of interest. The acceleration only ended when the ramp excited a chamber mode which caused wall temperatures to rise sharply and trigger a Redline, stopping the test. Although affording no control over the ramp start time, ramping speed, or ramp end, this technique was harnessed to achieve some of the major test objectives for the campaign. Figure 5.13 shows an example of the sequence from such a test.

One of the four combustion chamber wall temperature traces is shown in Figure 5.13. Wall temperature is measured approximately 15 mm downstream of the windows. The wall temperature is seen to rise in response to excitation of transverse acoustic modes; 1T, 1L1T, and 2L1T. The temperature rise has a delay of approximately 0.5 s compared to dynamic pressure (*PCCdyn2*), owing to the nature of heat transfer to the chamber walls and the response speed of the thermocouples. The rise in temperature indicates that transverse modulation of the flames increases heat transfer to the walls, as is the case in naturally occurring HF instability.

As far as could be determined from published literature at the time, these tests were the first of their kind with forced acoustic excitation of LOx/H_2 at pressures greater than 9 bar, and the first time a flame with cryogenic H_2 had been subjected to acoustic forcing.

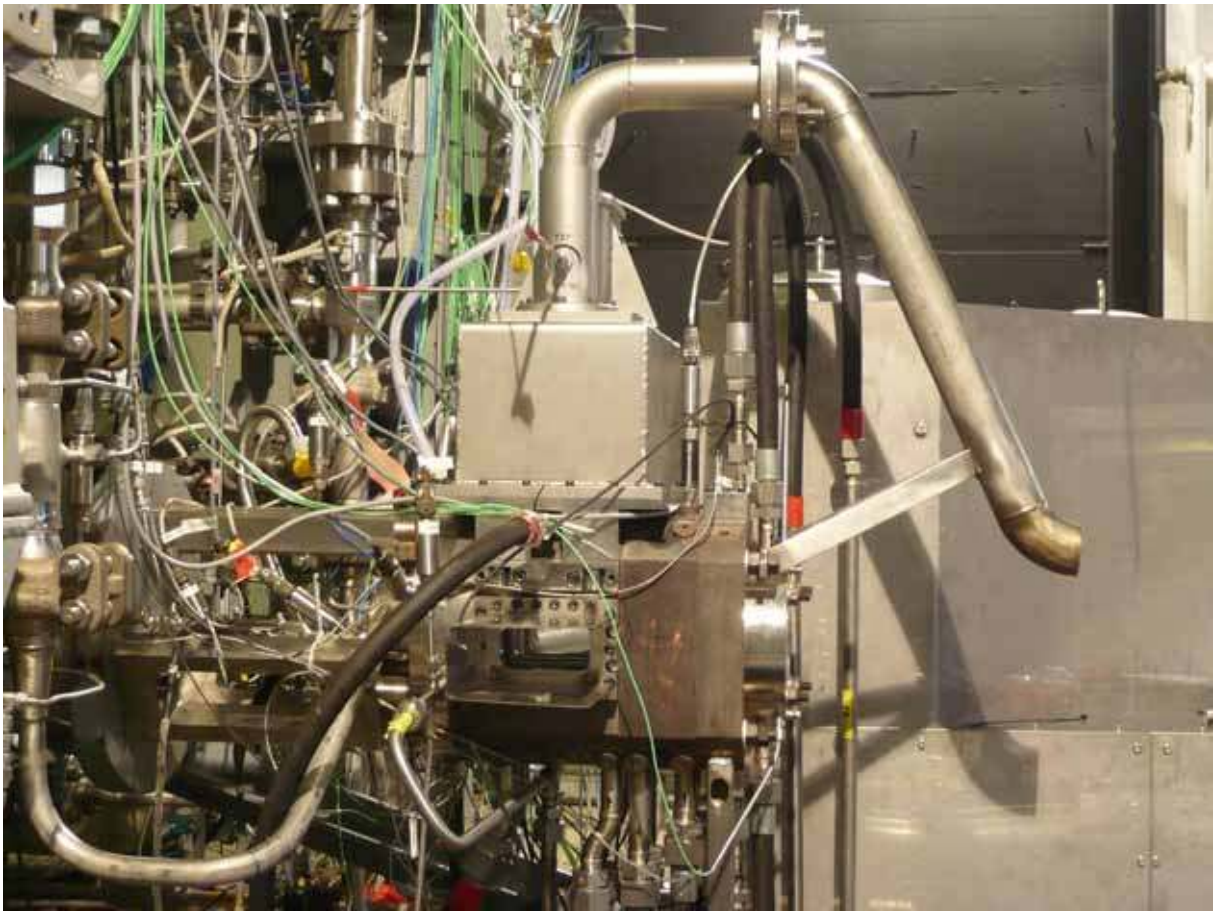

Figure 5.11: BKH configuration for test type 3; with excitation and optics.

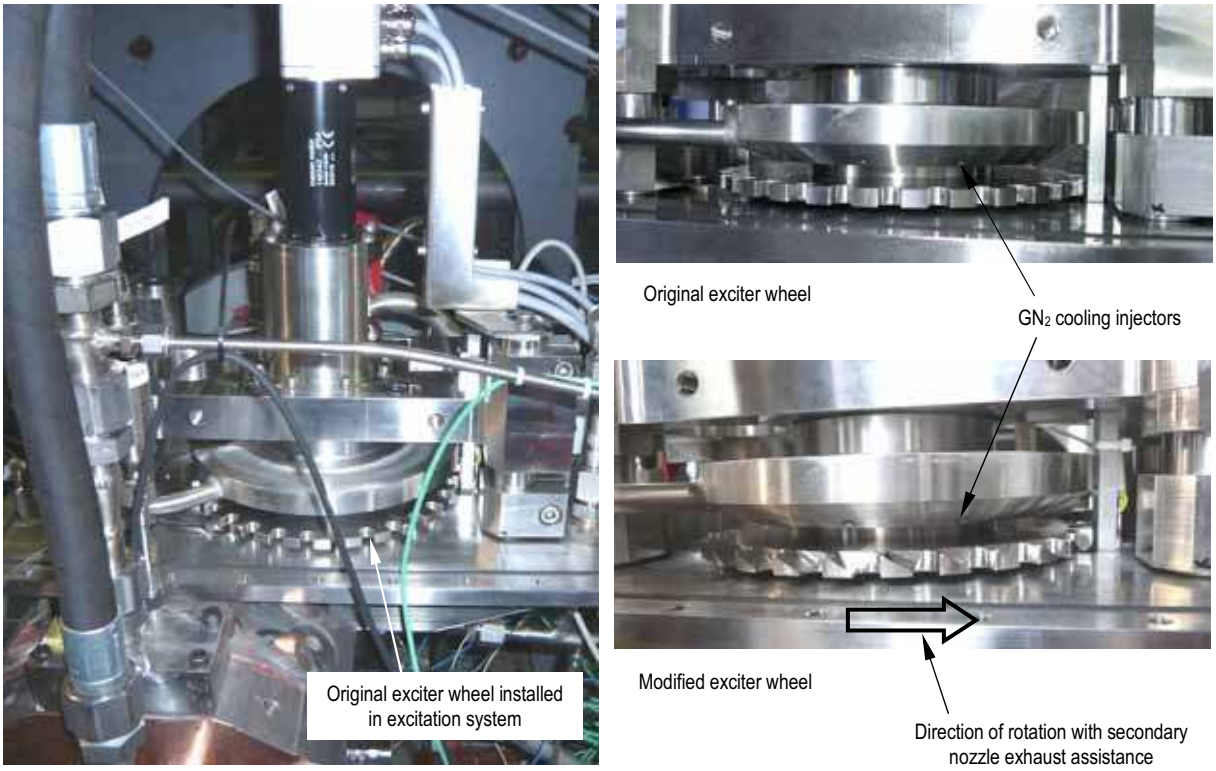

Figure 5.12: Exciter wheel modification.

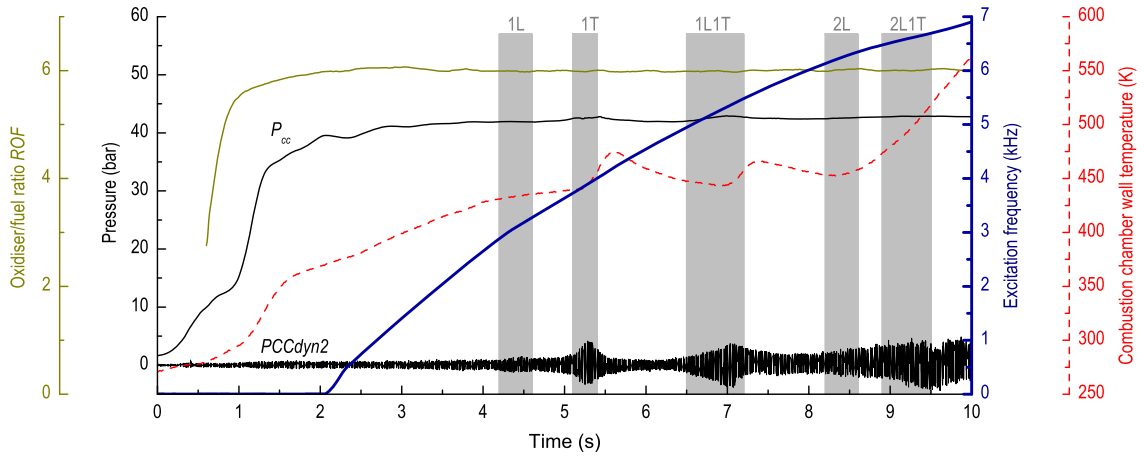

Figure 5.13: Example test sequence for test type 3; uncontrolled excitation ramp with optics.

The optical setup remained unchanged from test type 2. Due to the uncontrolled nature of the test, trigger timing for optical recordings could not be predicted. The high-speed cameras were therefore set to a lower frame rate for extended recording time and simply commanded to begin recording at t = -0.5 s. The shadowgraph camera allowed only relatively slow frame rates of 1000 frames per second (fps) to be used, while the OH* camera was set to 12,500 fps, allowing HF behaviour of the flame to be resolved.

The shadowgraph imaging setup was modified based on the experience from tests of type 2. A more powerful backlighting source with 500 W of power and different filters (RG665 and ND 0.25) allowed dense oxygen jets to be recognised. Two example frames, taken from off-

resonance excitation conditions, are shown in Figure 5.14. Despite the more powerful backlighting, and improved filter arrangement, infrared emission still features in the images, giving the surface of the oxygen jets a light grey colour. No shadowgraph images were captured during excitation of an acoustic mode.

While OH* imaging quality had reached a satisfactory state, only one test run yielded useful data due to unreliable camera function. During this run, OH* imaging captured the flame during a full ramp with acoustic mode excitation. Example instantaneous OH* images are shown in Figure 5.15. Analysis of OH* imaging from this test is presented in Chapter 7.

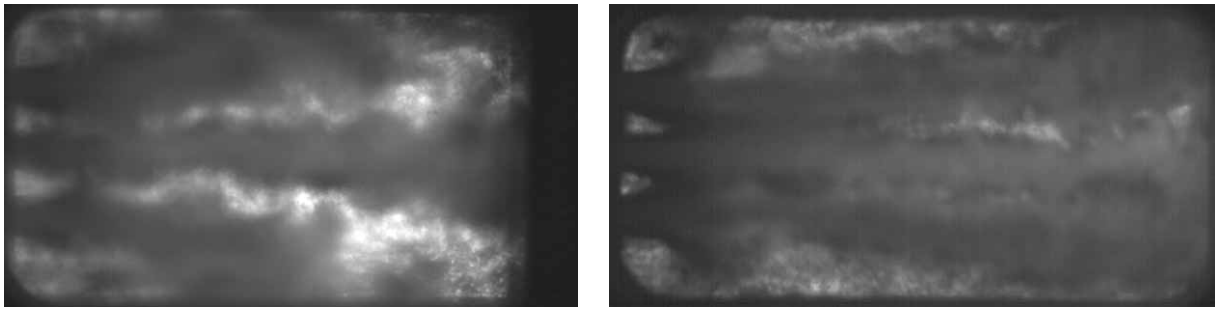

Figure 5.14: Example shadowgraph images from off-resonance conditions in test type 3, at 50 bar with *ROF* = 6 (left), and 60 bar with *ROF* = 6 (right).

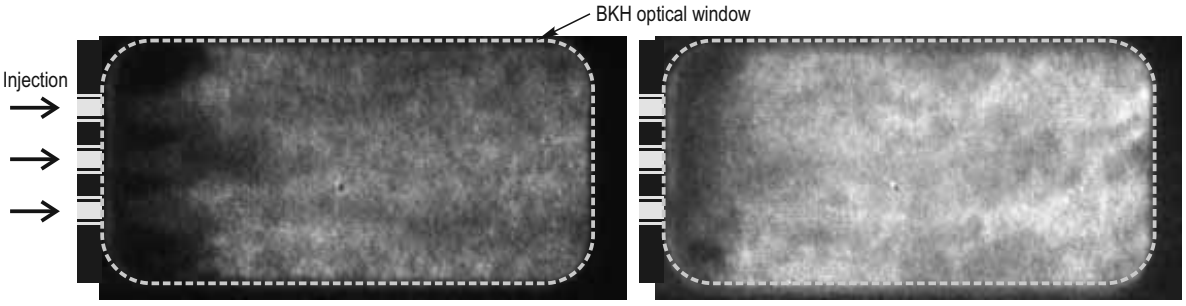

(a) Off-resonance (b) 1T mode excitation

Figure 5.15: Example instantaneous raw OH* images from test type 3, taken from off-resonance excitation at t = +4 s (a), and 1T mode excitation at t = +5.3 s (b).

5.5 Campaigns 3 and 4: excitation and optics with ambient hydrogen

The intention of the third test campaign was to begin addressing the experimental objectives of the project, namely collection of high-speed imaging while exciting acoustic resonance modes of the combustor. However, during the first hot-fire test run of the campaign, a sequencing error caused critical damage to the injector, burning the LOx posts and primary faceplate, as can be seen in Figure 5.16. This resulted in the cancellation of the campaign for hardware repairs to be undertaken.

The fourth test campaign then resumed execution of the tests originally planned for the failed third campaign. These include testing modifications to the excitation system, improvements in the optical diagnostic setup, and the application of photomultipliers. Primary injector operation was limited to warm (ambient temperature) H_2 for this campaign, and simultaneous high-speed shadowgraph and OH* imaging was collected during acoustic excitation for both

subcritical and supercritical operating conditions. As far as could be determined from published literature at the time, this campaign was the first time acoustic forcing had been applied to LOx/H_2 flames above the O_2 critical pressure.

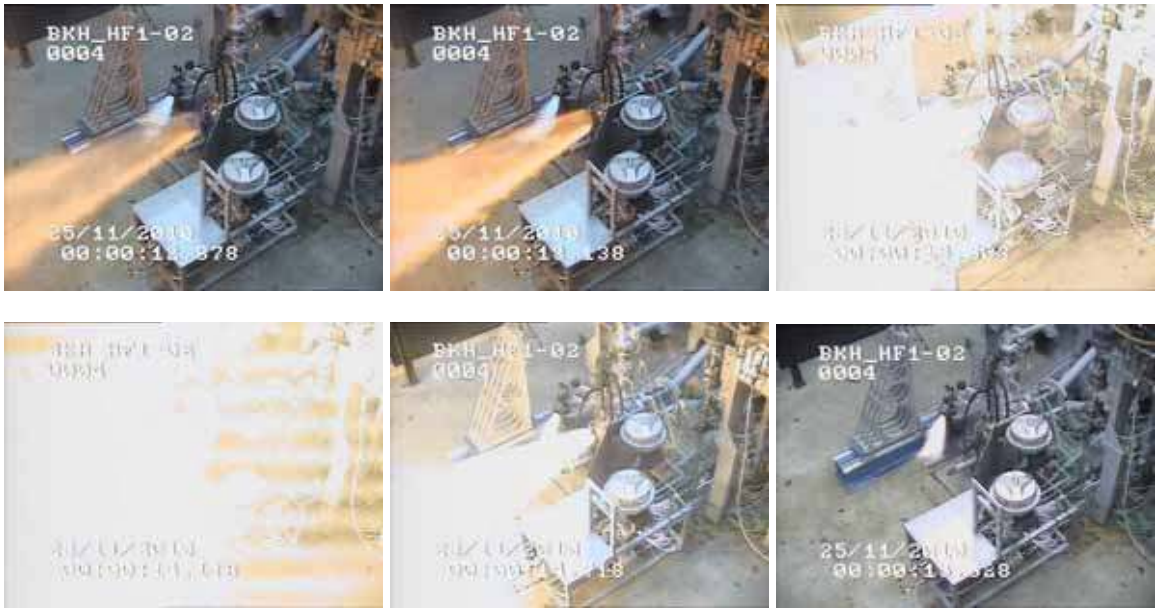

Test cell monitoring video

Burned LOx posts Faceplate damage

Figure 5.16: Video frames during sequence failure, and resulting hardware damage.

5.5.1 Test type 4; with excitation

Following the poor performance of the excitation system in the initial campaign, the servomotor driving the exciter wheel was exchanged for a more powerful model. This greatly improved the performance of the system, however the motor would still not be able to overcome the unexpectedly high resistance of the secondary nozzle exhaust jet and GN_2 cooling jets. The modified 'bladed' exciter wheel was therefore retained to take advantage of the driving torque from the secondary nozzle. Test sequences were carefully designed to balance the braking effect from the GN_2 cooling flow with the driving torque from the secondary nozzle flow, and to assist the motor when needed in order to achieve the full design

range of the excitation ramp in a well controlled manner. An example of such a test sequence is shown in Figure 5.17.

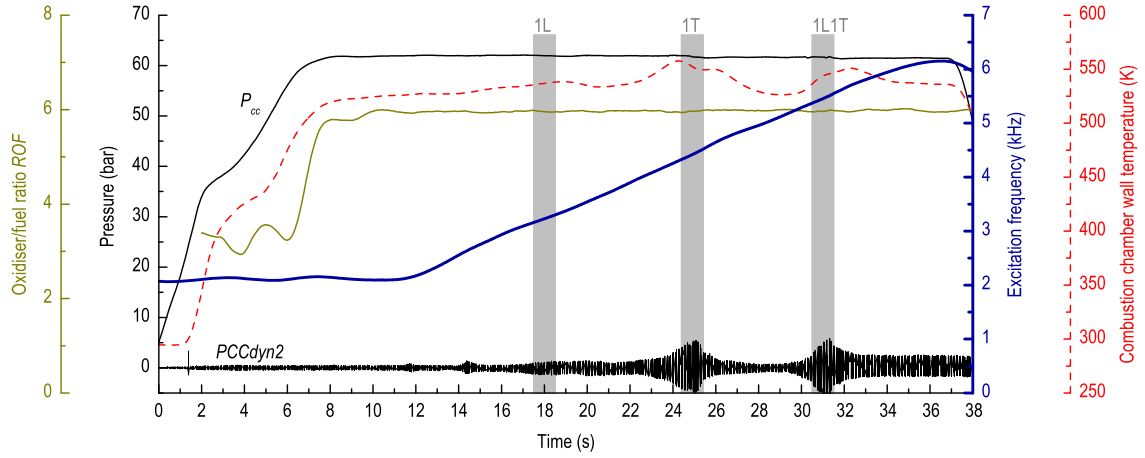

Figure 5.17: Example test sequence for test type 4; controlled excitation ramp.

5.5.2 Test type 5; with excitation and optics

Following successful testing of the modified excitation system, the optical windows were installed. The setup of optical diagnostics was modified compared to the previous campaign, as is illustrated in Figure 5.18, with photos in Figure 5.19.

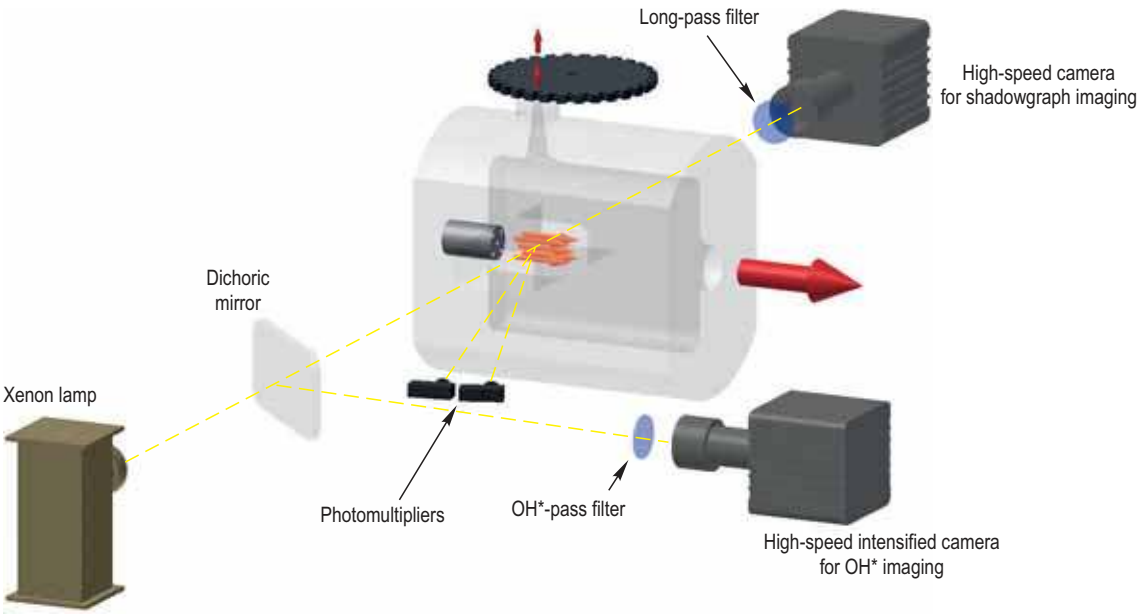

Figure 5.18: Modified optical setup.

The power of the backlighting source for shadowgraph imaging was increased further to 1000 W in order to try and overpower the infrared content of flame emission and reveal density gradients produced by the LOx core. An RG 850 replaced the previous filters. Example images are shown in Figure 5.20, where it is evident that the backlighting modifications were not completely successful in exceeding combustion luminosity; some

emission from combustion still appears in these images. Note that the sensing area of the image for the 40 bar test in Figure 5.20a was focussed on the central element and does not show the whole window. Analysis of shadowgraph imaging is presented in Chapter 8.

A new high-speed camera, a Photron FASTCAM SA5, was employed for shadowgraph imaging, which allowed the recording frame rate to be increased to 20,000 fps; high enough to resolve acoustic responses. The setup for OH* imaging was also modified. A dichroic mirror arranged at 45° to the optical axis was used to split the image from the optical window. The infrared light from the shadowgraph back-lighting source passes through unaffected, whereas ultraviolet light from the flame is reflected through 90° and directed into the intensified camera, via the OH* filter as before. This setup gives an image which is aligned with the optical axis (and therefore with the shadowgraph images), and also resulted in a better image composition with higher resolution by overcoming space restrictions in the test cell.

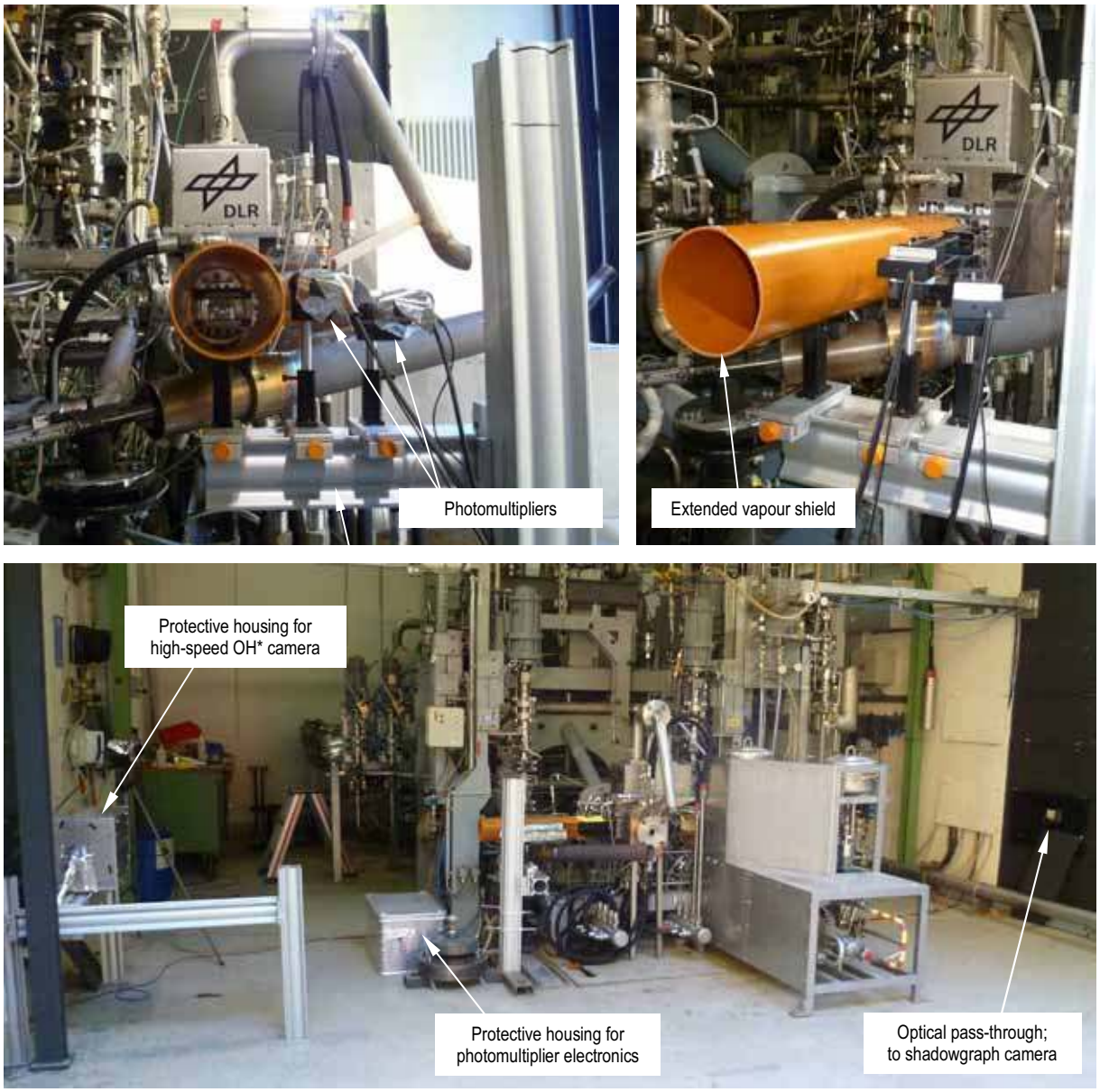

Figure 5.19: Photos of the modified optical setup.

(a) 40 bar, GH_2

(b) 60 bar, GH_2

Figure 5.20: Example shadowgraph images from a test at 40 bar with GH_2 (a), and a test at 60 bar with GH_2 (b).

With a controlled excitation ramp, and knowledge of the acoustic properties of the combustor from the initial test campaigns, triggers for the high-speed cameras could again be implemented in the test sequences. The frame rate of the OH* camera was increased to 24,000 fps and configured for short burst periods of recording; usually two periods of 1- to 2-s duration. Recording was triggered so as to capture images during on-resonance excitation of the 1L, 1T or 1L1T mode. An example test sequence showing the camera recording times is given in Figure 5.21. Note that this particular example is of a test with a half-speed excitation ramp, passing through only the 1L and 1T modes.

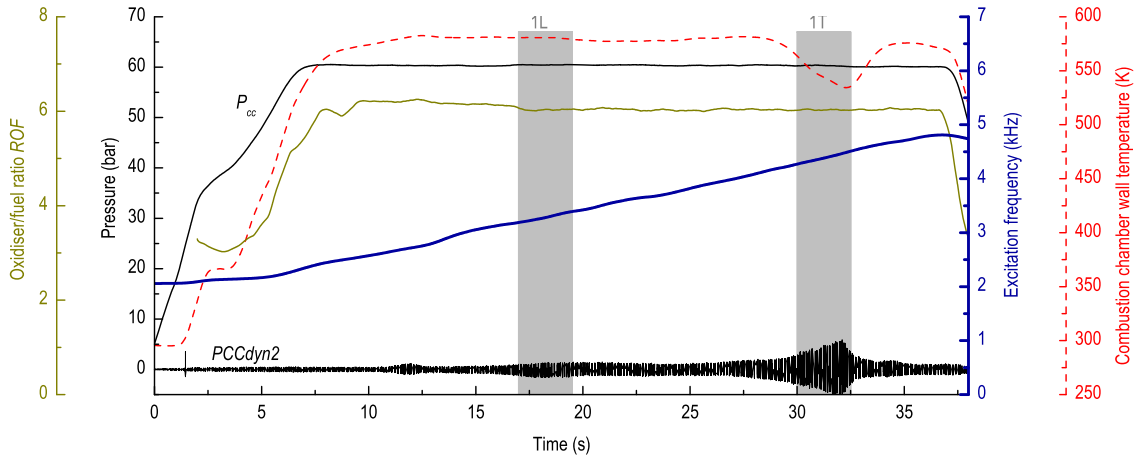

Figure 5.21: Example test sequence for test type 5; with excitation and optics.

Interesting to note in the test sequence plot is the behaviour of the combustion chamber wall temperature during 1T-mode excitation. As opposed to previous tests, where wall temperature was observed to increase during transverse modulation, the temperature decreases significantly. The reason quickly becomes clear when looking at the example OH* images from off-resonance and 1T excitation in Figure 5.22. Transverse modulation from 1T-mode excitation has caused the flame to retract towards the injection plane so that the flame no longer reaches the sensors for wall temperature, which are located downstream of the window. Analysis of OH* imaging from this and other tests is presented in Chapter 7.

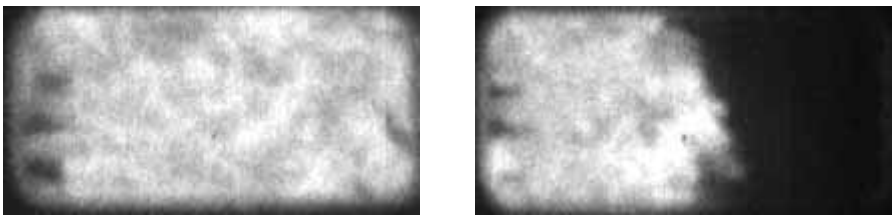

(a) Off-resonance excitation (b) 1T-mode excitation

Figure 5.22: Instantaneous raw OH* images from the test in Figure 5.21 during off-resonance (a) and 1T-mode excitation (b).

Two photomultipliers (PMs) were also tested, hoping to demonstrate the ability to acquire OH* emission signals with higher temporal resolution and dynamic range than the high-speed camera. The PM units were setup directed at the downstream part of the window, but were not focused to a particular point, rather obtained broad area images of roughly the entire second half of the window. The PMs were equipped with the same OH* band-pass filters as the high-speed camera, as well as a grey filter to lower the intensity of light entering the sensing element. After several adjustments the signals obtained were satisfactory and the spectral content could be clearly extracted, as seen in the example spectrogram in Figure 5.23.

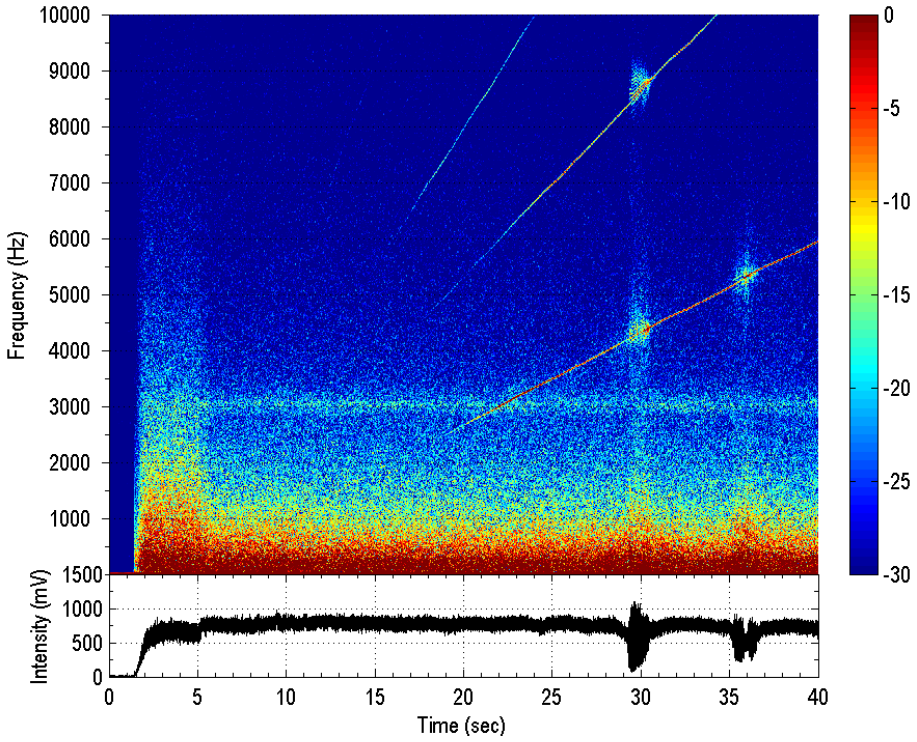

Figure 5.23: Example spectrogram from a photomultiplier.

5.6 Campaign 5: excitation and optics with cryogenic hydrogen

The fifth test campaign was used to repeat the subcritical and supercritical operating conditions of the previous campaign, with the same sequences and excitation ramps, except using cryogenic H_2 (below 50 K) for primary fuel injection. These tests satisfied the experimental objective to investigate the influence of H_2 injection temperature on flame response and stability characteristics. Data from these tests will be compared to that from the previous campaign at the same operating conditions using warm H_2. A modified secondary nozzle design was also tested.

5.6.1 Test type 6; cold flow with excitation

An extended cold-flow test, with only H_2 injection (cryogenic H_2 primary, warm H_2 secondary), was conducted with ramped excitation. This test provides baseline acoustic data with excitation but without combustion for comparison with hot-fire cases. A modified secondary nozzle design with a sine-profiled outlet was tested for comparison with the simple circular throat version from the previous campaigns. Results of this comparison are presented in Section 11.C.1.

5.6.2 Test type 7; with excitation and optics

These tests were essentially a repeat of test type 5 from campaign 4 (Section 5.5.2), using a linear excitation ramp and triggering the cameras to record as the ramp passes through an acoustic resonance mode. Shadowgraph settings were not changed from the previous campaign. It can be seen in the example images in Figure 5.24 that combustion luminosity was slightly higher compared to operation with GH_2 in the previous campaign. While LOx jets are recognisable, their full extent is difficult to distinguish, particularly at 60 bar chamber pressure. Note that the first few millimetres of the image in Figure 5.24a were obscured by the vapour shield which had shifted during the test.

The setup of the PMs was modified so that their sensing fields of view were focused to a small circular area approximately 10 mm in diameter. The areas were then aligned near the upper and lower corners of the downstream end of the window, as illustrated in Figure 5.25.

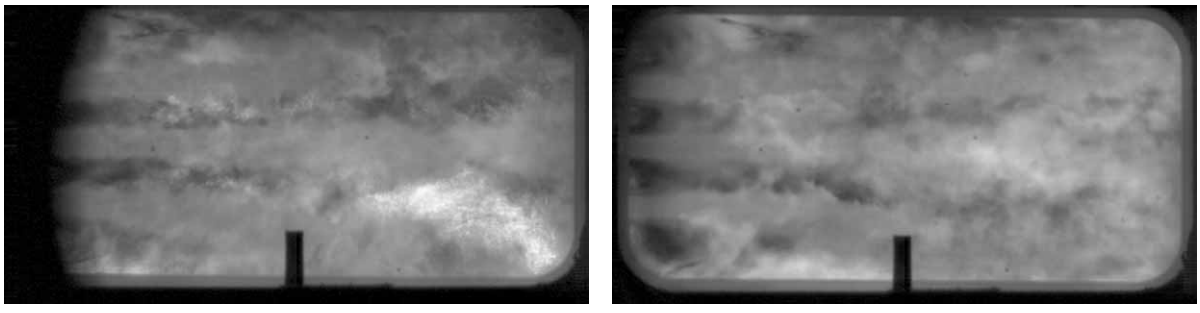

(a) 40 bar, LH_2 (b) 60 bar, LH_2

Figure 5.24: Example shadowgraph images from a test at 40 bar with LH_2 (a), and at 60 bar with LH_2 (b).

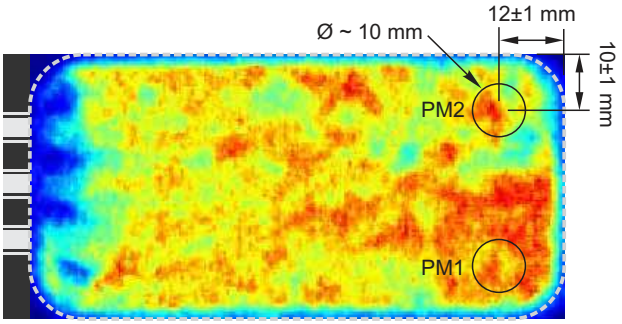

Figure 5.25: Sensing areas of the photomultipliers for test type 7.

5.7 Summary of achieved operating conditions

Over the course of these five test campaigns, the new BKH combustor hardware was brought into operation and then used to address the experimental objectives of the project. BKH has been operated throughout its complete design envelope, and studies with acoustic forcing have been conducted at the four main operating conditions of interest; namely 40 and 60 bar (subcritical and supercritical) with $ROF = 6$ and warm GH_2, and the same but with cryogenic LH_2. The final two campaigns produced simultaneous high-speed shadowgraph and OH* imaging during acoustic forcing of the combustor at the operating conditions of interest. Figure 5.26 displays the achieved operating conditions for the various configurations of BKH.

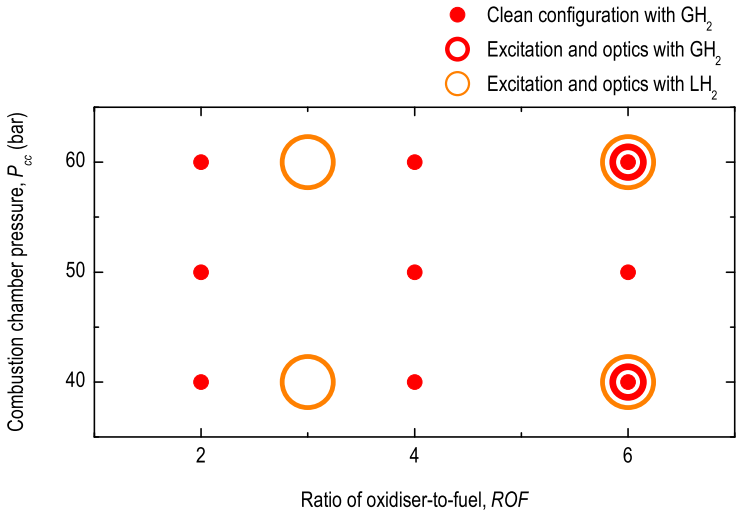

Figure 5.26: Achieved operating conditions of BKH.

6. ACOUSTIC CHARACTERISATION

In the first test campaigns, intended for initial hardware testing, the BKH combustor underwent hot-fire testing under a variety of operating conditions and hardware configurations. Before applying BKH to the study of flame-acoustic interaction, it was important to understand the acoustic characteristics of the new combustor so that the excitation system could be applied effectively. This chapter documents the acoustic characteristics of BKH, which were found to be well defined and suitable for the intended studies with forced excitation. The chapter begins with the acoustic characterisation of BKH using high frequency dynamic pressure measurements from the first hot-fire tests using LOx and GH_2 or LH_2 propellants. The measurements were compared with the predicted acoustic properties of the system which were calculated using finite element methods. Modifications to the injection system were made for subsequent test campaigns, and the impact of these changes on the acoustic properties is also explored. Following the initial characterisation, the performance of the acoustic excitation with nozzle modulation, and the resulting combustor response, are assessed.

6.1 Finite element acoustic model

Experience gained in interpreting experimental results from the CRC shows the importance of detailed acoustic modelling. Oschwald et al. (2008a) demonstrated how the acoustic spectra from hot fire testing of the CRC can only be fully understood with the help of a numerical model capturing the full two-dimensional symmetry of the chamber with the secondary nozzle installed. The impact of a ring of acoustic absorber cavities on the resonance frequencies of a rocket combustion chamber volume filled with air was also demonstrated by a three-dimensional finite element model. A further study by Searby et al. (2008) highlights the impact of coupled acoustic cavities on resonance frequencies using simplified two- and three-dimensional finite element models. It is therefore important to be aware of such coupling opportunities as they could have an influence on the desired acoustic environment for planned flame-acoustic interaction studies. A highly detailed, three-dimensional finite element model of BKH with its injection system was used to analyse the dynamic pressure measurements taken during initial hot-fire testing.

The acoustic model was developed using the commercial Finite Element (FE) analysis package ANSYS. The FE model of the internal volumes of BKH includes the combustion chamber, all injection elements and their respective supply manifolds, as well as the igniter chamber and port. Different fluid properties can be applied to each part of the model. Model

parts have been grouped according to their fluid contents. For example, the combustion chamber volume is one group, the secondary H_2 manifold together with all 50 injection elements is another, and so forth. These model groups are highlighted by different colours in Figure 6.1a. Fluid supply lines were not included as their length to an appropriate acoustic decoupling point would make the model impractical. Furthermore, only modes of relatively low frequency, less than 500 Hz, would be expected in the lines which are of several meters length at the P8 Test Facility. If such a model of a real, flight engine were to be made, it would be important to include supply lines which have much shorter lengths relative to the combustion chamber scale and their acoustic frequencies therefore become more important to HF instability considerations.

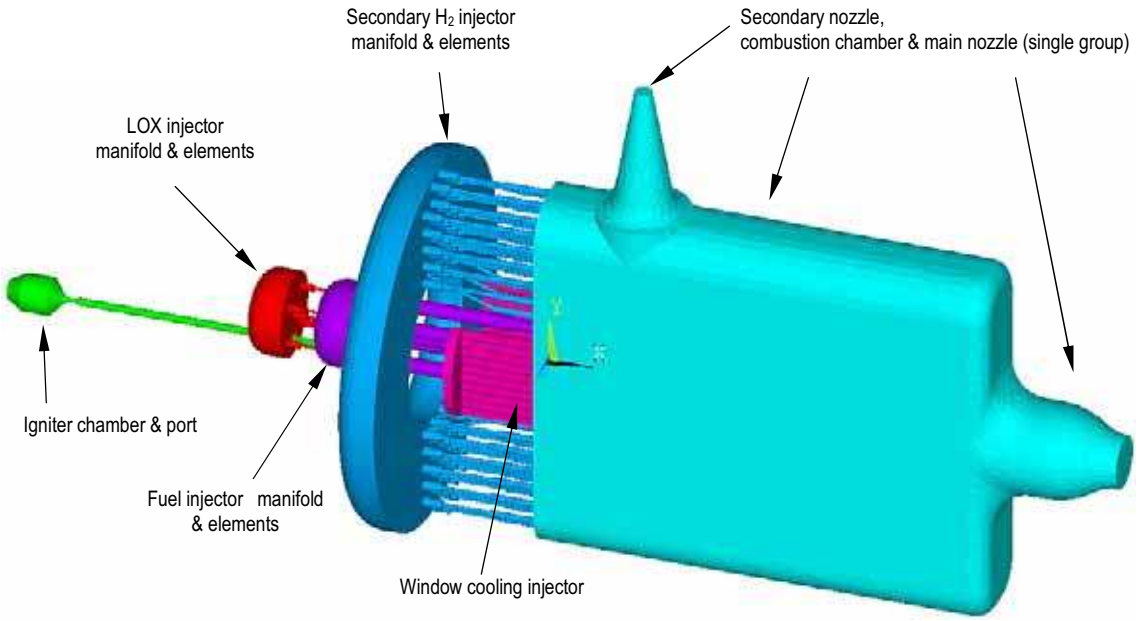

(a) Fluid property groups

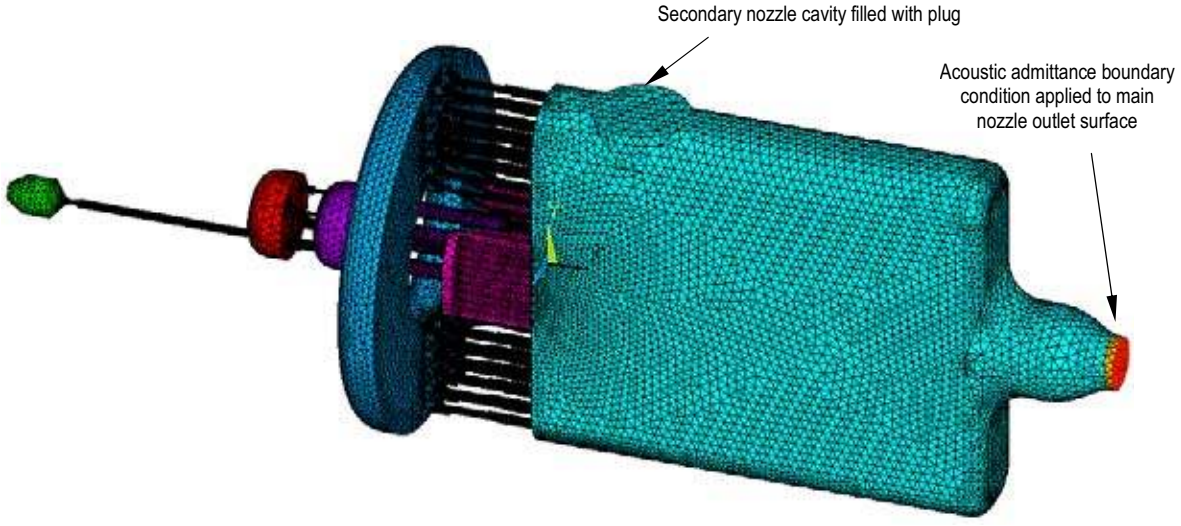

(b) Meshed model ('clean' configuration, without secondary nozzle)

Figure 6.1: Finite element model of BKH showing (a) the fluid property groups (for the configuration with secondary nozzle), and (b) the meshed model (without secondary nozzle).

The model volumes are meshed with Fluid30 elements which are used to solve the discretised three-dimensional acoustic wave equation. Acoustic pressure is calculated under the assumptions of linear acoustics as mentioned previously in Section 2.2. The assumption of no mean flow is not unreasonable since bulk chamber flow mach numbers for BKH are around $M_{bulk} = 0.04$, rendering a mach correction factor negligible. The automated meshing function in ANSYS was utilised. Mesh 'coarseness' level and allowable maximum element size were reduced until convergence of modes under 6 kHz was reached. The final settings were a coarseness level of 5 (out of 10) and a maximum element size of 5 mm. The meshed model of the 'clean' combustor configuration is shown in Figure 6.1b.

All wall surfaces are set to have a boundary condition of null normal acoustic particle velocity $u'\perp = 0$, as well as nozzle exit plane surfaces which is equivalent to them being fully closed. A modal analysis of the model is then executed, which calculates the resonance frequencies of the entire set of interconnected volumes. Essentially, the same calculation is performed as was demonstrated previously for the analytical case of a rectangular volume, except for a far more complex geometry for which there is no analytical solution.

The application of a nozzle exit plane boundary condition was tested using a reduced acoustic admittance value of $\beta^* = (\gamma\text{-}1)/2$, based on the compact nozzle assumptions of Marble and Candel (1977). The boundary condition had little to no detectable influence on mode frequencies or pressure distributions. This is due to the nature of the nozzle boundary condition being very close to that of a closed surface, and to the very small exit area of the nozzle in relation to the overall chamber surface area. The nozzle admittance boundary condition was therefore excluded in order to save greatly on computational time.

6.2 Spectrum characterisation

For the purposes of initial examination of the acoustic characteristics of BKH, data are taken from a test using the clean combustor configuration, i.e. without secondary nozzle. A 1-s long sample of dynamic pressure sensor data is taken from a period of steady state operation at 60 bar with GH_2. Time-series data are transformed into power spectra using the Welch method (Welch 1967) in combination with a high performance HFT70 flat-top window (Heinzel, Rüdiger & Schilling 2002). The spectral power values p'^2 are then scaled to decibels (dB):

$$\mathrm{dB} = 10\log\left(\frac{p'^2}{P_{cc}^{\,2}}\right), \tag{17}$$

normalised using the value of chamber pressure P_{cc} for the corresponding sample period. This P_{cc}-normalisation allows acoustic spectra for different operating chamber pressures to be compared directly. Figure 6.2a is a power spectrum of *PCCdyn2*, displayed here up to 20 kHz. At first glance the sharp peaks at 3073, 6146 and 12,292 Hz appear prominent. Inspection of the *PIHdyn* spectrum in Figure 6.2b shows the peaks to originate from the secondary H_2 manifold. The FE model was then used to try to identify the origin of these peaks. A calculation was performed using LOx and H_2 property values corresponding to temperature and pressure conditions measured in the respective injection manifolds from the actual test. Mode frequencies calculated by the FE model are indicated by the dashed lines overlayed on the *PIHdyn* spectrum. The FE model overestimates the frequency of the first sharp peak by only 61 Hz (2%), and reveals it to belong to the first circumferential (1C) mode of the toroidal

secondary H_2 injection manifold. To check this finding the FE calculation was run for several operating points with differing measured temperature and pressure conditions in the secondary H_2 manifold. The FE model consistently predicted this mode at a frequency 2% higher than that appearing in the measured *PIHdyn* spectra. The mode is strongly transmitted into the combustion chamber due to the alignment of the pressure antinodes with the upper and lower arrays of secondary H_2 injection elements.

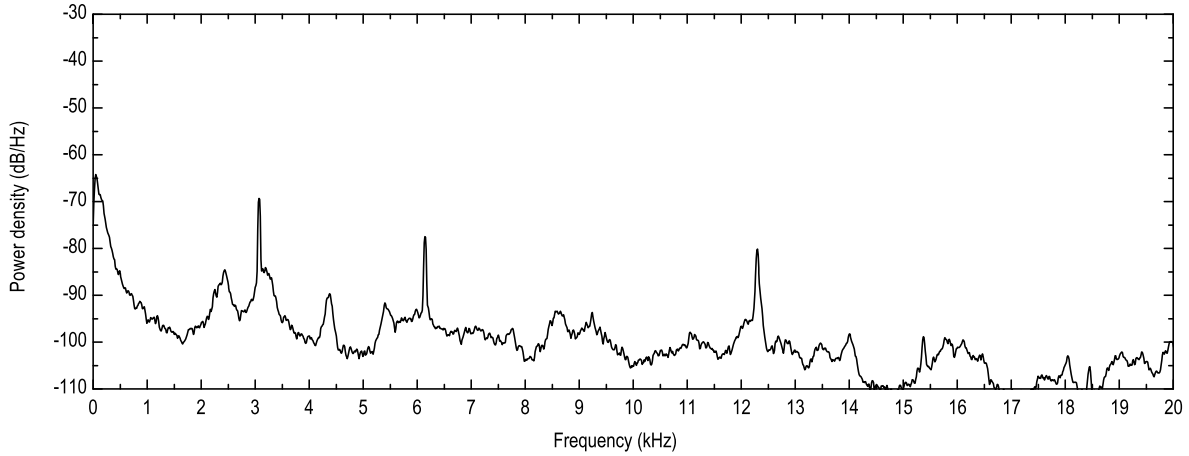

(a) PSD of *PCCdyn2* (in combustion chamber)

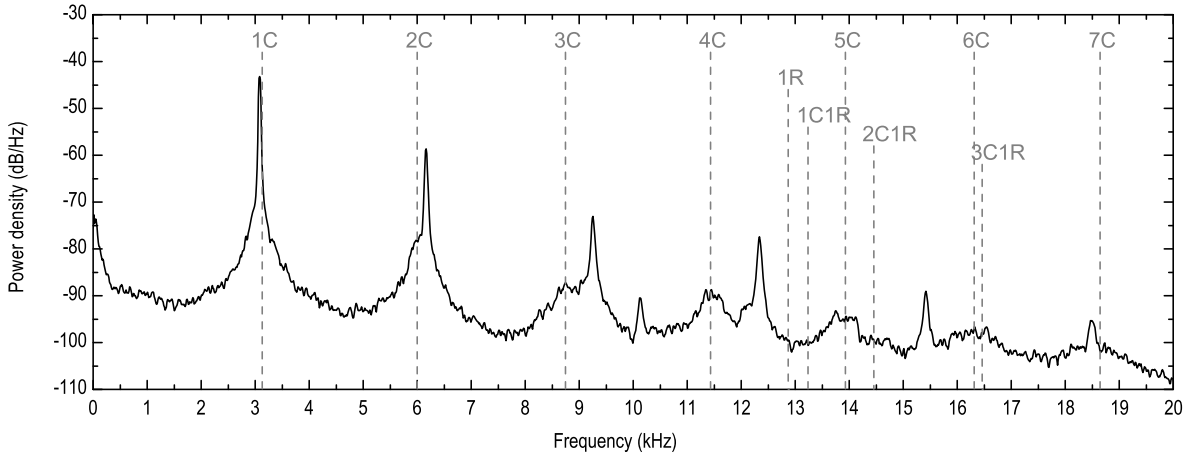

(b) PSD of *PIHdyn* (in secondary H_2 injection manifold)

Figure 6.2: PSD spectrum of dynamic pressure signals from *PCCdyn2* (a), and from *PIHdyn* (b). *PIHdyn* is shown with indicated mode frequencies as calculated using the FE model.

Due to the high amplitude nature of the first 1C mode peak, it follows that the other sharp peaks at multiples of the 1C mode frequency are simply overtones of this mode. The FE model also identifies other peaks in the *PIHdyn* spectrum as belonging to higher order modes of the manifold, including circumferential (labelled 2C, 3C etc.), radial (1R, 2R etc.), and combined circumferential-radial (1C1R, 2C1R etc.). The pressure distributions of some of these modes are shown by way of example in the FE model results in Figure 6.3. A sharp peak at 10,100 Hz is believed to be a sensor artefact, since its frequency does not change for varying sound speed conditions, and it does not appear to coincide with any of the many additional acoustic modes predicted by the FE model.

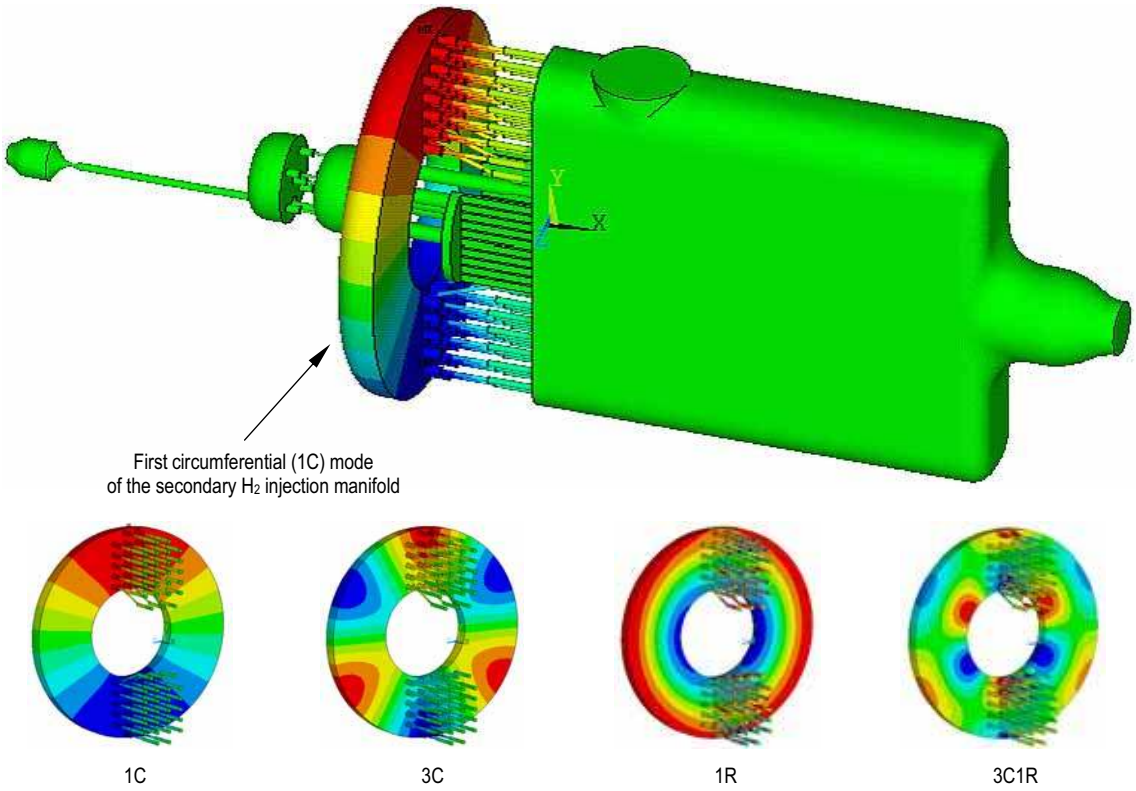

Figure 6.3: Example FE-calculated pressure distributions of some secondary H_2 manifold acoustic modes.

The primary modes of interest in the combustion chamber, 1L, 1T and 1L1T, are next to be identified. Figure 6.4a shows a closer view of the *PCCdyn2* spectrum of Figure 6.2a, overlayed with the analytical frequencies from Table 4 in Section 4.4.2 and those from the FE calculation for the corresponding test conditions. Actual mode identities, judged based on the analytical and FE values, are indicated in Figure 6.4b as 'selected'.

Firstly it should be mentioned that the peak at approximately 2400 Hz has been identified as an internal sensor resonance and can be safely ignored. It has a different frequency to the artefact in the *PIHdyn* spectrum (Figure 6.2b) because *PCCdyn2* is a different model sensor. It was discovered that a 2400 Hz internal resonance in *PCCdyn2* is excited by the flow of cooling water through the sensor itself, and the resonance peak can be removed simply by de-activating the cooling water.

Comparing the performance of the analytical and FE mode frequency predictions, we first see that the 1L frequency is poorly predicted analytically. For the analytical calculation the length of the rectangular volume representing the combustion chamber is taken simply as the distance from the injection plane to the nozzle throat. In reality, the chamber ends in a transition section where the rectangular cross-section contracts suddenly to a circular nozzle. The stepwise contraction causes the 1L mode to be 'pinched', effectively shortening the length of the chamber and raising the frequency of the 1L mode. The analytical 1L1T and 2L mode predictions are consequently also skewed. The influence of the actual chamber geometry is captured by the FE model, which only slightly overestimates the 1L frequency. In fact, all chamber modes are slightly overestimated by approximately the same spacing. This constant offset makes it easy to adjust the FE model frequencies by eye to fit the measured spectrum and thereby identify the modes.

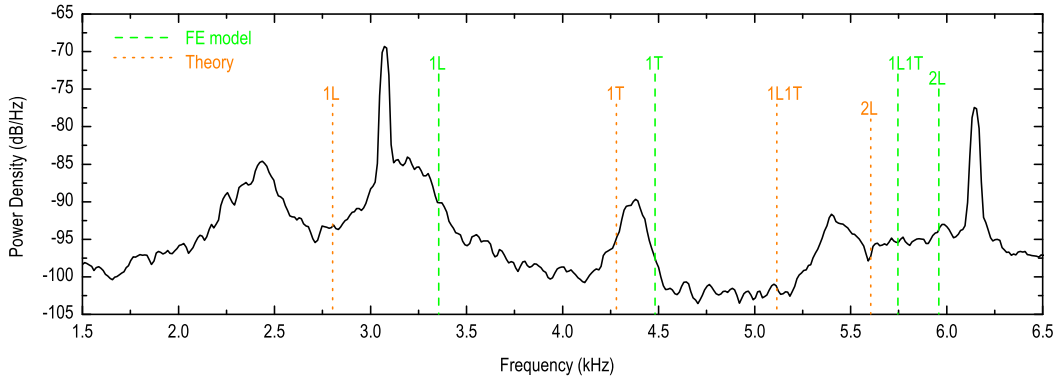

(a) PSD of *PCCdyn2* showing theoretical and FE-calculated mode frequencies

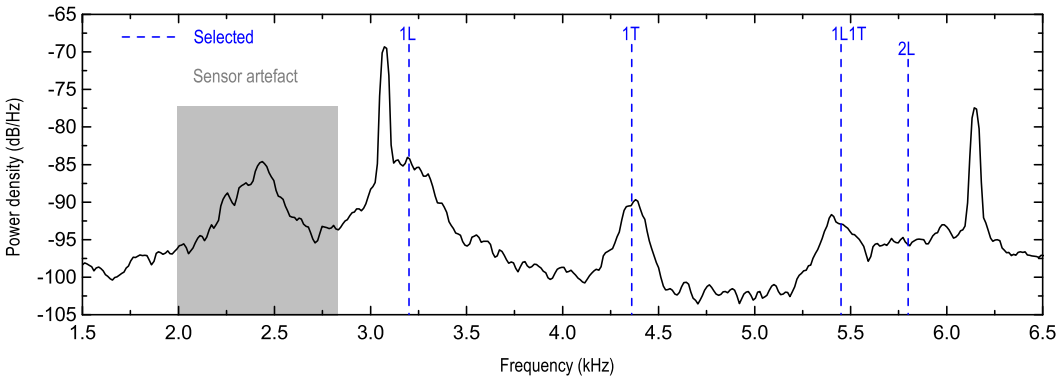

(b) PSD of PCCdyn2 showing properly identified mode frequencies

Figure 6.4: PSD of *PCCdyn2* with analytical and FE calculated mode frequencies indicated (a), and with actual chamber resonance modes identified as 'selected' (b).

The distribution of the dynamic pressure sensors *PCCdyn1* to *PCCdyn6* in the combustion chamber allows acoustic mode identity to be confirmed by comparing the phase of the individual sensor signals with the expected pressure distribution for the mode. Figure 6.5 illustrates positive identification of 1L, 1T, and 1L1T modes by comparing plots of the sensor signals with the corresponding FE-calculated pressure distributions. The sensor signals have been band-pass filtered to the respective mode frequency, using filter settings which do not introduce any artificial phase shift between sensors. Generally, the phase and amplitude relationships of the signals are as expected. For example, for the 1L mode, sensors *PCCdyn1* and *-2* are in phase with each other and in anti-phase with sensors *PCCdyn5* and *-6*. *PCCdyn3* and *-4* are not perfectly co-located with the nodal-line and therefore have non-zero amplitude. Some drift is evident in relative sensor phase and amplitude for all three modes. For example, *PCCdyn1* and *-2* are not identical in phase and amplitude in the 1L mode sample shown in Figure 6.5a. This imperfect relationship is due to the non-stationary nature of the acoustic conditions in the combustion chamber. Turbulent combustion, the fluctuating temperature field (and therefore sound speed distribution), and sources of damping all work to distort the natural resonances in the chamber. Richecoeur et al. (2009) have illustrated this random distortion of phase and amplitude using a simple theoretical model of acoustic resonance in the MIC, where a uniform oscillation in gas temperature in the combustion chamber was imposed on the resonance mode solution. The FE model of BKH does not contain sources of driving or damping, so an estimation of phase distortion or acoustic pressure amplitude is not possible. However, normalised values of relative acoustic pressure amplitude can be extracted from the locations corresponding to the *PCCdyn1* to *-6* sensor positions. These

values of expected relative amplitude for the sensor signals are displayed on the plots for comparison (circular, square and triangular markers). They have been normalised to the amplitude of the signal with the greatest amplitude, this being *PCCdyn2* in the case of the 1L and 1T modes, and *PCCdyn6* for the 1L1T mode. They show good prediction of the sensor behaviour, for example accurately predicting the amplitudes of sensors *PCCdyn3* and *-4* for the 1L mode.

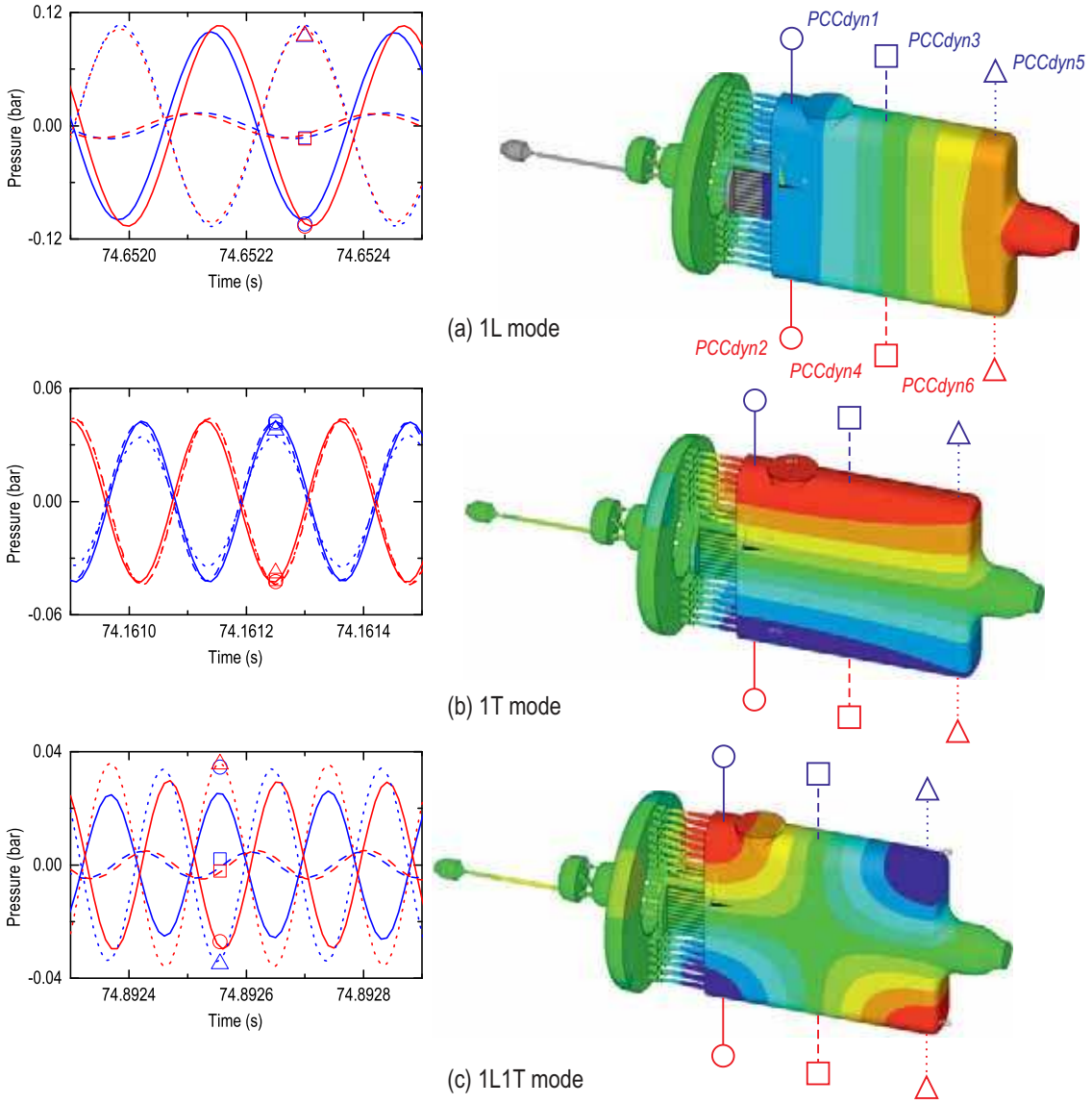

Figure 6.5: Mode identification by sensor phase analysis for the 1L mode at 3200 Hz (a), 1T mode at 4370 Hz (b), and 1L1T mode at 5370 Hz (c).

Discrepancy between the numerically calculated mode frequencies from the FE model and the measured frequencies is due to non-ideal conditions in the combustion chamber. The combustion chamber mode frequencies are consistently overestimated by the FE model because the sound speed values calculated by the CEA program assume perfect equilibrium combustion efficiency and adiabatic conditions. The combustion efficiency (η_{c*}) based on characteristic exhaust velocity (c^*) measured from the current test was $\eta_{c*} = 97.4$ %. It can be shown that $\eta_{c*} = c^*_{experimental}/c^*_{theoretical(CEA)} = c_{exp}/c_{th}$ (Sutton & Biblarz 2001). Thus the value of sound speed for the combustion chamber volume was adjusted and the FE calculation re-

run. The calculated mode frequencies for theoretical and η_{c^*}-corrected sound speed are compared against the selected frequencies in Figure 6.6, and show a slight improvement in the frequency prediction.

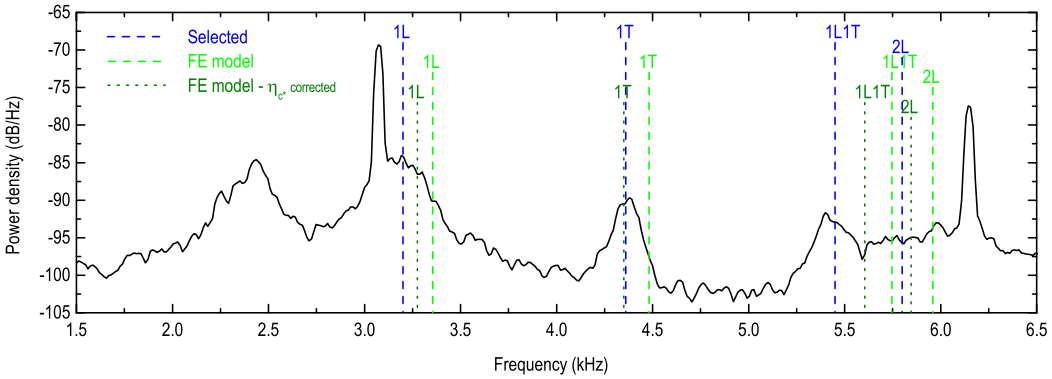

Figure 6.6: PSD of *PCCdyn2* with FE calculated mode frequencies indicated for both ideal sound speed and sound speed corrected for c* combustion efficiency.

It should be noted that sources of acoustic damping which would further lower the natural frequencies have also been neglected in the model. Furthermore, the non-uniform temperature distribution in the combustion chamber results in distortion of the mode shapes and frequencies. The inclusion of an estimated temperature distribution as well as damping in future versions of the FE model is expected to improve its accuracy. Despite these limitations, the FE model results are clearly far superior in their value as an interpretive tool.

6.3 System modification: acoustic baffle

The first peak from the 1C mode of the secondary H_2 injection manifold obscures the 1L mode of the combustion chamber and adds unwanted noise to the spectrum. The 1C mode resonance is thought to be driven by the incoming mass flow of H_2 since the supply line inlet to the manifold happens to be positioned in the pressure antinode of the mode. Mass addition at the location of, and in phase with, a pressure peak is an equally valid way to amplify acoustic oscillations, as explained by Lord Rayleigh (1945). Any small initial perturbation in the incoming mass flow rate may couple with the 1C mode of the manifold, establishing a powerful and uninterrupted driving source. This would explain the high amplitude reached by the mode and its nonlinear nature (and hence strong overtones).

In order to try to remove this resonance, an acoustic baffle for the secondary H_2 manifold was designed. Baffle plates were arranged so as to decouple the 1C mode antinode from the inlet flow of H_2, and to serve as obstacles to acoustic gas motions, as illustrated in Figure 6.7. The baffle design was added to the FE model for investigation. The three-dimensional geometry for the model is also shown in Figure 6.7. FE results showed a 300 Hz reduction of the manifold 1C mode frequency, sufficiently far away from the chamber 1L mode, but in the absence of viscous damping the model failed to predict any change in amplitude.

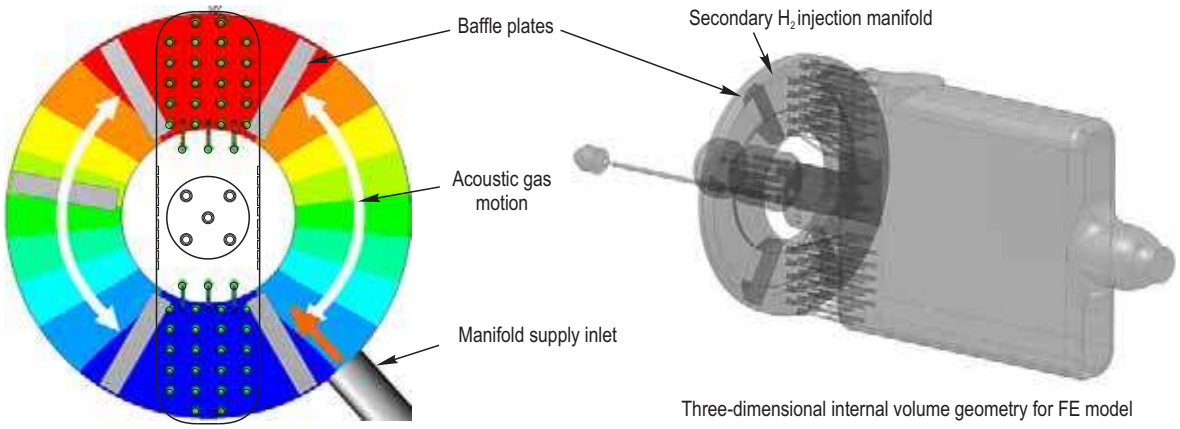

Figure 6.7: Design of the acoustic baffle for the secondary H_2 manifold. Also shown is the geometry of the FE model with the baffle included.

The baffle was installed in BKH and tested. The resulting *PCCdyn1* and *PIHdyn* spectra for a 60 bar test with GH_2 are shown in Figure 6.8b to Figure 6.8d. The original *PIHdyn* spectrum without baffle (from Figure 6.2b) is repeated here in Figure 6.8a for comparison. Secondary H_2 manifold mode frequencies from the FE calculation with baffle are overlayed on the *PIHdyn* spectrum in Figure 6.8b, and again indicate excellent agreement with measured mode frequencies. The 1C mode is no longer of high amplitude with strong overtones, rather strongly damped with a broad line width like the higher order modes. The arrangement of the baffles has resulted in multiple occurrences of some modes with varying orientations (labelled 2C2, 3C2 etc.). The secondary H_2 mode frequencies are also overlayed on the combustion chamber spectrum (from *PCCdyn1*) in Figure 6.8c, and Figure 6.8d is a closer view of the frequency range of interest indicating the chamber modes. Note that the *PCCdyn1* sensor spectrum is presented here since the artefact in the *PCCdyn2* spectrum would have obscured any evidence of the secondary H_2 mode. These two figures show that secondary H_2 manifold modes are no longer detectable in the chamber. In fact, the baffle has been effective in completely removing any sign of secondary H_2 modes from the combustion chamber for the complete operational range of BKH, and will therefore continue to be used in future BKH testing.

It is fortuitous that this injector resonance in BKH was manifest in the supply of secondary H_2, and not in the supply of primary propellants which take part in combustion. It is conceivable that, if the primary LOx or H_2 injector manifolds also had ring geometry, then such a circumferential acoustic resonance in either of those may have resulted in injection-driven combustion instability. Hulka and Hutt (1995) recount how, in a development version of the J-2 engine, ring manifold injectors always developed spontaneous HF when tested under start transient conditions, and had to be controlled with baffles. Similarly, full-scale development tests of Aerospike engines at Rocketdyne in the late 1960s experienced oscillations in the annular LOx manifold. These then coupled to a rotating mode of the same frequency in the annular combustion chamber. They could be controlled by isolating compartments of the manifold and introducing baffles into the combustion chamber. In these examples, as is suspected to be the case in BKH, the inlet feed flow to the manifold may have driven the mode. The manifold mode then modulates the mass flow injected into the combustion chamber. Oscillating combustion may then establish a rotating 1T mode in the combustion chamber which couples with the injection mode, further amplifying the instability. In this way, annular geometries in injection manifolds and/or combustion chambers may be particularly susceptible to injection-coupled HF instability. Perhaps the

annular geometry allows the travelling wave to organise more readily than in a cylinder. Regardless, this mechanism of coupling of rotating waves in the injection manifold and the combustion chamber may also afflict traditional cylindrical rocket engine configurations. Sliphorst, Gröning and Oschwald (2011) demonstrated theoretically and experimentally that the natural tendency of the 1T mode in cylindrical engines is to take on travelling, or rotating, character. Interestingly, response factors (Section 3.1) estimated by Heidmann and Groeneweg (1969) were larger when applying the rotating acoustic mode to their models. If injection-chamber coupling of rotating waves were identified as a driving mechanism for HF instabilities, suppression of such oscillations may be approached through appropriate acoustic design of the manifold-chamber system.

Applying the acoustic baffle as a countermeasure in BKH was a relatively simple matter in such a modular, experimental system, however the necessity to add acoustic countermeasures to a flight engine is extremely costly in both monetary and performance terms, especially if discovered so late in engine development as during full-scale testing. An acoustic characterisation should therefore be attempted at the design stage in order avoid the need for hardware modifications. Detailed FE modelling, such as that applied in this study, may provide an effective means to avoid such acoustic phenomena.

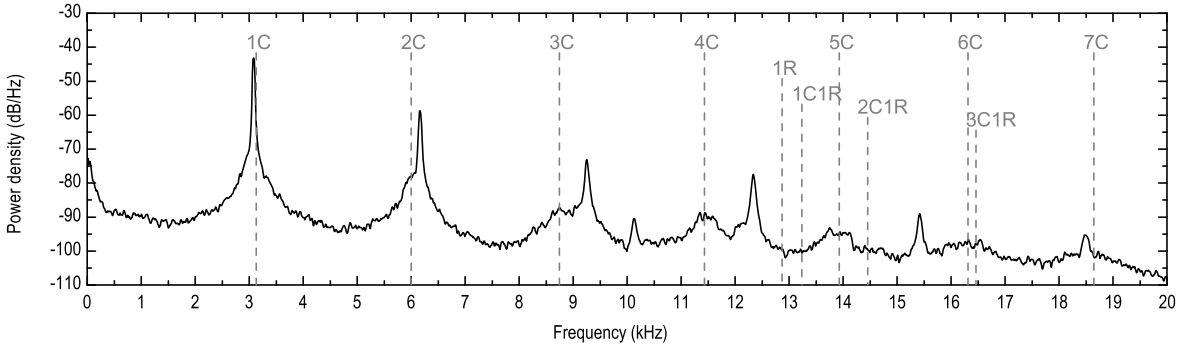

(a) Secondary H_2 manifold (*PlHdyn*) spectrum without baffle (Figure 6.2b), repeated here for comparison

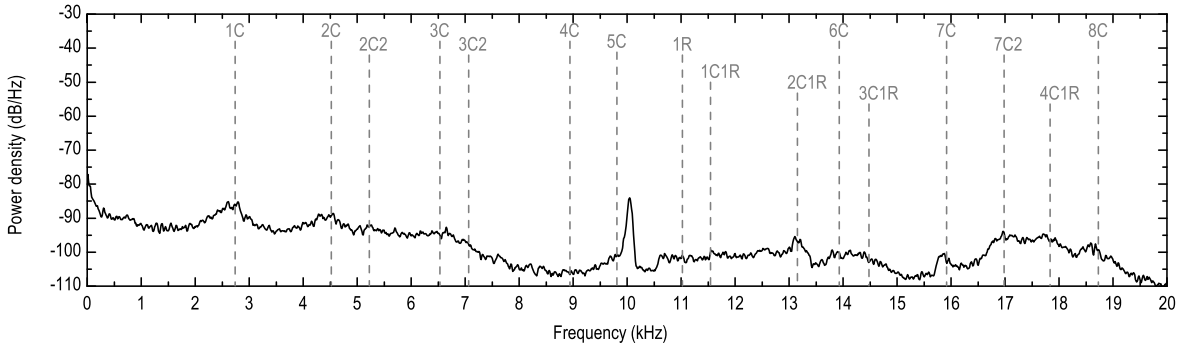

(b) Secondary H_2 manifold (*PlHdyn*) spectrum with baffle installed, with FE-calculated mode frequencies overlayed

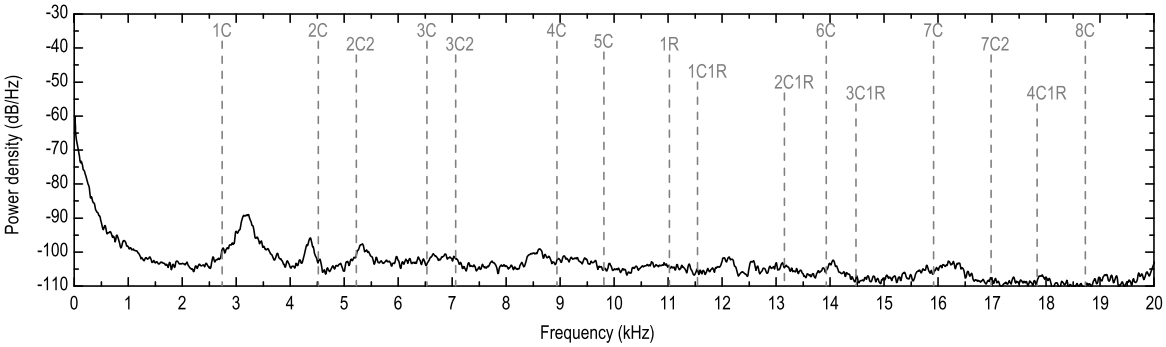

(c) Combustion chamber (*PCCdyn1*) spectrum

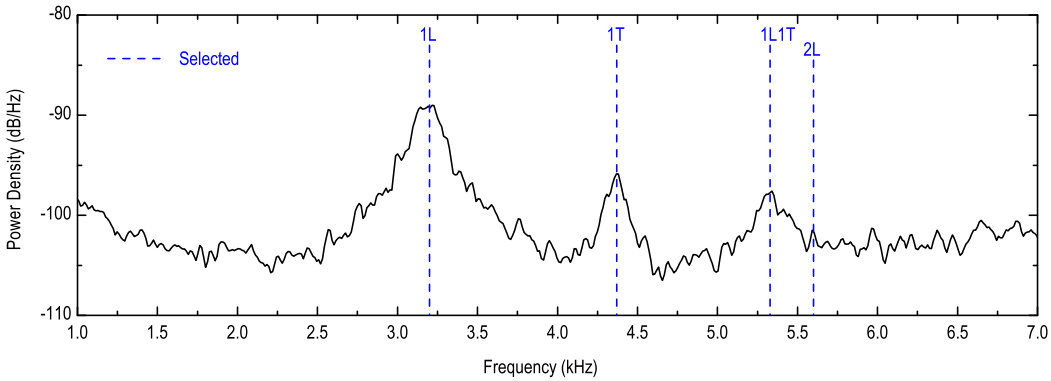

(d) Combustion chamber (*PCCdyn1*) spectrum with primary chamber modes frequencies identified

Figure 6.8: Results with the acoustic baffle installed in the secondary H_2 manifold; (a) PSD of *PlHdyn* without baffle (repeated here for convenience), (b) PSD of *PlHdyn* with baffle, and (c,d) the corresponding PSD of *PCCdyn1*.

6.4 Acoustic excitation

6.4.1 Spectrum characterisation

The acoustic behaviour of BKH with acoustic excitation through modulation of the secondary nozzle flow will now be explored. Firstly, the influence of the secondary nozzle on the combustion chamber modes is examined. Compared to the clean combustor configuration, one may expect a decrease in the frequency of the 1T mode due to the effective increase in chamber height with the secondary nozzle cavity. In fact one sees little shift in frequency in the measured spectra, as seen in Figure 6.9. In the figure, power spectra for two tests at 60 bar with GH_2 are overlayed; one with a clean combustor configuration and the other with the secondary nozzle installed (but without modulation – i.e. deactivated exciter wheel). Table 6 compares the corresponding FE calculated mode frequencies using η_{c^*}-corrected sound speed, which are overlayed on the spectrum in Figure 6.9. The FE model predicts a small decrease of 75 Hz in the 1T frequency and 109 Hz in the 1L1T, neither of which are convincingly evident in the spectrum. Comparison of the respective FE pressure distribution results in Figure 6.10 shows that extension of the 1T mode into the secondary hydrogen injectors appears to lessen the influence of the secondary nozzle. This means that acoustic data from tests using the clean configuration can be compared with confidence along side tests with the excitation configuration.

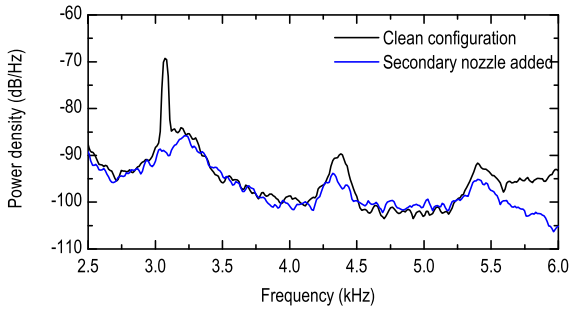

Figure 6.9: Power spectra comparing primary combustion chamber modes with and without secondary nozzle installed.

Table 6: FE calculated mode frequencies for BKH with and without secondary nozzle installed.

	Clean configuration	Secondary nozzle added
η_{c^*}-corrected sound speed	1668 m/s	1667 m/s
1L	3275 Hz	3252 Hz
1T	4350 Hz	4275 Hz
1L1T	5604 Hz	5495 Hz

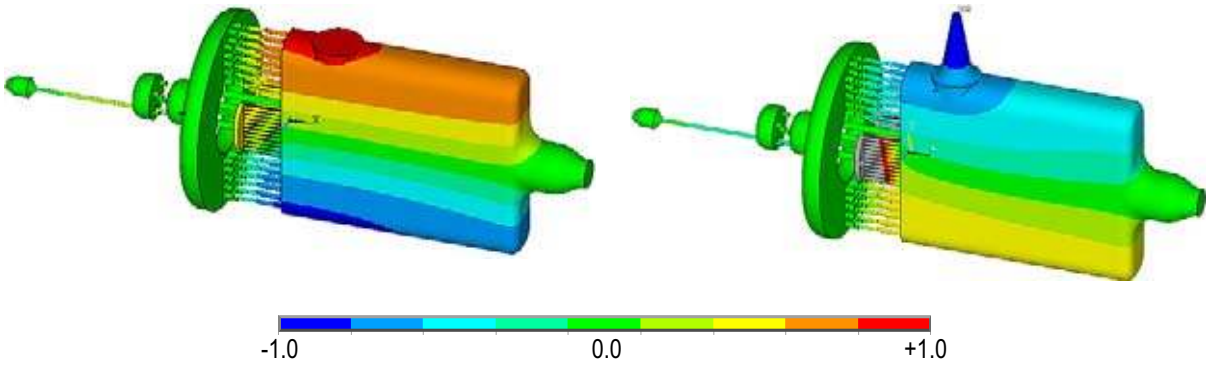

(a) clean configuration (b) with secondary nozzle

Figure 6.10: FE-calculated pressure distributions for the 1T mode; (a) without, and (b) with the secondary nozzle installed.

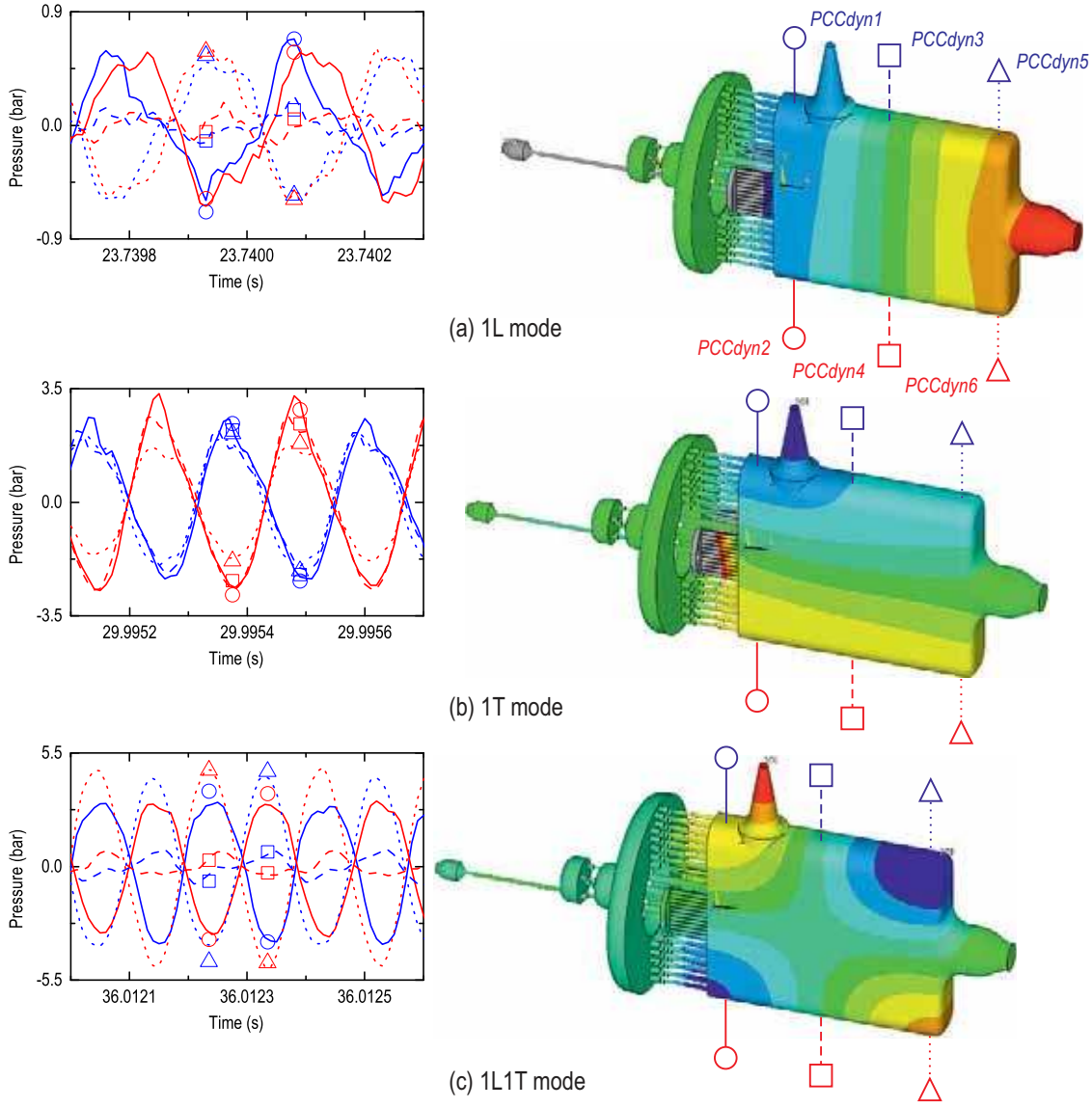

Figure 6.11: Mode identification by sensor phase analysis with on-resonance excitation for the 1L mode (a), 1T mode (b), and 1L1T (c).

With excitation, the 1L, 1T, and 1L1T modes can be positively identified from the relative phase of the *PCCdyn1* to *6* sensor signals using unfiltered data taken during excitation of the respective modes. Once again, the relative amplitudes of the sensor signals are compared with those from FE-calculated mode distributions, this time from an FE model with the secondary nozzle installed. The comparison is shown in Figure 6.11, noting that here the signals have been high-pass filtered with a cut-off frequency of 2800 Hz in order to centre the oscillations around zero bar and to remove any contribution from the sensor artefact at 2400 Hz. Note that the relative amplitudes of the sensor signals are again generally well predicted in the FE calculated mode distribution, although comparison is made more difficult by noise and contributions from overtones contained in the signals. For the 1T mode, *PCCdyn1* in the upper wall has a lower amplitude than its counterpart in the lower wall, *PCCdyn2* ($p'_{PCCdyn1} \sim 85\% \; p'_{PCCdyn2}$), due to the distortion of the acoustic field caused by the presence of the secondary nozzle in the upper wall. In Section 4.4.7, this distortion is also noted to displace the 1T nodal line upwards by approximately 12 mm.

While power spectra are used for examination of frequency content for steady-state acoustic measurements, spectrograms are employed for tests with excitation. The spectrogram consists of a series of short-time fast Fourier transforms (FFTs), and is useful for identifying the time-varying nature of the acoustic spectrum with changing excitation input. The spectrograms presented herein were calculated using a Hanning window to reduce spectral leakage for more pronounced peaks, and large sample sides to minimise peak spread, making identification by eye with the colour scaling easier.

Figure 6.12 shows a spectrogram of the *PCCdyn2* dynamic pressure signal over the course of a test of type 4 (Section 5.5.1); steady state operating conditions with a controlled excitation ramp. The spectrogram is viewed up to 8000 Hz, and the excitation frequency ramps from 1000 to 6000 Hz from t = +10 to +40 s; a ramping rate of 166.7 Hz/s. The 1T and 1L1T modes show strong response as the excitation sweep passes through them. The 1L mode is only weakly excited, which is to be expected considering the orientation of the secondary nozzle perpendicular to the chamber axis, which favours excitation of transverse modes. Figure 6.13 is the same spectrogram as Figure 6.12, viewed from 0 to 40,000 Hz. Overtones of the excitation signal, appearing at regular multiples of the primary excitation frequency, are labelled in Figure 6.13. The origin of these overtones is the nonlinear nature of the acoustic forcing, and is discussed further in Appendix C. It is evident that the overtones are also capable of exciting acoustic modes of the chamber. Occasionally the overtones illicit a greater response from higher order modes than the primary excitation frequency itself achieves when exciting fundamental chamber modes. In this work, however, analysis will be restricted to the 1L, 1T and 1L1T modes to retain focus in the flame response study.

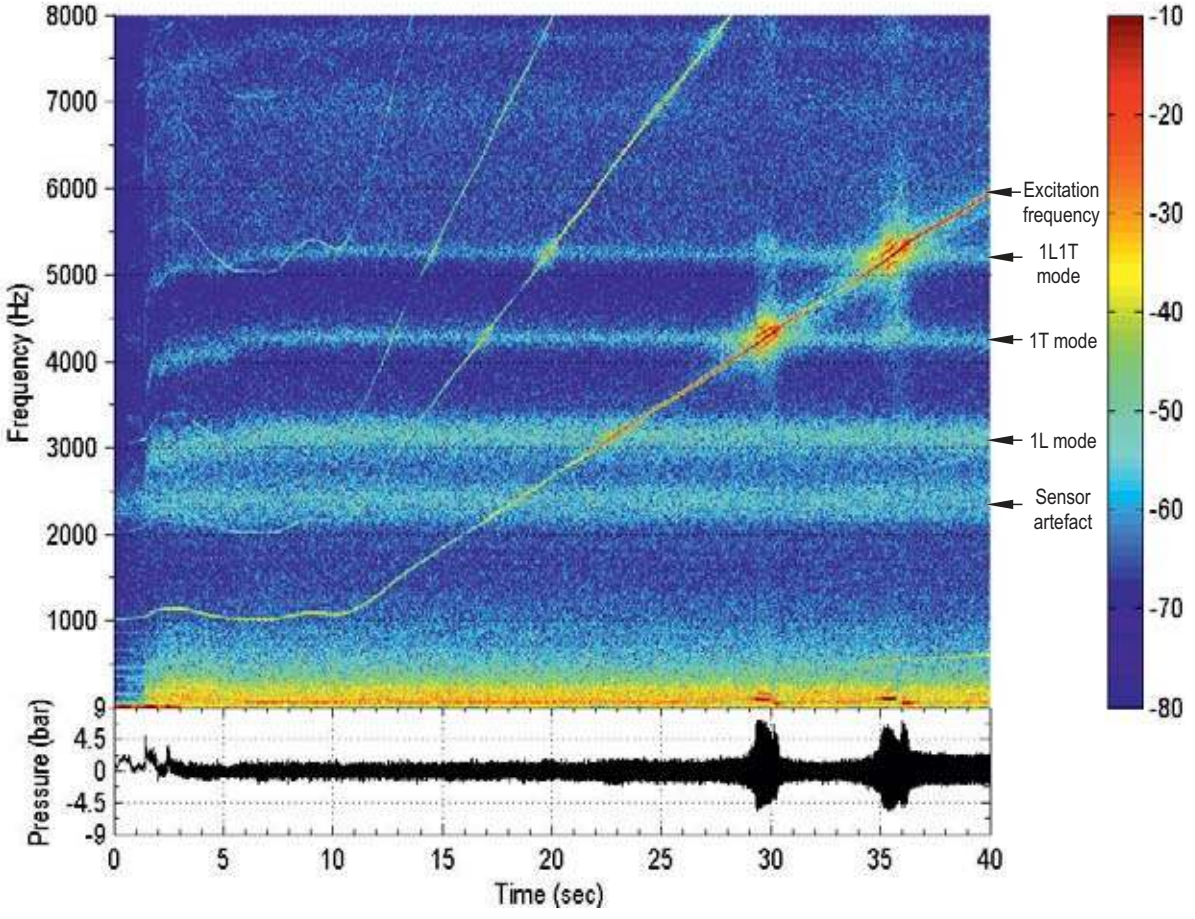

Figure 6.12: Spectrogram of a type 4 test; steady-state conditions with a controlled excitation ramp from 1000 to 6000 Hz.

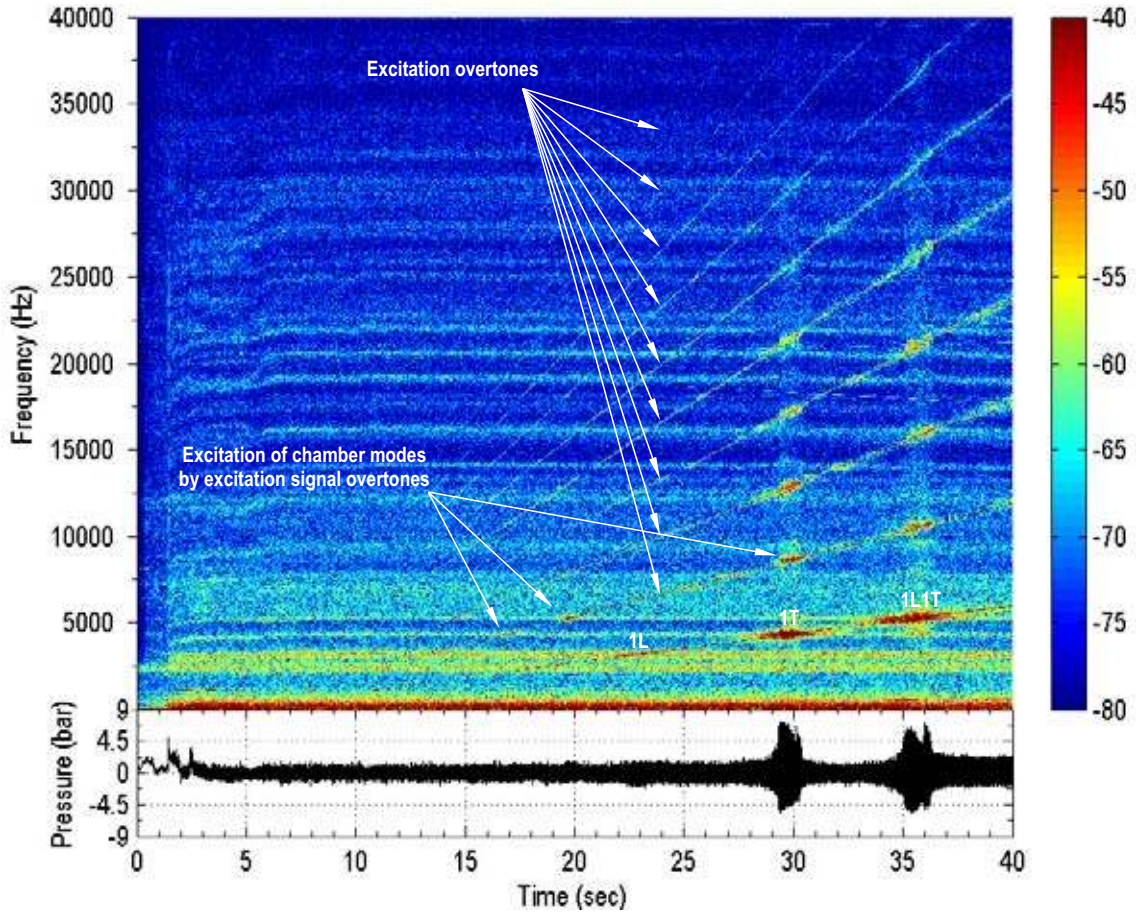

Figure 6.13: Spectrogram of Figure 6.12, viewed up to 40,000 Hz, with excitation signal overtones indicated.

6.4.2 Low frequency instability

For a short time during the combustor start-up transient from t = +0.0 to approximately +1.5 s, a strong, low frequency (LF), or 'chugging', mode of around 80 to 100 Hz is observed. This mode has amplitude of approximately 10% of P_{cc}, which according to Bragg (1963) is a typical level for injection-coupled chugging instability. Curiously, this chugging mode reappears during excitation of the 1T mode at around 3900 to 4200 Hz, and also during the 1L1T mode at around 5100 to 5500 Hz, then disappears again shortly after. In fact, chugging was consistently triggered in all tests at all operating conditions during excitation of transverse chamber modes. Furthermore, the chugging behaviour was observed to change over the course of exciting each transverse resonance mode. On approaching the mode from below, chugging with a frequency of either 80 or 100 Hz would quickly set in. The frequency appeared to depend on LOx mass flow rate, with 80 Hz appearing during 40 bar tests and 100 Hz for 60 bar tests. Upon passing the centre frequency and departing the up-side of the mode, the chugging frequency changed to half its initial value; 40 or 50 Hz, respectively. Non-linear coupling of the excitation frequency with the chugging frequency and its overtones is evident above and below the primary excitation frequency. At some point after departing the mode, when the on-resonance excitation amplitude had diminished sufficiently, the chugging would cease. Spontaneous chugging was never observed for off-resonance conditions, although a LF signal with the chugging frequency and with greatly diminished amplitude remains present during off-resonance conditions. Occasionally, during the transition from high to low frequency chugging, there was a delay of approximately 100 ms

before the low frequency chugging began, providing a brief window of clean, on-resonance excitation free of chugging. This situation is illustrated by example in the spectrogram of Figure 6.14. No explanation for the transitional behaviour of the chugging frequency can be offered. The analysis of flame-acoustic interaction in this work avoids chugging events, making use of periods of 'clean' excitation wherever possible.

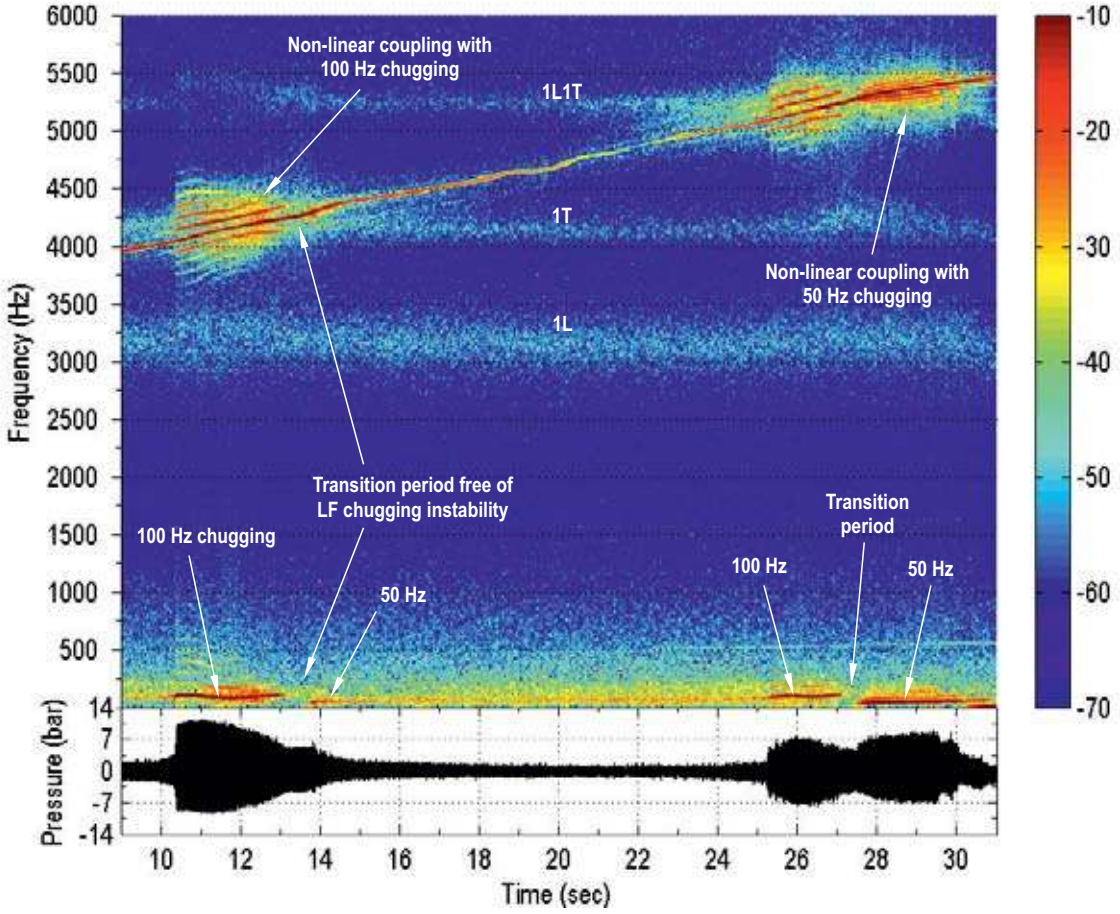

Figure 6.14: Spectrogram from a 60 bar test illustrating transitioning LF chugging during transverse mode excitation.

6.4.3 Excitation amplitude

Measured acoustic pressure amplitudes observed in BKH for various configurations and operating conditions will now be discussed. Acoustic pressure amplitudes are extracted from *PCCdyn2* data as follows. First the signal is high-pass filtered with a cut-off frequency of 2800 Hz, which excludes all low frequency content originating from turbulent combustion and injection noise, chugging, and the sensor artefact at 2400 Hz. A dynamic RMS value of the signal is calculated, using a sliding adjacent-averaging window of 100 samples. Finally, the RMS value is multiplied by the square root of 2 to return an estimate of acoustic pressure amplitude p'. Short samples of this acoustic pressure amplitude signal, usually 100 ms in duration, are taken from the test conditions of interest, for example during peak on-resonance excitation. The p' sample is averaged to return a single value of average acoustic pressure amplitude for the sample $\overline{p'}$. This sampling procedure is illustrated in Figure 6.15 using a signal from a test at 40 bar with GH_2 using ramped excitation.

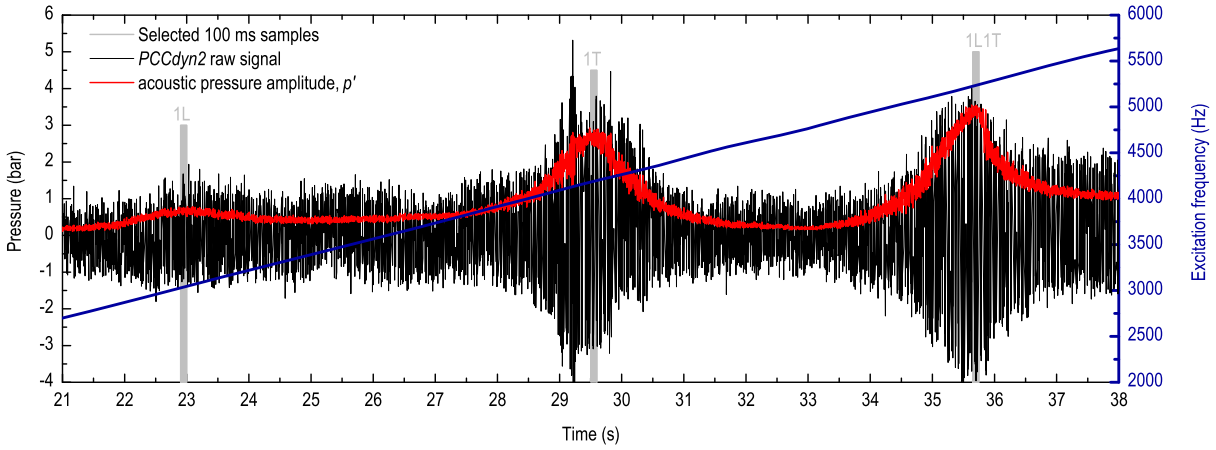

Figure 6.15: Dynamic pressure signal during ramped excitation of the 1L, 1T and 1L1T modes. The calculated acoustic pressure amplitude is overlayed (red line). The ramped excitation frequency (blue line) is also overlayed for information.

Table 7 contains a summary of the range of $\overline{p'}$ values measured for various test conditions. The first two rows compare sample amplitudes for clean configuration tests before and after the acoustic baffle was installed in the secondary H_2 manifold. The greater amplitude in the natural combustor noise without the baffle can be attributed to the 1C mode of the secondary H_2 manifold (Section 6.2). Values of $\overline{p'}$ measured in the combustion chamber from early tests without the baffle were found to be dependent on the supply mass flow rate of secondary H_2. The natural acoustic pressure amplitude in BKH during steady state operation would be classified as classically stable. Classically stable refers to the guidelines laid out by the CPIA (Section 2.6.4), which considers amplitudes less than 5% (10% peak-to-peak) of P_{cc} to be stable. Typical pressure amplitudes in BKH from clean configuration tests (with baffle) are between 0.2% and 0.3%. It should be noted that the CPIA guidelines only give the value of 5% as a recommended criterion. Often, vehicle and payload requirements dictate a much smaller level of allowable fluctuations.

Table 7: Summary of measured acoustic pressure amplitudes for various BKH configurations and excitation conditions.

Sample type	Average acoustic pressure amplitude, as % of P_{cc}
Clean configuration	0.2–0.3
Clean configuration, without baffle	0.3–1.3
1L mode excitation	1.4–1.9
1T mode excitation	6.5–8.3
1L1T mode excitation	8.4–9.5

On-resonance excitation of the 1L mode achieves only modes amplitudes up to 1.9%, which is still considered stable. During on-resonance excitation of the 1T and 1L1T modes, the amplitude reaches values between 6.5 and 9.5%, which is classically unstable. Therefore the conditions achieved with excitation of transverse modes in BKH can be considered representative of real HF instabilities. Interesting to note is that the average pressure amplitudes reached during excitation of the 1L1T mode are consistently higher than those for

the 1T mode. Assuming the excitation amplitude is the same as for the 1T mode, the higher 1L1T resonance amplitude may be attributed to the higher mode frequency, whereby system damping acts over a shorter duration between cycles.

The achieved amplitude of excitation can be compared to an expected, theoretical value. The ideal characteristic exhaust velocity relation is employed;

$$c^* = \frac{P_{cc}\ A_{MN}}{\dot{m}}\ , \tag{18}$$

where A_{MN} is the nozzle exit area, and the mass flow rate is the total for all injectants entering the chamber. The theoretical pressure fluctuation p'_{th} resulting from secondary nozzle mass flow modulation is taken to be the difference in combustion chamber pressure between the chamber with only the main nozzle and the chamber with both the main nozzle and fully-open secondary nozzle, as expressed here:

$$p'_{th} = \dot{m}\ c^* \left(\frac{1}{A_{MN}} - \frac{1}{A_{MN} + A_{SN}} \right)\ . \tag{19}$$

This equation is of course only an estimate of the difference between steady-state conditions, and is only valid for off-resonance excitation.

Appropriate values are taken from the conditions for which the highest 1T amplitude in Table 7 was achieved, a test with $P_{cc} = 43.5$ bar using LH_2. A theoretical excitation amplitude of $p'_{th} = 3.95$ bar is estimated, or normalised with chamber pressure, $p'_{th}/P_{cc} = 9.1\%$. Measured pressure amplitudes for off-resonance conditions are far lower, reaching only 0.2–0.3%. During on-resonance excitation, acoustic energy can build up from cycle to cycle and the fluctuations can be larger than those estimated by Equation 19. Acoustic pressure amplitude during 1T mode excitation in the 43.5 bar test was also extracted, using *PCCdyn2* data and the method described previously. The measured 1T-mode pressure amplitude is $\overline{p'} = 3.48 \pm 0.04$ bar, or a normalised amplitude of $\overline{p'}/P_{cc} = 8.0\%$. This is still somewhat lower than the expected theoretical level (for off-resonance) of 9.1%.

Imperfect closure of the secondary nozzle outlet by the exciter wheel teeth may be responsible for the excitation amplitude not reaching its potential. The spacing between the nozzle outlet and the teeth is known from experience with the CRC to strongly affect the excitation amplitude achieved in the chamber. Care was taken during BKH testing to maintain a constant spacing from test to test, however small variations in this spacing are probably responsible for some of the spread in measured excitation amplitudes.

Other sources of acoustic damping in the system undoubtedly also conspire to lower achievable amplitudes. Fluid viscosity causes losses in the boundary layer at the combustion chamber walls. The nozzle exit area, for both the main and secondary nozzles, is only partially reflective to acoustic waves. The injection spray is a source of drag to acoustic velocity. Fluctuations in sound speed, due to temperature fluctuations, are known to reduce the clarity of combustion chamber resonances. Richecoeur et al. (2009) explain how fluctuating temperature from turbulent combustion reduces the overall amplitude of excitation in the MIC by effectively increasing system damping. During on-resonance excitation in BKH, there is occasionally enhanced fluctuation of temperature resulting from chugging instability, although samples from such conditions are avoided where possible.

6.5 Combustion response

Features of the BKH acoustic spectrum observed during tests with excitation show evidence of a response in combustion to the imposed acoustic field. Figure 6.16 shows a spectrogram of the *PCCdyn2* dynamic pressure signal over the course of a test of type 3 (Section 5.4.3); steady state operating conditions with an uncontrolled excitation ramp. During excitation of the 1T mode, there is a noticeable increase in the natural frequency of the 1L1T mode, as indicated in Figure 6.16. The 2.7% (140 Hz) increase in frequency corresponds to a bulk temperature increase inside the combustion chamber of approximately 5.5%, or 62 K. A wall temperature increase of about the same is also observed, as seen in Figure 5.13. The increase in bulk-gas and wall temperatures was accompanied by an increase in c^* combustion efficiency from 96% to 98% (with an uncertainty of ±1.9%). This response is interpreted as an indication of increased heat release rate from combustion resulting from the influence of the acoustic velocity field of the 1T mode.

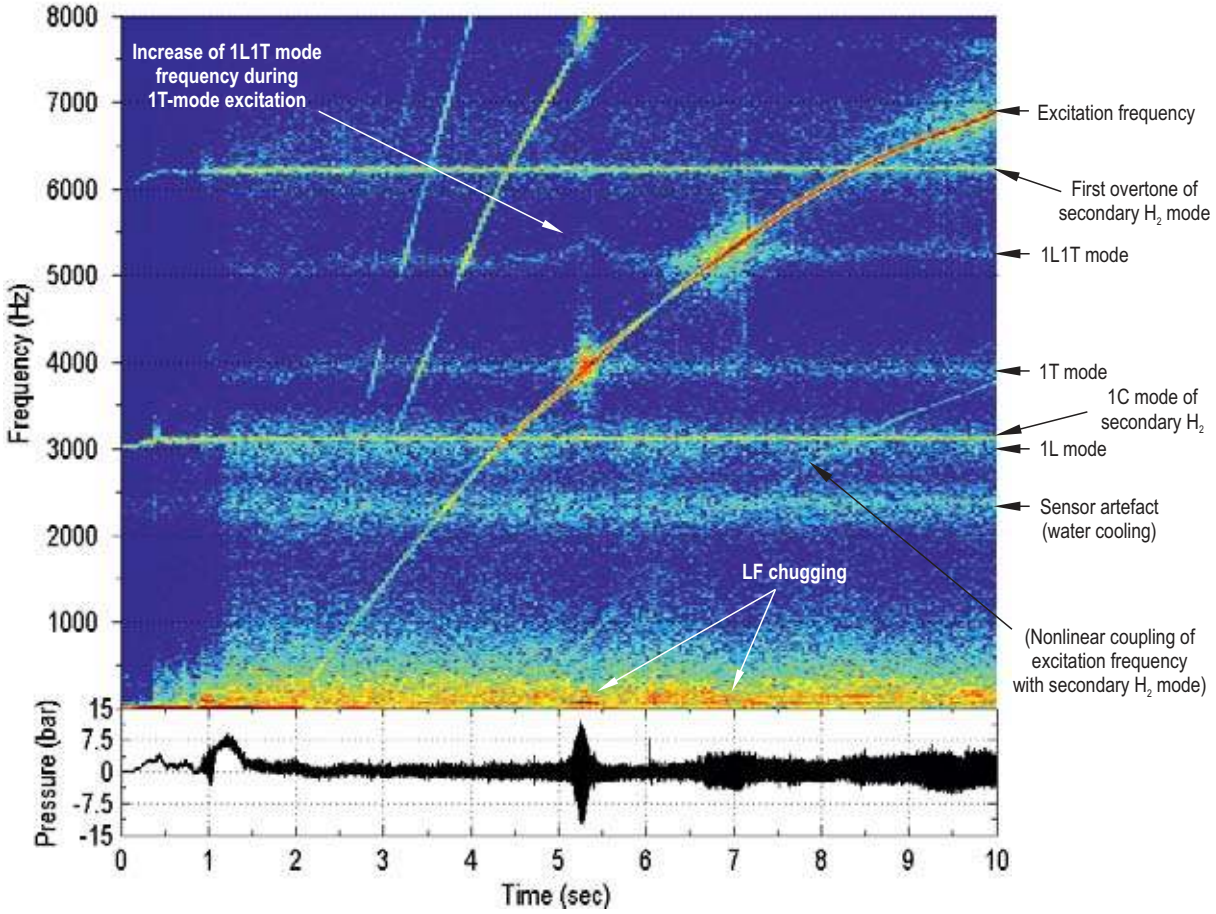

Figure 6.16: Spectrogram of the *PCCdyn2* signal from an early test with uncontrolled excitation ramp.

As a side note to the spectrum in Figure 6.16, it was also noticed that additional lines appear to shadow both above and below the excitation frequency and its overtones with a constant spacing of approximately 3100 Hz. These lines are postulated to be the result of nonlinear coupling between the excitation signal and the secondary H_2 mode, which has a frequency of 3100 Hz. Coupling between these clearly nonlinear acoustic pressure signals would explain the presence of peaks in the spectrum at both the sum and the difference of the excitation and secondary H_2 mode frequencies. Elimination of the secondary H_2 mode from the spectrum

also removed these lines, as seen in Figure 6.13 which is from a later test with the acoustic baffle installed.

As discussed with regard to Figure 6.16, forcing of the 1T mode results in a response from combustion. The resulting increase in mode frequency has a further consequence to the progression of acoustic pressure amplitude during ramped excitation. Example p' signals from tests with ramped excitation of the 1T mode are given in Figure 6.17, one from a hot-fire test at 60 bar, and one from a cold-flow test where only GH_2 is injected into the chamber. In the cold flow case in Figure 6.17a the progression of p' is symmetrical about resonance. In the hot-fire test in Figure 6.17a the profile is elongated on approach to peak resonance amplitude, and falls off steeply on departing resonance. This behaviour can be explained by the increase in gas temperature and mode frequency in response to transverse acoustic excitation. On approaching resonance, the mode frequency increases and moves away from the excitation frequency. Following peak resonance, the excitation amplitude begins to decrease, which is accompanied by a decreasing combustion response. The mode frequency decreases back to its natural state, moving away from the excitation frequency and accelerating the decrease in p'.

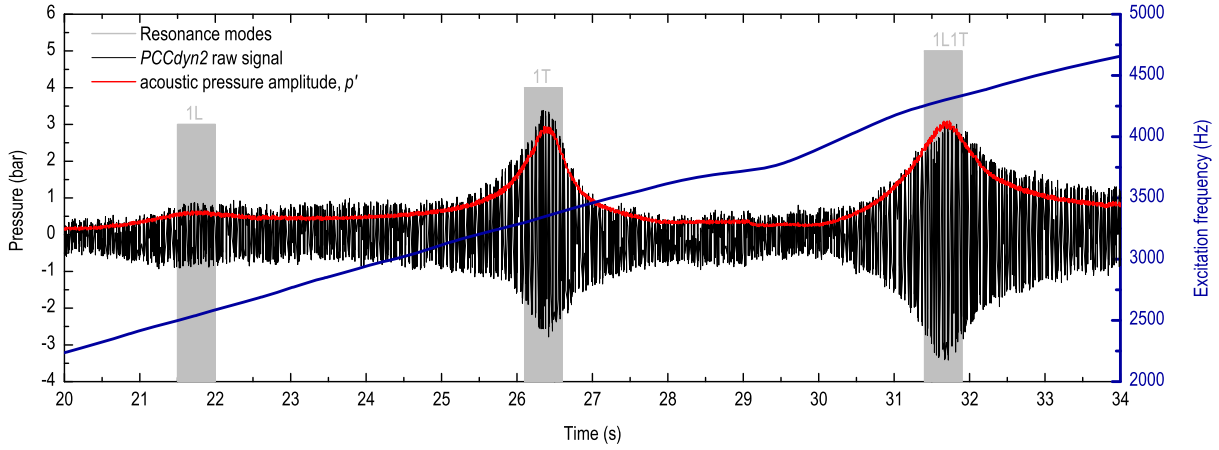

(a) Cold-flow test (GH_2 injection only)

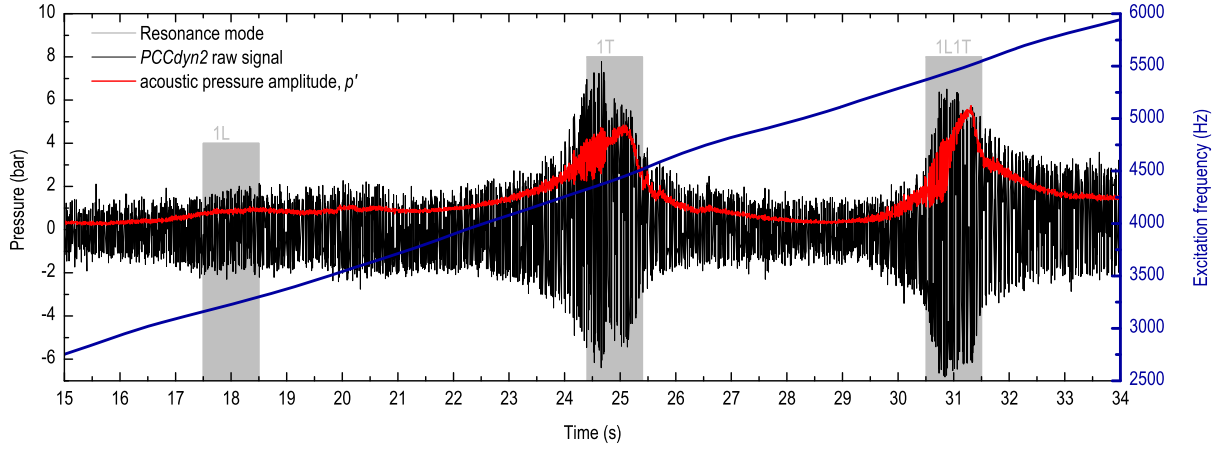

(b) Hot-fire test (60 bar with GH_2)

Figure 6.17: Progression of acoustic pressure amplitude during 1T mode excitation for a cold-flow test without combustion (a), and a hot-fire test at 60 bar with GH_2 (b).

The influence of combustion response on the excitation profile was observed to be greater for lower H_2 injection temperatures. An example of the situation typically observed for tests with LH_2 is shown in the spectrogram in Figure 6.18. LF chugging instability sets in while approaching the 1T mode from below, as discussed previously. However, rather than transitioning to another chugging frequency and then diminishing gradually as the excitation frequency departs the mode, as is typically the case in tests with GH_2 and exemplified in Figure 6.15, spectral content appears to concentrate on the excitation frequency. Peak acoustic pressure amplitude is maintained for far longer durations than in GH_2 tests, up to 1 s. The peak amplitude persists although the excitation frequency has departed the natural bandwidth of the 1T mode. At some point, approximately 400 Hz from the 1T centre frequency, the resonance ceases abruptly and the spectrum returns to its natural state with normal, off-resonance excitation pressure amplitude. The excitation ramping rate used in the test in Figure 6.18 was 83.3 Hz/s, however the same behaviour was also observed under identical operating conditions with the faster ramp rate of 166.6 Hz/s.

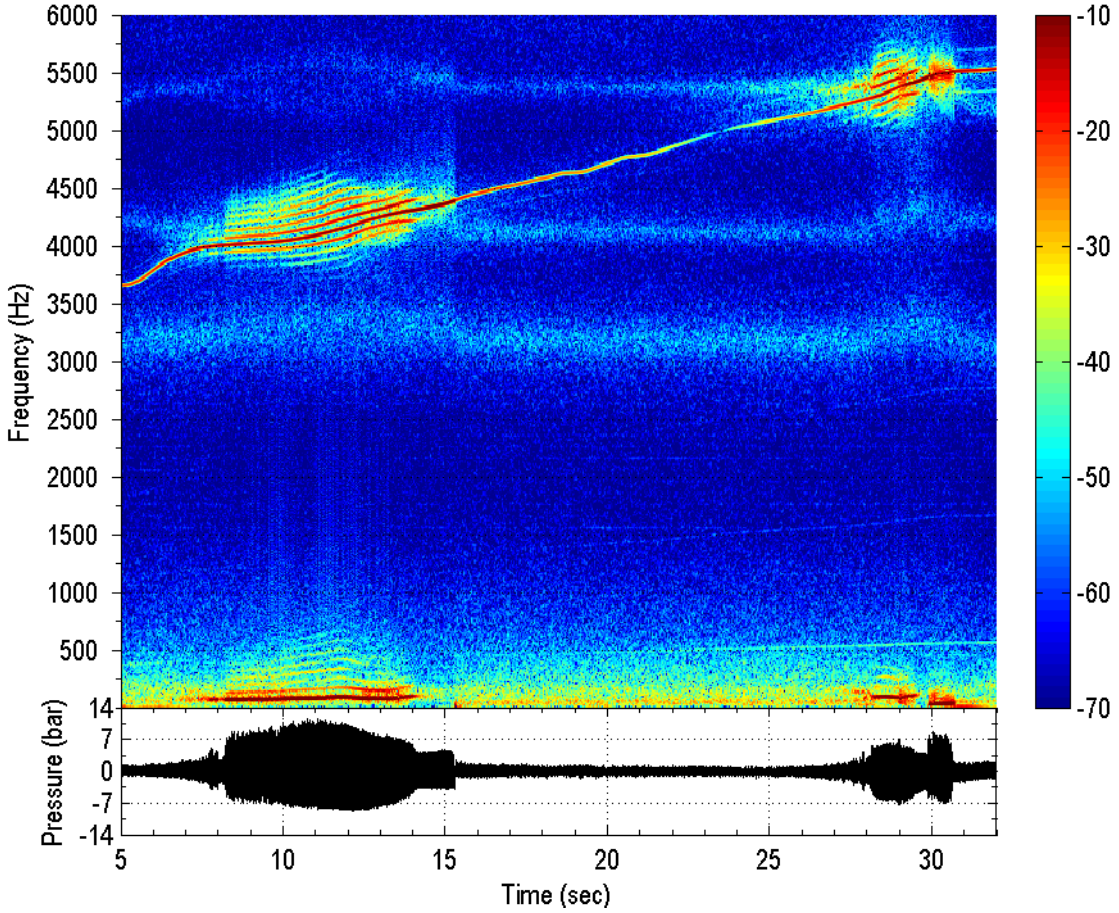

Figure 6.18: Spectrogram showing ramped excitation of the 1T and 1L1T modes for a 40 bar test with LH_2.

Because this kind of response was never observed for tests with GH_2, the cause is thought to be an enhanced response of combustion to the acoustic field for H_2 at low injection temperatures. Increased tendency for instability is commonly observed in systems operating with lower H_2 injection temperature, as was explored in Chapter 3. From extensive H_2 temperature-ramping tests, Wanhainen, Parish and Conrad (1966) found LOx/H_2 to be particularly susceptible for velocity ratio (*VR*) values below 6.5. For the example shown here in Figure 6.18, this boundary was not crossed, with a *VR* of 10.7. Wanhainen's group also

correlated their data to an approximate H_2-transition temperature, below which HF instability occurred. The transition temperature is given by Conrad et al. (1968) as

$$T_{H,Tr} \approx \sqrt{\frac{P_{cc}\ ROF}{\Delta P_H}} \frac{1}{\rho_O D_O^{1.25}} \ . \tag{20}$$

Using the operating conditions from the Figure 6.18, $T_{H,Tr} = 12$ K, which is far from the temperature measured in the H_2 injection manifold of $T_H = 75$ K.

6.6 Injection coupling

Considering further the expression for $T_{H,Tr}$ in Equation (20), for a given injector and operating condition (as defined by P_{cc} and ROF), it is the pressure drop through the hydrogen injector, ΔP_H, which determines stability. Motivated by this insight, the possibility of injection coupling explaining the enhanced response during 1T mode resonance was investigated.

Frequency spectra from the dynamic pressure sensors in the injection manifolds during the peak resonance period between $t = +14.6$ and $+15.1$ s in the 40 bar, LH_2 test are given in Figure 6.19. The excitation frequency and its overtones are strong in the combustion chamber. These frequencies also appear to be transmitted to a degree into each of the injection manifolds. This is not surprising, since the pressure drops for all injectors are subsonic; 7% of P_{cc} for H_2, 31% for LOx, and 25% for secondary H_2. The off-resonance excitation frequency can also be distinguished in the injection manifold spectra in Figure 6.20, sampled from $t = +20$ to $+20.5$ s. Based on this observation, it is possible that modulation of the mass flow through the primary injectors may be coupling with the 1T mode acoustic pressure in the combustion chamber.

Baillot et al. (2009) studied the interaction of acoustic pressure with a coaxial jet of water and air by forcing a pressure antinode at the injector location. They observed modulation of the gas annulus injection flow, leading to enhanced liquid jet atomisation, but only when the acoustic pressure amplitude equalled or exceeded the dynamic pressure (ρu^2) of the gas jet at injection. The primary injector in BKH may also be affected by the acoustic pressure distribution of the 1T mode, noting that the expected offset of the pressure node (Section 4.4.7) may further increase amplitudes at this location. Using the numerically calculated 1T mode pressure distribution to scale the signal from the *PCCdyn2* sensor, the acoustic pressure amplitude at the locations of the primary injection elements was estimated. In the particular BKH test condition examined here, the injection dynamic pressure exceeds the acoustic pressure by a factor of two. Significant modulation of the H_2 injection flow is therefore not expected in this case.

The gas modulation criterion reported by Baillot et al. was checked for all other BKH operating conditions. The injection dynamic pressure of H_2 ranges from 4.5 to 16.0 bar in tests with GH_2, and 1.5 to 6.6 bar with LH_2. Estimated acoustic pressure amplitudes of the 1T mode at the location of the primary injector were found to reach 1.46 ± 0.04 bar. While this value closely approaches the lower end of the range of injection dynamic pressures for tests with LH_2, the minimum difference was 0.42 bar, representing a margin of 27% of $\rho_H u_H^2$. Excitation of the 1L mode in BKH also forces a pressure antinode at the injector. 1L mode

acoustic pressure amplitudes reach only 1.05 ± 0.04 bar. Any influence of acoustic pressure on injection flow or jet atomisation is therefore not expected to be significant in BKH results.

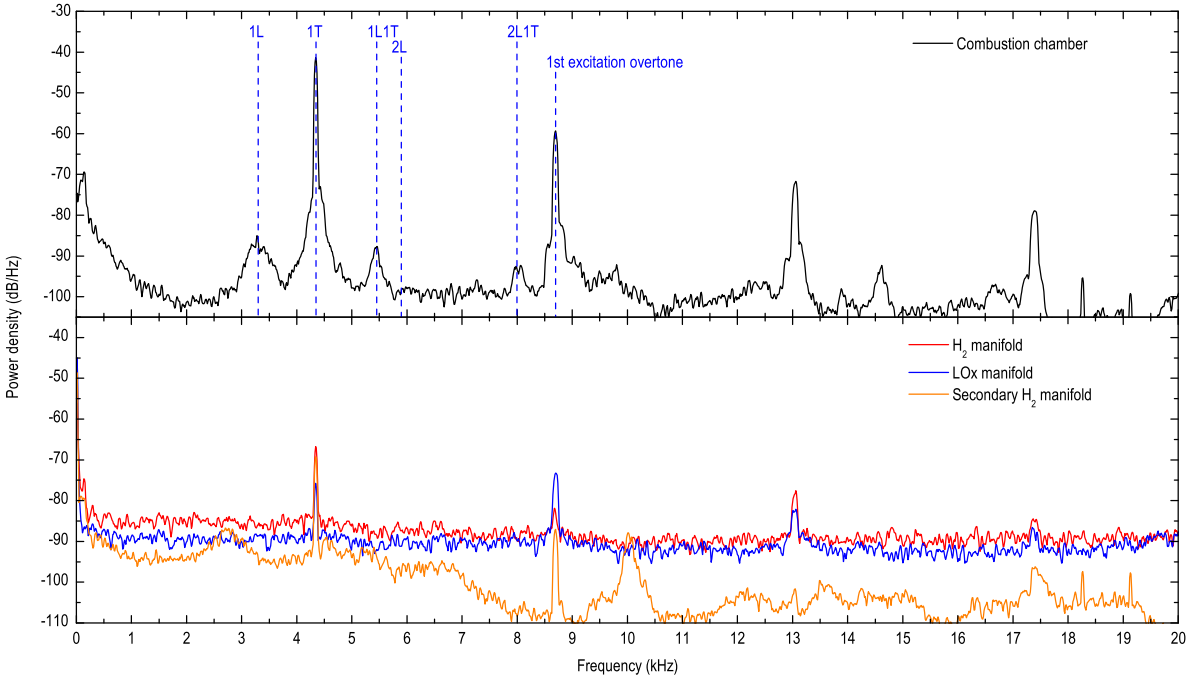

Figure 6.19: Combustion chamber and injection manifold acoustic spectra during peak 1T-mode resonance amplitude from the 40 bar test with LH_2 in Figure 6.18.

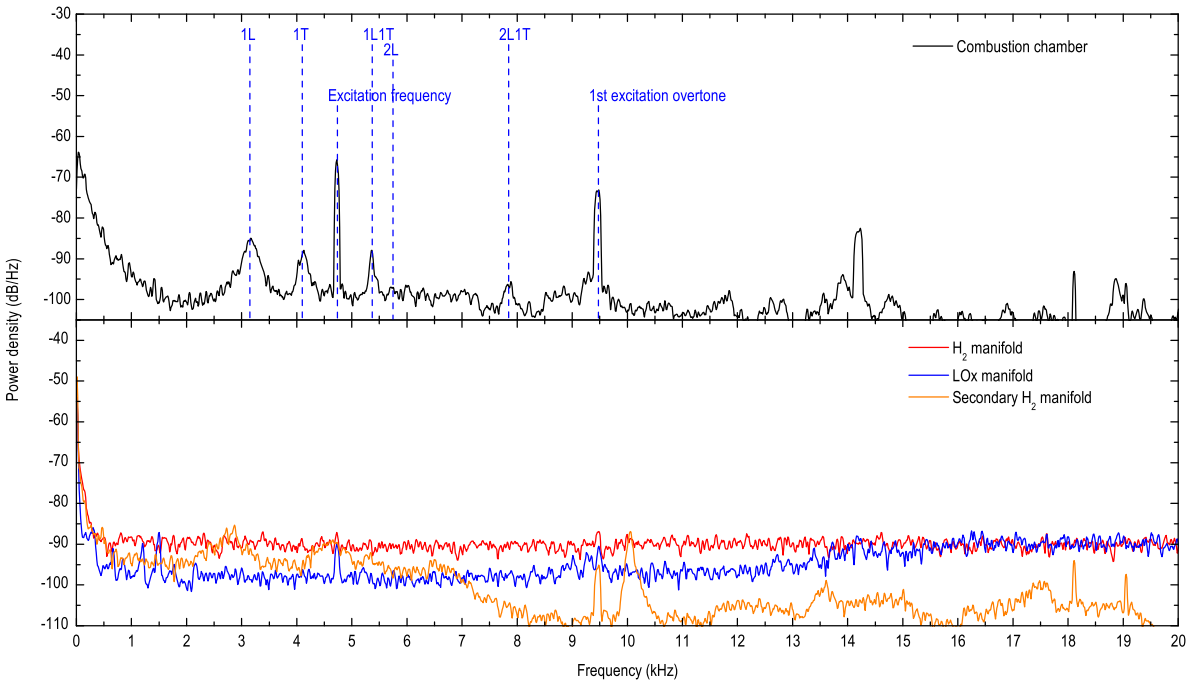

Figure 6.20: Combustion chamber and injection manifold acoustic spectra during off-resonance excitation from the 40 bar test with LH_2 in Figure 6.18.

A further mechanism for injection coupling found in literature was that of resonances inside the LOx post, as experienced by the research group at JAXA (Section 3.4.2). A simple estimation of the first resonance mode of the BKH LOx posts using $f_{post} = c_O/2L_{post}$, with $c_O = 576$ m/s, gives a frequency of $f_{post} = 1694$ Hz. Looking to the LOx manifold spectrum in the off-resonance sample in Figure 6.20, a small peak near 1500 Hz is evident, however its presence in the combustion chamber is insignificant compared to the chamber modes. This LOx post mode appears to be suppressed during 1T mode excitation as seen in Figure 6.19. The first resonance mode of the H_2 injectors is in the same way estimated as $f_H = c_H/2L_H$, with $c_H = 764$ m/s, giving $f_H = 4835$ Hz. Apart from the small peaks of the excitation frequency and overtones, the H_2 manifold spectrum is more or less featureless in the entire range shown. There is also no evidence of a significant response near the corresponding injector frequencies in the combustion chamber spectrum in either Figure 6.19 or Figure 6.20.

The FE model was run with the corresponding test conditions in order to study the injector modes in more detail. Three resonance mode results of interest for the H_2 injector and LOx injector are displayed in Figure 6.21. The first result is the bulk mode for each of the injector manifolds. These are at low frequencies, 503 Hz for the H_2 manifold (Figure 6.21a) and 290 Hz for the LOx manifold (Figure 6.21b), and are therefore of little interest. The second result is the first longitudinal mode for the H_2 injectors and LOx posts, with frequencies of 4128 Hz and 1798 Hz (Figure 6.21c and Figure 6.21d) respectively. These values are close to the corresponding estimations discussed in the previous paragraph.

The multiple peaks in the LOx spectrum near the calculated post-mode frequency can be explained by multiple instances of the first post-mode which were captured by the FE model. Several instances of the LOx-post mode are predicted within a small range of frequencies whereby each element resonates separately. The result shown in Figure 6.21c and Figure 6.21d is for all five elements in simultaneous resonance. The final result given in Figure 6.21e and Figure 6.21f is of the first transverse mode of the H2 and LOx manifolds respectively. These modes do not appear to be present in the spectra in either Figure 6.19 or Figure 6.20.

As an aside, the transverse mode of the H_2 dome in Figure 6.21e was the 52nd resonance mode of the BKH combustor-injector system calculated by the FE model. This highlights the acoustic complexity of a rocket combustion chamber coupled with multiple injector volumes.

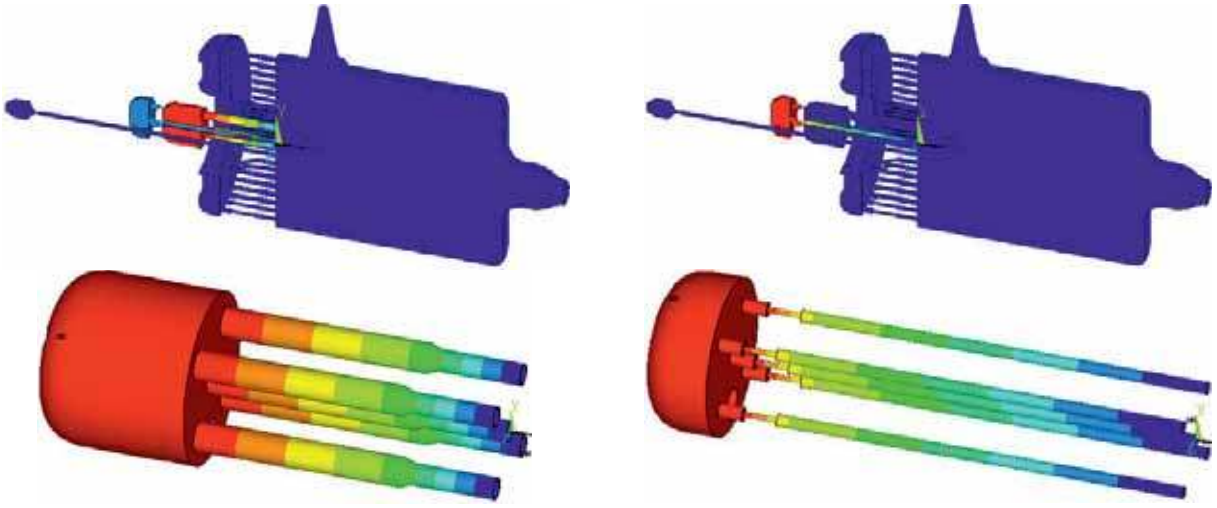

(a) First bulk mode of H_2 manifold ~ 503 Hz

(b) First bulk mode of LOx manifold ~ 290 Hz

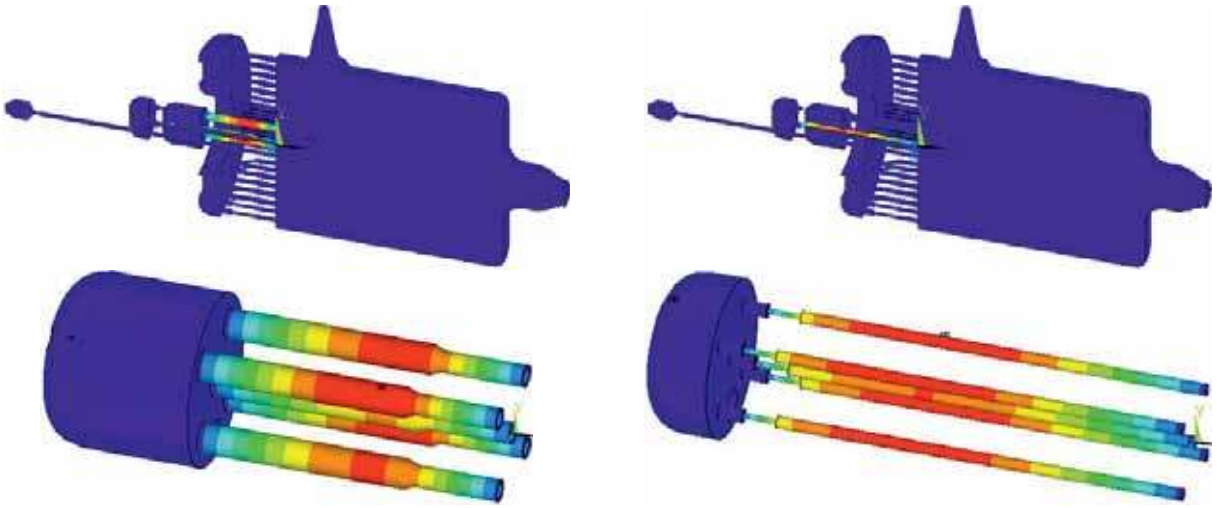

(c) First longitudinal mode of H_2 injector ~ 4218 Hz

(d) First longitudinal mode of LOx injector ~ 1798 Hz

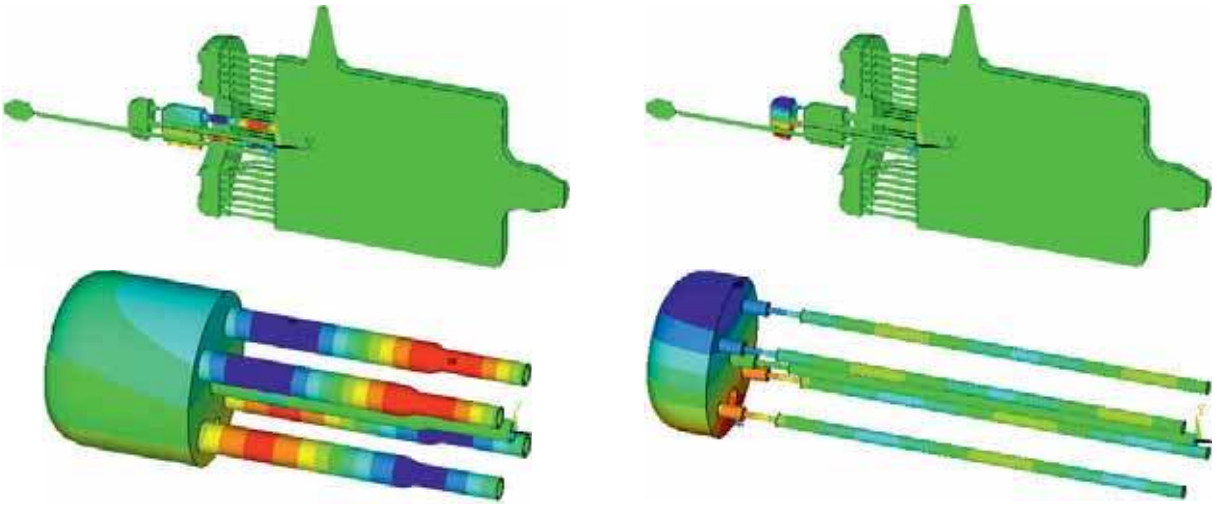

(e) First transverse mode of H_2 manifold ~ 9294 Hz

(f) First transverse mode of LOx manifold ~ 7320 Hz

Figure 6.21: FE model results for acoustic modes of the H_2 injector (left column) and the LOx injector (right column).

6.7 Summary

The use of a highly detailed finite element acoustic model of the combustion chamber and injection system was found to be invaluable in the interpretation of the acoustic spectra obtained from hot-fire testing. By including all nozzles, injection elements, igniter ports and as many other geometrical features of the system as possible, the model is able to capture the influence of all these features on the resonance modes. Not only does this allow more accurate prediction of the fundamental combustion chamber mode frequencies and acoustic pressure distributions, but also prediction of all additional modes involving the injection elements and manifolds. Spectral features were identified using the model which would otherwise not have been identifiable, including complex injector-coupled modes. The finite element method proved to be a highly effective way of characterising the acoustic modes of a reacting rocket combustor coupled with its injection system.

The extensive use of secondary hydrogen is an important feature of BKH. A drawback to its application is that the associated injection manifold introduced dominant features to the frequency spectrum of the combustion chamber which are not relevant to the intended experiment and serve only to clutter the spectrum. An acoustic baffle, designed with the help of the finite element model, was successfully implemented to remove these unwanted modes. However, this experience serves as a reminder that care should be taken at the design stage to understand the acoustic behaviour of the injector, whether for experimental or flight hardware. The consistency and strength of the secondary H_2 manifold mode observed in BKH leads one to ponder if similar injector manifold acoustic resonances may serve as a driving mechanism for HF instabilities in full-scale engines.

Excitation of transverse modes in BKH through modulation of secondary nozzle flow achieves acoustic pressure amplitudes which are classified as unstable and therefore representative of real HF instabilities. An unexpected side effect of transverse mode excitation was the triggering of a strong injector-coupled LF chugging instability. Strange is the fact that this chugging was under no circumstances triggered by excitation of the 1L mode, even though the 1L mode is expected to subject the injector to greater amplitudes of oscillating pressure than the 1T, which has a pressure node located at the primary injector. Short periods of transition between LF frequencies afford samples of pure HF excitation, which were utilised for the study of flame-acoustic interaction in this work.

An observed increase in mode frequency during transverse excitation could be interpreted as an observation of velocity response, whereby the action of the 1T mode acoustic velocity antinode increases the heat release rate from the flame. The accompanying increase in gas temperature and acoustic mode frequency in the combustion chamber result in asymmetry in the pressure amplitude profiles during ramped excitation. This asymmetry effect was greater for tests with LH_2 fuel, where peak, on-resonance amplitude appears to persevere after the excitation has departed the mode. This may be evidence of a velocity response mechanism which is more receptive to lower H_2 injection temperatures. Injection coupling with acoustic pressure may also have played a role in the response to transverse excitation.

7. FLAME RESPONSE

In this chapter the spatial and temporal response of the flames to forced excitation is analysed. Primarily this includes study of the high-speed hydroxyl-radical (OH*) emission imaging, as well as photomultiplier recordings of filtered OH* emission. Reponses to both transverse oscillations in acoustic velocity and oscillations in acoustic pressure are examined, through excitation of the chamber 1T and 1L acoustic modes, respectively.

The observed responses to both types of excitation may be important to instability coupling mechanisms. Transverse acoustic velocity results in a change in the distribution of combustion and oscillating convective displacement of the flame. Acoustic pressure causes a coupled response in combustion, with a measurable, positive value of response factor. Tests at combustion chamber pressures of 40 and 60 bar are reported herein in order to compare the response for subcritical and supercritical conditions.

7.1 Review of flame response studies

Several state-of-the-art experiments investigating flame-acoustic interactions under LPRE-like conditions were identified in Sections 3.4.2 and 4.1. A shared feature of these systems is optical access to the combustion chamber to allow the application of optical imaging techniques to capture the response of the flames to the acoustic field. Significant findings from notable previous experiments are reviewed here before results from BKH are presented.

The MIC has a rectangular cross-section and uses modulation of the flow through an additional exhaust nozzle to excite the first transverse (1T) mode of the combustion chamber (Section 4.1.3). Richecoeur (2006) has conducted MIC testing with LOx/CH_4 at pressures up to 60 bar, which reaches into the supercritical fluid regime of oxygen, where most modern rocket engines operate. Investigation at supercritical pressures is important since fluid dynamic properties dramatically change and traditional models of flame-acoustic interaction may no longer apply. The MIC has either three or five injection elements arranged in a row allowing the interaction of neighbouring flames to be observed. The interaction is observed to increase during 1T mode excitation, as high-speed OH* imaging shows the flames spreading and turbulent mixing increasing. Photomultipliers showed emission intensity fluctuations from the flame in phase with the acoustic pressure (Richecoeur et al. 2008). Reported operation of the MIC with LOx/H_2 propellants by Rey et al. (2003) extends only to 9 bar and the very rich *ROF* value of 2. Excitation amplitudes were not great enough to illicit a significant response from the flame. The VHAM is a modified version of the MIC where twin

main nozzles are modulated in place of a secondary nozzle and promises high excitation amplitudes, however only results of cold flow tests by Méry et al.(2008) have been published to date.

The CRC is a flat, cylindrical combustor which also uses nozzle modulation to excite the first transverse mode of the combustion chamber (Section 4.1.2). Knapp et al. (2007) and Oschwald and Knapp (2009) applied high-speed imaging of the entire, 200-mm diameter combustion chamber volume to record LOx/H_2 flame response to 1T mode excitation. The distribution of OH* intensity fluctuation reflected the acoustic pressure distribution, with high amplitude emission intensity fluctuations at locations corresponding to the acoustic pressure antinodes. They also observed emission fluctuation in these locations to be in phase with acoustic pressure. Although Knapp and colleagues admit their results lack a level of fidelity required to draw definitive conclusions, the spatially and temporally resolved combustion response suggested that combustion couples with acoustic pressure. A similar investigation by Sliphorst (2011) with a LOx/CH_4 flame in the CRC led to the contradictory conclusion that velocity coupling was responsible for the emission fluctuations near the pressure antinodes. Relocating the modulated secondary nozzle to achieve quasi-longitudinal acoustic excitation, with a pressure antinode at the injector location, did not produce compelling results to suggest otherwise.

A rectangular combustor with multiple, linearly-arranged shear coaxial injectors running LOx/CH_4 and with multiple exhaust nozzles was run by Marshall (2006a) at Pennsylvania State University (Section 4.1.4). The combustor has no means of forced excitation, rather various combinations of active injectors and nozzles were tested to search for a naturally unstable configuration. Marshall et al.(2006b) reported that the greatest amplitudes of transverse mode pressure oscillations were achieved when the injection elements located in the pressure antinodes of the mode were active, suggesting that heat release fluctuations are coupled with acoustic pressure.

At Purdue University, a two-dimensional (rectangular) combustor is driven to high amplitude 1T mode instabilities by gas-centred swirl coaxial (GCSC) elements deliberately tuned to an unstable frequency (Section 4.1.5). Whichever type of ‘study element’ is then located in the centre of the injector face, where transverse acoustic velocity is greatest, can be studied optically through windows. Pomeroy et al. (2011) studied the unstable ‘driving elements’ themselves, having placed another GCSC element in the study-element location. High-speed backlit shadowgraph and CH* emission imagery were recorded simultaneously to study combustion emission distribution and phase. Emission fluctuation was greatest at the outer ‘lobes’ of the flame. Its distribution and phase suggested this was the result of transverse gas motion deflecting the inner gas stream into the outer kerosene spray.

BKH has been developed to address a lack of similar data for externally forced LOx/H_2 coaxial injection at representative LPRE conditions. High-speed imaging as well as photomultiplier recordings of OH* emission have been collected during periods of forced velocity and pressure fluctuations. The image sequences collected during testing have subsequently been processed in order to extract information about the distribution and phase of fluctuation of the OH* emission in response to the acoustic fluctuation. This chapter presents a comparison of the response of the flame to velocity and pressure fluctuations for both subcritical and supercritical operating pressure. Operation with cryogenic, ‘liquid’ hydrogen (LH_2), in addition to ambient temperature, gaseous hydrogen (GH_2) further addresses operating conditions not previously attempted with forced acoustic excitation.

7.2 Flame structure

In this chapter, imaging results are examined from tests with 40 bar or 60 bar chamber pressure, using either ambient temperature, gaseous hydrogen (GH_2) or cryogenic, 'liquid' hydrogen (LH_2), and with ROF = 6. Injection parameters corresponding to each operating condition are summarised in Table 8. Results from two different tests for both the 40 bar, LH_2 operating condition and the 60 bar, GH_2 condition are examined. These tests are distinguished by the designation case A or case B. The structure of the natural and excited states of the flame is qualitatively described first, to serve as a basis for later discussion of temporal flame response. An instantaneous OH* emission image and the corresponding shadowgraph image for off-resonance conditions in the 60 bar test with GH_2, case B, is shown in Figure 7.1. Off-resonance excitation amplitudes are very low. Where the natural, unfiltered noise in the combustor without excitation is around 0.8 to 0.3% of P_{cc}, off-resonance excitation increases this to around 1.2 to 1.4%. Image samples from off-resonance conditions are therefore taken to show the natural, undisturbed state of the flame. The instantaneous OH* image in Figure 7.1a, shown in false colour, is taken to represent the reaction zone of the flames, where species concentration of OH* is greatest. In this line-of-sight image, three distinct flames are recognisable at the injection plane and originate from the central element and the upper and lower elements nearest the camera. The flames are fully attached at the injector exit, although they may appear lifted. In the first 10 to 20 mm following injection, OH* emission can be seen originating from the shear layer between the coaxial LOx and H_2 streams. The low level of emission intensity here is the result of adjusting the sensitivity range of the camera intensifier to the luminosity levels of the expanded flame downstream. At a distance around 10 to 20 mm downstream of injection the flames expand dramatically. The flames from the five elements overlap due to their realistically tight spacing, making it difficult to distinguish them from one another. This gives the appearance of a well mixed, turbulent combustion distribution. In the shadowgraph image in Figure 7.1b, the dense oxygen jets of the same three elements are visible. The filter was not able to fully block near-infrared emission, so the surface of the LOx jets appears in a light shade of gray. The core of the central injection element extends to a length approximately the same as the window (100 mm), while those of the outer elements deflect somewhat into the spaces above and below the injection array. Shadowgraph images and behaviour of the LOx core will be examined in greater detail in Chapter 8.

Table 8: Injection parameters for studies of flame response.

Test designation			40 bar GH_2	40 bar LH_2 A	40 bar LH_2 B	60 bar GH_2 A	60 bar GH_2 B	60 bar LH_2
Chamber pressure	P_{cc}	(bar)	40.7	43.5	42.5	60.4	59.9	60.2
Mixture ratio	ROF		6.4	6.0	6.0	6.0	6.0	6.0
Fuel injection temperature	T_H	(K)	280	75	50	288	286	62
Oxygen injection temperature	T_O	(K)	130	132	126	123	125	126
Per-element mass flow rate	$\dot{m}$	(g/s)	84	112	234	132	132	140
Injection velocity ratio	VR		44.6	10.7	6.0	35.2	35.2	6.3
Momentum flux ratio	J		7.4	1.9	1.1	6.2	6.3	1.1

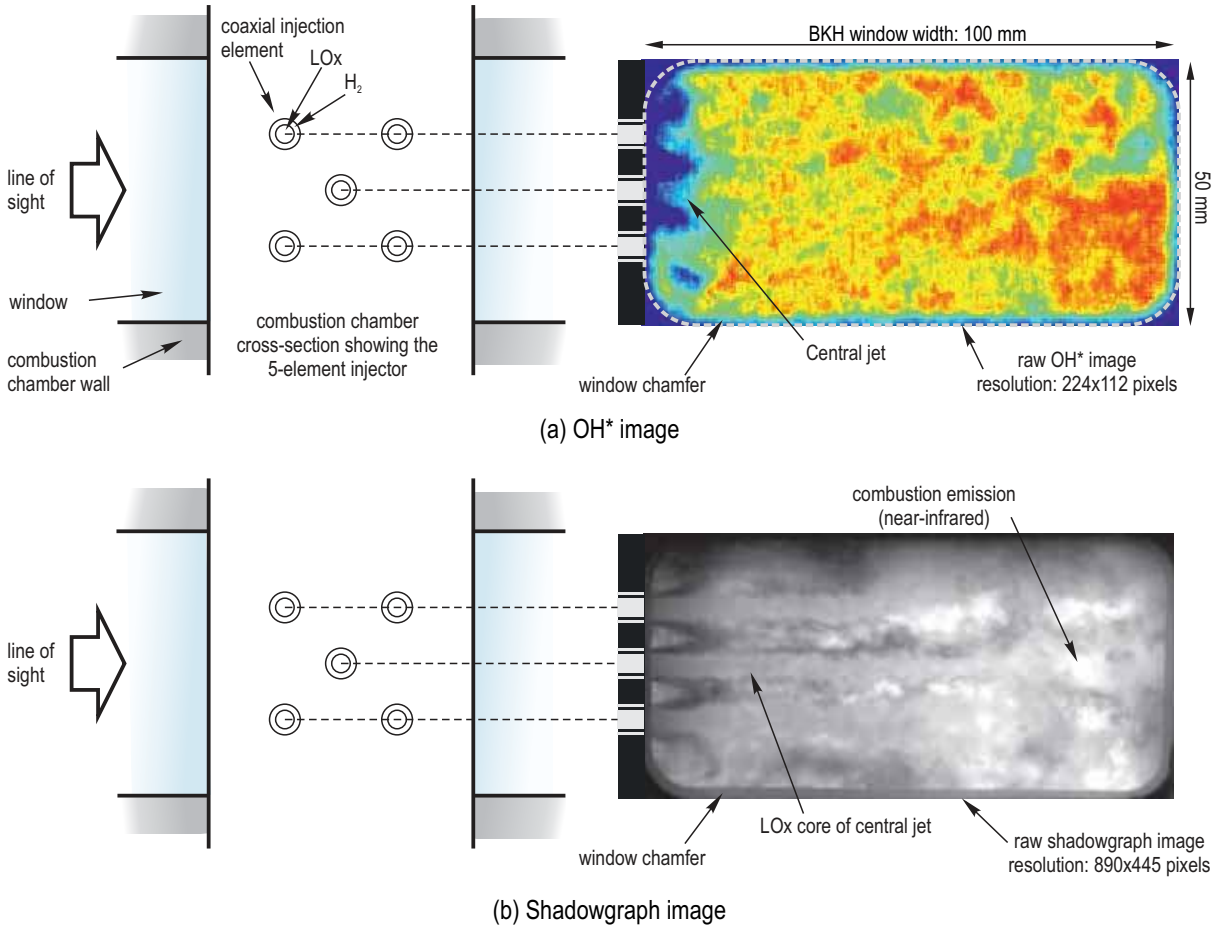

Figure 7.1: Instantaneous OH* emission image, shown in false-colour (a), and corresponding shadowgraph image (b), during off-resonance conditions.

The instantaneous OH* image in Figure 7.1a is typical of those from off-resonance conditions. Unprocessed, instantaneous OH* images such as this are, however, difficult to interpret. This is because they are integrated line-of-sight readings through multiple flames which are highly turbulent and overlapping due to the closely packed injector arrangement. A time averaged OH* image from a 5-ms duration sample, and its shadowgraph counterpart, are presented for ease of interpretation in Figure 7.2. Flame structure is identifiable. The centre lines of the two upper and lower flames nearest the camera can be traced as the flames develop downstream. These centrelines have been indicated by dashed lines in Figure 7.2b. The approximate extremities of the flames have also been indicated. Regions of high intensity either side of the centre lines is the result of the integrated line-of-sight through the thickest part of the flames. The central flame becomes obscured by the two nearest flames approximately 25 mm downstream of injection. There is some deflection of the outer flames into the dead spaces above and below the five-element injector. Apparent too, is some asymmetry in the intensity distribution in the upper part of the image, which is explained by the fraction of mean chamber flow (approximately 10%) exiting through the secondary nozzle in the upper wall of the combustion chamber, resulting in slightly greater upwards deflection of the upper flames as compared to the downwards deflection of the lower flames. A further example is given in Figure 7.3, which compares samples from cases A and B of the 40 bar test with LH_2. Case B (Figure 7.3b) has a greater injection mass flow rate than case A (Figure 7.3a), and the centrelines of the outer flames do not deflect as sharply as in case A. Although there is no accompanying shadowgraph image to confirm, this lesser deflection is assumed to

be due to the greater inertia of the jets in case B. In both cases, there is also a pronounced centralised region of high intensity from approximately 50 mm downstream. This represents the region where the two nearest flames overlap.

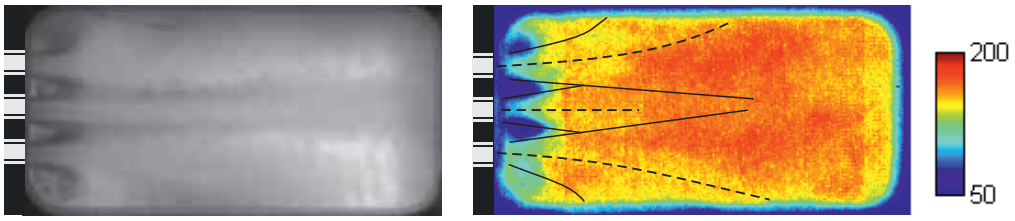

(a) Shadowgraph (b) OH* emission

Figure 7.2: Time-averaged shadowgraph (a) and OH* emission (b) images during off-resonance conditions in a 60 bar test with GH_2.

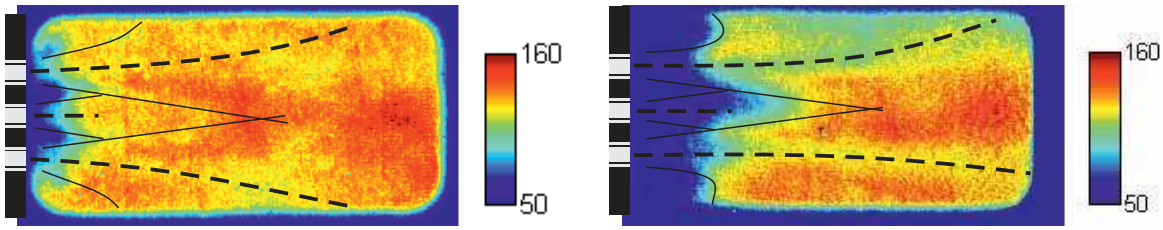

(a) 40 bar, LH_2 test A (b) 40 bar, LH_2 test B

Figure 7.3: Time-averaged OH* emission images during off-resonance conditions in 40 bar, LH_2 test A (a), and in 40 bar, LH_2 test B (b).

Time-averaged OH* and shadowgraph images from a period of 1T mode excitation are presented in Figure 7.4. The averaging time period of 5 ms equates to around 20 cycles of the 1T mode. The measured acoustic pressure amplitude was $p' = 4.45 \pm 0.04$ bar, or $p'/P_{cc} = 7.4\%$. In the shadowgraph image in Figure 7.4a the length of the LOx jets is greatly reduced compared to their natural state, now only extending approximately one quarter the length of the window. The axial extent of the flame in Figure 7.4b is diminished accordingly. The flame is no longer well distributed through the entire window as the LOx core travels downstream; rather there are compact regions of high emission intensity as all combustion is taking place in a space approximately half the length of the window (50 mm). A threshold-detected outline of the flame is superimposed on the shadowgraph image for reference.

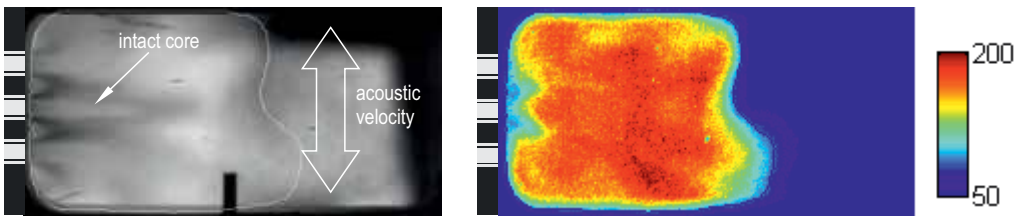

(a) Shadowgraph (b) OH* emission

Figure 7.4: Time-averaged shadowgraph (a) and OH* emission (b) images during 1T mode excitation with p'/P_{cc} = 7.4%.

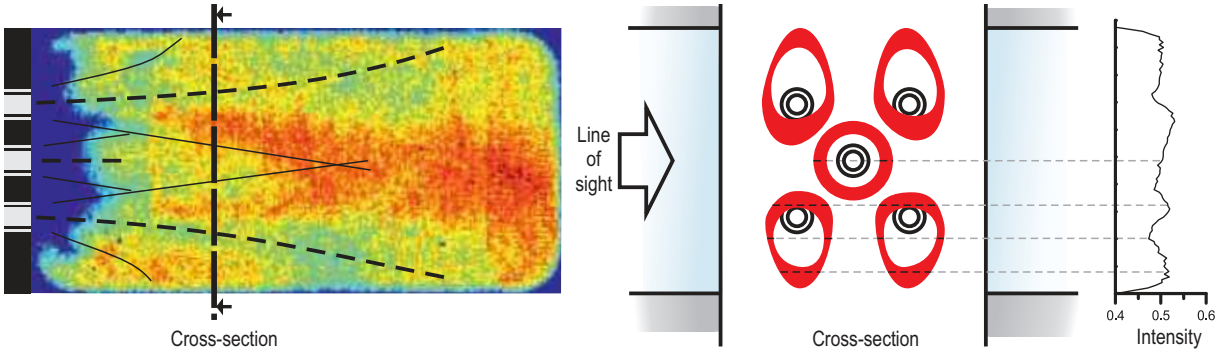

(a) Off-resonance, p'/Pcc = 1.2%.

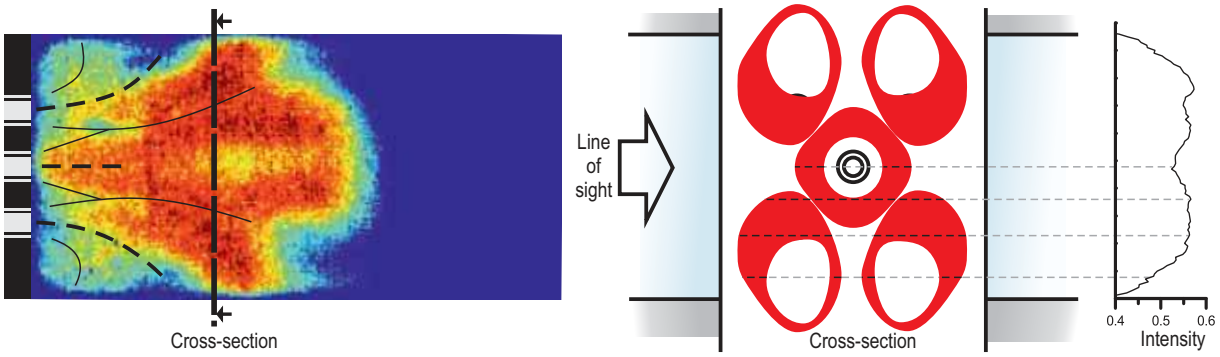

(b) 1T mode resonance, p'/Pcc = 8.0%.

Figure 7.5: Projected cross-section of the flames from the 40 bar test with LH_2, case A.

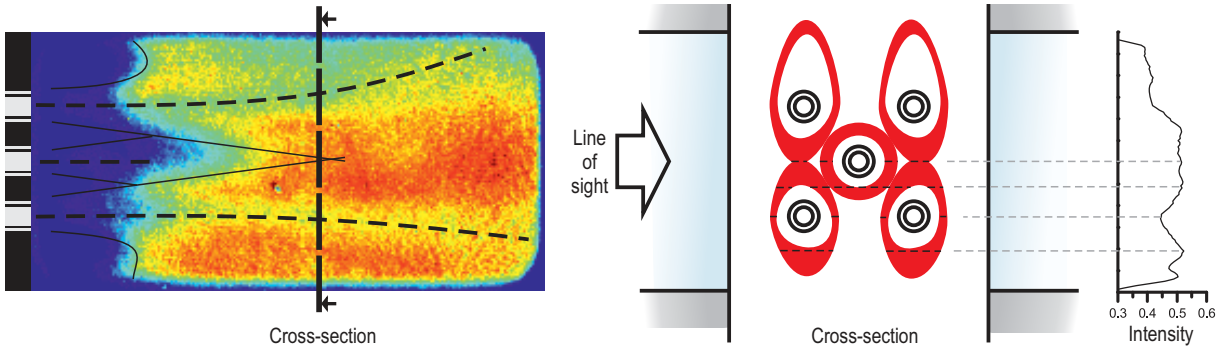

(a) Off-resonance, p'/P_{cc} = 0.7%

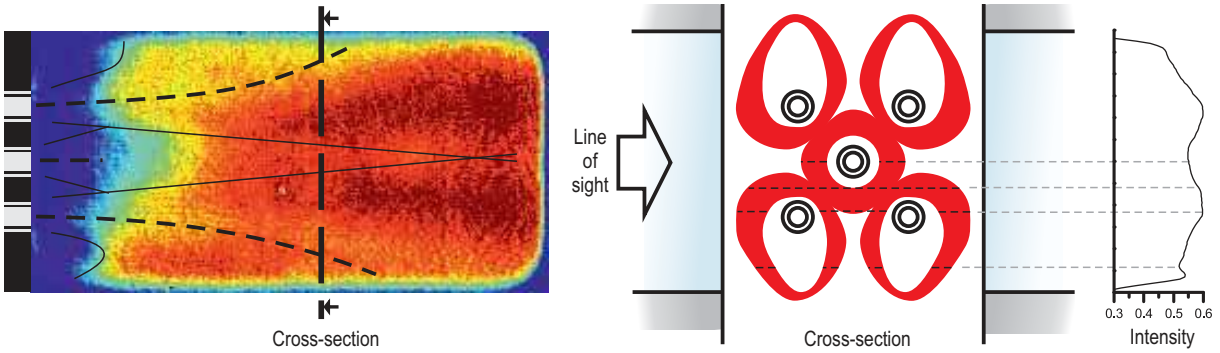

(b) 1T-mode resonance, p'/P_{cc} = 6.0%

Figure 7.6: Projected cross-section of the flames from the 40 bar test with LH_2, case B.

The time-averaged images from off-resonance and 1T-mode excitation are discussed further with reference to Figure 7.5 and Figure 7.6, which are for the 40 bar tests with LH_2, cases A and B, respectively. A vertical intensity distribution was extracted from the time-averaged OH* images at an axial distance of 30 mm downstream of injection for case A, and 55 mm downstream for case B. These locations are labelled 'cross-section' in the corresponding figures. It is noted again that the OH* images are integrated line-of-sight measurements through the entire thickness of the flame. With this in mind, the one-dimensional intensity distributions were used to construct two-dimensional, cross-sectional views of the flames, shown on the right side of Figure 7.5 and Figure 7.6. During off-resonance conditions for case A in Figure 7.5a, the cross-section illustrates how the upper and lower flames are stretched vertically somewhat owing to the deflecting paths of their parent LOx jets. The central jet does not deflect and so the central flame is expected to be more-or-less axisymmetric in cross-section. Under 1T-mode excitation in Figure 7.5b, all the flames have moved back towards the faceplate. The expansion angle of the flames has increased, resulting in greater thickness of the flames at the same cross-sectional location. The greater thickness accounts for the global increase in integrated emission intensity at this location. Spreading of the central flame forces the outer flames to deflect further into the spaces above and below the injection array. For case B in Figure 7.6, the greater inertia of the injected jets results in greater resistance to the 1T mode transverse acoustic velocity. It should also be noted that the acoustic pressure amplitude was not as high as in case A. For these two reasons far lesser retraction of the flames towards the injection plane is seen in Figure 7.6b. Compared to the off-resonance condition, the centralised region of high intensity has increased in both size and intensity and split into more or less symmetrical upper and lower halves. The split results from the increased deflection of the outer flames, meaning they no longer meet and overlap at the position of the cross-section, as they do in Figure 7.6a. Rey et al. (2004) and Richecoeur (2006) have also observed an increase in the flame expansion angle in the MIC during 1T mode excitation (Section 3.4.2). The expansion resulted in the linearly arranged flames spreading sufficiently to overlap with neighbouring flames. In BKH, the spacing between the injectors is smaller (9.2 mm compared to 17 mm for the MIC), so the influence of neighbouring flames on each other is more pronounced.

7.3 Flame displacement

Excitation of the 1T mode results in oscillating acoustic gas velocity transverse to the direction of injection. The expected amplitude of acoustic particle velocity u' can be calculated using the equation

$$\frac{u'}{c} = \frac{1}{\gamma}\frac{p'}{p} \quad . \tag{21}$$

For mean pressure p the combustion chamber pressure P_{cc} is used. For illustrative purposes the relative acoustic amplitude of $p'/P_{cc} = 9\%$ is considered here. For a 60 bar test with GH_2, and assuming homogeneous, equilibrium gas properties throughout the combustion chamber, estimates of $c = 1731$ m/s (speed of sound) and $\gamma = 1.38$ (ratio of specific heats) are obtained using the well-known chemical equilibrium analysis (CEA2) software by Gordon and McBride (1994). These properties result in an acoustic particle velocity amplitude of $u' = 113$ m/s. Thus, during 1T-mode excitation, the coaxial jets are subjected to oscillating transverse gas motion with velocity on the order of the H_2 injection velocity.

Sequential frames from high-speed OH* imaging were analysed to determine any motion of the flames in response to the acoustic velocity. As described in the previous section, the length of the flame is reduced during 1T mode excitation and its axial extremities become visible within the extent of the optical window. A semi-automated process was developed to measure transverse displacement of the flame, taking advantage of the boundaries visible in the window. First, short image sequences were sampled from periods of high acoustic pressure amplitude. The samples were then converted from 8-bit (256-level greyscale) OH* images to binary (black-and-white) images using an adaptive threshold routine. The adaptive threshold compensates for fluctuations in global intensity of the image, ensuring consistent representation of the boundaries of the flame. A point on the visible boundary of the flame in the binary image was selected manually. Finally, the vertical coordinate of the selected point is recorded for each image in the sequence. Figure 7.7 shows some example frames from one of the image sequences sampled. Both the raw OH* image and its binary counterpart are shown.

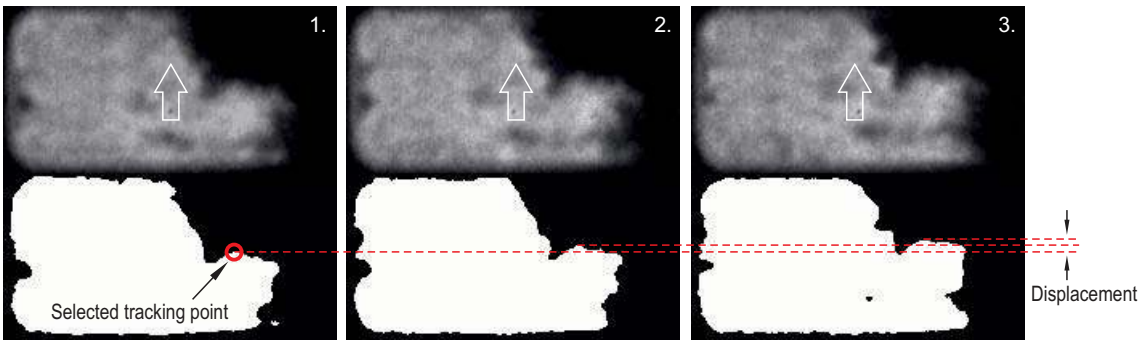

Figure 7.7: Example sequence of images used to measure transverse (i.e. vertical) displacement of the flame during 1T-mode excitation. The raw OH* image (upper row) and its converted binary counterpart (lower row) are shown.

The signals from the tracking points in the samples processed are taken to be a measurement of the bulk displacement of the flame. Flame displacement was compared to estimated transverse acoustic particle displacement, δ', which is calculated using

$$\delta' = \frac{u'}{\omega}\cos(\omega t) \ , \tag{22}$$

where u' is estimated using Equation 21. Samples of OH* image sequences were collected from tests at each BKH operating condition. Samples consisted of 24 frames, or 1-ms duration, from periods of maximum 1T mode excitation amplitude. The flame displacement measurements are overlayed on the corresponding acoustic particle displacement signals for comparison in Figure 7.8. Turbulence in the flame is reflected in the vertical displacement measurements, which do not oscillate evenly around a fixed axis. Despite the turbulence, the signals are in good agreement. Amplitude of flame displacement is comparable to acoustic particle displacement. Flame displacement appears to lag acoustic displacement slightly, although the phase relationship is somewhat inconsistent, possibly owing to flame turbulence. During 1T mode excitation, the flame moves more or less in unison with the transverse acoustic gas motion.

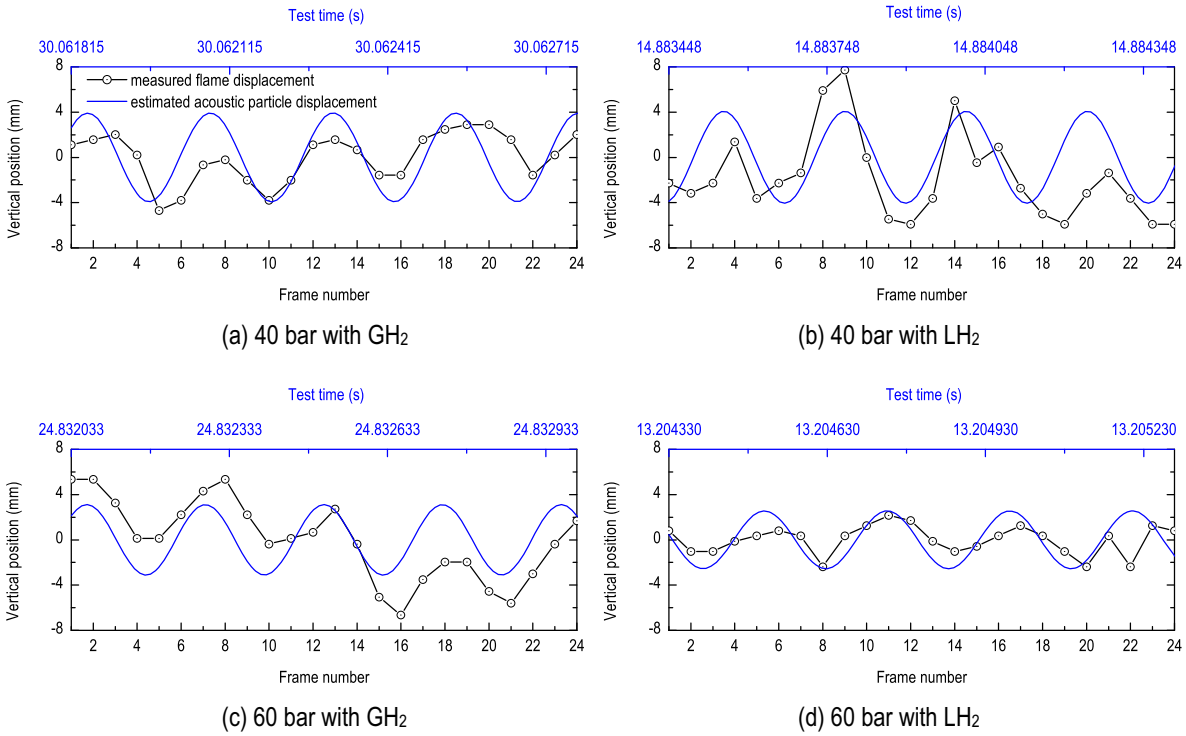

Figure 7.8: Comparison of transverse flame displacement measurements and acoustic particle displacement signals.

7.4 Dynamic OH* emission response

The temporal fluctuation of measured OH* emission intensity was investigated to determine if the heat release rate of the flame is affected by acoustic field interaction. An overall mean value of intensity from the entire image for each frame was used to produce OH* emission intensity spectrograms. The first example shown here, in Figure 7.9, is from an early test at the 40 bar, LH_2 condition B with an uncontrolled excitation ramp. For this test the camera frame-rate was 12,500 fps and it recorded the entire 10-s duration of the test. The spectrum is dominated by several sharp lines whose frequencies change little with time. These peaks have been identified as artefacts resulting from cycle frequencies in the camera electronics; the main frequency being at 2700 Hz, the first overtone at 5400 Hz, and several aliases of further overtones. The main artefact frequency fluctuates slightly depending on mean image intensity. This fluctuation is also seen in the frequencies of the artefact overtones. Despite the camera artefacts, the progression of the ramped excitation frequency can be traced over the course of the test, from 2750 Hz at $t = +4.7$ s, when the excitation frequency passes through the 1L mode, to above 6250 Hz at $t = +10$ s. This compares directly to the excitation frequency signal in the acoustic pressure spectrogram in Figure 6.16 (Section 6.5). Also visible is the alias of the first overtone of the excitation frequency, mirrored around the Nyquist frequency for the high-speed OH* images of 6250 Hz. The progression of the overtone appears to be ramping downwards from 6250 Hz at $t = +4.4$ s to 0 Hz at $t = +8.3$ s, when in reality it has exactly double the excitation frequency.

That the progression of the excitation frequency can be traced in the OH* emission intensity, even during off-resonance periods, shows that the OH* emission intensity responds to acoustic pressure fluctuations. The intensity is strong as excitation passes through the 1L mode around 3100 Hz, then drops off noticeably as excitation passes through the 1T mode at

4000 Hz, despite the comparatively high acoustic pressure amplitudes measured for the 1T mode. It should be noted that the 1L mode has high acoustic pressure levels in the injector region, whereas the 1T mode has low acoustic pressure levels and high acoustic velocity in the injector region. It should also be noted that during the same period as 1T mode excitation from $t = +5.2$ to $+5.4$ s the intensity at the frequency of the first excitation overtone increases, as seen in the alias signal around 4500 Hz. This can be explained by noting that the first overtone of the 1T mode takes on the form of the 2T mode in the rectangular combustion chamber. The 2T mode has an acoustic pressure antinode at the location of the window, as does the 1L mode, and so the high intensity indicates a response to acoustic pressure at double the excitation frequency. All these features indicate response of the flame to acoustic pressure fluctuations.

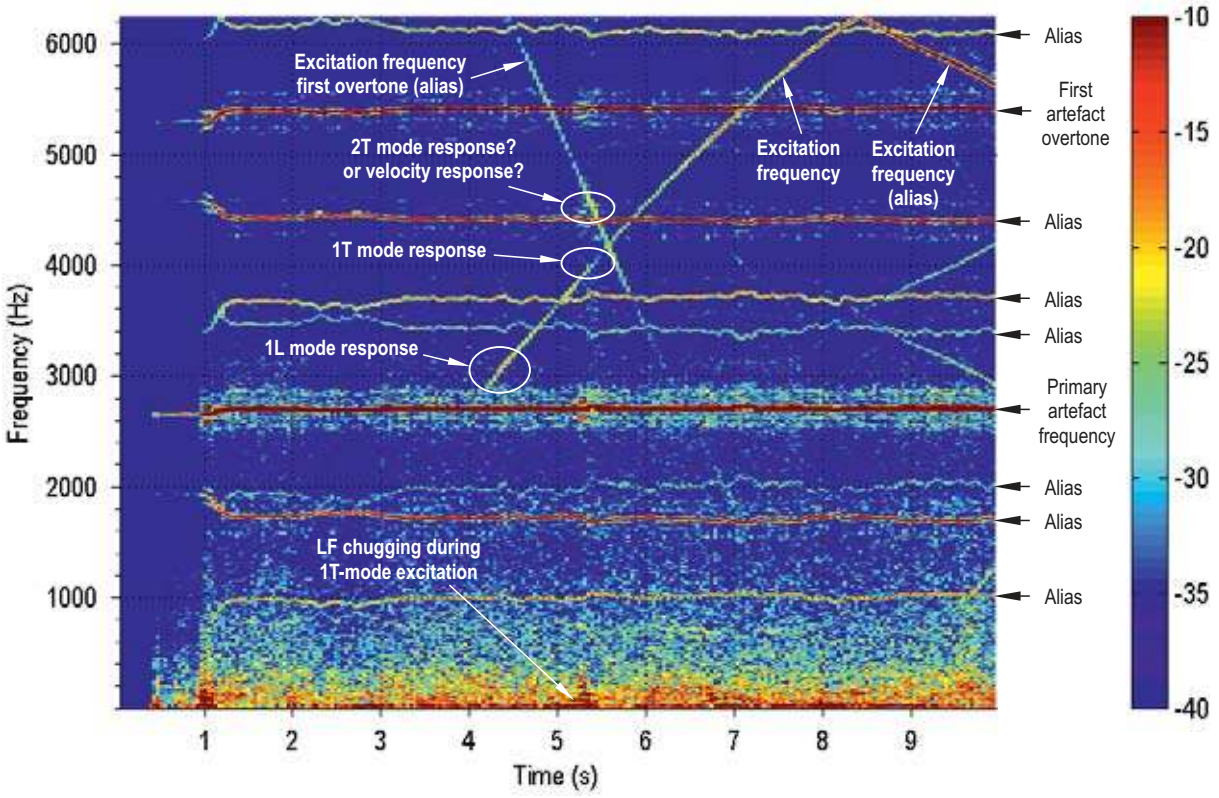

Figure 7.9: Spectrogram of mean OH* emission from high-speed imaging at 40 bar with LH_2, case B.

Further examples are presented here from later tests with recording rates of 24,000 fps. The higher frame rate resulted in shorter recording durations of around 4 s long. Spectrograms of high-speed camera recordings during ramped excitation of the 1T mode from 40 bar and 60 bar tests with GH_2 are shown in Figure 7.10 and Figure 7.11 respectively. The mean OH* signal, displayed below the spectrogram, is seen to decrease in global intensity during 1T mode excitation. This is due to the retraction of the flame towards the injector, as discussed in the preceding section, which lowers the mean intensity value for the whole image. Note that the artefact frequency and its overtones differ between 40 bar and 60 bar tests due to different camera settings required. A regrettable consequence is that the excitation frequency is obscured by the first artefact overtone in the 60 bar case, rendering further analysis of spectral content impossible for tests at 60 bar.

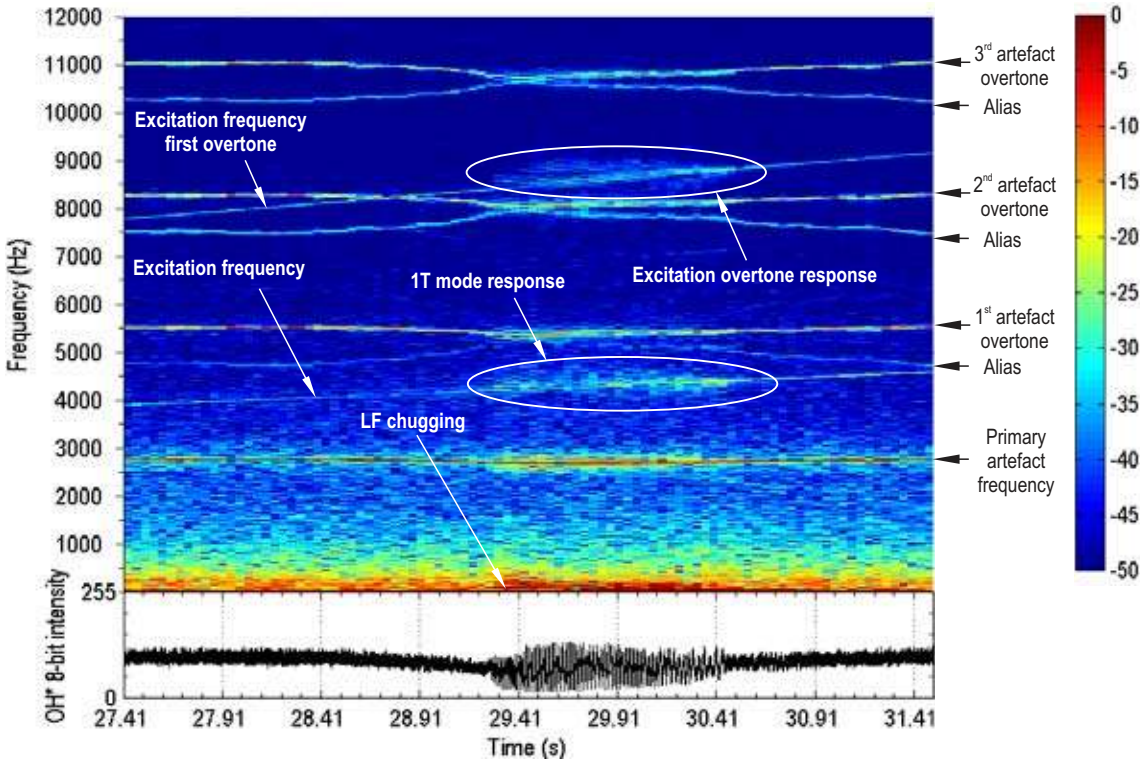

Figure 7.10: Spectrogram of mean OH* emission from high-speed imaging at 40 bar with GH_2.

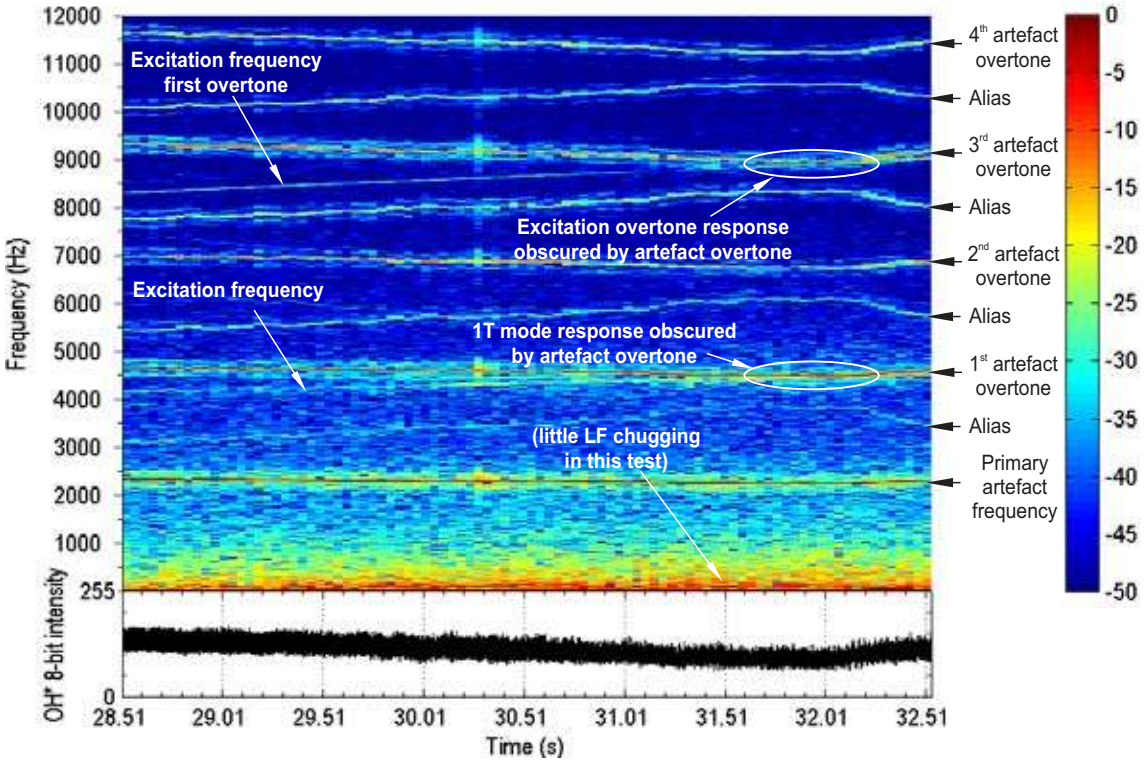

Figure 7.11: Spectrogram of mean OH* emission from high-speed imaging at 60 bar with GH_2.

Signals from the photomultipliers (PMs) recording OH* emission do not suffer from such artefacts, and do not have a limited recording duration. Spectrograms of PM signals over the course of entire 40 bar and 60 bar tests with GH_2 are shown in Figure 7.12 and Figure 7.13, respectively. The ramped excitation signal and its overtones are also clearly visible in the PM spectra. Stronger responses at the 1L, 1T and 1L1T modes are also evident. Flame retraction during transverse mode excitation precludes quantitative analysis of PM signals at these times because it is unknown when the flame is present in the field of view of each PM unit. A signal is continuously present at the 1L mode frequency in both recordings, except during transverse mode excitation. This signal is presumed to be emission response to the natural presence of the 1L mode in the combustion chamber acoustic spectrum.

The phase of the PM signals during 1L mode resonance compared to acoustic pressure was investigated. PM and dynamic pressure signal samples of 100-ms duration during peak 1L resonance were collected from all BKH test conditions, and their relative phase systematically evaluated. The PM and dynamic pressure signals (from sensor *PCCdyn2*) were first band-pass filtered with a band-width of 100 Hz around the 1L excitation frequency. A cross-correlation routine was then implemented to compare the phase of the filtered signals. With a margin of uncertainty of ±10 μs (approximately 11.8 degrees at the 1L mode frequency), a zero phase shift was measured. The PM recordings therefore indicate direct response of OH* emission to acoustic pressure.

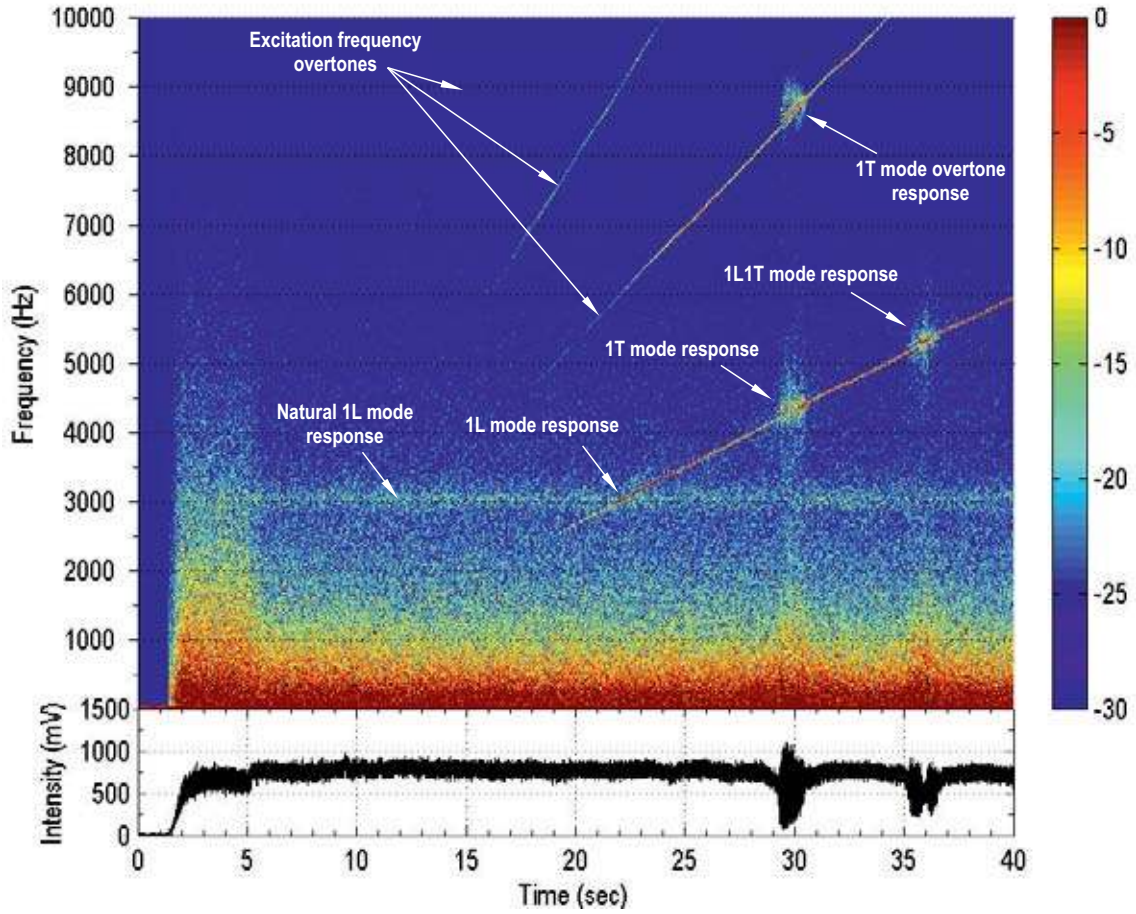

Figure 7.12: Spectrogram of photomultiplier signal at 40 bar with GH_2.

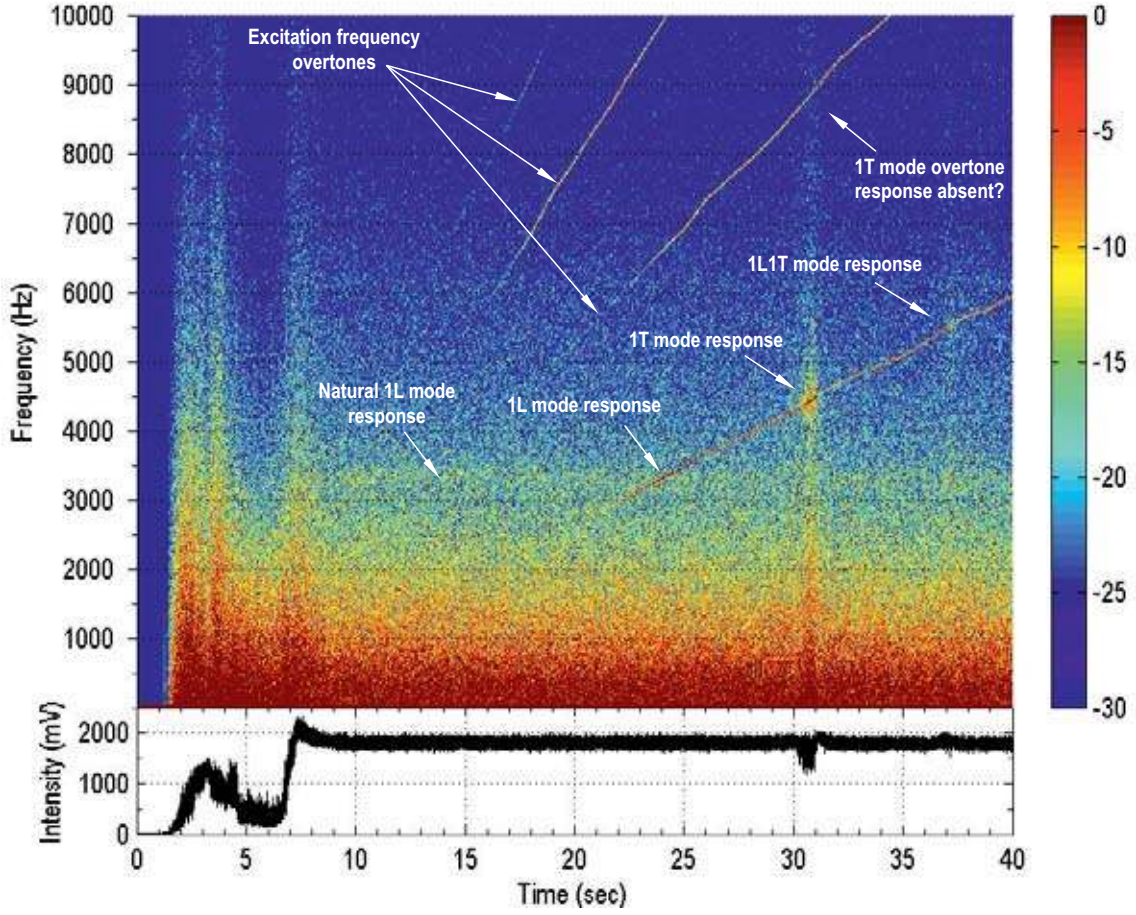

Figure 7.13: Spectrogram of photomultiplier signal at 60 bar with GH_2.

7.5 Dynamic response to transverse excitation

High-speed OH* images were analysed further in order to study the temporal and spatial flame response with respect to the acoustic field. Sequences of high-speed OH* images were extracted from periods of 1T mode excitation where the response signal is sufficiently clear of any camera artefacts frequencies. The emission intensity signal at each pixel location $I'(x,y)$ was band-pass filtered to the corresponding excitation frequency in order to extract flame emission fluctuations in response to the acoustic field fluctuation. Target samples are extracted from periods of maximum acoustic pressure amplitude. The samples, which are four acoustic cycles in duration (approximately 1 ms), are used to calculate Rayleigh index distributions for acoustic pressure and velocity, $R_p(x,y)$ and $R_u(x,y)$, respectively. The Rayleigh index is so named because it is an expression of the well-known Rayleigh criterion (Section 2.6.3) for positive reinforcement of acoustic pressure waves, given in Expression (4). The Rayleigh criterion is reformulated here to reflect the need to consider the condition throughout the volume of an LPRE combustion chamber:

$$\iint_{V,t} p'\,\dot{q}'\,dtdV > 0\ . \tag{23}$$

In the definition of the Rayleigh index used for the following analysis, relative OH* emission intensity $I'/\bar{I}$ is substituted as an indicator of heat release rate, $\dot{q}'$. Therefore the index

highlights general in-phase behaviour of emission intensity and acoustic pressure or velocity. The pressure based Rayleigh index is calculated using

$$R_p(x,y) = \frac{p'(x,y)}{P_{cc}} \frac{I'(x,y)}{\bar{I}(x,y)} \ , \tag{24}$$

where $p'(x,y)$ is the acoustic pressure distribution. The distribution $p'(x,y)$ is reconstructed by numerically calculating a two-dimensional resonance mode distribution and scaling the solution to the signal from the dynamic pressure sensor *PCCdyn2*. An example of the reconstructed acoustic pressure distribution for the 1T mode is given on the left side of Figure 7.14. Note that the pressure nodal line is slightly offset from the chamber centreline owing to the secondary nozzle in the upper wall. The region of $p'(x,y)$ corresponding to the area of the optical window is then extracted and normalised with the combustion chamber pressure P_{cc}. The band-pass filtered intensity fluctuation $I'(x,y)$ is normalised using the corresponding local time-averaged intensity value for the sample duration, $\bar{I}(x,y)$. The velocity based index is calculated using

$$R_u(x,y) = \frac{u'(x,y)}{c} \frac{I'(x,y)}{\bar{I}(x,y)} \ , \tag{25}$$

where the acoustic velocity distribution $u'(x,y)$ is derived from the pressure field using

$$u'(x,y) = -\frac{1}{\rho\omega} \nabla p_o(x,y) \frac{\partial p'}{\partial t} \ , \tag{26}$$

and is normalised using the bulk mean sound speed for the combustion chamber volume, c. An example of the reconstructed acoustic velocity distribution is given on the right side of Figure 7.14.

Rayleigh index results for 1T mode excitation in a test at 40 bar with GH_2 are examined in Figure 7.15. Figure 7.15a is the time-averaged image of the raw OH* image sequence sample, $\bar{I}(x,y)$, which is used to normalise $I'(x,y)$. Time-averaged values of the Rayleigh index for each pixel over the course of the image sequence are calculated. Plots of the resulting time-averaged pressure- and velocity-based Rayleigh index distributions are given in Figure 7.15b and Figure 7.15c, respectively. To assist in interpreting the Rayleigh index plots, pixel-by-pixel cross-correlations of the pressure/velocity and OH* emission signals were performed. These are presented in the phase plots in Figure 7.15d and Figure 7.15e, respectively. A cyclic colour-scale was developed to ease interpretation of the phase plots. White represents in-phase behaviour, black anti-phase, orange lagging by one-quarter cycle (90 degrees), and turquoise leading by one-quarter cycle (-90 degrees). The Rayleigh index and phase plots for 1T mode excitation show no cohesive in-phase behaviour for either acoustic pressure or velocity. Furthermore, they bear no resemblance to the structure of the flame in the corresponding time-averaged image from the unprocessed OH* data. The boundary of the flame from Figure 7.15a is overlayed on the Rayleigh index and phase plots to indicate its average structure. Regions of seemingly high response levels correspond to regions where the flame was in fact, on average, absent. Similar behaviour was observed for all test conditions under 1T mode excitation.

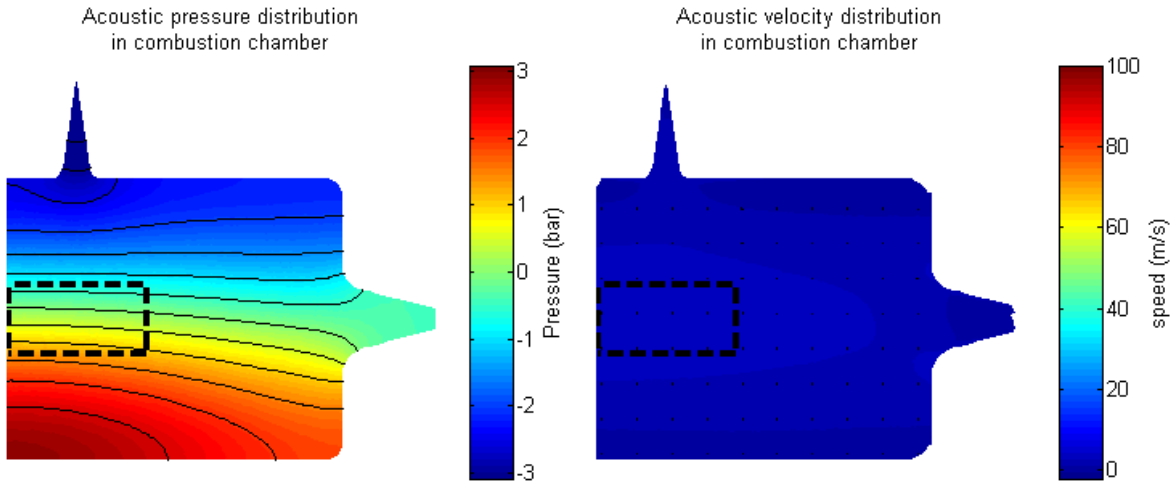

(a) Peak acoustic pressure amplitude

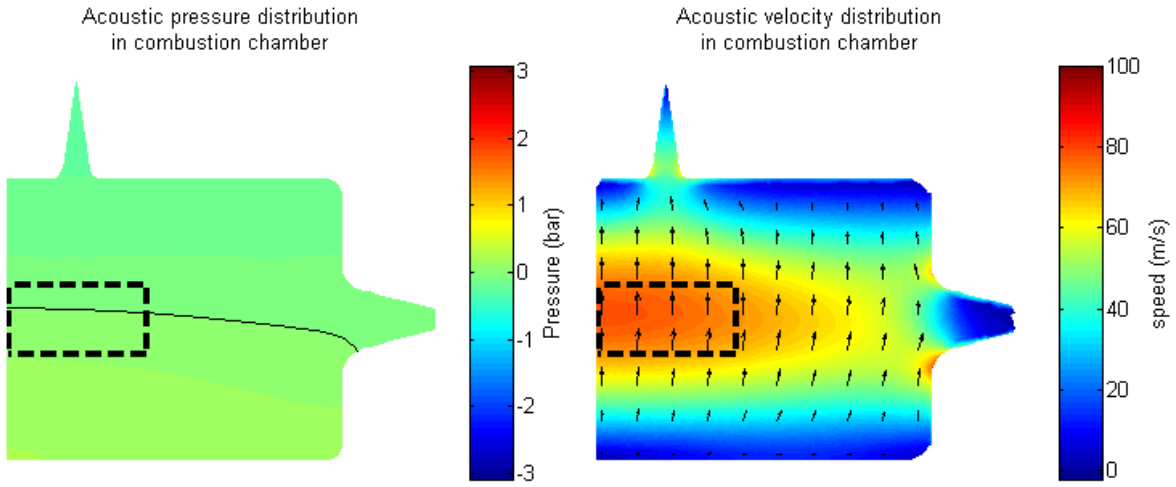

(b) Peak acoustic velocity amplitude

Figure 7.14: Reconstructed acoustic pressure and velocity distributions of the 1T mode used for the calculation of Rayleigh indices; (a) at the point of peak acoustic pressure for PCCdyn2 (a), and one-quarter of a cycle later at the point of peak velocity amplitude (b).

This non-cohesive behaviour can be explained by comparing the band-pass filtered emission distributions to the raw images, as presented in Figure 7.16. Transverse acoustic velocity causes transverse convective displacement of the flame in unison with the acoustic oscillation, as demonstrated previously in Section 7.3 and as can also be seen in the raw OH* images in Figure 7.16. Regions of high signal amplitude in the filtered images in Figure 7.16 correspond to regions with alternating presence and absence of flame. As a flame structure exits a given region in the image, the filtered intensity value in that region becomes negative (blue). Half a cycle later, acoustic velocity forces the flame back in the opposite direction and it re-enters the region, resulting in a strong positive swing in intensity (red). This effect is particularly evident at the edges of the flames, however it is also present within regions of permanent flame presence. Here, flamelet structures moving in and out of a particular region result in the same intensity fluctuation effect, except that the variation in average intensity is lower than at the edge of the flame, and so the intensity fluctuation values are also lower. In all locations, peak amplitude in fluctuating intensity is reached shortly before acoustic pressure peaks, since acoustic velocity also wanes as pressure builds to its maximum and the flame motion ceases

briefly. Thus band-pass filtering can be said to have resolved temporal combustion distribution, or flame location, rather than resolving localised fluctuations in heat release rate within the flame, as was intended.

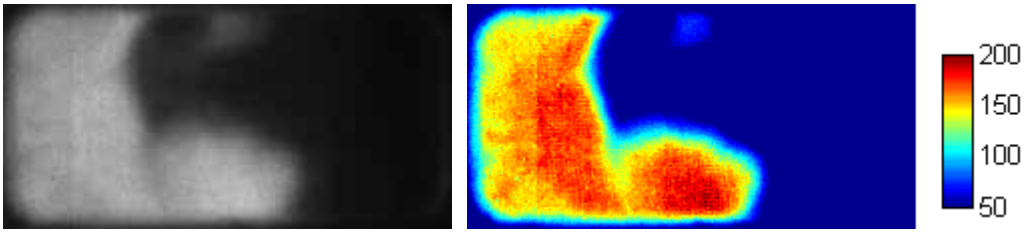

(a) Time-averaged raw OH* image, $\bar{I}(x,y)$

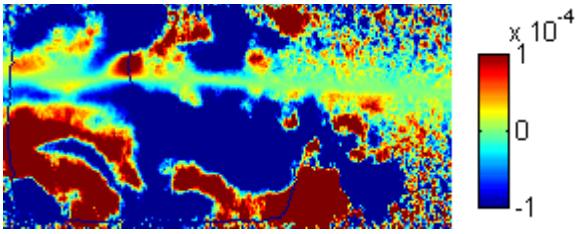

(b) Time-averaged pressure Rayleigh index

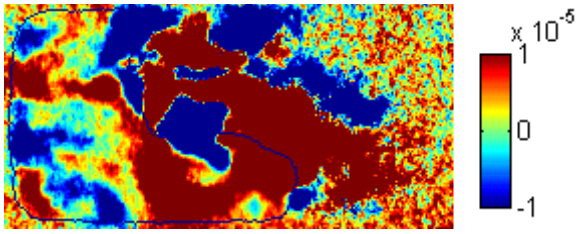

(c) Time-averaged velocity Rayleigh index

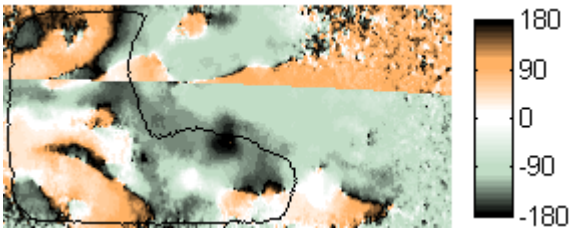

(d) Time-averaged pressure phase

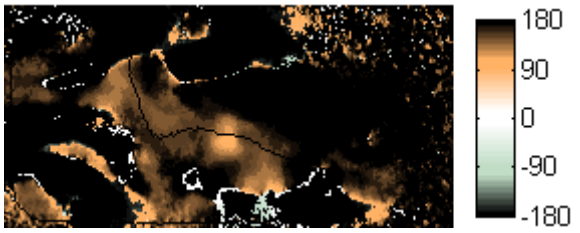

(e) Time-averaged velocity phase

Figure 7.15: Response of the flame to 1T mode resonance comparing time-averaged distributions of the raw OH* images (a), the pressure based Rayleigh index (b), the velocity based Rayleigh index (c), acoustic pressure phase (d), and acoustic velocity phase (e).

Results from similar investigations of transverse mode influence on coaxial injection, for example by Wierman, Nugent and Anderson (2011), Pomeroy et al. (2011), or Sliphorst (2011), suggest that convective transverse motion also prevented isolated extraction of combustion intensity response in those cases. Maximum response amplitudes were usually observed in the outer lobe regions of single flames, where the transverse motion caused alternating presence and absence of combustion. It also explains the phase behaviour where filtered response values lag velocity somewhat, peaking shortly before maximum pressure. This is also consistent with the observations of flame displacement herein.

Further processing of high-speed imaging may be called for if emission intensity fluctuation is to be resolved. Compensating for convective motion during transverse mode excitation may allow local fluctuations in heat-release in response to either acoustic pressure or velocity to be resolved. Wierman, Nugent and Anderson (2011), for example, have suggested using motion tracking to measure intensity perturbation of individual regions within the image. Application of such techniques has not been addressed within the scope of the current work.

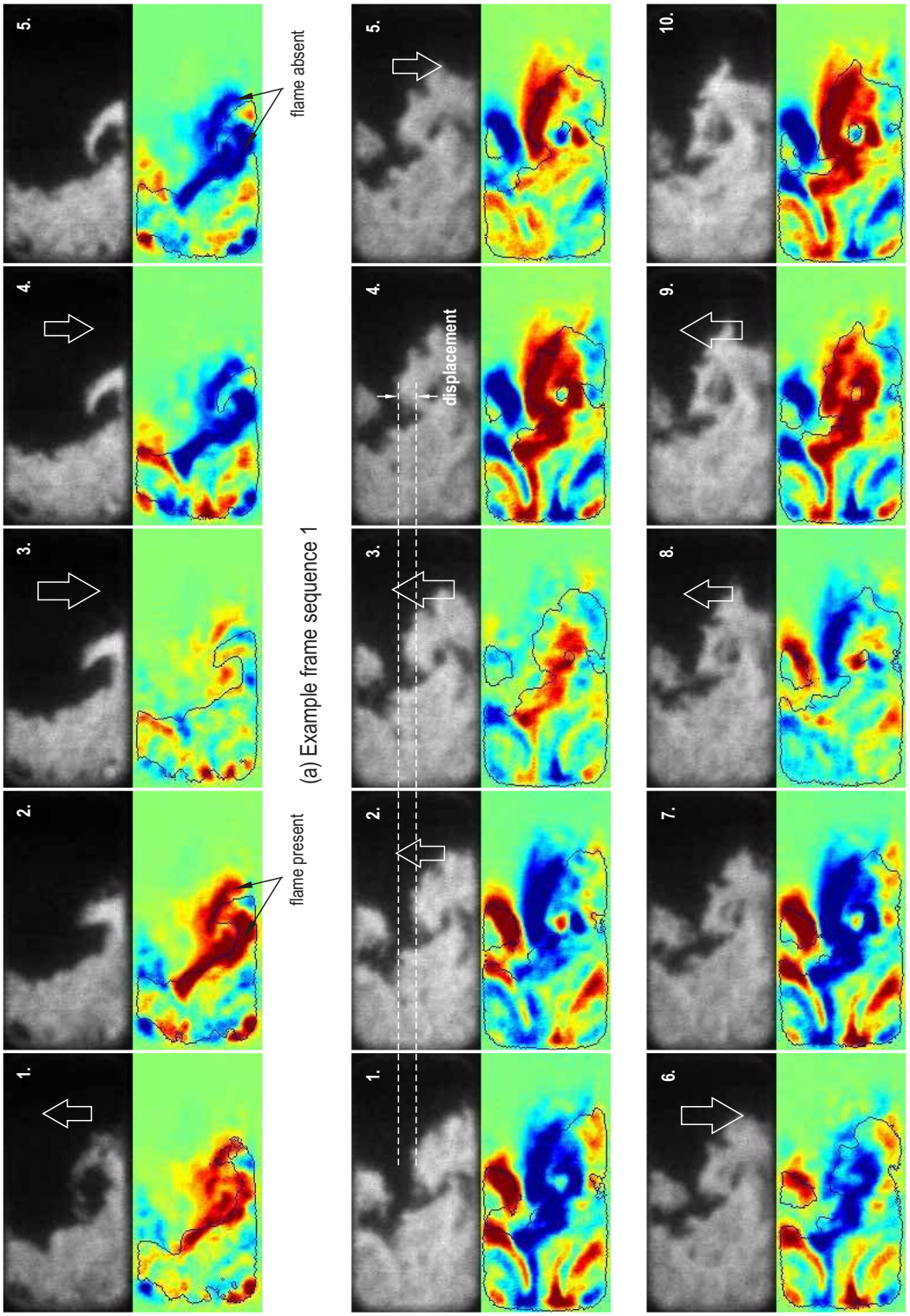

Figure 7.16: Sequence of raw OH* images (upper row) and band-pass filtered emission distribution (lower row) illustrating how transverse (up and down) convective motion results in artefact signals in band-pass images. Two example frame sequences are given from excitation of the 1T mode at 4350 Hz.

7.6 Dynamic response to longitudinal excitation

Flame response is now considered for 1L mode resonance. An example of the reconstructed acoustic pressure and velocity distributions for the 1L mode is given in Figure 7.17. The difference in colour-scale limits compared to the 1T mode case in Figure 7.14 should be noted, with far lower amplitudes in the 1L case. Convective motion artefacts are not so severe in the 1L mode case since very little influence of acoustic velocity is present. The axial flame development is largely undisturbed, as can be seen in the $\bar{I}(x,y)$ image in Figure 7.18a, because acoustic velocity increases from zero at the left hand boundary of the window (injection plane) to only low amplitude, axially oriented oscillations by the downstream boundary. The entirety of the window is under the influence of the acoustic pressure antinode.

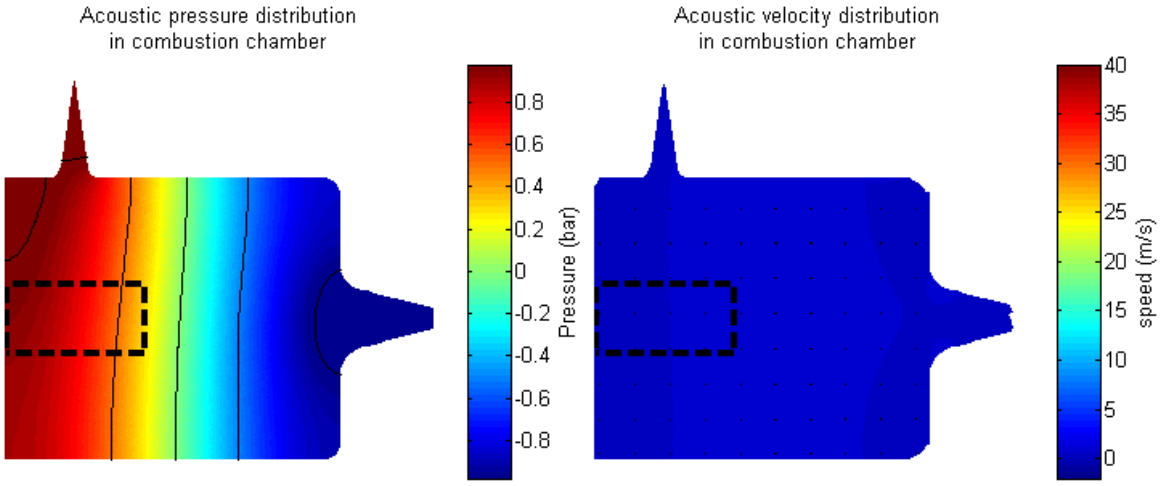

(a) Peak acoustic pressure amplitude

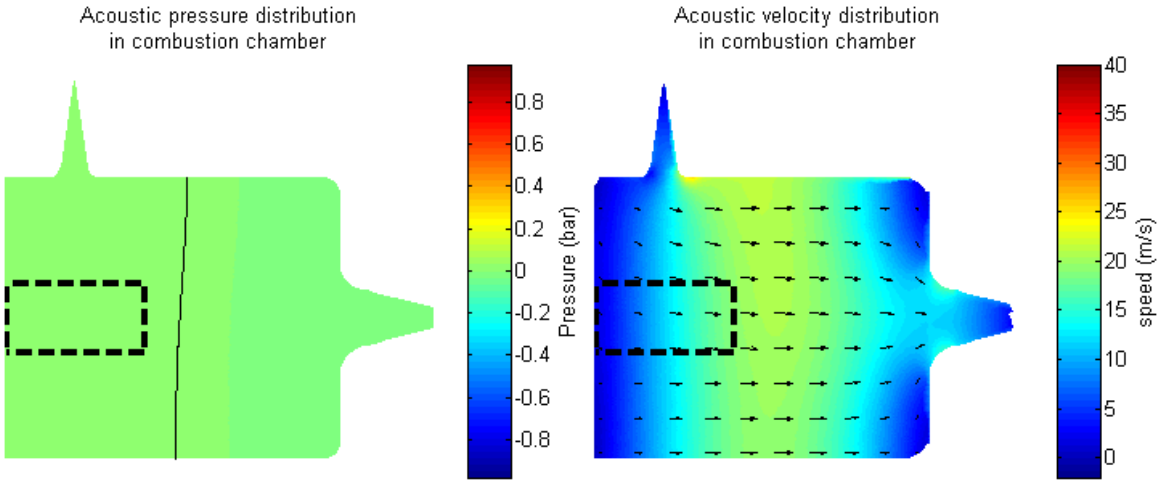

(b) Peak acoustic velocity amplitude

Figure 7.17: Reconstructed acoustic pressure and velocity distributions of the 1L mode used for the calculation of Rayleigh indices; at the point of peak acoustic pressure in the window (a), and one-quarter of a cycle later at the point of peak velocity amplitude (b). The velocity antinode is located downstream of the window.

Considering now the pressure Rayleigh index for a 60 bar test with GH_2 in Figure 7.18b, emission fluctuations are largely coherent and in-phase with both positive and negative oscillations in acoustic pressure, resulting in a time-averaged distribution of largely positive

index values. This condition satisfies the Rayleigh criterion and can theoretically amplify the acoustic wave. The predominantly in-phase behaviour (white colour) is confirmed in the corresponding phase diagram in Figure 7.18d.

Scattered throughout the diagrams are small pockets of out-of-phase emission fluctuation. These are due to the downstream convection of turbulent flamelet structures. Towards the downstream boundary of the image there appears to be increasing patches of anti-phase behaviour. This is explained again by comparing the band-pass filtered and raw images, which show convective acoustic motion causing the trailing edge of the flame to enter and exit the image at certain locations, particularly the top and bottom corners of the window. The resulting motion artefacts are in anti-phase with the acoustic pressure, as confirmed in the phase diagram in Figure 7.18d. Such regions with anti-phase behaviour would be interpreted as contributing to damping the acoustic wave, according to the formulation of Rayleigh index.

Since these near-injector and far downstream regions are known to contain spurious behaviour, they have been excluded in subsequent quantitative analysis by only considering values inside an 'area of interest' (AoI). The AoI is defined by the dashed rectangle overlayed on the $\bar{I}(x,y)$ image on the right side of Figure 7.18a. The mean phase value inside the AoI of the phase diagram for pressure (Figure 7.18d) is 8.5 ± 5.6 degrees, meaning that, on average, OH* emission lags acoustic pressure slightly. The velocity based Rayleigh index distribution in Figure 7.18c has time-averaged values near zero. The temporal progression of this index alternates between in-phase and anti-phase behaviour, which on average cancels and results in no positive coupling with acoustic velocity. The phase diagram in Figure 7.18e gives a mean phase shift of -98.7 ± 5.6 degrees in the AoI, meaning emission lags acoustic velocity by just over one quarter cycle, which is consistent with the phase relationship to acoustic pressure.

With the knowledge that OH* emission couples with acoustic pressure during 1L mode excitation, the analysis was extended to include calculation of response factors. The general definition of response factor N was first used by Heidmann and Wieber (1966a) and reads:

$$N = \frac{\iiint_V \int_t p'(V,t)\, q'(V,t)\, dt dV}{\iiint_V \int_t p'(V,t)^2\, dt dV} \,. \tag{27}$$

Here, N is an indicator of the degree of gain in heat release resulting from the acoustic pressure fluctuation. A discretised version of this expression was used here, again substituting two-dimensional OH* emission intensity for volumetric heat release rate:

$$N = \frac{\sum_A \sum_t \frac{p'(x,y,t)}{P_{cc}} \frac{I'(x,y,t)}{\bar{I}(x,y)}}{\sum_A \sum_t \left(\frac{p'(x,y,t)}{P_{cc}} \right)^2} \,. \tag{28}$$

The time-integrated response factor distribution for 1L excitation in the case A test at 60 bar with GH_2 (corresponding to the sample in Figure 7.18) is given in Figure 7.19a. Overall, the distribution is mostly uniform, indicating OH* emission response which is in proportion to the local amplitude of acoustic pressure. The area-integrated response factor, calculated for the same AoI as in Figure 7.18a, is $N = 0.81 \pm 0.16$.

While the complexity and expense of BKH testing rules out a statistical analysis, this result appears to be repeatable. A similar value of $N = 0.78 \pm 0.35$ was measured from a different test with the same operating conditions, namely the case B test at 60 bar with GH_2. This second result is displayed in Figure 7.19b. The response factor values from the two tests are very close, despite far lower excitation amplitude in test B. Response factors for 1L mode excitation in 40 bar tests could not be obtained. The 1L mode frequency lies too near to the primary camera artefact frequency in 40 bar tests to be properly isolated.

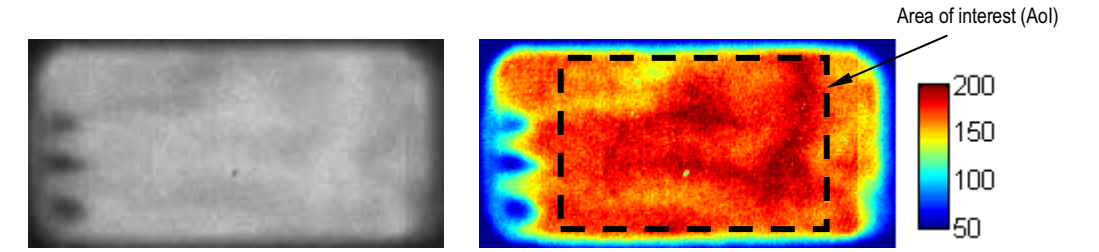

(a) Time-averaged raw OH* image

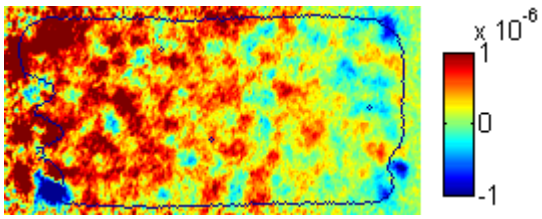

(b) Pressure-based Rayleigh index

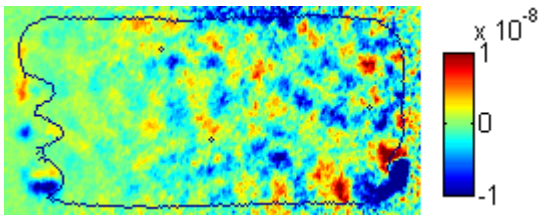

(c) Velocity-based Rayleigh index

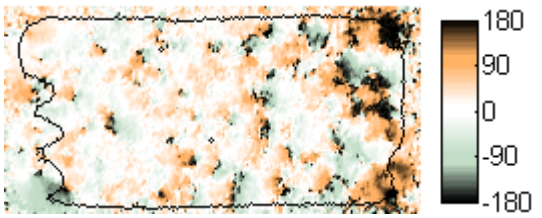

(d) Pressure phase

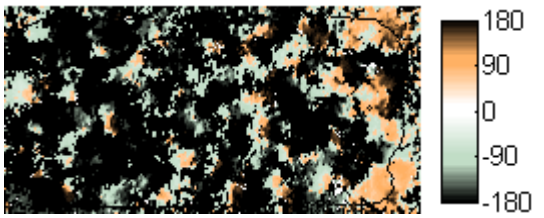

(e) Velocity phase

Figure 7.18: Response of the flame to 1L mode resonance comparing time-averaged distributions of the raw OH* images (a), the pressure-based Rayleigh index (b), the velocity-based Rayleigh index (c), acoustic pressure phase (d), and acoustic velocity phase (e).

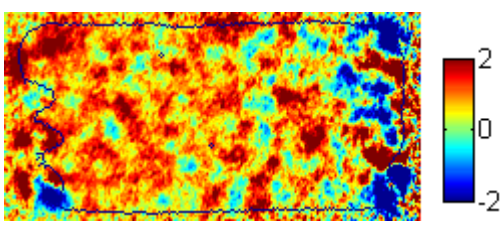

(a) 60 bar with GH_2, case A

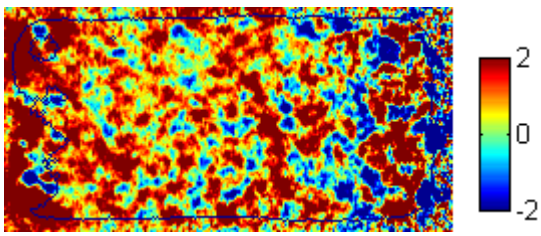

(b) 60 bar with GH_2, case B

Figure 7.19: Response factor distribution for coupling of OH* emission with acoustic pressure during 1L-mode resonance in tests at 60 bar with GH_2, cases A (a) and B (b).

While the measured N value is greater than zero, and therefore indicates positive coupling with acoustic pressure, its magnitude does not speak for significant amplification of heat release rate. By comparison, a theoretical nozzle response factor as derived by Heidmann and Wieber (1966a) has a value of $N_{\gamma=1.38} = -0.86$; the negative sign indicating a damping effect. Therefore the amplification in heat release rate resulting from acoustic pressure in BKH is insufficient to overcome the expected damping influence of the main nozzle alone. Hence it is expected to accomplish little against the combination of all other damping mechanisms which may be acting inside the combustion chamber, including the secondary nozzle, viscous damping on the combustion chamber walls, and thermal losses.

The measured value of N may, however, underestimate the true response of the flame. As discussed previously, the convective motion of flamelet structures in the turbulent combustion field manifest as artefacts in the filtered OH* intensity distribution. These motion artefacts have spurious phase behaviour and are interpreted as scattered pockets of negative coupling. Somehow compensating for convective motion artefacts and removing the scattered regions of negative coupling may result in a greater global value of N.

7.7 Photomultiplier response measurements

Pressure-coupling response factors were also calculated from photomultiplier OH* emission recordings. Photomultiplier and corresponding *PCCdyn2* signal samples of 100-ms duration were collected from periods of peak 1L-mode excitation amplitude. These signals were then processed using Equation 28, in a one-dimensional sense. Photomultiplier OH* emission recordings are available for the complete set of BKH operating conditions, as they are free of artefacts. All response factor values are plotted against chamber pressure in Figure 7.20. Response factor values are all greater than zero, ranging from 0.6 to 1.1. There does not appear to be any dependence of the results on combustion chamber pressure, nor on operation with GH_2 or LH_2. A measurement from off-resonance conditions is included, to show that the response during 1L-mode excitation is not anomalous. The two response factor values obtained from high-speed OH* imaging, presented previously in Figure 7.19, are included in the plot for comparison. These high-speed camera results (in red) fall within the range of values from photomultiplier measurements at 60 bar chamber pressure.

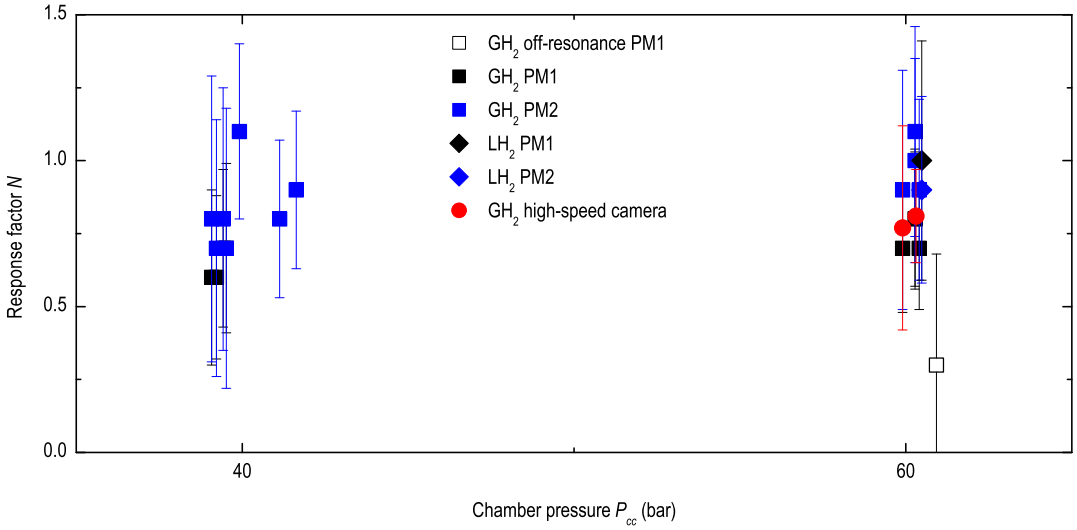

Figure 7.20: Response factors for coupling of OH* emission with acoustic pressure during 1L-mode resonance.

7.8 Summary

OH* emission imaging shows a well distributed reaction zone for the multi-element flame in BKH. During excitation of the 1T mode, shadowgraph images show significant reduction in the length of the oxygen jet. In the corresponding OH* images, the flame is consequently seen to retract towards the injection plane, with spreading of the flames also increasing. Such increased spreading of the flames during transverse acoustic forcing has also been observed in the MIC. Spreading and overlapping of adjacent flames appears to be more pronounced in BKH, presumably because the injectors are more tightly spaced than in the MIC.

Analysis of sequential flame images during 1T mode excitation indicates vertical oscillation of the entire imaged flame at the same frequency as the signal from the dynamic pressure sensor. Displacement amplitude also appears to be comparable to estimated acoustic gas displacement.

Temporal OH* emission fluctuation mirrors the ramping excitation frequency, in both high-speed OH* imaging and photomultiplier recordings. This indicates response of OH* emission to acoustic pressure. Because there is near-zero phase shift measured in the pressure response to 1L mode excitation, the response is not expected to be due to injection coupling. Response to 1T and 1L mode excitation was studied in the high-speed OH* imaging. The extraction of local OH* emission fluctuation during 1T mode resonance was made difficult by the convective motion of the flame driven by transverse acoustic velocity. It is possible that band-pass filtering the images for particular frequency response may only provide an indication of the displacement of heat release.

Convective motion artefacts in the high-speed imaging were not so severe in the 1L mode case, and Rayleigh indices show coherent in-phase behaviour. A response factor of around 0.8 was measured for 1L mode excitation. This value is consistent with response factor measurements from photomultiplier recordings from the full range of BKH operating conditions. While confirming an enhancement to heat release rate through pressure-coupling, this modest value of response factor would not be considered high enough to drive self-sustaining HF instability. It is conceivable that the combination of the actions of acoustic velocity and acoustic pressure during 1T mode oscillation in a real rocket engine could result in response values great enough to account for self-sustained HF instability.

Based on the observations made in BKH testing, coupling mechanisms can be theorised to explain how naturally occurring HF combustion instabilities may be sustained in real, cylindrical, LPRE rocket engines. In an engine experiencing 1T mode instability, the most commonly occurring and destructive mode in HF instability, the highest amplitudes of acoustic pressure are concentrated at the injection plane. As is observed during 1T resonance in BKH, transverse acoustic velocity results in an extreme reduction in the axial extent of the flame. This effectively retracts the bulk of the energy release from combustion into the region of maximum acoustic pressure oscillation. Other researchers, for example Heidmann (1965b), have also observed a retraction in the extent of the injection spray under the influence of transverse oscillations. Crocco (1972) had predicted this to be a destabilising influence using his sensitive time-lag theory in the 1960s. During development of the F-1 engine, concentrating the combustion zone near the injection plane through injector design was found to be destabilising (Oefelein & Yang 1993).

In BKH, the flame is convectively displaced by the transverse acoustic gas motion. Rey et al. (2004) and Richecoeur (2006) argue that the collective displacement of the flames comprises

a velocity-coupled driving mechanism, whereby the resulting increased concentration of combustion in the pressure antinodes reinforces the natural HF instability. The transverse displacement of the flame also causes overlapping of adjacent flames and improved mixing of propellants. Freshly premixed propellants are then encouraged to release their energy in phase with acoustic pressure, thereby reinforcing the instability. In-phase fluctuation in OH* emission intensity, assumed to indicate heat release rate from the flame, has been observed during 1L mode resonance in BKH in the current study. Due to the small phase delay of around 8 degrees (approximately 7 μs) following peak acoustic pressure, the OH* emission fluctuation is assumed to be in response to the pressure fluctuation. If such pressure coupling were to act on a region of premixed propellants following the action of a passing transverse acoustic velocity wave during 1T mode oscillation, the resulting combustion response could conceivably be greater than that measured in BKH for pure 1L mode pressure coupling.

Flame displacement need not play a definitive role in such a mechanism. Rotating 1T modes are known to be the main culprit in destructive HF instability. Litchford and Luo (2008) argue for a mechanism of travelling waves fed by well-premixed propellants located near to the injection plane. Recirculating and collecting propellants may cause the injector faceplate and chamber walls to “serve as a transpiring reactive boundary”. Such a mechanism may be reconciled with observations from BKH. An approaching wavefront of a rotating mode consists of transverse acoustic velocity directed towards the wavefront; against the direction of wave travel. Transverse modulation of the injection jets and flames causes accumulation of propellants near the injection plane and enhances propellant vaporisation and mixing. The well pre-mixed propellants react intensely in response to the passing pressure wave of the instability. Such a mechanism provides a closed feedback cycle for sustaining the instability. Due to the rotating nature of the wave, energy addition to the instability is continuous, maximising the chance of overcoming damping influences.

8. OXYGEN CORE RESPONSE

Dense oxygen core structures have been detected using high-speed backlit shadowgraph imaging in BKH. This chapter presents analysis of the imaging and discusses the behaviour of the oxygen core in response to acoustic excitation. The qualitative behaviour of the core for both off- and on-resonance excitation conditions is described. Here, the mechanism of core breakup and atomisation is found to differ between the two conditions. Measurements of the LOx core have shown the intact length to decrease with increasing acoustic excitation amplitude. This dependence is shown to be distinguishable for differing operating conditions of the combustor. The significance of this dependence with relation to theorised coupling mechanisms for combustion instabilities is discussed.

8.1 Review of oxygen core studies

The behaviour of the LOx core after injection via a shear coaxial type element is thought to be important to the coupling of acoustic disturbances with combustion. For example, the form that the core develops, the distance it penetrates into the combustion chamber before breaking up, and the manner in which it breaks up and is consumed are aspects which may influence the triggering or driving of HF instabilities. Numerous experimental investigations of length of the intact part of the LOx core using shadowgraph photography can be found in literature.

Intact core length is commonly defined as the axial length from the injection plane to the first complete end or separation of the visible dense-oxygen jet structure. It is used as a measure of LOx penetration into the combustion chamber. Woodward et al. (2006) and Yang, Cuoco and Oschwald (2007), for example, have both made intact core length measurements in lab-scale combustors with a single shear coaxial element burning LOx/H_2. The core length was in both studies found to scale inversely with the gas-to-liquid injection momentum flux ratio (J). This is in agreement with most correlations found in literature, although all were developed for cold-flow measurements and greatly underestimate the core lengths measured with combusting LOx/H_2. Yang and colleagues also made measurements of the core length with LOx/methane combustion using high-speed shadowgraph imaging with 4000 frames per second (fps). By systematically evaluating core lengths for subsequent frames, preferred shedding frequencies of large dense-oxygen structures from the end of the core were determined (Yang et al. 2007).

Frequent shedding and sudden combustion of large oxygen structures is a potential source of unsteady heat release for driving instabilities. The shedding frequencies measured by Yang et

al. were all relatively low, below 120 Hz, and decreased with increasing *J*. Nevertheless, regular shedding of LOx core structures is known to be a common feature of coaxial jet breakup in the Reynolds and Weber number range where rocket injectors operate, even with steady supply and combustion conditions. Farago and Chigier (1992) classified this regime as the "super-pulsating mode" of jet disintegration, and Chigier and Reitz (1995), and Lasheras and Hopfinger (2000) have presented in-depth reviews on the topic.

Locke et al. (2010) measured the core length in a LOx/H_2 combustor but with a co-flow of gas surrounding the single coaxial element, intended to more closely resemble conditions in a real, multi-element rocket engine. The co-flow resulted in core lengths longer than those without, and core length correlations again grossly underestimated measured lengths. Locke et al. used a frame rate of 20,000 fps, which allowed higher frequencies of core shedding to be resolved. Frequencies were found to reach into the range of HF instabilities; above 1000 Hz.

Others have studied the behaviour of the LOx core under simulated conditions of HF instabilities. The type of acoustic resonance modes known to be the most destructive in HF instabilities are the transverse modes. The term transverse refers to acoustic gas motions transverse to the direction of injection, oscillating across the face of the injector. Early tests by Miesse (1955) showed a single jet of water contracting when subjected to an externally-forced acoustic field. Later, Davis and Chehroudi (2006) conducted non-reacting coaxial injection tests with acoustic forcing. Liquid and gaseous nitrogen (LN_2/GN_2) were used as simulants for cryogenic propellants such as LOx/H_2. Tests were conducted under subcritical, near-, and supercritical pressures for nitrogen because modern rocket engines often operate at pressures above the critical pressure for oxygen (P_{crit} = 50.4 bar). The jet breakup and atomisation behaviour of cryogenic coaxial injection is known to differ between subcritical and near- to supercritical conditions (Mayer & Tamura 1996; Mayer et al. 1996; Mayer et al. 1998b; Chehroudi et al. 2003), and it is therefore important to make experimental observations in both regimes. Davis and Chehroudi observed a reduction in measured intact core length when acoustic forcing was active. Furthermore, the measured RMS fluctuation in core length increased. Increased core length fluctuation is interpreted by Davis and co-workers as increased sensitivity to potential feedback mechanisms which could drive HF instability. Both absolute core length and RMS were significantly lower under near- and supercritical pressures.

Heidmann (1965b) investigated LOx core behaviour in a sub-scale LOx/H_2 combustor with optical access and acoustic oscillations. The combustor did not use classical shear coaxial injection; H_2 was injection from slots spaced above and below the LOx jet. Heidmann induced transverse mode acoustic oscillations in the combustor and recorded back-lit shadowgraph images of the core. Both reduction in core length and deflection of the core in concert with the transverse acoustic gas motion were observed. Sliphorst (2011) measured intact core lengths in a laboratory scale combustor running coaxially injected LOx/methane, but was unable to establish any influence of the externally forced transverse acoustic field on core length. In this case, the surrounding annulus of high velocity gas flow may have acted to shield the LOx core from the influence of the transverse acoustic velocity.

Higher gas-to-liquid injection velocity ratios (*VR*) are known to reduce the susceptibility of shear coaxial LOx/H_2 systems to instability, as was established in extensive engine testing by Wanhainen et al. (1966). Most industrial engines operate stably with *VR* values greater than 10 (Hulka & Hutt 1995). In the cold-flow experiments of Davis and Chehroudi, increasing *VR* was also determined to be a stabilising parameter because it decreased core length RMS and reduced the difference in core length between tests with and without acoustic forcing. Leyva

and colleagues (Leyva, Chehroudi & Talley 2007; Leyva et al. 2008) and Rodriguez et al. (Rodriguez et al. 2008) found similar dependence on J, with acoustic forcing having a far lesser impact for $J > 5$. The core length measurements by Sliphorst were however made under relatively low acoustic pressure amplitudes, up to only 2.5% of combustion chamber pressure, P_{cc}. Traditionally, a case of HF instability is considered to have occurred when acoustic pressure amplitudes are greater than 5% (10% peak-to-peak) of P_{cc} (Fry & Klem 1997).

Richecoeur and colleagues (Richecoeur et al. 2008; Richecoeur et al. 2009) have acoustically forced a linear array of three or five coaxial injectors burning LOx/methane in the MIC with transverse mode amplitudes up to 4%. Previous attempts by Rey et al. (2004) to excite three injectors with the same hardware running LOx/H_2 achieved only 0.8%. Knapp, Farago and Oschwald (2007) reached 5% amplitude using the same hardware as Sliphorst (i.e. the CRC) but with LOx/H_2. No measurements of the LOx core length were reported in any of these studies, and no core length correlations with combustion under unsteady acoustic conditions exist in literature.

Repeating LOx core length measurements similar to those of Davis and Chehroudi and Sliphorst under combusting conditions with representative injector scaling and greater acoustic pressure amplitudes would be valuable to the understanding of flame-acoustic interactions. To this end, high-speed shadowgraph recordings made in BKH during excitation of transverse mode acoustic resonance were collected and analysed.

8.2 Oxygen core structure

In this chapter, imaging results are examined from tests with P_{cc} = 40 bar or 60 bar, using either ambient temperature, gaseous hydrogen (GH_2) or cryogenic, liquid hydrogen (LH_2), and with ROF = 6. Injection parameters corresponding to each operating condition are summarised in Table 9. Results from multiple tests running the 60 bar, GH_2 condition will be examined, and these tests are distinguished by the designator A, B or C.

Table 9: Injection parameters for tests with shadowgraph imaging.

Test designation			40 bar GH_2	40 bar LH_2	60 bar GH_2 A	60 bar GH_2 B	60 bar GH_2 C	60 bar LH_2
Combustion chamber pressure	P_{cc}	(bar)	39.5	43.5	60.4	59.9	60.4	60.2
Ratio of oxidiser to fuel	ROF		5.9	6.0	6.0	6.0	6.0	6.0
Hydrogen temperature	T_H	(K)	292	75	283	286	287	62
Oxygen temperature	T_O	(K)	129	132	129	125	123	126
Per-element mass flow rate	$\dot{m}$	(g/s)	95	112	132	132	132	140
Oxygen injection velocity	u_O	(m/s)	8.8	11.1	12.4	12.1	12.0	13.1
Hydrogen injection velocity	u_H	(m/s)	476	118	405	423	422	84.2
Velocity ratio	VR		52	10.7	33	35	35	6.3
Momentum flux ratio	J		9.7	1.9	5.9	6.3	6.2	1.1
Oxygen injection Reynolds no.	Re_O		3.3x105	4.1x105	4.4x105	4.2x105	4.0x105	4.4x105
Hydrogen injection Weber no.	We_H		5.7x105	1.7x105	6.7x105	5.9x105	5.3x105	8.9x104

First, the qualitative character of the shadowgraph image in Figure 8.1a is considered, with this example taken from off-resonance conditions in 60 bar, GH_2 test A. The dense LOx core of the central injection jet and those of the nearest outer (upper and lower) elements are clearly visible. They are identifiable by the light shade of grey which masks the surface of the dense LOx structures. This shade of grey is near-infrared emission from hot combustion products (H_2O) forming in the thin shear layer between the surface of the LOx core and the surrounding H_2 where primary mixing and reaction takes place. The presence of infrared emission in the image is due to the necessary compromise of using a continuous backlighting source in order to capture high-speed images. The continuous lamp used has lower intensity than low frequency flash sources which are often used for shadowgraphy. As a consequence, the exposure time must be increased which also allows more visible and near-infrared emission to pass through the filter.

There is some deflection of the outer flames into the dead spaces above and below the injector, following the paths of the outer LOx cores as seen in Figure 8.1a. While the outer LOx jets and their encompassing flames deflect outwards somewhat, the central LOx jet appears to continue more or less axially, as would be expected inside a real engine. The outer four injectors appear to have served their somewhat sacrificial purpose of providing a representative environment for the central injector.

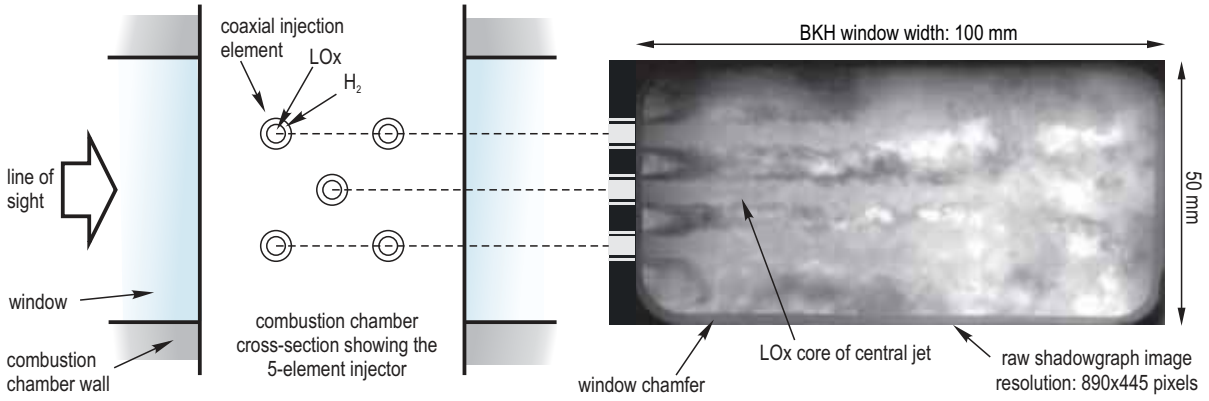

(a) Instantaneous shadowgraph image

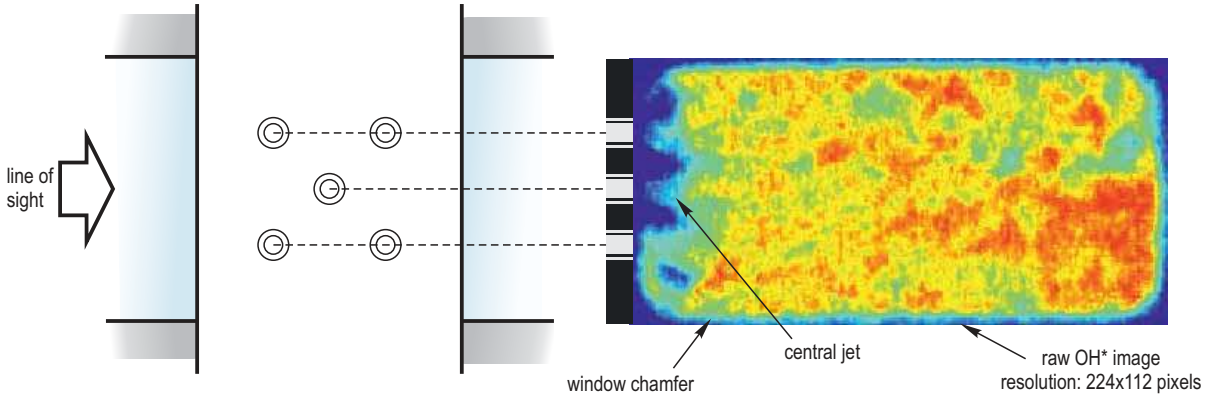

(b) Instantaneous OH* image

Figure 8.1: Example instantaneous shadowgraph image (a) and corresponding instantaneous OH* emission image, shown in false colour (b), for a 60 bar test with GH_2.

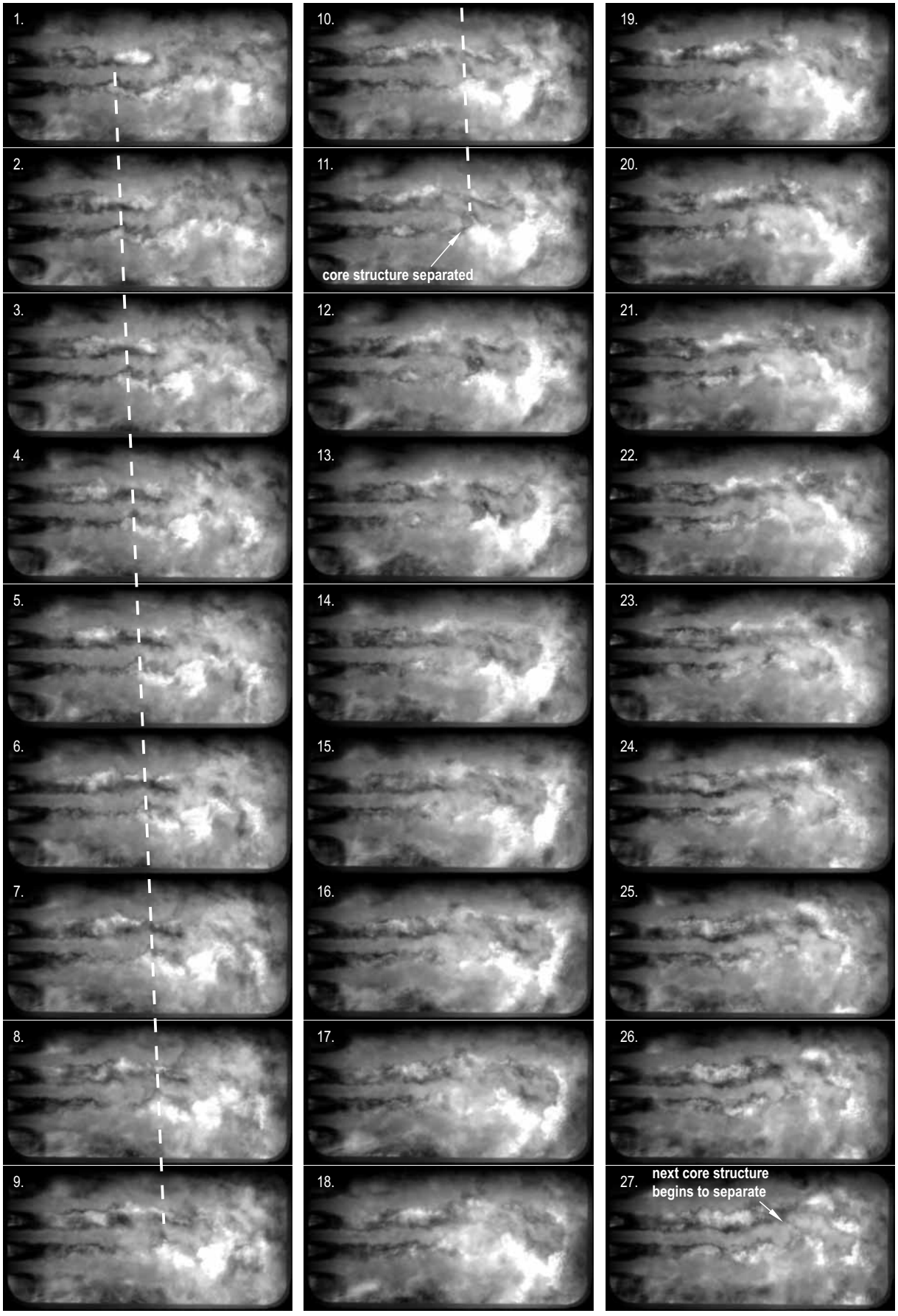

Figure 8.2: Natural LOx core breakup behaviour at 60 bar with GH_2.

Dynamic behaviour of the central LOx core is examined by observation of the high-speed images. The central core is long and sinuous, with little atomisation or dispersion evident along the intact extent of the core. Deformation and breakup into larger structures begins at a distance of approximately 13 L/D downstream of injection. Large dense-oxygen structures gather as the core develops downstream and eventually break away from the end of the core. This natural shedding behaviour, illustrated in the image sequence in Figure 8.2, is consistent with the observations from other researchers.

BKH operating points were superimposed on a map of coaxial-jet disintegration modes as presented by Chigier and Reitz (1995). The super-pulsating mode of disintegration, which involves large oscillations in jet atomisation and breakup, occurs when the relation $Re_O/(We_H)^{0.5} < 100$ is satisfied. All BKH operating conditions, from all test campaigns, fail to satisfy this condition. According to the map, BKH injection conditions lie in the fibre-type breakup regime. The fibre-type regime is characterised by a relatively stable jet with short wavelength surface instabilities. Bending and formation of wave-like structures begins after around 10 L/D downstream. Liquid fibres form and separate from the main liquid core, subsequently breaking up into droplets. The size of fibres, ligaments, and droplets being shed from the jet increases with increasing downstream distance. The form of the coaxial air and liquid jet in Figure 8.4, presented by Chigier and Reitz to illustrate the fibre-type regime, resembles well the behaviour of the central jet in BKH as seen in Figure 8.2. The formation of fibres and droplets is not evident in the shadowgraph images from BKH, although it is possible that they are consumed quickly under combusting conditions. Super-pulsating behaviour is therefore not expected to influence natural LOx core breakup in BKH.

Figure 8.3: Map of shear-coaxial breakup regimes defined by Chigier and Reitz (1995).

Figure 8.4: Coaxial air and liquid injection with breakup in the fibre-type regime (Chigier & Reitz 1995, p.120).

From observation of the high-speed images, the intact structure of the LOx core appears on average to have around the same length as the window. In approximately 50% of the images

an end to the core is identifiable within the last 15 mm of the window, and in the remaining images the core extends beyond the end of the window making it impossible to measure. For the purpose of this discussion it is said to have the same length as the window; around 100 mm, or 28.5 times the inner diameter of the LOx injector ($L/D \sim 28.5$). An intact core-length correlation by Davis and Chehroudi (2006), developed from LN_2/GN_2 measurements for single-phase, or supercritical, conditions, has the form

$$L/D = \frac{12}{J^{0.5}} \ . \tag{29}$$

For the 60 bar, GH_2 operating condition in BKH it predicts a core length of $L/D = 4.8$, greatly underestimating the length seen here. In the same work, Davis and Chehroudi adjusted this correlation for two-phase, or subcritical, conditions, giving

$$L/D = \frac{25}{J^{0.2}} \ . \tag{30}$$

This expression yields a better estimate of $L/D = 17.4$ for the BKH core length. The closest estimate of $L/D = 25.7$ is by a correlation from Woodward (1993), also developed from non-reacting nitrogen tests;

$$L/D = 0.0025\left(\frac{\rho_H}{\rho_O}\right)^{-0.44} Re_O^{\ 0.76} We_H^{\ -0.22} \ . \tag{31}$$

This expression contains the LOx jet Reynolds number and the gas-to-liquid Weber number. The Weber number is calculated using a value of surface tension from a study by Vieille, Chauveau and Gökalp (1999), who found LOx droplets in helium atmospheres to have measureable surface tension even at supercritical pressures. The Woodward correlation was tested against hot-fire LOx/H_2 intact core measurements by Woodward et al. (2006). Although also somewhat under-predicting the core lengths in that study, it performed better than all other correlations available from an extensive survey of literature.

In their single injector combustor with co-flow, Locke et al. (2010) measured core lengths on average of $L/D = 40$. Longer core lengths in the Locke et al. tests are to be expected since the J values were less than half that of the current tests. Furthermore, it was a single-element injector experiment. In BKH, flames from the four surrounding injectors produce an additional heat load on the central jet which almost certainly has an influence on LOx core temperature and breakup. This effect has not yet been captured in single-element experiments such as those by Locke et al. or Woodward et al.

Shadowgraph images from all operating conditions listed in Table 9, zoomed on the central jet, are presented for comparison in Figure 8.5. Note that the first few millimetres of Figure 8.5c are dark because the line of sight of the camera was unintentionally blocked by a piece of hardware in this particular test. The image quality in Figure 8.5d suffers from a high degree of infrared-emission encroachment. Qualitatively, the appearance of the LOx core structure boundaries in the shadowgraph imaging, as well as its natural atomisation behaviour, are indistinguishable for images taken from operation at subcritical or supercritical chamber pressures, namely $P_{cc} = 40$ or 60 bar.

(a) 40 bar, GH_2

(b) 60 bar, GH_2

(c) 40 bar, LH_2

(d) 60 bar, LH_2

Figure 8.5: Comparison of shadowgraph images for subcritical (40 bar) and supercritical (60 bar) chamber pressures, from tests at 40 bar with GH_2 (a), 60 bar with GH_2 (b), 40 bar with LH_2 (c), and 60 bar with LH_2 (d).

Locke et al. (2010) made the same observation from their shadowgraph imaging at 40 and 60 bar. Furthermore, they measured similar core lengths for subcritical and supercritical pressure conditions. They speculate that the core may not reach temperatures above the oxygen critical temperature (T_{crit} = 154.59 K) and therefore is never strictly supercritical, even at a supercritical chamber pressure of 60 bar. Local subcritical behaviour under supercritical pressure has previously been considered by other researches, since the critical point of mixtures differs from that of the component fluids. For example, the critical point for liquid oxygen in a gaseous helium atmosphere is higher than in a gaseous oxygen atmosphere, which is how the critical point of oxygen is defined (as for all fluids) (Gökalp et al. 2000). Figure 8.6 shows critical mixing temperatures for several binary systems, plotted as a function of pressure. Binary mixtures no longer have a single critical point as do pure fluids. Rather,

critical mixing lines now define the boundaries below which liquid-gas phase equilibrium exists and above which supercritical conditions prevail. The general trend with increasing system pressure is that of decreasing critical temperature for the binary mixtures. Figure 8.7 plots lines of surface tension of the binary O_2/H_2 system against pressure for various pressure isobars, calculated using the Macleod-Sugden correlation. It shows that surface tension is still present above the critical pressure of oxygen, provided the critical mixing temperature is not exceeded. The consequence is that local conditions on the surface of the LOx jet may still behave according to subcritical conditions, despite operation at P_{cc} = 60 bar.

NOTE:
These figures/tables/images have been removed to comply with copyright regulations.
They are included in the print copy of the thesis held by the University of Adelaide Library.

Figure 8.6: Critical mixing lines of common binary systems (Mayer & Smith 2004, p.8).

Figure 8.7: Surface tension of the oxygen/hydrogen binary system (Mayer & Smith 2004, p.8).

8.3 Dynamic response to transverse excitation

As the images previously discussed were taken during periods of off-resonance excitation they are considered to represent the natural state of the flame. During 1T mode excitation the near-injector region is subjected to oscillating transverse gas motion with velocity on the order of the H_2 injection velocity. Time-averaged shadowgraph and OH* images from conditions with and without 1T mode excitation, which appeared previously in Section 7.2, are presented here again in Figure 8.8 side-by-side for comparison. In the shadowgraph image in Figure 8.8b, the central LOx core length is greatly reduced compared to its natural state in Figure 8.8a, now only extending ~ 7 L/D downstream of injection.

In order to understand the mechanism by which the core length is so significantly reduced, the high-speed imaging from which Figure 8.8b originates was examined more closely. Observing periods of 1T mode excitation as movies, it is evident that the core is given no opportunity to develop downstream because the high velocity transverse acoustic gas motion shears material away from the core. In the image sequence in Figure 8.9, for example, a pocket of LOx can be seen being torn away from the core only a short distance (~ 1.5 L/D) downstream of injection. In frame 3 of the sequence, the pocket begins gathering on the upper side of the core, or the ‘downwind’ side relative to the acoustic gas flow from below. In frame 4, approximately one-quarter of a cycle later following peak acoustic velocity magnitude in frame 3, the pocket has broken away completely and has travelled a short distance both downstream and away from the core, having been entrained in the acoustic gas motion. A sizable portion of the LOx core has thus been removed even before reaching half the intact

core length downstream. This process repeats for every upwards and downwards pass of acoustic gas motion. Noteworthy is that the intact LOx core is not observed to bend, deflect, or take on a sinusoidal shape under the influence of acoustic gas motion as was observed for cold-flow conditions by Chehroudi, Davis and Talley (2003), Davis and Chehroudi (2006), and Richecoeur (2006b), and for hot-fire conditions by Heidmann (1965b). In BKH the LOx jet has a greater mass flow rate and injection velocity, and hence momentum, than in those experiments, giving it greater resistance to the transverse acoustic gas motion. Such LOx core behaviour has only now become evident from testing conducted at a larger, more representative scale.

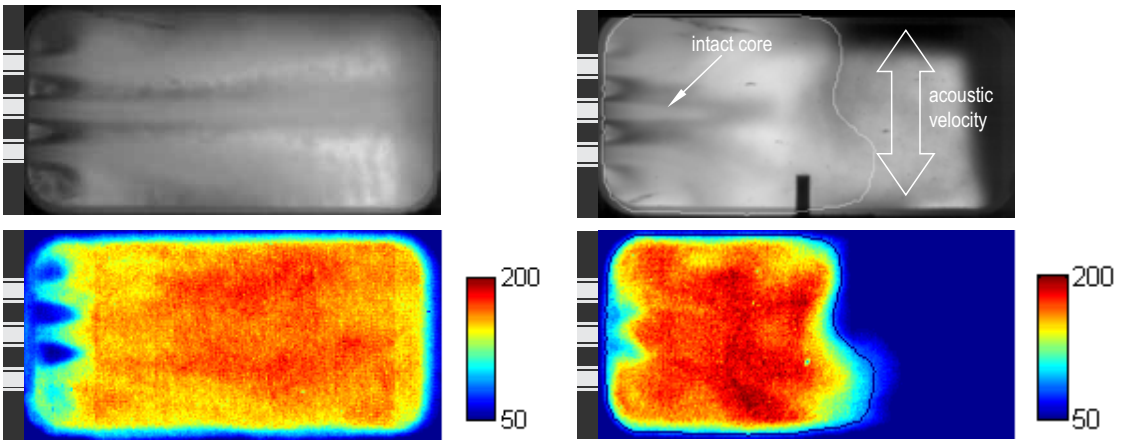

(a) Off-resonance (b) 1T-mode resonance

Figure 8.8: Time-averaged shadowgraph (upper row) and OH* emission images (lower row) during off-resonance excitation (a), and 1T-mode excitation with p'/P_{cc} = 7.4% (b).

In the image sequence in Figure 8.9, a pocket of material was seen tearing away from the intact core and becoming entrained in the acoustic gas motion over the course of an acoustic cycle. This behaviour was consistently observed in all high-speed imaging to occur regularly during periods of 1T mode resonance. Such effective stripping of the core greatly accelerates atomisation and mixing with surrounding H_2. This mechanism is probably responsible to a large degree for the acceleration in combustion and contraction of the heat-release region observed in the OH* images. It can also be reconciled with the HF instability driving mechanism proposed by Rey et al. (2003), whereby transverse velocity displaces freshly injected and mixed propellants into a pressure antinode, where they subsequently burn and release heat in phase with acoustic pressure. In the previous chapter, combustion was seen to respond to acoustic pressure. Freshly mixed propellants supplied by core-stripping as seen here may produce a pressure response far greater than those observed for pure pressure interaction with the 1L mode. Marshall et al. (2006b) may have already observed such a response in their multiple-injector rectangular combustor (Section 4.1.4). In that experiment, naturally higher amplitudes were observed when injector flames were aligned with pressure antinodes. Later testing introduced an additional flow of GN_2 between two of the coaxial elements. This flow increased the amplitude of pressure oscillations, theorised to be the result of simultaneous disruption of atomisation in the neighbouring elements, allowing them to couple more readily with chamber acoustics. This GN_2 flow may have had an effect analogous to the externally-driven transverse velocity in BKH, whereby it allowed multiple injectors to synchronise enhancement to their atomisation, thereby allowing increased energy release in phase with pressure.

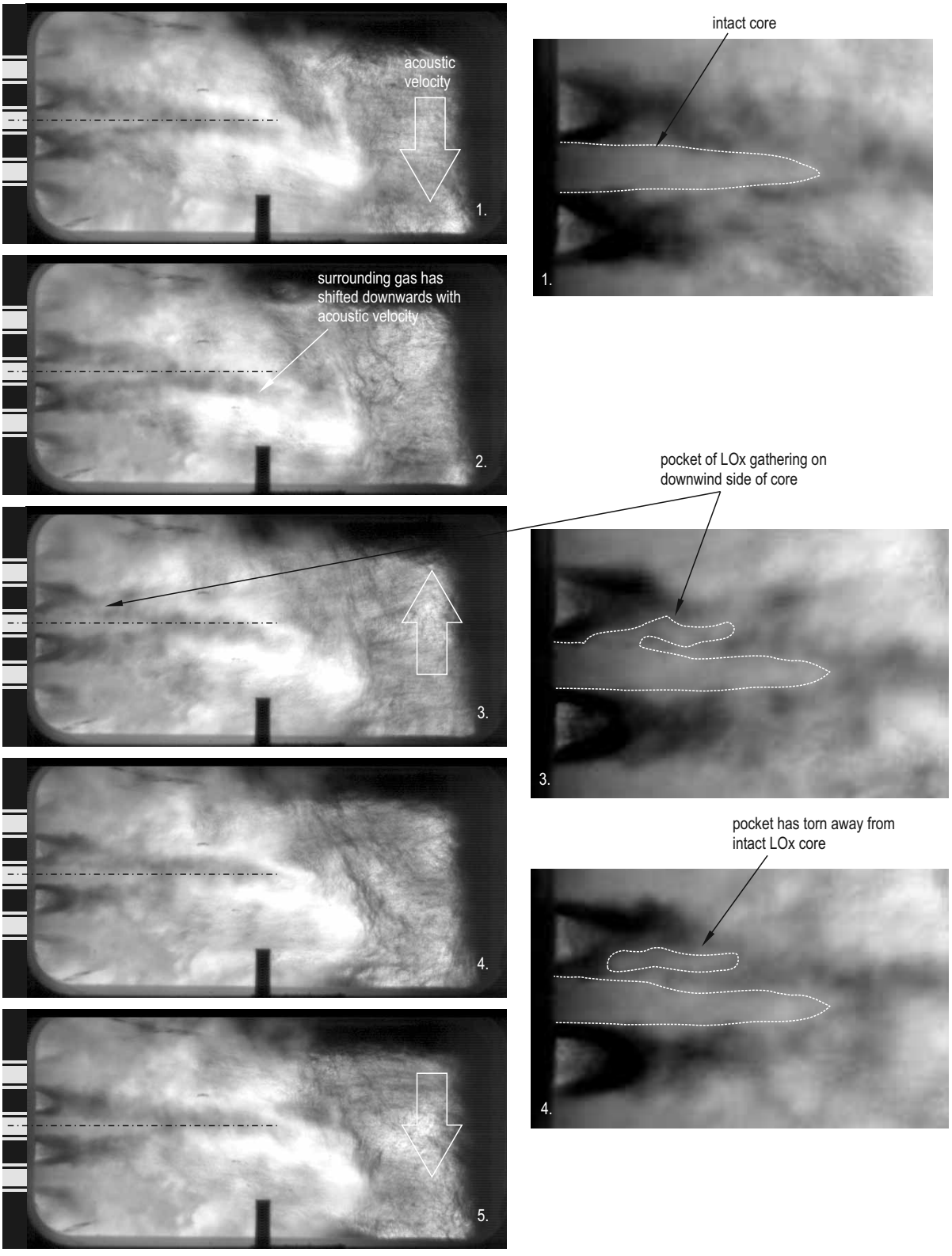

Figure 8.9: Sequential shadowgraph images from a 60 bar test with GH_2, recorded at 20,000 fps during 1T mode excitation with p'/P_{cc} = 7.4%.

Previous studies of the influence of transverse acoustic velocity fields on single jets have revealed flattening of the jets in the direction perpendicular to the acoustic velocity. Chehroudi and Talley (2003), for example, observed this effect in cold-flow experiments at subcritical pressures (Section 3.4.1). The jet flattening is understood to be due to the Bernoulli

effect, where pressures are lower at the jet shoulders compared to in the stagnation regions at the front and back of the jet. Such an effect cannot be distinguished in the current images from BKH owing to line-of-sight imaging from only a single point-of-view.

Jet flattening has also been observed by Baillot et al. (2009) to result from acoustic radiation pressure on a coaxial jet positioned at an acoustic velocity antinode. Water and air were used as simulants in their experiment. During forcing of the transverse resonance mode in their acoustic chamber, a net gas flow was detected arising from acoustic radiation pressure, or 'acoustic streaming'. The flow was from the pressure antinodes at the sides of the chamber to the velocity antinode in the centre, and caused the liquid jet to be flattened in the plane perpendicular to the flow. This only worked, however, when the acoustic streaming was powerful enough to overcome the injection impulse. Whether the same effect observed in Baillot's relatively low injection velocity jets would be significant for realistic injection conditions is debateable. For Baillot et al., the influence of acoustic streaming was not strong enough when the coaxial jet operated in the fibre-type atomisation regime ($Re_O > 10^3$, $We_H > 10^2$, $J > 1$). BKH operates well inside this regime, and acoustic streaming would therefore not be expected to have a noticeable influence on atomisation. Furthermore, it is unlikely that an acoustic streaming flow, such as that inferred in Baillot's case, is at all present in BKH. The forced acoustic field inside BKH is unsteady (varying amplitude and frequency) and nonlinear (with strong overtones), whereas Baillot et al. state the requirement of a pure standing wave arising from a sinusoidal source as a requirement for the establishment of such an acoustic radiation flow field. It is difficult to imagine that such pure conditions giving rise to acoustic streaming would be present in naturally occurring HF in real engines.

8.4 Intact core length measurements

Systematic measurements of the intact core length were made from the shadowgraph images. A semi-automated routine to extract core length measurements from the high-speed shadowgraph images was developed. First, the image is pre-processed in order to enhance the contrast gradients in the image and reduce noise. The enhanced image is then converted to a binary image using a threshold value which was selected through trial and error during development. User input is then required to specify an analysis target area encompassing the extent of the intact core and excluding as best as possible the upper and lower surrounding jets and the turbulent mixing region downstream. Morphological operations are then performed within this area, applying erosion and dilation operations to skeletonise the LOx core and produce a trace of the centreline of the intact core. The horizontal coordinate of the end of the centreline is converted to a measurement of core length. Figure 8.10 illustrates the major steps in this routine.

The automated core detection technique has a success rate of approximately 75%. Measurements are made difficult by the encroachment of infrared emission into the shadowgraph imaging. Contrast between the core and surrounding gas is weak and inconsistent. Despite image enhancement carried out during pre-processing, the light grey core is sometimes indistinguishable from the surrounding back-lit, turbulent gas mixture. Furthermore, clouds of combustion products travelling downstream either in front or behind the central jet occasionally obscure the end of the core. This resulted in the need to visually check each core detection image and discard spurious measurements. To avoid a doubling of effort, the automated detection technique was set aside and core end points were manually located by eye. Manual location of the core end point is taken to have a subjective judgement uncertainty of $\pm 0.5\ L/D$.

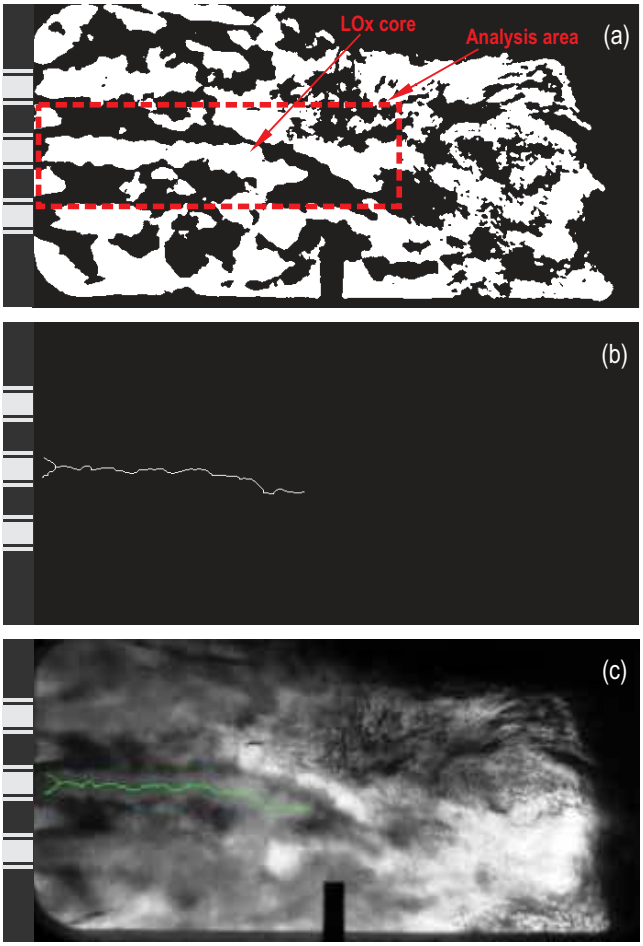

Figure 8.10: Major steps in the semi-automated core detection routine; the binary image created following pre-processing with the user-specified analysis area (a), the intact core centreline (b), and the centerline overlaid on the raw image (c).

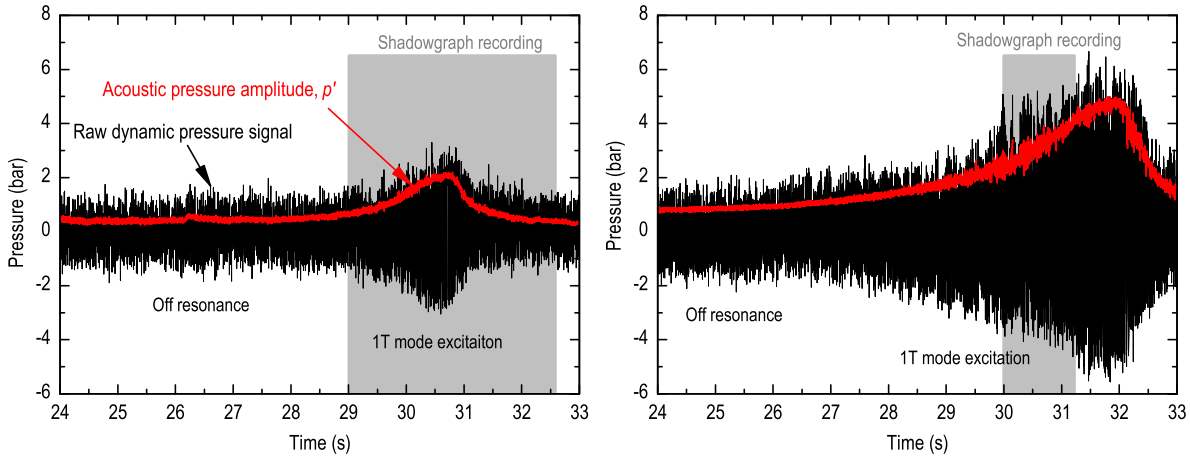

(a) Recording rate 7000 fps

(b) Recording rate 20,000 fps

Figure 8.11: Acoustic pressure signals and shadowgraph recording durations for 60 bar, GH_2 case A (a), and case C (b), with shadowgraph recording rates of 7000 fps and 20,000 fps, respectively.

Core measurements were made to investigate the relationship with 1T mode acoustic pressure amplitude. Acoustic pressure amplitude, p', is estimated the same way as described in Section 6.4.3; by calculating a sliding RMS value from the high-pass filtered dynamic pressure signal and multiplying it by the square root of 2. The calculated p' signal is overlayed on the raw signal in Figure 8.11 for 60 bar, GH_2 cases A and C with ramped excitation. While operating conditions were very close for these two tests, the configuration of the excitation system differed and resulted in lower peak resonance amplitude being achieved in the first. Also, in test A the camera recording rate was 7000 fps and 20,000 fps in test C. The active recording time of the high-speed camera is indicated in grey. Sample periods of 5-ms duration were selected for various p' levels throughout this recording time. These samples consist of 35 and 100 frames respectively for the 7000 and 20,000 fps recordings. Although the excitation frequency is continuously ramped through the resonance mode, during these sample times the excitation conditions can be considered quasi-steady.

Example results from two 5-ms samples are shown in Figure 8.12. The samples come from test C (20,000 fps), with the first sample in Figure 8.12a taken from the beginning of the recording duration where relative acoustic pressure was around 4%, and the second sample in Figure 8.12b taken from the end of the recording where pressure reached over 7%. In the first sample, where acoustic forcing amplitude is still relatively low, the core disintegrates naturally, resulting in sudden detachment of large, dense oxygen structures accompanied by a significant drop in the measured length of the remaining intact core. As p' increases, the shedding mechanism becomes influenced by the transverse gas motion. Before large, dense oxygen structures are given the opportunity to gather and detach from the end of the core, reactants and products are removed by, and become entrained in, the oscillating transverse acoustic flow. For this reason the growth-and-detachment behaviour is not seen in the second sample.

Mean L/D values measured from multiple samples from all tests listed in Table 9 are plotted against p' in Figure 8.13. The intact core length decreases to around 30% of its natural length (for off-resonance conditions) over the course of increasing acoustic pressure amplitude to around 8%. The reduction in L/D with increasing p' appears to follow a linear relationship to an amplitude of around 6%. In this range the behaviour of the LOx jet breakup as observed in the high-speed images appears to be transitioning from natural growth-and-detachment behaviour to the 'transverse stripping' mechanism. Above $p' \sim 6\%$, the trend flattens somewhat, with core length decreasing more gradually in this transverse stripping regime. Leyva and colleagues (Leyva, Chehroudi & Talley 2007; Leyva et al. 2008) studied LN_2/GN_2 jets for a range of J values from 1.2 to 23 and the reduction in jet length to be greatest for $1 < J < 4$. Rodriguez et al. (2008) measured length reductions between 30% and 50% of the natural core length in this J-range. In the current tests, a similar level of core length reduction has been observed while operating at a J value above this range. However, the relative p' levels reached here are greater than those used by Leyva and colleagues.

The congruence of measurements from various test conditions is remarkable. The largest set of measurements is from the three tests at 60 bar with GH_2. The linear trend line in Figure 8.13 belongs to these three data sets, and is set to pass through the natural core length of $\sim 28.5\ L/D$. The measurements from the 40 bar test with GH_2 come from a period of excitation with $p' \sim 3.5\%$, and fall in line with the 60 bar, GH_2 trend. Measurements at 40 bar with LH_2 were made with $p' \sim 7.3\%$ to 8.2%. These points appear to continue the trend of measurements from 60 bar, GH_2 test C. Measurements from a test at 60 bar with LH_2 at $p' \sim 5.4\%$ fall somewhat below the trend line for all other measurements. These measurements should be considered with caution as they were taken during a period of strong, low-

frequency chugging. They are from samples of only 1-ms duration, taken during quasi-steady conditions at the peak of LF cycles. They are included here only to provide a complete set of operating conditions, and are not regarded with confidence as are the other measurements.

The error bars for core length in Figure 8.13 represent the standard deviation (Std) in core length from the individual measurements for each sample period. Std also decreases with increasing p' due to the declining growth-and-detachment behaviour. Aside from this, intact core detection becomes more reliable as the acoustic amplitude increases. The ever-increasing transverse gas motion pulls infrared-emitting combustion products away from the core either upwards or downwards, leaving a clear line-of-sight to the core from the side.

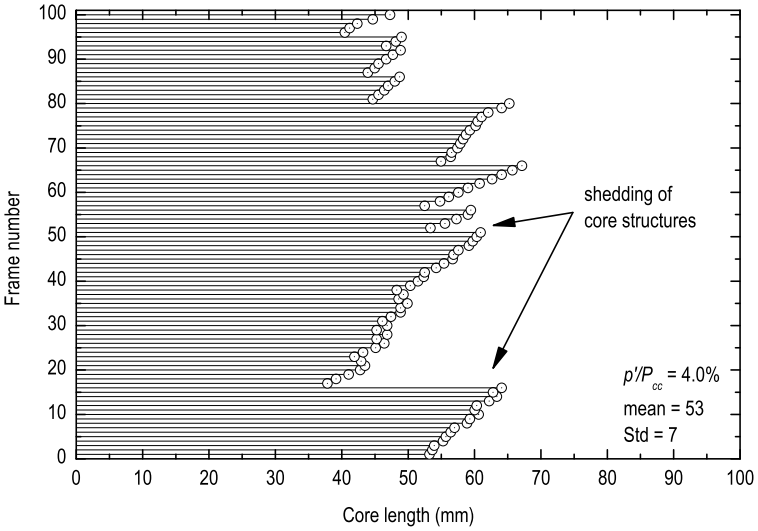

(a) Low acoustic pressure amplitude

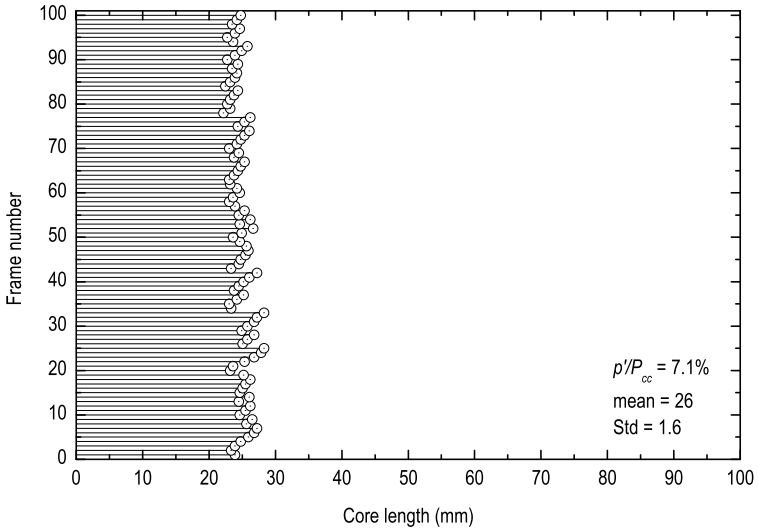

(b) High acoustic pressure amplitude

Figure 8.12: Frame-by-frame measurements of the intact LOx core length from 5-ms duration (100-frame) samples from the case C test at 60 bar with GH_2. The first sample is from the beginning of the shadowgraph recording in b with low excitation amplitude (a), and the second is from the end of the recording (b) with greater amplitude.

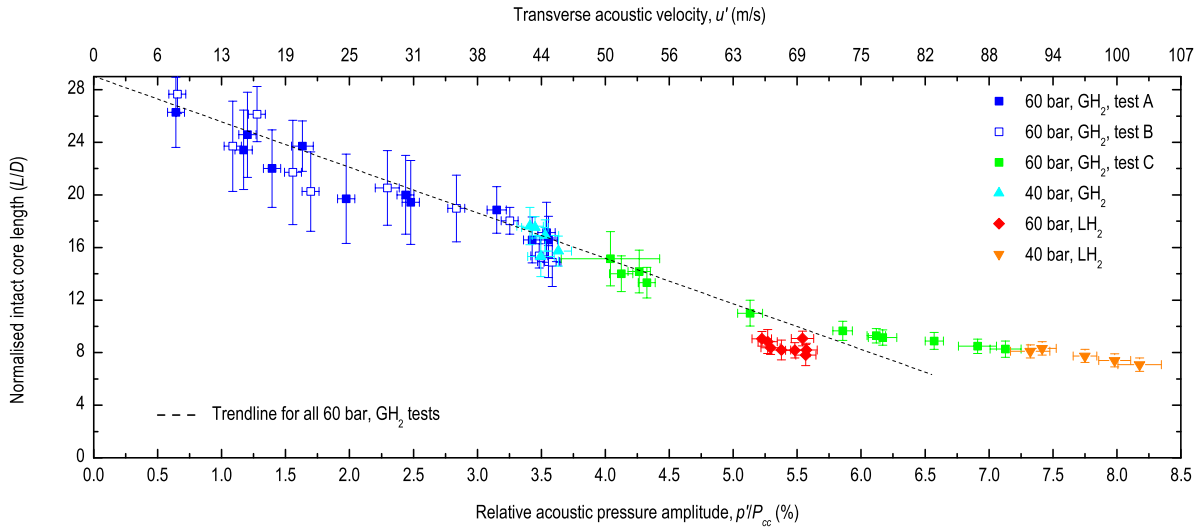

Figure 8.13: Normalised intact core length (L/D) plotted against relative acoustic pressure amplitude (p'/P_{cc}).

The reduction in core length Std with p' can also be interpreted as a reduction in core length fluctuation. Davis and Chehroudi (2006) used RMS as a measure of core length fluctuation. The trend observed here is clearly in opposition to the cold-flow observations of Davis and Chehroudi. The arguments of Davis and Chehroudi, and their co-workers (Davis & Chehroudi 2006; Leyva, Chehroudi & Talley 2007; Leyva et al. 2008; Rodriguez et al. 2008), that core fluctuation tendency is a coupling mechanism for HF instability, may therefore not be valid during fully established instability. In BKH, the intact core length is observed to shorten and stabilise under representative injection and acoustic conditions. It should also be noted that the levels of p' reached in BKH are still modest compared to those observed in full-scale, natural instabilities. The effect on the core during real instabilities is likely to be even more extreme, and it is therefore considered unlikely that significant length fluctuations and axial shedding of large-scale, dense oxygen structures plays a role in the driving mechanism. However, such behaviour remains plausible as a triggering mechanism for the initiation of HF instabilities.

In Figure 8.13, transverse acoustic velocity, u', which corresponds to the relative acoustic pressure amplitude p'/P_{cc}, is also displayed on the horizontal axis scale. Here, u' is arguably the better parameter to consider since it is the acoustic field component interacting directly with the central LOx core. Two ways of normalising u', which are thought to better represent the physical processes influencing the coaxial injection jet, are presented here for discussion. The first, plotted in Figure 8.14, is the ratio of transverse-acoustic to H_2-injection momentum flux;

$$\frac{\rho_{bulk}\ u'^2}{\rho_H\ u_H^{\ 2}}\ . \tag{32}$$

The numerator in this expression, where ρ_{bulk} is the density of the bulk equilibrium gas mixture in the combustion chamber, represents the momentum flux of the transverse acoustic gas flow impinging on the LOx core. The denominator is the momentum flux of H_2 at the injection plane. The H_2 annulus surrounding the LOx core is here assumed to play a stabilising role, shielding the LOx core from the transversally impinging acoustic gas. This parameter, therefore, represents the competition between the disruptive influence of transverse acoustic gas flow and the protective influence of the coaxial fuel injection annulus.

This formulation separates the tests with GH_2 from those with LH_2 in Figure 8.14, by virtue of the far slower injection of LH_2. Tests with GH_2 appear to lie on a curve of exponential decay with increasing acoustic-injection momentum flux ratio. It is possible that the 40 bar and 60 bar tests with LH_2 now lie on a similar curve parallel to that for GH_2. However, more measurements would be needed for valid construction of a trend line for LH_2 data.

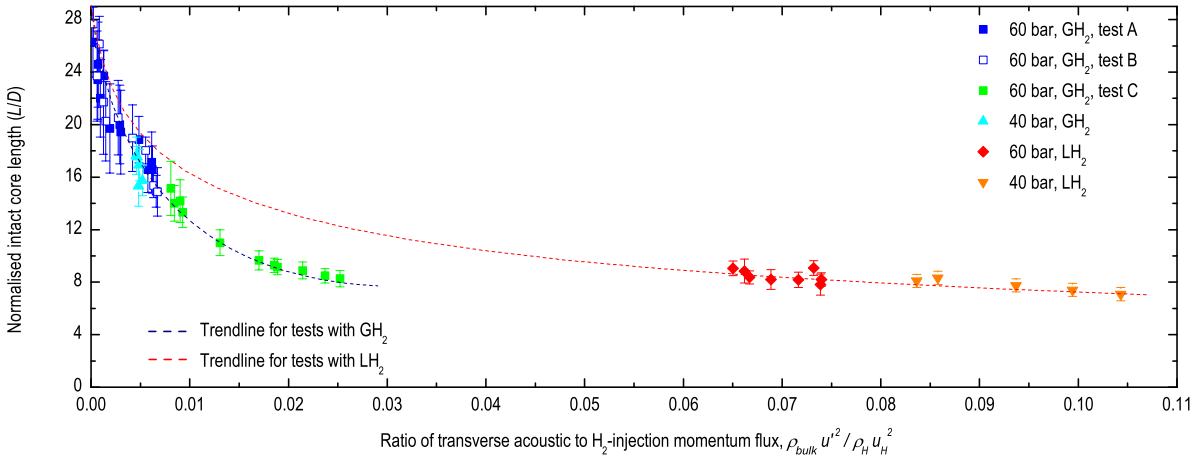

Figure 8.14: Normalised intact core length (*L*/*D*) plotted against the ratio of transverse-acoustic to H_2-injection momentum flux.

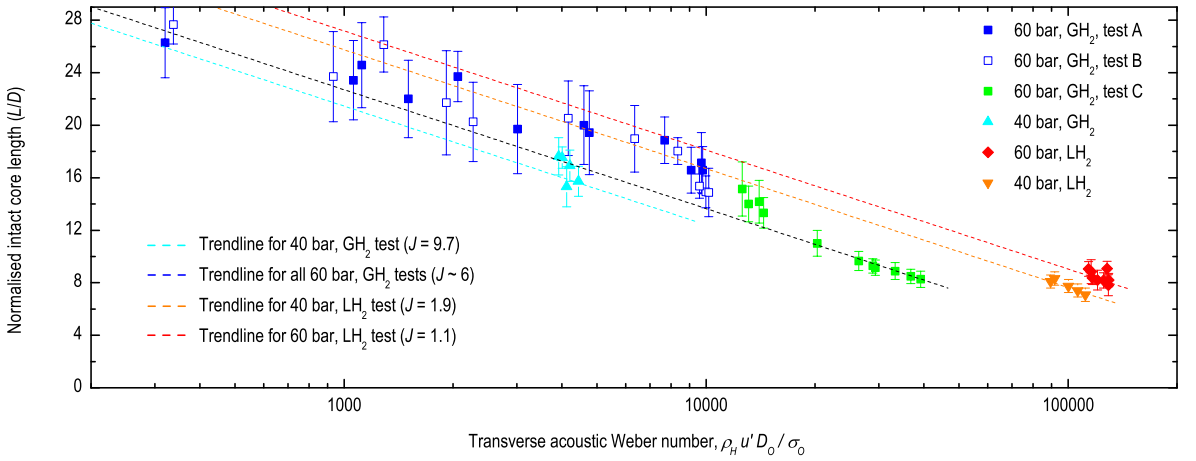

Figure 8.15: Normalised intact core length (*L*/*D*) plotted against transverse acoustic Weber number.

A second attempt at normalising the transverse acoustic velocity parameter, shown in Figure 8.15, uses a formulation of the Weber number. The transverse acoustic Weber number,

$$We_T = \frac{\rho_H \, u'^2 \, D_O}{\sigma_O} \,, \tag{33}$$

represents the ratio of aerodynamic forces from the transverse acoustic gas flow acting on the LOx core, to the surface tension of the core. Here it is assumed that the transverse acoustic gas motion forces injection H_2 to impinge onto the LOx core, hence the use of ρ_H. Values of LOx surface tension, σ_O, were taken from the experimental studies of Vieille, Chauveau and Gökalp (1999, p.4), where a value of $\sigma_O = 5.5$ mN/m was measured for LOx in a helium

atmosphere at 40 bar, and σ_O = 3.5 mN/m at 60 bar. The resulting transverse acoustic Weber number again separates the GH_2 and LH_2 tests owing to the different H_2 densities. Furthermore, the different values of surface tension separate the 40 bar and 60 bar tests. With greater surface tension, the 40 bar tests with GH_2 and LH_2 lie below their respective 60 bar counterparts. In Figure 8.15, each category of test condition may lie on parallel straight lines converging on their respective natural intact-core lengths. The order of the trend lines is in agreement with the *J*-dependence of natural core length found in literature.

8.5 Secondary atomisation

Secondary atomisation, or secondary droplet breakup, is known to play an important role in spray combustion (Section 2.5.3). Droplet lifetimes under conditions in real LPREs are between approximately 1 and 2 ms, according to Sirignano et al. (1995). The time scales for secondary atomisation are typically shorter than those for primary droplet vaporisation. Hence primary droplets usually undergo secondary breakup before they vaporise, and secondary atomisation is therefore considered a rate-controlling process in spray combustion. In shear-coaxial injection under rocket engine-like conditions the shear/stripping/catastrophic breakup regime of secondary atomisation is usually active due to the large shear forces and high pressures present (Gökalp et al. 2000). The shear forces referred to in this sense are those arising from the velocity difference of the injected liquid and gaseous propellants. As is observed in BKH, however, transverse mode acoustic oscillations are accompanied by significant transverse gas velocities. Image analysis presented previously in Section 7.3 indicates a strong influence of the acoustic velocity field on the flame, causing the flame to move in unison with the acoustic gas displacement in the direction transverse to the injection axis. What this may mean in terms of a coupling mechanism was considered from the point of view of secondary LOx droplet breakup, which is traditionally considered as one of the main processes potentially responsible for velocity coupling in HF instabilities.

A hypothetical analysis of 1T mode conditions in BKH was made. For the sake of this hypothetical analysis, two main assumptions are made. The first is that coherent LOx droplets, produced by primary atomisation, are present in the spray flame. Although the shadowgraph images collected to date in BKH do not have the resolution capable of resolving droplet sizes expected in shear-coaxial spray flames, the assumption is in accordance with traditional models and experimental observations of shear-coaxial spray flames at chamber pressures subcritical for oxygen, for example by Mayer and colleagues (Mayer & Tamura 1996; Mayer et al. 1998a). The second assumption is that, by virtue of their greater inertia, LOx droplets remain stationary, at least initially, relative to the acoustically-driven transverse motion of the flame. This is consistent with the interpretation of Sliphorst (2011) from experimental results obtained in the CRC operating with LOx/CH_4. Weber and Reynolds numbers can be calculated for the droplets in the transversally oscillating acoustic gas motion to classify the breakup regime according to those established by the LOx droplet studies of Vieille, Chauveau and Gökalp (1999).

The Weber number and Reynolds number are defined as $We_d = \rho_{gas} U^2 D_d / \sigma_d$ and $Re_d = \rho_{gas} U D_d / \mu_{gas}$, respectively. LOx droplet diameter D_d is chosen for BKH operating conditions based on droplet size measurements and correlations found in literature. The choice of values is discussed further in the following paragraph. The relative velocity of the LOx droplets to the surrounding atmosphere U is taken as the acoustic particle velocity u'. The amplitude of the acoustic velocity is estimated from p' in the usual way (Section 7.3). A value of p' = 3.48 bar was used, which is the maximum acoustic pressure amplitude measured

in BKH testing at 40 bar during 1T mode excitation at 4244 Hz. The resulting acoustic velocity amplitude is $u' = 106$ m/s.

Literature was consulted for appropriate estimates of LOx droplet sizes which might be present in BKH at 40-bar chamber pressure. Droplet Sauter mean diameters, D_{32}, measured in water-air experiments by Lasheras, Villermaux and Hopfinger (1998) fall between $D_{32} = 35$ and 80 μm, depending on downstream position. However, traditional theory-based droplet size estimations and correlations of cold-flow droplet size measurements are usually considered inadequate for predicting droplet size in reacting LOx/H_2 sprays, as emphasised for example in a review by Rahman and Santoro (1994). Gicquel and Brisson (1996) measured a D_{32} of around 74 μm from a single shear coaxial element running LOx/H_2 at 10 bar chamber pressure. Micci and Gandilhon (2008) measured droplet Sauter and arithmetic mean diameters in a LOx/H_2 combustor at 27.5 bar. The injector dimensions and operating conditions mimic those of the SSME pre-burner injector, and also bear close similarity to those of the BKH injector. Their arithmetic droplet diameter results were correlated to a two-parameter log-normal equation, with a range of validity covering their test conditions of $VR = 12$ to 21 and $J = 0.63$ to 1.28. BKH injection conditions for 40 bar, LH_2 operation fall just outside this range, but for want of a closer match the Micci and Gandilhon correlation was used here. Sauter mean diameters were approximately 20 μm larger than the arithmetic mean, and this difference has been added to the correlation result here, giving a droplet diameter of 48 μm. Sauter mean diameter was chosen as it is the diameter of an ideal, spherical droplet with the same volume-to-surface area ratio as the experimentally measured droplets, and is therefore believed to better represent the behaviour of the overall spray. BKH injection conditions for 40 bar tests with GH_2 lie well outside the J range covered by Micci and Gandilhon. Sauter mean diameter D_{32} is shown by Baillot et al. (2009) and Gökalp et al. (2000) to decrease with increasing We_H. Thus for the higher H_2 injection velocity conditions of the GH_2 test, smaller droplet sizes are expected. A droplet size 20 μm smaller than that for the LH_2 condition is guessed, giving 28 μm, which also corresponds to the arithmetic mean diameter estimated with the Micci and Gandilhon correlation for the LH_2 condition. Droplet size is not expected to be affected by the acoustic field, as was concluded by Baillot et al. from their cold-flow tests with acoustic forcing.

Values for LOx droplet surface tension are obtained from the REFPROP fluid properties program (National Institute of Standards and Technology 2002). The values used are in agreement with those from the experimental studies of Vieille et al. (1999, p.4), who give values of σ_O ranging from 2 mN/m in an oxygen atmosphere to 6 mN/m in a helium atmosphere at 40 bar. Density ρ_{gas} and viscosity μ_{gas} depend on the properties of the atmosphere surrounding the LOx droplet in the reacting coaxial spray. Here are considered three possible environments the LOx droplet may find itself in; gaseous hydrogen (GH_2) of the injected coaxial spray, gaseous oxygen (GOx), originating from the vaporising droplet itself, which is warming in the vicinity of the flame, or equilibrium combustion products from primary injection with $ROF = 6$. The reality is probably a mixture of these three cases, but for this analysis three different Weber and Reynolds numbers were calculated for the three types of atmosphere. The correlating ratio of $We_d/Re_d^{0.5}$ was also compared, as it is used by Vieille et al. to establish the regime of secondary breakup.

Droplet and gas properties used for each case processed are gathered in Table 10. Also presented are the maximum values of We_d, Re_d, and $We_d/Re_d^{0.5}$ attained. According to the premise of this analysis, droplets come into being at the point in the acoustic cycle with peak magnitude of acoustic velocity, and immediately experience the maximum values of We_d and Re_d. Figure 8.16 and Figure 8.17 show the LOx droplet breakup regimes established

experimentally by Vieille et al. (1999), reproduced here for comparison with the current results. Due to the large values of We_d obtained in the current analysis, conditions for the hypothetical LOx droplet in BKH appear to lie strongly in the shear breakup regime for all three atmospheric conditions considered in Table 10.

As mentioned at the start of this Section, the typical range of injection velocity ratios *VR* for shear coaxial injectors already places droplets in the shear breakup regime. However, injected jets quickly decelerate following injection, and droplets are produced along a large extent of the core, beginning a few *L*/*D* downstream of injection (see for example Figure 8.4). This means that droplets may exist throughout the spray flame under flow conditions which have relaxed below the threshold for the shear breakup regime. The result summarised in Table 10 thus offers shear-type secondary breakup of LOx droplets, driven by transverse acoustic motion of the flame and gases surrounding the LOx stream of a coaxial injection element, as a process potentially involved in a velocity-coupled driving mechanism for combustion instabilities.

If such a velocity-coupled process were taking place and its influence resulted in an increase in heat release rate from the flame, then an increase in emission intensity might be observed at twice the acoustic frequency. Acoustic particle displacements occur twice for each acoustic pressure cycle, once in the upwards direction and once downwards, thus allowing the proposed shear-breakup process to act twice, assuming directionality of the acoustic displacement to be unimportant. In the OH* emission spectra examined in Section 7.4, intensity fluctuations at double the 1T excitation frequency were often observed to exceed those at the 1T frequency itself. This was previously assumed to be the result of pressure response to the 2T mode, however the action of such a velocity-coupled process proposed here may also explain the response. In order to prove that secondary shear-breakup were responsible for this response, measurements of the relative motion of LOx droplets to the surrounding gas would be required. Interestingly, a similar response at double the 1T mode frequency in tests at 60 bar is absent, seen for example in Figure 7.13. This observation is consistent with the expected absence of LOx droplets at 60 bar, and therefore the absence of acoustic velocity-coupled secondary atomisation.

Table 10: Gas properties and correlating ratios for three different types of atmospheres surrounding LOx droplets in the reacting coaxial spray.

BKH operating condition		40 bar with GH_2			40 bar with LH_2		
LOx droplet diameter	D_d (µm)	28			48		
LOx density	ρ_d (kg/m^3)	920			916		
LOx surface tension	σ_d (mN/m)	4.0			3.6		
Acoustic gas properties (type of atmosphere)		GH_2	GOx	*ROF*=6[a]	GH_2	GOx	*ROF*=6[a]
Temperature	T_{gas} (K)	280	300	3422	75	300	3422
Density	ρ_{gas} (kg/m^3)	3.4	55	1.9	15	55	1.9
Viscosity	μ_{gas} (µPa.s)	8.6	21.5	105	3.9	21.5	105
Droplet Reynolds number	Re_d	1181	7532	53	19,454	12,687	91
Droplet Weber number	We_d	269	4183	147	2253	8289	284
Correlating ratio	$We_d/Re_d^{0.5}$	7.8	48.2	20.1	16.2	73.6	29.7

[a]Properties for *ROF*=6 equilibrium conditions calculated using the CEA2 program (Gordon & McBride 1994)

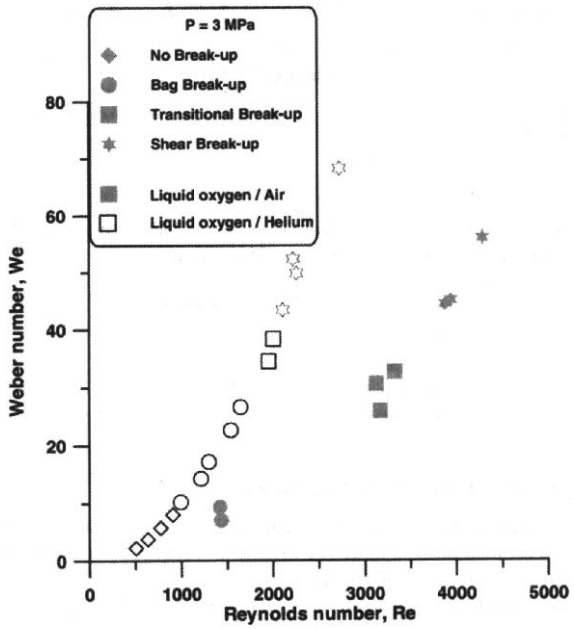

Figure 8.16 Comparison of break-up regime transitions for LOx in dry air and helium under 30 bar (Vieille, Chauveau & Gokalp 1999).

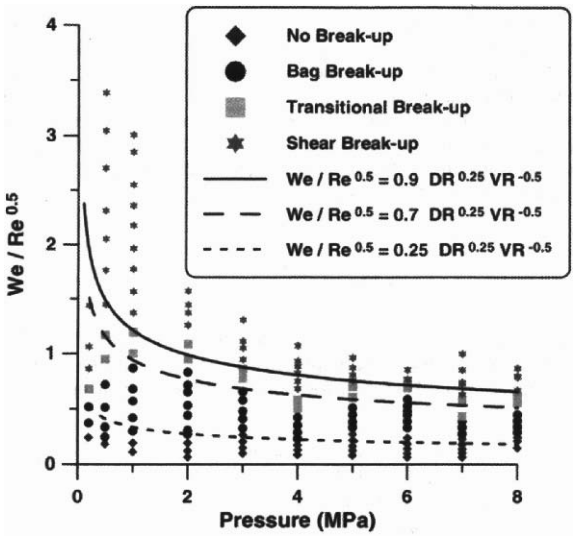

Figure 8.17 Experimental data and the corresponding transition criteria for liquid oxygen droplet breakup regimes (Vieille, Chauveau & Gokalp 1999).

8.6 Summary

High-speed shadowgraph imaging was used to characterise the atomisation and breakup behaviour of the central LOx jet. For off-resonance excitation conditions, the behaviour is considered to be the natural state of the jet, representative of injection in a stable rocket engine. The natural length of the intact LOx core for the operating conditions tested was around 28.5 L/D. This value could not be measured with greater certainty because of the limited axial extent of the optical windows. The natural core breakup mechanism involves the accumulation of large structures of dense oxygen which eventually break free of the end of the core. According to the map of coaxial jet disintegration modes, BKH injection conditions lie in the fibre-type breakup regime. Qualitatively, the fibre-type regime describes well the behaviour of the jet, although the presence of liquid droplets could not be confirmed due to the imaging setup used.

The current experiments were conducted at injection conditions representative of industrial rocket engines, and under acoustic conditions which approach those of naturally occurring HF instabilities in real engines. As far as could be determined from available literature, these are the first optical LOx-core measurements made of an injection element surrounded on all sides by identical elements. Traditional correlations, developed from non-combusting experiments, tend to underestimate the intact length. The applicability of these correlations to realistic LPRE-like conditions is perhaps limited by the lack of co-flow and heat load from surrounding elements. Co-flow from surrounding elements presumably assists the jet to develop further downstream, rather than being forced to expand radially to fill the volume around it, as is the case in single-jet experiments. Intuitively, one may expect the heat load from surrounding elements to increase vaporisation rate and reduce core length. Perhaps the reaction zone in the LOx/H_2 shear layer may act as a shield, with the H_2O combustion product absorbing radiation from surrounding jets. Perhaps the influence of surrounding jets in

establishing an assisting flow-field outweighs the additional heat load from the presence of neighbouring flames. Regardless, more work is required in the field of scaling between cold-flow experiments and realistic rocket engine conditions.

Qualitatively, the appearance of the LOx core structure boundaries in the shadowgraph imaging, as well as its natural atomisation behaviour, are indistinguishable for 40 or 60 bar chamber pressure. It is possible that, despite operation at 60 bar, local conditions on the surface of the LOx jet may still behave according to subcritical conditions, as has been considered by other researchers.

During 1T mode excitation the intact extent of the LOx core decreased to around 30% of its natural length. The decrease in the length is the result of the action of transverse acoustic gas motion. High-speed shadowgraph imaging facilitated observation of a transverse core-stripping mechanism which prevents the core from developing naturally downstream. Material is observed to be removed from the core shortly after injection by entrainment in the oscillating transverse acoustic gas flow. Core length measurements for various excitation amplitudes revealed a somewhat linear decrease in core length with acoustic pressure amplitude (or transverse acoustic velocity). The length also stabilised for higher excitation amplitudes, with fluctuation in the core length also decreasing with acoustic pressure. This reflects the transition from the natural growth-and-detachment behaviour of core breakup to the transverse stripping mechanism observed during 1T-mode acoustic forcing. This observation is hoped to improve understanding of the coupling mechanisms involved in driving instabilities and provide a basis for validation of models of the phenomenon.

Jet flattening is known from other studies to occur under the influence of transverse mode acoustic oscillations, but could not be investigated with the current BKH configuration.

The influence of 1T mode excitation on the secondary breakup of LOx droplets was investigated, assuming LOx droplets may exist in BKH for subcritical chamber pressures. Transverse acoustic gas motion was found to place secondary breakup of LOx droplets strongly in the shear breakup regime, providing context for shear breakup as a process potentially involved in velocity-coupling of HF combustion instabilities. In order to confirm this process is taking place, measurements of the relative motion of LOx droplets to the surrounding gas would be required.

9. CONCLUSIONS

The experimental combustor 'BKH' was developed to address a lack of data for coaxially injected LOx/H_2 at representative liquid propellant rocket engine (LPRE) conditions with externally forced acoustics. A tightly-packed pattern of five injection elements provides a representative environment for the central flame, which was the focus of analysis using optical diagnostic techniques. Using nozzle modulation, two forms of acoustic excitation were applied to the flame; transverse acoustic velocity, and acoustic pressure. Higher operating pressures have been achieved, up to 60 bar, than have previously been attempted with such devices using LOx/H_2 propellants. Operation at 40 and 60 bar includes both the subcritical and supercritical pressure regimes. Operation with cryogenic, 'liquid' hydrogen (LH_2), in addition to ambient temperature, gaseous hydrogen (GH_2) further addresses operating conditions not previously attempted with forced acoustic excitation.

Initial testing was aimed at characterising the acoustic environment in BKH. The primary resonance modes of interest in the BKH combustion chamber were identified. Acoustic baffles in the injection manifold were necessary to render the primary modes free of interference from a powerful injector-coupled mode. This mode was identified and eliminated using a detailed, three-dimensional, finite element acoustic model of the combustor with its injection system. The injector mode originated from the torus-shaped manifold of the secondary H_2 injector. The high power and consistency of this mode suggests annular geometries may be particularly susceptible to spontaneous acoustic resonances. The experience with BKH may serve as a reminder that the acoustic characteristics of an engine should be well understood at the design stage to avoid the potential for injector-coupled instabilities. An effective means studying system acoustics is afforded by finite element models such as that developed for BKH.

With an understanding of the acoustic characteristics of BKH, application of the excitation system was targeted to produce conditions desired for studies of flame-acoustic interaction. Acoustic forcing in BKH simulates well high frequency (HF) combustion instability in real engines, with acoustic pressure amplitude reaching 8.3% (16.6% peak-to-peak) of chamber pressure during excitation of the first transverse (1T) mode. During 1T mode excitation, an increase in c^* efficiency was measured, suggesting that transverse modulation of the flames increases the rate of mixing and combustion.

Flame response to acoustic excitation under subcritical and supercritical operating conditions, with both GH_2 and LH_2, was examined using optical diagnostic techniques. Shadowgraph imaging showed the natural length of the intact LOx core, without acoustic excitation, to be

around 28.5 *L*/*D*. The natural core shedding mechanism involves the accumulation of large structures of dense oxygen which eventually break free of the end of the core. There was no difference in the appearance of the core for subcritical or supercritical chamber pressure, or for injection with GH_2 or LH_2. OH* emission imaging showed a well distributed, turbulent reaction zone which reflects the paths of the LOx jets. Flames from adjacent injectors expand and overlap after a distance of approximately 10 *L/D* downstream of injection.

High-speed shadowgraph and OH* emission imaging revealed the significant influence of 1T-mode excitation on LOx jet and flame development. During 1T mode excitation the core length decreased to around 30% of its natural length. The mode of core breakup changes from its natural growth-and-detachment behaviour to a transverse stripping mechanism resulting from the oscillating transverse acoustic gas motion. High-speed shadowgraph imaging facilitated direct observation of the core-stripping mechanism. With each transverse sweep of acoustic velocity, pockets of reactants and products are removed from the intact part of the core a short distance (2–5 *L/D*) after injection, which prevents the core from developing naturally downstream. The remaining intact part of the core does not bend or deviate from its direction of injection. Simultaneous OH* imaging showed that reduction in LOx core length was accompanied by a retraction of the flame towards the injection plane. Whereas the intact LOx core remains straight, the flame was observed to move in unison with transverse acoustic velocity.

Core length measurements for various excitation amplitudes revealed a linear decrease in core length with acoustic pressure amplitude, or equivalently with transverse acoustic velocity amplitude. The fluctuation in core length also decreased with higher acoustic amplitude. Qualitatively, LOx jets at subcritical and supercritical pressures, and with GH_2 or LH_2 injection, responded similarly to the imposed transverse excitation. However, LOx core measurements for the different pressure regimes and hydrogen injection temperatures may be separated through conditioning with respect to various physical parameters. For example, the ratio of H_2-injection to transverse-acoustic momentum flux separated GH_2 and LH_2 injection, whereas a transverse acoustic Weber number isolated both operating pressure and H_2 temperature. More measurements would be required to better map the responses for various operating conditions, and to determine which conditions most influence the LOx core response.

Study of temporal fluctuation in OH* emission intensity reveals direct response to acoustic pressure. Direct response suggests an increase in heat-release rate due to acceleration of reaction kinetics with increased pressure. During excitation of the first longitudinal (1L) mode, a response factor *N* of around 0.8 was measured from both the intensified camera and photomultiplier readings. Based on the responses to acoustic pressure and velocity observed in BKH, a driving mechanism for HF instabilities involving both may be postulated as follows. The action of the transverse acoustic velocity on the LOx jets causes significant retraction of the region of heat release towards the injection plane. This retraction places the region of heat release into the region of maximum acoustic pressure amplitude of the transverse acoustic mode. Each peak in acoustic pressure is preceded by a sweep of acoustic velocity, which strips material from the LOx core and mixes it with the surrounding H_2. The energy source for driving the instability has thus been prepared and concentrated where it is most needed for coupling with the instability. The mixture then combusts with an accelerated reaction rate in response to the passing pressure peak, which amplifies the instability in accordance with the Rayleigh criterion.

10. OUTLOOK

This work has contributed to the understanding of flame-acoustic interactions in the context of HF instability in LOx/H_2 LPREs. However, there remain many avenues in the BKH project open for further investigation.

A thorough analysis of the acoustic response of BKH to various operating conditions is recommended. Analysis of the phase and amplitude of dynamic pressure measurements from all dynamic pressure sensors in the combustion chamber and injector can provide information about the level and distribution of acoustic energy in the system. System damping, for example, can be determined by measuring the bandwidth of resonance peaks. Such analysis, conducted systematically for all tested operating conditions, may reveal relationships between system responses and different operating conditions. From such relationships, the responsible injection or combustion processes may be inferred.

There remains potential for improvement in the quality of high-speed imaging. The frequency artefacts in the OH* imaging complicated the extraction of flame response measurements, and even led to many data sets having to be discarded. The source of this artefact in the camera has not yet been confirmed, and it is unknown if it can be removed. Removing this artefact from the intensified camera would allow flame responses from a complete set of operating conditions and acoustic excitation profiles to be processed. The shadowgraph imaging suffered from encroachment of infrared emission. Modifying the shadowgraph setup to better resolve the dense oxygen phase would improve the accuracy of LOx core length measurements.

The spread of operating conditions investigated in the current work was relatively narrow. Only one value of mixture ratio was run, $ROF = 6$, and only two values of hydrogen injection temperature, $T_H \sim 50$ or 290 K. The injector geometry of BKH could also be modified to investigate the influence of, for example, LOx-post recess, hydrogen injection annulus area, or injector pattern orientation. Extending the variety of operating conditions and injector configurations tested may lead to the emergence of new relationships between operating conditions and combustor response.

In chapter 6, an unexpected resonance in the secondary H_2 injection system was described. This resonance was removed in BKH through system modification, as it was unwanted in the current experiments. The resonance was thought to arise from the annular geometry of the injection manifold and the positioning of the supply line inlet to the manifold. A similar configuration could be used to intentionally introduce resonance into the injection manifold of

a primary injector. This could either be used to study injection-coupled instability itself, or as an alternative to nozzle-modulation for the excitation of combustion chamber resonance modes.

The finite element model used for acoustic analysis of BKH is based on simple linear acoustics and includes no sources of damping. Inclusion of damping sources and perhaps driving from the location of the secondary nozzle may allow acoustic mode amplitudes to be predicted.

Assessment of flame-acoustic interaction in BKH would benefit from better understanding of the acoustic environment inside the combustion chamber volume. More accurate modelling of acoustic field distributions requires knowledge of the distribution of gas properties in the chamber volume. Higher resolution temperature or dynamic pressure measurements are impractical. Numerical modelling of injection and combustion in BKH could be used to provide a property distribution for integration with the acoustic model.

Natural 1T mode instability in a LPRE subjects the near-injection region to both oscillating acoustic pressure and transverse acoustic velocity. The configuration of BKH made possible the separation of these two types of acoustic interaction. By exciting the chamber 1L mode, coupling of combustion with acoustic pressure was observed, whereas exciting the 1T mode revealed the influence of transverse acoustic velocity on the LOx jet. The observation of these two types of response from the combustion process led to the proposal of a driving mechanism for combustion instabilities which involves both processes. The same methodology could be applied to study an injector design which is known to be unstable in a full-scale engine. Installing the injector in BKH, for example, would allow the interaction of spray-flame and acoustics for unstable injectors to be understood in more detail.

Implementing optical access in experimental rocket combustors is challenging. It is, of course, desirable to directly observe natural HF instability in a cylindrical combustor configuration which experiences natural HF instabilities. The acoustic disturbance in BKH is forced artificially, so it can only be speculated how the response to natural HF instabilities may differ. High-speed optical diagnostics similar to those used with BKH could be applied for the simultaneous observation of LOx jet behaviour and combustion emission. This may allow the two types of response seen in BKH to be identified as they operate in concert during natural 1T-mode instability. However, applying optical access in a cylindrical geometry would be particularly difficult.

Numerical simulation of natural HF instability may be a viable alternative for gaining insight into coupling processes in natural HF instability. It was suggested above that numerical simulation of injection and combustion could be used to improve the accuracy of the acoustic model in BKH. The simulation could be extended to a transient analysis under forced acoustic excitation. Existing acoustic and optical data obtained from BKH testing could be used for validation of the numerical simulation. BKH data would allow the acoustic pressure and velocity responses to be validated separately, before application of the simulation architecture to a naturally unstable engine configuration.

11. REFERENCES

ANSYS Inc (2011) *ANSYS Academic Research* [Computer Software], Release 13.0, ANSYS, Inc., Canonsburg, PA.

Arianespace (2012) *Image library*, Arianespace, viewed 4 June 2012, <http://www.arianespace.com/news-image_library/index.asp>.

Baillot, F., Blaisot, J. B., Boisdron, G. and Dumouchel, C. (2009) 'Behaviour of an air-assisted jet submitted to a transverse high-frequency acoustic field', *Journal of Fluid Mechanics,* vol. 640, pp. 305-342.

Baker, L. J. and Steffen, F. W. (1958) *Screaming tendency of the gaseous-hydrogen - liquid-oxygen propellant combination*, NACA RM E58E09, Lewis Flight Propulsion Laboratory, National Advisory Committee for Aeronautics, Cleveland, Ohio, 30 Sept 1958.

Bellows, B. D. and Lieuwen, T. (2004) *Nonlinear response of a premixed combustor to forced acoustic oscillations*, 42nd AIAA Aerospace Sciences Meeting and Exhibit, AIAA, Reno, Nevada, 5-8 January 2004.

Berman, K. and Cheney Jr., S. (1955) 'Rocket motor instability studies', *Journal of the American Rocket Society,* vol. 25, no. 10, pp. 513-518.

Bibik, O., Lubarsky, E., Shcherbik, D., Hadjipanayis, M. and Zinn, B. T. (2008) *Rotational traveling of tangential wave in multi-injectors LRE combustor simulator*, 46th AIAA Aerospace Sciences Meeting and Exhibit, AIAA, Reno, Nevada, 7-10 January 2008.

Boeing (2007) *Boeing launch services*, viewed 8 Oct 2007, <http://www.boeing.com/defense-space/space/bls/index.html>.

Bracco, F. V. and Harrje, D. T. (1972) 'Axial energy release', in *Liquid propellant rocket combustion instability*, eds Harrje, D. T. and Reardon, F. H., NASA, Washington, DC, pp. 318-322.

Bragg, S. L. (1963) 'Combustion noise', *Journal of the Institute of Fuel,* vol. 36, pp. 12-16.

Breisacher, K. J. (1993) *Axisymmetric single shear element combustion instability experiment*, 29th AIAA/ASME/SAE/ASEE Joint Propulsion Conference & Exhibit, AIAA, Monterey, California, 28-30 June 1993.

Candel, S., Herding, G., Synder, R., Scouflaire, P., Rolon, C., Vingert, L., Habiballah, M., Grisch, F., Péalat, M., Bouchardy, P., Stepowski, D., Cessou, A. and Colin, P. (1998) 'Experimental investigation of shear coaxial cryogenic jet flames', *Journal of Propulsion and Power,* vol. 14, no. 5, pp. 826-834.

Candel, S., Juniper, M., Scouflaire, P., Rolon, C., Clauss, W., Klimenko, D. N., Oschwald, M., Grisch, F., Bouchardy, P. and Vingert, L. (2003) *Investigations of subcritical and transcritical cryogenic combustion using imaging and laser techniques*, 5th International Symposium on Liquid Space Propulsion, Chattanooga, TN, 28-30 October 2003.

Candel, S., Juniper, M., Singla, G., Scouflaire, P. and Rolon, C. (2006) 'Structure and dynamics of cryogenic flames at supercritical pressure', *Combustion Science and Technology,* vol. 178, pp. 161-192.

Chehroudi, B. (2009) *A unified approach on combustion instability in cryogenic liquid rockets*, 47th AIAA Aerospace Sciences Meeting, AIAA, Orlando, Florida, 5-8 January 2009.

Chehroudi, B., Davis, D. W. and Talley, D. (2003) *Initial results from a cryogenic coaxial injector in an acoustic field*, 44th Aerospace Sciences Meeting & Exhibit, AIAA, Reno, Nevada, 6-9 January 2003.

Chehroudi, B., Talley, D., Mayer, W., Branam, R., Smith, J. J., Schik, A. and Oschwald, M. (2003) *Understanding injection into high pressure supercritical environments*, 5th International Symposium on Liquid Space Propulsion, Chattanooga, TN, October 28-30.

Cheuret, F. (2005) *Instabilités thermo-acoustiques de combustion haute-fréquence dans les moteurs fusées*, PhD Thesis, Institut de Recherche sur les Phénomènes Hors Équilibre, Université de Provence - Aix-Marseille, Marseille.

Chigier, N. and Reitz, R. D. (1995) 'Regimes of jet breakup and breakup mechanisms (physical aspects)', in *Recent advances in spray combustion: spray atomization and droplet burning phenomena*, vol. 166, ed. Kuo, K., AIAA, New York, pp. 109-136.

Conrad, E. W., Bloomer, H. E., Wanhainen, J. P. and Vincent, D. W. (1968) *Interim summary of liquid rocket acoustic-mode-instability studies at a nominal thrust of 20000 pounds*, NASA TN D-4968, Lewis Research Center, NASA, Cleveland, Ohio, December 1968.

Crocco, L. (1951) 'Aspects of combustion stability in liquid propellant rocket motors Part I: Fundamentals. Low frequency instability with monopropellants', *Journal of the American Rocket Society,* vol. 21, no. 6, pp. 163-178.

Crocco, L. (1952) 'Aspects of combustion stability in liquid propellant rocket motors Part II: Low frequency instability with bipropellants. High frequency instability', *Journal of the American Rocket Society,* vol. 22, no. 1, pp. 7-16.

Crocco, L. (1972) 'The sensitive time lag theory', in *Liquid propellant rocket combustion instability*, eds Harrje, D. T. and Reardon, F. H., NASA, Washington, DC, pp. 170-194.

Crocco, L. and Cheng, S.-I. (1953) 'High-frequency combustion instability in rocket motor with concentrated combustion', *Journal of the American Rocket Society,* vol. 23, no. 5, pp. 301-313,322.

Crocco, L., Grey, J. and Harrje, D. T. (1960) 'Theory of liquid propellant rocket combustion instability and its experimental verification', *ARS Journal,* vol. 30, no. 2, pp. 159-168.

Crocco, L., Harrje, D. T. and Reardon, F. H. (1962) 'Transverse combustion instability in liquid propellant rocket motors', *ARS Journal,* vol. 32, no. 3, pp. 366-373.

Culick, F. E. C. (2006) *Unsteady Motions in Combustion Chambers for Propulsion Systems*, Research and Technology Organisation, North Atlantic Treaty Organisation.

Curreri, P. A. (2006) *Processing of space resources to enable the Vision for Space Exploration*, International Conference on Solidification Science and Processing, Jaipur, India, 20-23 November 2006.

Davis, D. W. and Chehroudi, B. (2006) *Shear-coaxial jets from a rocket-like injector in a transverse acoustic field at high pressures*, 44th AIAA Aerospace Sciences Meeting and Exhibit, AIAA, Reno, Nevada, 9-12 Jan 2006.

Davis, D. W. and Chehroudi, B. (2007) 'Measurements in an acoustically driven coaxial jet under sub-, near-, and supercritical conditions', *Journal of Propulsion and Power,* vol. 23, no. 2, pp. 364-374.

de Izarra, C. (2000) 'UV OH spectrum used as a molecular pyrometer', *Journal of Physics D: Applied Physics,* vol. 33, pp. 1697-1704.

DKimages (2007) *Ariane*, viewed 8 Oct 2007, <http://www.dkimages.com/discover/Home/Technology/Space-Exploration/Rockets-and-Launch-Vehicles/Ariane/Ariane-08.html>.

Docquier, N. and Candel, S. (2002) 'Combustion control and sensors: a review', *Progress in Energy and Combustion Science,* vol. 28, pp. 107-150.

Dranovsky, M. L. (2007) *Combustion instabilities in liquid rocket engines: testing and development practices in Russia*, American Institute of Aeronautics and Astronautics, Washington, D.C.

Dykema, O. W. (1972) 'Injector patterns', in *Liquid propellant rocket combustion instability*, eds Harrje, D. T. and Reardon, F. H., NASA, Washington, DC, pp. 336-373.

Farago, Z. and Chigier, N. (1992) 'Morphological classification of disintegration of round jets in a coaxial airstream', *Atomization and Sprays,* vol. 2, pp. 137-153.

Feiler, C. E. and Heidmann, M. F. (1967) *Dynamic response of gaseous-hydrogen flow system and its application to high-frequency combustion instability*, NASA TN D-4040, Lewis Research Center, NASA, Cleveland, Ohio, June 1967.

Fortunier, P. (1999) *R&T Program on high frequency combustion instabilities in liquid rocket engines*, DLA/SDT/P/L/99.031, Centre National D'Etudes Spatiales, Paris, 3 March 1999.

Fry, R. S. and Klem, M. D. (1997) *Guidelines for combustion stability specifications and verification procedures for liquid propellant rocket engines*, Chemical Propulsion Information Agency, Columbia, Maryland, January 1997.

Gaydon, A. G. (1974) *The spectroscopy of flames*, Chapman and Hall, London.

Gaydon, A. G. and Wolfhard, H. G. (1978) *Flames - their structure, radiation and temperature*, 4 Ed., Chapman and Hall, London.

Ghosh, A., Diao, Q. and Yu, K. H. (2006) *Flame-acoustic interaction in GOx/GH2 shear-coaxial injector flow-field*, 44th AIAA Aerospace Sciences Meeting and Exhibit, AIAA, Reno, Nevada, 9-12 Jan 2006.

Ghosh, A., Diao, Q. and Yu, K. H. (2007) *Experimental Investigation of Shear-Coaxial Injector Flame Stability on Flow Parameters*, 43rd AIAA/ASME/SAE/ASEE Joint Propulsion Conference, American Institute of Aeronautics and Astronautics, Cincinnati, Ohio, 8-11 Jul 2007.

Gicquel, P. P. and Brisson, E. (1996) *Spray Characterization in two phase reactive flows*, 5^{e} Congrès Francophone de Vélocimétrie Laser, Office National D'Études et de Recherches Aérospatiales, Rouen, France, 24-27 September 1996.

Glogowski, M., Bar-Gill, M., Puissant, C., Kaltz, T., Milicic, M. and Micci, M. (1994) *Shear Coaxial Injector Instability Mechanisms*, 30th AIAA/ASME/SAE/ASEE Joint Propulsion Conference, Indianapolis, Indiana, 27-29 Jun 1994.

Gökalp, I., Chauveau, C., Morin, C., Vieille, B. and Birouk, M. (2000) 'Improving droplet breakup and vaporization models by including high pressure and turbulence effects', *Atomization and Sprays,* vol. 10, pp. 475-510.

Gordon, S. and McBride, B. J. (1994) *Computer Program for Calculation of Complex Chemical Equilibrium Compositions and Applications. Part 1: Analysis*, NASA-RP-1311, Glenn Research Center, NASA, Cleveland, Ohio, 1 October 1994.

Grisch, F., Bouchardy, P., Vingert, L., Clauss, W., Oschwald, M. and Smirnov, V. V. (2004) 'CARS measurements at high pressure in cryogenic LOX-GH2 jet flames', in *Liquid rocket thrust chambers: aspects of modeling, analysis, and design*, vol. 200, eds Hulka, J., Habiballah, M., Yang, V. and Popp, M., AIAA, Washington, DC.

Haberzettl, A. (2000) *European research and technology test bench P8 for high pressure liquid rocket propellants*, 36th AIAA/ASME/ASEE Joint Propulsion Conference and Exhibit, AIAA, Huntsville, Alabama, 16-19 July 2000.

Harrje, D. T. (1972) 'Historical survey', in *Liquid propellant rocket combustion instability*, eds Harrje, D. T. and Reardon, F. H., NASA, Washington, DC, pp. 30-34.

Harrje, D. T. and Reardon, F. H. (eds) (1972) *Liquid propellant rocket combustion instability,* National Aeronautics and Space Administration, Washington, DC.

Harvazinski, M. E., Anderson, W. E. and Merkle, C. L. (2011) *Combustion instability diagnostics using the Rayleigh index*, 47th AIAA/ASME/SAE/ASEE Joint Propulsion Conference & Exhibit, AIAA, San Diego, California, 31 July - 3 August 2011.

Heidmann, M. F. (1965a) *Oscillatory combustion of a liquid-oxygen jet with gaseous hydrogen*, NASA TN D-2753, Lewis Research Center, NASA, Cleveland, Ohio, March 1965.

Heidmann, M. F. (1965b) *Oxygen-jet behavior during combustion instability in a two-dimensional combustor*, NASA TN D-2725, Lewis Research Center, NASA, Cleveland, Ohio, March 1965.

Heidmann, M. F. and Groeneweg, J. F. (1969) *Analysis of the dynamic response of liquid jet atomization to acoustic oscillations*, NASA TN D-5339, NASA Lewis Research Center, Cleveland, Ohio.

Heidmann, M. F. and Wieber, P. R. (1966a) *Analysis of frequency response characteristics of propellant vaporization*, NASA TN D-3749, Lewis Research Centre, NASA, Cleveland, Ohio.

Heidmann, M. F. and Wieber, P. R. (1966b) *Analysis of n-Heptane vaporization in unstable combustor with traveling transverse oscillations*, NASA TN D-3424, NASA, Cleveland, Ohio, May 1966.

Heinzel, G., Rüdiger, A. and Schilling, R. (2002) *Spectrum and spectral density estimation by the Discrete Fourier transform (DFT), including a comprehensive list of window functions and some new flat-top windows*, Max-Planck-Institut für Gravitationsphysik, Hannover, Germany, 15 February 2002.

Hornstein, B. (1965) *Research study of light emission caused by pressure fluctuations in rocket engines*, RMD 5516-F, Thiokol Chemical Corporation, Denville, New Jersey, May 1965.

Hornstein, B., Budnik, C. and Courtney, W. (1966) *Research study of light emission caused by pressure fluctuations in rocket engines*, RMD 5520-F, Thiokol Chemical Corporation, Denville, New Jersey, March 1966.

Hulka, J. and Hutt, J. J. (1995) 'Instability phenomena in liquid oxygen/hydrogen propellant rocket engines', in *Liquid rocket engine combustion instability*, vol. 169, eds Yang, V. and Anderson, W., AIAA, Washington, DC, pp. 39-72.

Hurlbert, E. A., Sun, J. L. and Zhang, B. (1995) 'Instability phenomena in earth storable bipropellant rocket engines', in *Liquid Rocket Engine Combustion Instability*, vol. 169, eds Yang, V. and Anderson, W., AIAA, Washington, DC, pp. 113-142.

Hutt, J. J. and Rocker, M. (1995) 'High-frequency injection-coupled combustion instability', in *Liquid rocket engine combustion instability*, vol. 169, eds Yang, V. and Anderson, W., AIAA, Washington, DC, pp. 345-356.

Ivancic, B. and Mayer, W. (2002) 'Time- and length scales of combustion in liquid rocket thrust chambers', *Journal of Propulsion and Power,* vol. 18, no. 2, pp. 247-253.

Kathan, R., Kaess, R., Pieringer, J. E. and Sattelmayer, T. (2010) *Nozzle admittance for higher modes*, 59. Deutscher Luft- und Raumfahrtkongress, Deutsche Gesellschaft für Luft- und Raumfahrt, Hamburg, 31 August - 2 September 2010.

Kawashima, H., Kobayashi, K. and Tomita, T. (2010) *A Combustion Instability Phenomenon on a LOX/Methane Subscale Combustor*, 46th AIAA/ASME/SAE/ASEE Joint Propulsion Conference & Exhibit, AIAA, Nashville, Tennessee, 25-28 July 2010.

Kim, B.-D., Heister, S. D. and Collicott, S. H. (2005) 'Three-dimensional flow simulations in the recessed region of a coaxial injector', *Journal of Propulsion and Power,* vol. 21, no. 4, pp. 728-742.

Knapp, B., Farago, Z. and Oschwald, M. (2007) *Interaction of LOx/GH2 spray-combustion with acoustics*, 45th AIAA Aerospace Sciences Meeting and Exhibit, AIAA, Reno, Nevada, 8-11 January 2007.

Knapp, B. and Oschwald, M. (2006) *High speed visualization of flame response in a LOx/H2 combustion chamber during external excitation*, 12th International Symposium on Flow Visualization, German Aerospace Centre (DLR), Gottingen, Germany, 10-14 September 2006.

Kobayashi, K., Daimon, Y., Iizuka, N., Tamura, H., Mitani, T. and Onodera, T. (2011) *Studies on combustion instability for liquid propellant rocket engines*, 47th AIAA/ASME/SAE/ASEE Joint Propulsion Conference & Exhibit, AIAA, San Diego, California, 31 July - 3 August 2011.

Lasheras, J. C. and Hopfinger, E. (2000) 'Liquid jet instability and atomization in a coaxial gas stream', in *Annual Review of Fluid Mechanics*, Annual Review, pp. 275-308.

Lasheras, J. C., Villermaux, E. and Hopfinger, E. (1998) 'Break-up and atomization of a round water jet by a high-speed annular air jet', *Journal of Fluid Mechanics,* vol. 357, pp. 351-379.

Lecourt, R. and Foucaud, R. (1987) *Experiments on Stability of Liquid Propellant Rocket Motors*, AIAA/SAE/ASME/ASEE 23rd Joint Propulsion Conference, American Institute of Aeronautics and Astronautics, San Diego, California, 29 Jun - 2 Jul 1987.

Leyva, I. A., Chehroudi, B. and Talley, D. G. (2007) *Dark core analysis of coaxial injectors at sub-, near-, and supercritical pressures in a transverse acoustic field*, 43rd AIAA/ASME/SAE/ASEE Joint Propulsion Conference & Exhibit, AIAA, Cincinnati, OH, 8-11 July 2007.

Leyva, I. A., Rodriguez, J. I., Chehroudi, B. and Talley, D. G. (2008) *Preliminary Results on Coaxial Jet Spread Angles and the Effects of Variable Phase Transverse Acoustic Fields*, 46th Aerospace Sciences Meeting & Exhibit, AIAA, Reno, Nevada, 7-10 January 2008.

Litchford, R. J. and Luo, W. (2008) *On Destructive Liquid Rocket Resonant Combustion*, 44th AIAA/ASME/SAE/ASEE Joint Propulsion Conference & Exhibit, American Institute of Aeronautics and Astronautics, Hartford, Connecticut, 21-23 Jul 2008.

Liu, T., Zong, N. and Yang, V. (2006) *Dynamics of shear-coaxial cryogenic nitrogen jets with acoustic excitation under supercritical conditions*, 44th AIAA Aerospace Sciences Meeting and Exhibit, AIAA, Reno, Nevada, 9-12 Jan 2006.

Locke, J. M., Pal, S., Woodward, R. D. and Santoro, R. J. (2010) *High speed visualization of LOX/GH2 rocket injector flowfield: hot-fire and cold-flow experiments*, 46th AIAA/ASME/SAE/ASEE Joint Propulsion Conference & Exhibit, AIAA, Nashville, Tennessee, 25-28 July 2010.

Lord Rayleigh, J. (1878) 'The explanation of certain acoustical phenomena', *Nature,* vol. 18, pp. 319-321.

Lord Rayleigh, J. (1945) *The theory of sound*, 2nd Ed., Dover Publications, New York.

Lubarsky, E., Hadjipanayis, M., Shcherbik, D., Bibik, O. and Zinn, B. T. (2008) *Control of tangential instability by asymmetric baffle*, 46th AIAA Aerospace Sciences Meeting and Exhibit, AIAA, Reno, Nevada, 7-10 January 2008.

Lux, J. and Haidn, O. (2009) 'Effect of Recess in High-Pressure Liquid Oxygen/Methane Coaxial Injection and Combustion', *Journal of Propulsion and Power,* vol. 25, no. 1, pp. 24-32.

Marble, F. E. and Candel, S. (1977) 'Acoustic disturbance from gas non-uniformities convected through a nozzle', *Journal of Sound and Vibration,* vol. 55, no. 2, pp. 225-243.

Marshall, W., Pal, S., Woodward, R. D., Santoro, R. J., Smith, R., Xia, G., Sankaran, V. and Merkle, C. L. (2006a) *Experimental and computational investigation of combustor acoustics and instabilities, part II: transverse modes*, 44th AIAA Aerospace Sciences Meeting and Exhibit, AIAA, Reno, Nevada, 9-12 Jan 2006.

Marshall, W. M., Pal, S., Woodward, R. D. and Santoro, R. J. (2006b) *combustion instability studies using gaseous methane and liquid oxygen*, 42nd AIAA/ASME/SAE/ASEE Joint Propulsion Conference & Exhibit, AIAA, Sacramento, California.

Mayer, W., Ivancic, B., Schik, A. and Hornung, U. (1998a) *Propellant atomization in LOx/GH2 rocket combustors*, 34th AIAA/AME/SAE/ASEE Joint Propulsion Conference & Exhibit, AIAA, Cleveland, Ohio, 13-15 July 1998.

Mayer, W., Schik, A., Schweitzer, C. and Schaffler, M. (1996) *Injection and mixing processes in high pressure LOx/GH2 rocket combustors*, 32nd AIAA/ASME/SAE/ASEE Joint Propulsion Conference, AIAA, Lake Buena Vista, FL, 1-3 July 1996.

Mayer, W., Schik, A. H., Vieille, B., Chauveau, C., Gokalp, I., Talley, D. G. and Woodward, R. D. (1998b) 'Atomization and breakup of cryogenic propellants under high-pressure subcritical and supercritical conditions', *Journal of Propulsion and Power,* vol. 14, no. 5, pp. 835-842.

Mayer, W. and Tamura, H. (1996) 'Propellant injection in a liquid oxygen/gaseous hydrogen rocket engine', *Journal of Propulsion and Power,* vol. 12, no. 6, pp. 1137-1147.

Mayer, W. O. H. and Smith, J. J. (2004) 'Fundamentals of supercritical mixing and combustion of cryogenic propellants', in *Liquid Rocket Thrust Chambers: Aspects of Modeling, Analysis and Design*, vol. 200, ed. Zarchan, P., AIAA, Washington, DC.

Méry, Y., Ducruix, S., Scouflaire, P. and Candel, S. (2008) *Injection coupling with high amplitude transverse modes : experimentation and simulation*, 2nd Colloque INCA, Rouen, France, 23-24 October 2008.

Micci, M. M. and Gandilhon, D. (2008) 'Shear coaxial injector LOX droplet measurements as a function of hydrogen injection temperature', *Atomization and Sprays,* vol. 18, pp. 85-96.

Miesse, C. C. (1955) 'The effect of ambient pressure oscillations on the disintegration and dispersion of a liquid jet', *Journal of the American Rocket Society,* vol. 25, no. 10, pp. 525-530,534.

Miller, K. J., Sisco, J. C., Nugent, N. and Anderson, W. (2005) *Experimental study of combustion instabilities in a single-element coaxial swirl injector*, 41st AIAA/ASME/SAE/ASEE Joint Propulsion Conference & Exhibit, AIAA, Tucson Arizona, 10-13 July 2005.

Monteil, V. H. and Dykema, O. W. (1972) 'Dynamic stability', in *Liquid propellant rocket combustion instability*, eds Harrje, D. T. and Reardon, F. H., NASA, Washington, DC, pp. 23-29.

NASA (2007) *NASA - Discovery's journey to the pad*, viewed 8 Oct 2007, <http://www.nasa.gov/mission_pages/shuttle/multimedia/120_rolloutgallery.html>.

National Institute of Standards and Technology (2002) *Reference Fluid Thermodynamic and Transport Properties (REFPROP)* [Computer Software], Version 7.0, U.S. Department of Commerce, Gaithersburg, MD.

National Institute of Standards and Technology (2005) *Thermophysical properties of fluid systems*, U.S. Department of Commerce, <http://webbook.nist.gov/chemistry/fluid>.

Newman, J. A. and Brzustowski, T. A. (1971) 'Behavior of a liquid jet near the thermodynamic critical region', *AIAA Journal,* vol. 9, no. 8, pp. pp. 1595-1602.

Nunome, Y., Onodera, T., Sasaki, M., Tomita, T., Kobayashi, K. and Daimon, Y. (2011) *Combustion instability phenomena observed during cryogenic hydrogen injection temperature ramping tests for single coaxial injector elements*, 47th AIAA/ASME/SAE/ASEE Joint Propulsion Conference & Exhibit, AIAA, San Diego, California.

Nunome, Y., Takahashi, M., Kumakawa, A., Miyazaki, K., Yoshida, S. and Onga, T. (2008) *High-frequency Flame Oscillation Observed at a Coaxial LOX/LH2 Injector Element*, 44th AIAA/ASME/SAE/ASEE Joint Propulsion Conference & Exhibit, American Institute of Aeronautics and Astronautics, Hartford, Connecticut, 21-23 July 2008.

Nunome, Y., Tamura, H., Onodera, T., Sakamoto, H., Kumakawa, A. and Inamura, T. (2009) *Effect of liquid disintegration on flow instability in a recessed region of a shear coaxial injector*, 45th AIAA/ASME/SAE/ASEE Joint Propulsion Conference & Exhibit, AIAA, Denver, Colorado, 2-5 August 2009.

Oefelein, J. C. (2006) 'Mixing and combustion of cryogenic oxygen-hydrogen shear-coaxial jet flames at supercritical pressure', *Combustion Science and Technology,* vol. 178, pp. 229-252.

Oefelein, J. C. and Yang, V. (1993) 'Comprehensive Review of Liquid-Propellant Combustion Instabilities in F-1 Engines', *Journal of Propulsion and Power,* vol. 9, no. 5, pp. 657-677.

Osborn, J. R. (1972) 'Transverse energy release distribution', in *Liquid propellant rocket combustion instability*, eds Harrje, D. T. and Reardon, F. H., NASA, Washington, DC, pp. 322-325.

Oschwald, M., Farago, Z., Searby, G. and Cheuret, F. (2008a) 'Resonance Frequencies and Damping of a Combustor Acoustically Coupled to an Absorber', *Journal of Propulsion and Power,* vol. 24, no. 3, pp. 524-533.

Oschwald, M. and Knapp, B. (2009) 'Investigation of the combustion chamber acoustics and its interaction with LOX/H2 spray flames', in *Progress in Propulsion Physics*, eds DeLuca, L. T., Bonnal, C., Haidn, O. J. and Frolov, S. M., Torus Press and EDP Sciences, pp. 243-262.

Oschwald, M. and Micci, M. (2002) 'Spreading angle and centerline variation of density of supercritical nitrogen jets', *Atomization and Sprays,* vol. 12, pp. 91-106.

Oschwald, M., Naclerio, S., Yang, B. and Cuoco, F. (2008b) *Experimental investigation of flame stabilization in coaxial LOX/H_2 and LOX/CH_4 spray flames*, International Conference on Liquid Atomization and Spray Systems, ILASS, Como Lake, Italy.

Oschwald, M. and Schik, A. (1999) 'Supercritical nitrogen free jet investigated by spontaneous Raman scattering', *Experiments in Fluids,* vol. 27, pp. 497-506.

Oschwald, M., Schik, A., Klar, M. and Mayer, W. (1999) *Investigation of coaxial LN2/GH2-injection at supercritical pressure by spontaneous Raman scattering*, 34th AIAA/ASME/SAE/ASEE Joint Propulsion Conference & Exhibit, AIAA, Los Angeles, CA, 20-24 June 1999.

Oschwald, M., Smith, J. J., Branam, R., Hussong, J., Schik, A., Chehroudi, B. and Talley, D. (2006) 'Injection of fluids into supercritical environments', *Combustion Science and Technology,* vol. 178, pp. 49-100.

Pauly, C. (2008) *CFD simulation report: combustion chamber "BKB HF" modelling*, DLR-LA-BK-RP-001, German Aerospace Center, Institute for Space Propulsion, Hardthausen, 4 July 2008.

PDE Solutions Inc. (2002) *FlexPDE 3.01d Professional* [Computer Software], PDE Solutions Inc., Spokane Valley, WA.

Pomeroy, B. R., Morgan, C. and Anderson, W. E. (2011) *Response of a gas-centered swirl coaxial injector to transverse instabilities*, 47th AIAA/ASME/SAE/ASEE Joint Propulsion Conference & Exhibit, AIAA, San Diego, California, 31 July - 3 August 2011.

Pomeroy, B. R., Sisco, J. C., Eckstein, J. R. and Anderson, W. E. (2008) *Characterization of Gas-Centered Swirl-Coaxial Injector Stability in a Subscale Multi-Element Combustor*, 44th AIAA/ASME/SAE/ASEE Joint Propulsion Conference & Exhibit, AIAA, Hartford, CT, 21-23 July 2008.

Preclik, D. and Spagna, P. (1989) *Low frequency and high frequency combustion oscillation phenomena inside a rocket combustion chamber fed by liquid or gaseous propellants*, AGARD Conference Proceedings vol. 450, NATO Advisory Group for Aeronautical Research and Development, Neuilly Sur Seine, France.

Priem, R. J. and Guentert, D. C. (1962) *Combustion instability limits determined by a nonlinear theory and a one-dimensional model*, NASA TN D-1409, Lewis Research Center, NASA, Cleveland, Ohio, Oct 1962.

Putnam, A. A. (1971) *Combustion-driven oscillations in industry*, American Elsevier Publishing Company Inc., New York.

Rahman, S. A. and Santoro, R. J. (1994) *A Review of Coaxial Gas/Liquid Spray Experiments and Correlations*, 30th AIAA/ASME/SAE/ASEE Joint Propulsion Conference, American Institute of Aeronautics and Astronautics, Indianapolis, Indiana, 27-29 Jun 1994.

Reardon, F. H. (1972) 'Injector-face baffles', in *Liquid propellant rocket combustion instability*, eds Harrje, D. T. and Reardon, F. H., NASA, Washington, DC, pp. 156 - 159.

Rey, C., Ducruix, S., Richecoeur, F., Scouflaire, P., Vingert, L. and Candel, S. (2004) *High Frequency Combustion Instabilities Associated with Collective Interactions in Liquid Propulsion*, 40th AIAA/ASME/SAE/ASEE Joint Propulsion Conference & Exhibit, AIAA, Fort Lauderdale, Florida, 11-14 July 2004.

Rey, C., Ducruix, S., Scouflaire, P., Vingert, L. and Candel, S. (2003) *Experimental Analysis of High Frequency Combustion Instabilities associated with Collective Interactions*, 4th Pacific Symposium on Flow Visualization and Image Processing, Pacific Center of Thermal-Fluids Engineering, Chamonix, France, 3-5 June 2003.

Richecoeur, F. (2006) *Expérimentations et simulations numériques des interactions entre modes acoustiques transverses et flammes cryotechniques*, PhD Thesis, Laboratoire d'Énergétique Moléculaire et Macroscopique, Combustion (EM2C) du CNRS et de l'ECP, Ecole Centrale Paris, Paris.

Richecoeur, F., Ducruix, S., Scouflaire, P. and Candel, S. (2008) 'Experimental investigation of high-frequency combustion instabilities in liquid rocket engine', *Acta Astronautica,* vol. 62, no. 1, pp. 18-27.

Richecoeur, F., Ducruix, S., Scouflaire, P. and Candel, S. (2009) 'Effect of temperature fluctuations on high frequency acoustic coupling', *Proceedings of the Combustion Institute,* vol. 32, no. 2, pp. 1663-1670.

Richecoeur, F., Scouflaire, P., Ducruix, S. and Candel, S. (2006a) 'High frequency transverse acoustic coupling in a multiple injector cryogenic combustor', *Journal of Propulsion and Power,* vol. 22, no. 4, pp. 790-799.

Richecoeur, F., Scouflaire, P., Ducruix, S. and Candel, S. (2006b) *Interactions between propellant jets and acoustic modes in liquid rocket engines : experiments and simulations*, 42nd AIAA/ASME/SAE/ASEE Joint Propulsion Conference & Exhibit, American Institute of Aeronautics and Astronautics, Sacramento, California, 9-12 Jul 2006.

Rodriguez, J. I., Leyva, I. A., Chehroudi, B. and Talley, D. G. (2008) *Results on Subcritical One-Phase Coaxial Jet Spread Angles and Subcritical to Supercritical Acoustically-Forced Coaxial Jet Dark Core Lengths*, 44th AIAA/ASME/SAE/ASEE Joint Propulsion Conference & Exhibit, American Institute of Aeronautics and Astronautics, Hartford, Connecticut, 21-23 Jul 2008.

Rosner, D. E. (1967) 'On liquid droplet combustion at high pressures', *AIAA Journal,* vol. 5, no. 1, pp. 163-166.

Rosner, D. E. (1972) 'Liquid droplet vaporization and combustion', in *Liquid propellant rocket combustion instability*, eds Harrje, D. T. and Reardon, F. H., NASA, Washington, DC, pp. 74-99.

Schmitt, T., Mery, Y., Boileau, M. and Candel, S. (2011) 'Large-Eddy Simulation of oxygen/methane flames under transcritical conditions', *Proceedings of the Combustion Institute,* vol. 33, pp. 1383-1390.

Searby, G., Nicole, A., Habiballah, M. and Laroche, E. (2008) 'Prediction of the Efficiency of Acoustic Damping Cavities', *Journal of Propulsion and Power,* vol. 24, no. 3, pp. 516-523.

Sirignano, W. A. (1972) 'Analytical models of high frequency combustion instability: Introduction', in *Liquid propellant rocket combustion instability*, eds Harrje, D. T. and Reardon, F. H., NASA, Washington, DC, pp. 167-170.

Sirignano, W. A., Delplanque, J.-P., Chiang, C. H. and Bhatia, R. (1995) 'Liquid-propellant droplet vaporization: a rate-controlling process for combustion instability', in *Liquid rocket engine combustion instability*, vol. 169, eds Yang, V. and Anderson, W., AIAA, Washington, DC, pp. 307-344.

Sisco, J. C., Smith, R. J., Sankaran, V. and Anderson, W. E. (2006) *Examination of mode shapes in an unstable model rocket combustor*, 42nd AIAA/ASME/SAE/ASEE Joint Propulsion Conference & Exhibit, AIAA, Sacramento, California, 9-12 July 2006.

Sliphorst, M. (2011) *High Frequency Combustion Instabilities of LOx/CH4 Spray Flames in Rocket Engine Combustion Chambers*, PhD Thesis, Technische Universiteit Delft, Delft, The Netherlands.

Sliphorst, M., Gröning, S. and Oschwald, M. (2011) 'Theoretical and experimental identification of acoustic spinning mode in a cylindrical combustor', *Journal of Propulsion and Power,* vol. 27, no. 1, pp. 182-189.

Smith, J. J. (2007) *High pressure LOx/H_2 rocket engine combustion*, PhD Thesis, School of Mechanical Engineering, The University of Adelaide, Adelaide.

Smith, J. J., Bechle, M., Suslov, D., Oschwald, M., Haidn, O. J. and Schneider, G. M. (2004) *High pressure LOx/H_2 combustion and flame dynamics - Preliminary results*, 40th AIAA/ASME/SAE/ASEE Joint Propulsion Conference & Exhibit, AIAA, Fort Lauderdale, Florida, 14 Jul 2004.

Smith, J. J., Schneider, G., Suslov, D., Oschwald, M. and Haidn, O. (2007) 'Steady-state high pressure LOx/H_2 rocket engine combustion', *Aerospace Science and Technology,* vol. 11, pp. 39 - 47.

Spalding, D. B. (1959) 'Theory of particle combustion at high pressures', *ARS Journal,* vol. 29, pp. 828-835.

Suslov, D., Woschnak, A., Greuel, D. and Oschwald, M. (2005) *Measurement techniques for investigation of heat transfer processes at European Research and Technology Test Facility P8*, European Conference for Aero-space Sciences, Moscow, Russia.

Sutton, G. P. and Biblarz, O. (2001) *Rocket propulsion elements*, 7th Ed., John Wiley and Sons, New York.

Tischler, A. O. and Male, T. (1956) *Oscillatory combustion in rocket propulsion engines*, Gas Dynamics Symposium on Aerothermochemistry, Northwestern University, Evanston, Illinois, 22-24 August 1955.

Tomazic, W. A., Conrad, E. W. and Godwin, T. W. (1968) 'M-1 Injector Development - Philosophy and Implimentation', *Journal of Spacecraft,* vol. 5, no. 3, pp. 282-287.

Vieille, B., Chauveau, C. and Gokalp, I. (1999) *Studies on the Break-up Regimes of Lox Droplets*, 37th AIAA Aerospace Sciences Meeting and Exhibit, AIAA, Reno, Nevada, 11-14 January 1999.

Wanhainen, J. P., Feiler, C. E. and Morgan, J. C. (1968) *Effect of chamber pressure, flow per element, and contraction ratio on acoustic-mode instability in hydrogen-oxygen rockets*, NASA TN D-4733, Lewis Research Center, NASA, Cleveland, Ohio.

Wanhainen, J. P. and Morgan, J. C. (1969) *Effect of injection element radial distribution and chamber geometry on acoustic-mode instability in a hydrogen oxygen rocket*, NASA TN D-5375, Lewis Research Center, NASA, Cleveland, Ohio, Aug 1969.

Wanhainen, J. P., Parish, H. C. and Conrad, E. W. (1966) *Effect of propellant injection velocity on screech in 20,000-pound hydrogen-oxygen rocket engine*, NASA TN D-3373, Lewis Research Centre, NASA, Cleveland, Ohio, April.

Welch, P. D. (1967) 'The use of fast fourier transform for the estimation of power spectra: a method based on time averaging over short, modified periodograms', *IEEE Transactions on Audio and Electro-acoustics,* vol. 15, no. 2, pp. 70-73.

Wieber, P. R. and Mickelsen, W. R. (1960) *Effect of transverse acoustic oscillations on the vaporization of a liquid-fuel droplet*, NASA TN D-287, Lewis Research Centre, NASA, Cleveland, Ohio, May 1960.

Wierman, M., Nugent, N. and Anderson, W. E. (2011) *Combustion response of a LOX/LCH4 element to transverse instabilites*, 47th AIAA/ASME/SAE/ASEE Joint Propulsion Conference & Exhibit, AIAA, San Diego, California, 31 July - 3 August 2011.

Woodward, R. D. (1993) *Primary atomization of liquid jets issuing from rocket engine coaxial injectors*, PhD Thesis, Department of Mechanical Engineering, Pennsylvania State University, University Park, PA.

Woodward, R. D., Pal, S., Farhangi, S. and Santoro, R. J. (2006) *LOX/GH_2 shear coaxial injector atomization studies at large momentum flux ratios*, 42nd AIAA/ASME/SAE/ASEE Joint Propulsion Conference & Exhibit, AIAA, Sacramento, California, 9-12 July 2006.

Woschnak, A., Suslov, D. and Oschwald, M. (2003) *Experimental and numerical investigations of thermal stratification effects*, 39th AIAA/ASME/SAE/ASEE Joint Propulsion Conference & Exhibit, AIAA, Huntsville, AL.

Xia, G., Harvazinski, M. E., Anderson, W. E. and Merkle, C. L. (2011) *Investigation of modeling and physical parameters on instability prediction in a model rocket combustor*, 47th AIAA/ASME/SAE/ASEE Joint Propulsion Conference & Exhibit, AIAA, San Diego, California, 31 July - 3 August 2011.

Yang, B., Cuoco, F. and Oschwald, M. (2007) 'Atomization and Flames in LOX/H2- and LOX/CH4-Spray Combustion', *Journal of Propulsion and Power,* vol. 23, no. 4, pp. 763-771.

Yang, B., Cuoco, F., Wang, L. and Oschwald, M. (2007) *Experimental investigation of reactive liquid oxygen/CH_4 coaxial sprays*, 43rd AIAA/ASME/SAE/ASEE Joint Propulsion Conference & Exhibit, AIAA, Cincinnati, OH, 8-11 July 2007.

Yang, V. and Anderson, W. (eds) (1995) *Liquid rocket engine combustion instability,* AIAA, Washington, DC.

Yeralan, S., Pal, S. and Santoro, R. J. (2001) 'Experimental study of major species and temperature profiles of liquid oxygen/gaseous hydrogen rocket combustion', *Journal of Propulsion and Power,* vol. 17, no. 4, pp. 788-793.

Younglove, B. A. (1982) 'Thermophysical properties of fluids. 1. Argon, Ethylene, para-Hydrogen, Nitrogen, Nitrogen Trifluoride and Oxygen', *Journal of Physical and Chemical Reference Data,* vol. 11, no. Supplement No.1, pp.

Yu, Y. C., Koeglmeier, S. M., Sisco, J. C. and Anderson, W. E. (2008) *Combustion instability of gaseous fuels in a continuously variable resonance chamber (CVRC)*, 44th AIAA/ASME/SAE/ASEE Joint Propulsion Conference & Exhibit, AIAA, Hardford, CT, 21-23 July 2008.

Yu, Y. C., O'Hara, L., Sisco, J. C. and Anderson, W. E. (2009) *Experimental Study of High-Frequency Combustion Instability in a Continuously Variable Resonance Combustor (CVRC)*, 47th AIAA/ASME/SAE/ASEE Joint Propulsion Conference & Exhibit, AIAA.

Zinn, B. T. (1972) 'Contraction ratio', in *Liquid propellant rocket combustion instability*, eds Harrje, D. T. and Reardon, F. H., NASA, Washington, DC, pp. 314-317.

Zong, N. and Yang, V. (2006) 'Cryogenic fluid jets and mixing layers in transcritical and supercritical environments', *Combustion Science and Technology,* vol. 178, pp. 193-227.

Appendix A. Twin resonator segment design study

Following initial selection of the TRS as the favoured concept, a more detailed design study was carried out to better define design parameters and attempt to predict its performance. This study included more thorough acoustic mode characterisation, computational fluid dynamics (CFD) simulation of the internal flow field of the chamber, thermal load prediction and design of water cooling for the chamber walls, design of secondary injection, and investigation of manufacturing feasibility.

A.1 Twin resonator segment geometry

TRS geometries with both square and circular profiled resonator cavities were considered. The square profiled cavity, illustrated in Figure A.1, was expected to result in a more uniform acoustic pressure field distribution across the injector face than for a cylinder-cylinder cross-section, although 3D acoustic mode studies showed little difference for the respective profiles. The intersection for the square profiled TRS would provide a compatible surface for optical access windows either side of the primary injector. However, concerns about the ability to manufacture a square profiled secondary nozzle and a square to circular chamber transition section lead to a circular profile TRS being favoured, although the intersection of a circular resonator and circular chamber still presents a manufacturing challenge, particularly due to the need for a radius at the intersection to reduce the heat load on the corner.

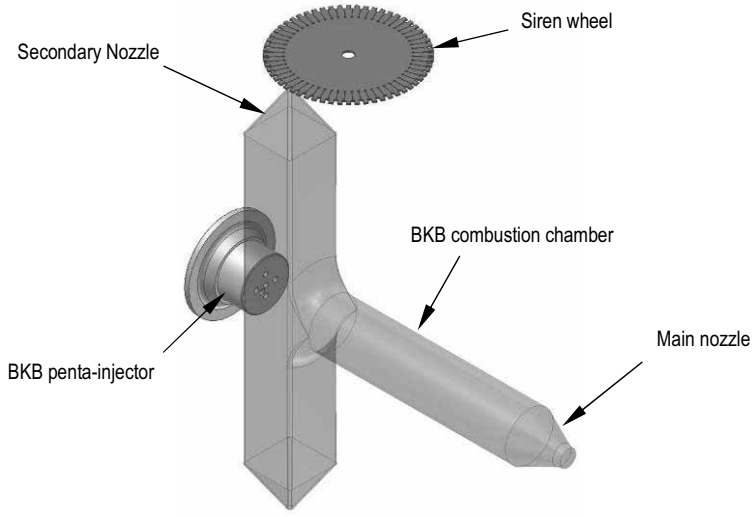

Figure A.1: Twin resonator segment concept with square resonator (internal geometry).

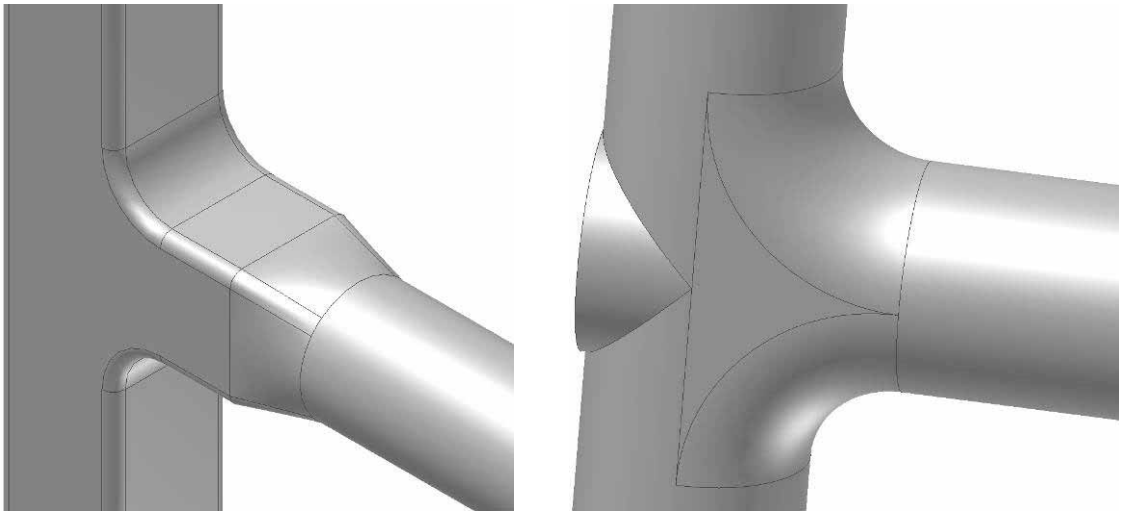

Square resonator-chamber intersection Circular resonator-chamber intersection

Figure A.2: Concepts for internal geometry at the resonator chamber intersection

Figure A.2 shows a closer view of possible geometries for the intersection between the resonator and main chamber for both square and circular resonators. Although implying the exclusion of optical access windows, manufacturing constraints seemed to favour a circular profile TRS and hence subsequent development was focused on this design. The acoustic modes of the circular cross section resonator were studied in more detail by varying the depth of the resonator cavities and length of the main chamber. The effect of varying sound speed was also studied. The results were used to refine the geometry and select dimensions of the chamber based on the desired mode frequencies for expected operating conditions. The resulting choice of internal chamber dimensions is shown in Figure A.3. Note that the overall chamber length is shown as an acceptable range since the actual length would ultimately depend on manufacture of the resonator segment.

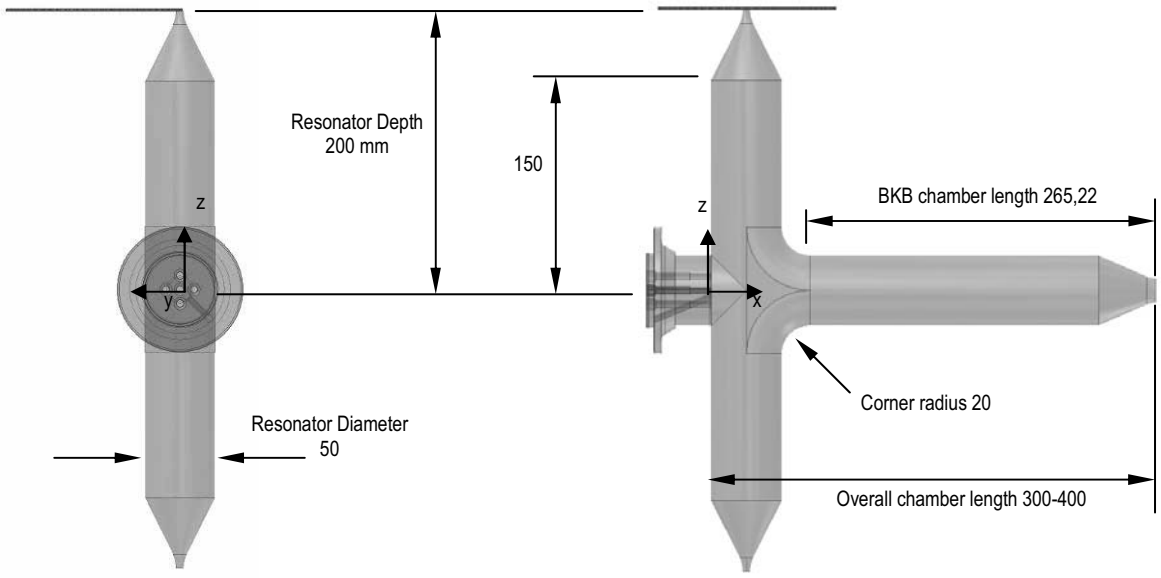

Figure A.3: Dimensions of twin resonator chamber internal geometry.

A.2 Internal flow

Addition of the resonator cavities either side of the main combustion chamber and flow through the secondary nozzle is expected to significantly influence the flow field inside the chamber. Recirculation zones immediately above and below the primary injector in the resonator cavities are to be expected. With flow diverting to fill the resonator cavities, most likely from the upper and lower elements in the penta-injector pattern, a stagnation point would be established at some location on the corner of the resonator-chamber intersection. This supposed flow pattern is illustrated in Figure A.4.

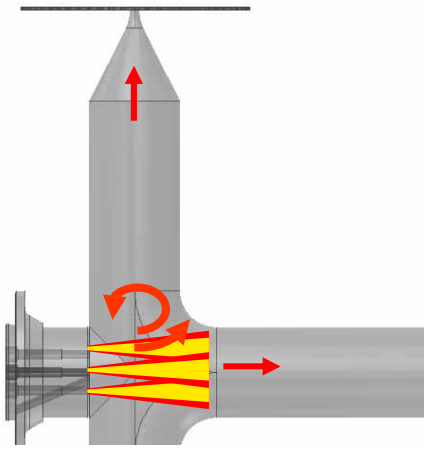

Figure A.4: Estimated flow pattern near the resonator-chamber intersection.

There are potential problems arising from this flow configuration in the chamber. Firstly, combustion gases impinging on the resonator-chamber corner will result in high heat loads at that location. Secondly, diverting flow may cause unburned oxygen to impinge on the chamber walls, posing a threat to the structure. Images of coaxial injection streams from representative injectors, such as those by Mayer and Tamura (1996), show liquid oxygen still present 70 mm downstream, whereas the resonator-chamber corner is only 50 mm downstream. Thirdly, diverting the flow of injectants before combustion is complete will change the intended *ROF* in the main combustion chamber and may cause it to rise above the operational limit for BKB of $ROF = 6$, also posing a threat to the structure. Fourthly, with the lower resonator cavity being closed and flow exiting the upper through the secondary nozzle outlet the injection stream may be deflected upwards, resulting in an asymmetrical flow field. Finally, this flow field asymmetry, strong recirculation zones, and interaction with the resonator-chamber corner may affect the way the injection streams interact with the acoustic field.

In an effort to characterise the extent of these potential problems, computational fluid dynamics (CFD) was conducted to estimate how the chamber flow field may be developed at steady state (Pauly 2008). The ANSYS CFX 11.0 software package was used to conduct a simplified analysis with a single, gaseous injectant with properties equal to an equilibrium LOx/H_2 combustion mixture of $ROF = 6$. The chamber pressure was set to the intended maximum operating pressure of 60 bar and a representative hydrogen injection velocity was used. The penta-injector was aligned in the 45° orientation. The model geometry and mesh are shown in Figure A.5. Three model cases were calculated with conditions as follows:

- CFD Case 1
  - Course mesh
  - Steady state
  - Adiabatic walls
  - K-epsilon turbulence model (model strength is shear layer turbulence)
- CFD Case 2
  - Fine mesh
  - Steady state
  - Adiabatic walls
  - SST Menter turbulence model (model strength is boundary layer turbulence)
- CFD Case 3
  - Fine mesh
  - Steady state
  - Imposed wall temperature of 400 K
  - SST Menter turbulence model

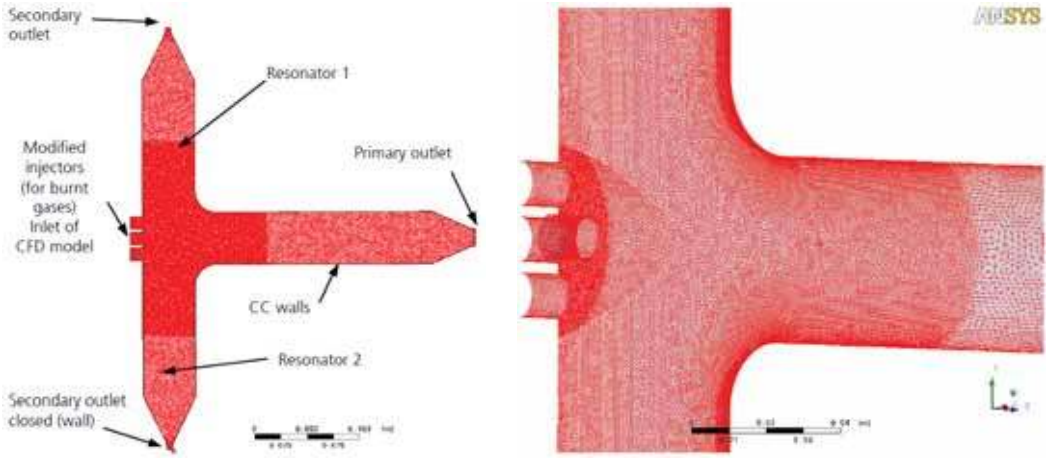

Figure A.5: Meshed model of the TRS for CFD analysis.

Results for the velocity field calculated for CFD Case 1 are shown in Figure A.6. Strong recirculation zones above and below the injector are indeed apparent and seem to 'pinch' the outer jets inwards up to a point where they diverge sharply and impinge on the downstream edge of the resonator-chamber corner. This behaviour is consistent in the results of all three analysis cases, and indicates the region where high convective heat loads are to be expected.

The degree of deflection of the upper and lower injection streams, particularly in Case 3, suggests that oxygen impingement on the chamber walls near the stagnation point may be possible. However, a two phase liquid-gaseous coaxial injection stream would behave differently to this simplified single phase stream, and therefore no conclusion is drawn.

As expected, the velocity field also displays asymmetry due to flow exiting from the secondary nozzle of the upper resonator cavity. The asymmetry even results in a recirculation zone in the first half of the main chamber, evident in the vector field in Figure A.6b. However, in the finely meshed Case 2, as seen in Figure A.7, the same region is no longer a recirculation zone, merely a transverse perturbation to the otherwise axial flow direction. In Case 3, in Figure A.8, the asymmetry in the main flow appears to have disappeared, perhaps due to energy removal from the flow stream by the non-adiabatic walls. Because the flow field differs so between the model cases, care must be taken in interpreting the results and the conclusion of possible asymmetry in the main chamber flow field is tentatively drawn.

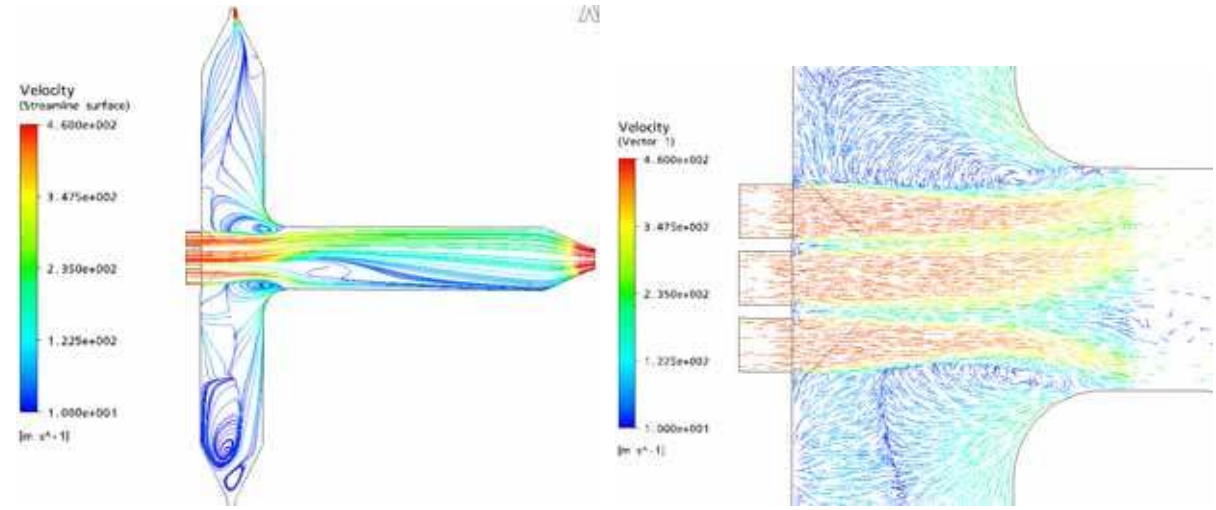

a) Streamline velocity surface b) Vector velocity surface

Figure A.6: Velocity field results for CFD Case 1.

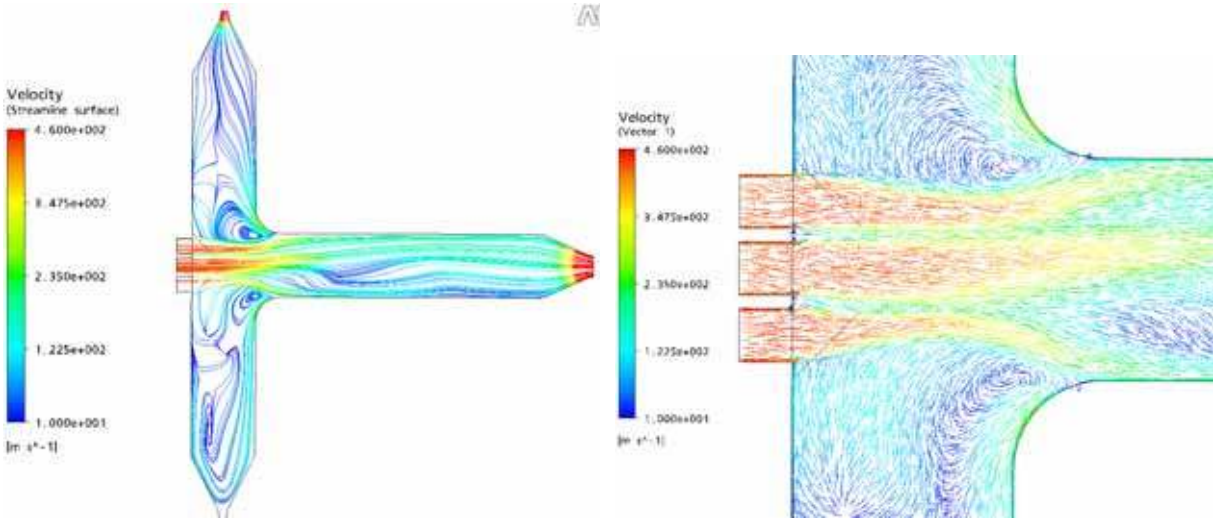

a) Streamline velocity surface b) Vector velocity surface

Figure A.7: Velocity field results for CFD Case 2.

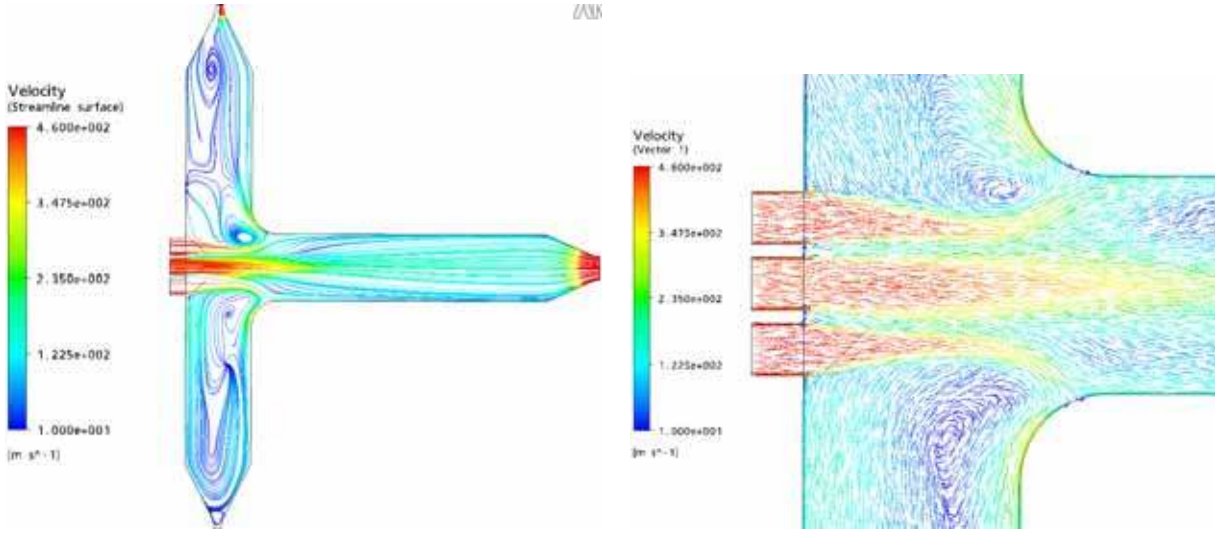

a) Streamline velocity surface b) Vector velocity surface

Figure A.8: Velocity field results for CFD Case 3.

A.3 Secondary injection

Figure A.9 shows the flow field results for Case 3 with streamlines originating from each element of a different colour. It appears as though the majority of the flow from the upper and lower elements diverts to supply the resonator cavities. It was therefore proposed to use secondary injection to supply flow for the resonator cavities and secondary nozzle so that the primary injection streams would not be affected so dramatically.

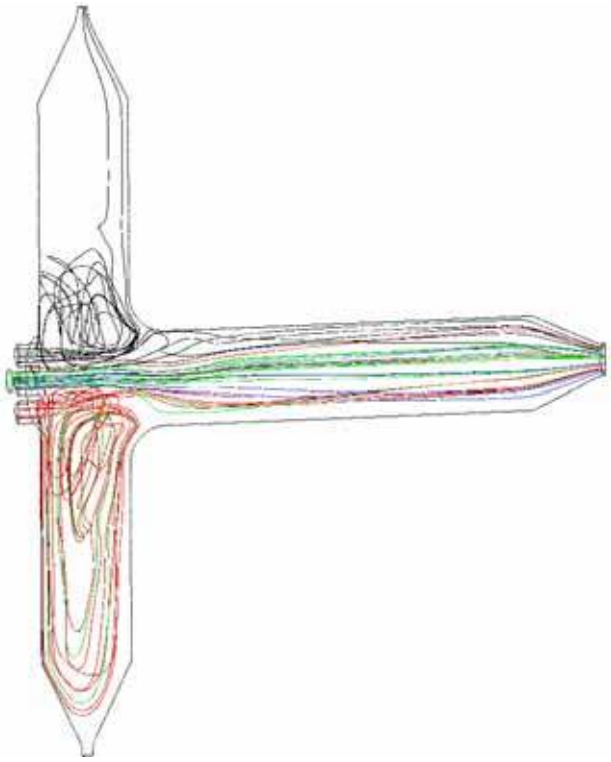

Figure A.9: Individual jet streamlines for CFD Case 3.

The proposal for secondary injection was to continuously purge the resonator cavities with gaseous hydrogen during operation. Further motivations for using secondary hydrogen injection in this manner include;

- reduce the heat load on the resonator-chamber corner due to impinging combustion gases,
- reduce the likelihood of oxygen impingement on the resonator-chamber corner due to main flow field deflection,
- prevent the maximum allowable ROF being exceeded in the main chamber due to loss of hydrogen from primary injection to feed the resonators,
- reduce the size and strength of the primary injector recirculation zones by providing the required secondary nozzle mass flow from secondary hydrogen,
- reduce the heat load on the exciter wheel teeth by providing a cool, predominantly hydrogen rich flow through the secondary nozzle,
- and create controlled acoustic conditions in the resonator cavities.

One possible concept for the use of secondary hydrogen injection in the TRS is illustrated in Figure A.10. Providing a secondary flow directly above and below the primary injector may reduce the severity of the primary injection stream deflection and of the impact on the resonator-chamber corner, as well as supplying the majority of mass flow through the resonator and secondary nozzle.

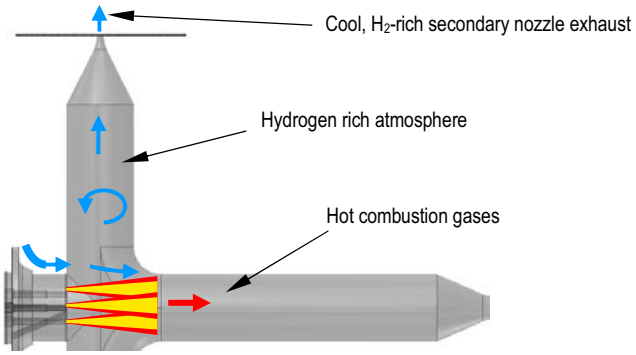

Figure A.10: Concept for secondary hydrogen injection.

This injection configuration was investigated using the model geometry shown in Figure A.11 and the same CFD method described previously. The velocity streamline result in Figure A.12 shows significantly less disturbance to the primary injection jets when secondary injection is supplied since they do not need to turn sharply to fill the resonator cavities. This also results in more uniform flow through the main combustion chamber.

The final of the aforementioned motivations to use secondary injection, to create controlled acoustic conditions, is made possible by the fortunate coincidence that the sound speed of ambient temperature gaseous hydrogen (c ~ 1350 m/s at T ~ 290 K - source: NIST Refprop (National Institute of Standards and Technology 2005)) is very close (15 % difference) to that of the hot equilibrium combustion mixture (c ~ 1580 m/s for LOx/H_2 with ROF = 6 at T ~ 3530 K – calculated using CEA2). The CFD calculated temperature distribution in Figure A.13 shows that largely uniform temperature distributions would be maintained in the resonator cavities when supplied with secondary H_2. Thus continuously purging the resonator

cavities with hydrogen would result in predictable acoustic conditions throughout most of the combustor.

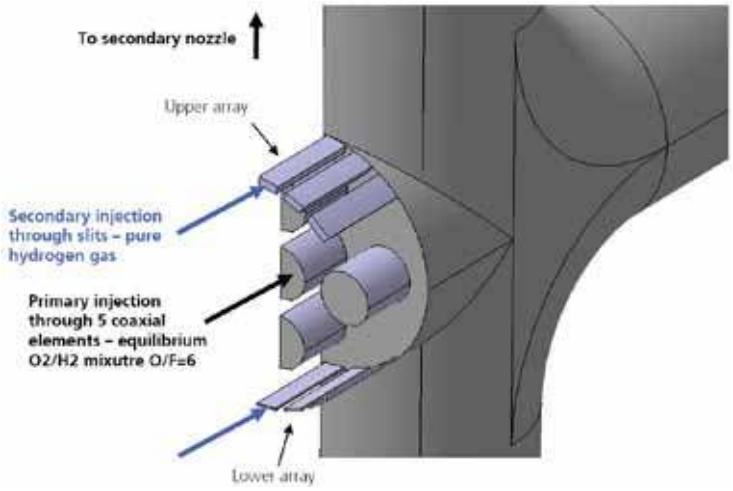

Figure A.11: Secondary injection CFD model geometry.

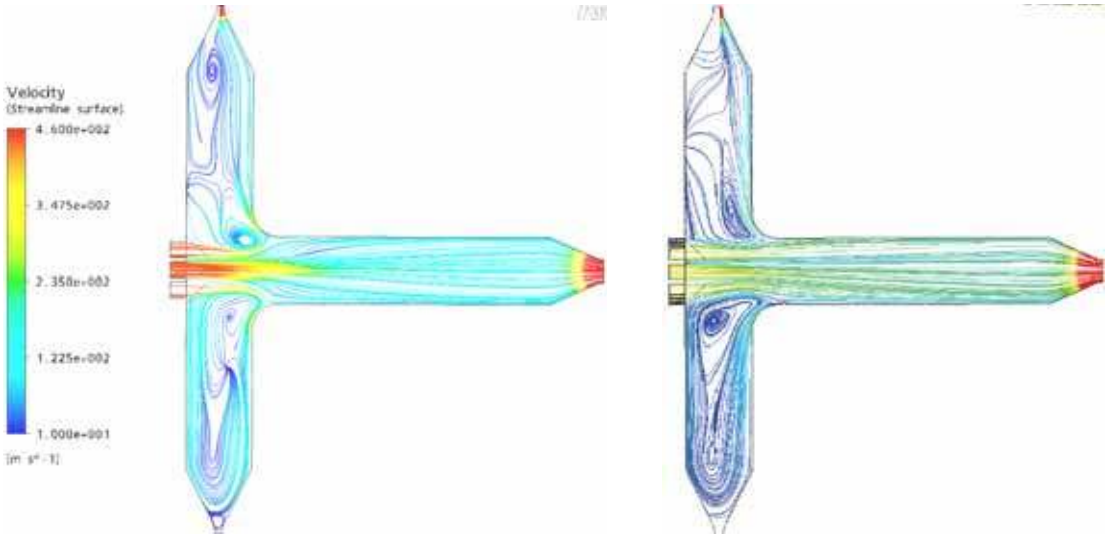

Without secondary H_2 injection With secondary H_2 injection

Figure A.12: CFD streamline results comparison for TRS secondary injection.

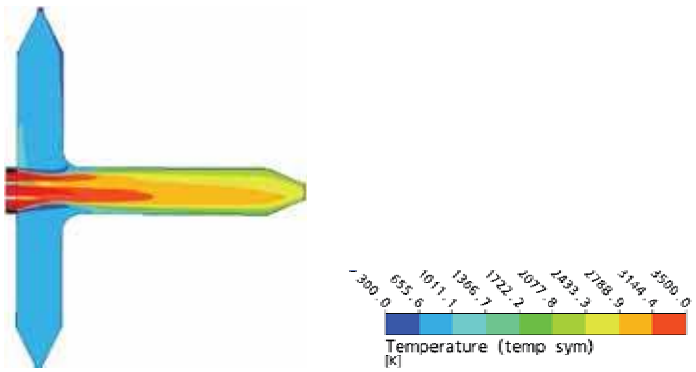

Figure A.13: CFD calculated gas temperature distribution for the TRS with secondary H_2 injection.

To test the influence of secondary injection on the acoustic properties of the chamber, the acoustic modes were re-calculated modelling the presence of secondary hydrogen in the resonator cavities. For this purpose, numerical calculation of modes was conducted using the two-dimensional, finite-element, partial differential equation solving software FlexPDE 3.01d (PDE Solutions Inc. 2002). This choice of software was made to enable faster parametric study of a wide range of conditions. Two cases were compared, firstly using the assumed ambient injection temperature for hydrogen of 290 K with a sound speed of 1350 m/s, and secondly assuming the hydrogen could reach a temperature of up to 1000 K, as seen in the CFD result in Figure A.13, with a corresponding sound speed of 2400 m/s. Only minor differences in the frequencies of the respective modes result, with all modes remaining in an acceptable range of frequencies, and modes maintain their desired pressure distributions in the vicinity of the injector, as seen in Figure A.14.

CFD results also confirmed the benefit of using secondary H_2 to control the heat load on the resonator-chamber corner. Figure A.15 shows a clear reduction (approximately 75%) in the magnitude of the expected heat flux at the corner due to the presence of a significant amount of cool secondary hydrogen in the gases impinging on the corner.

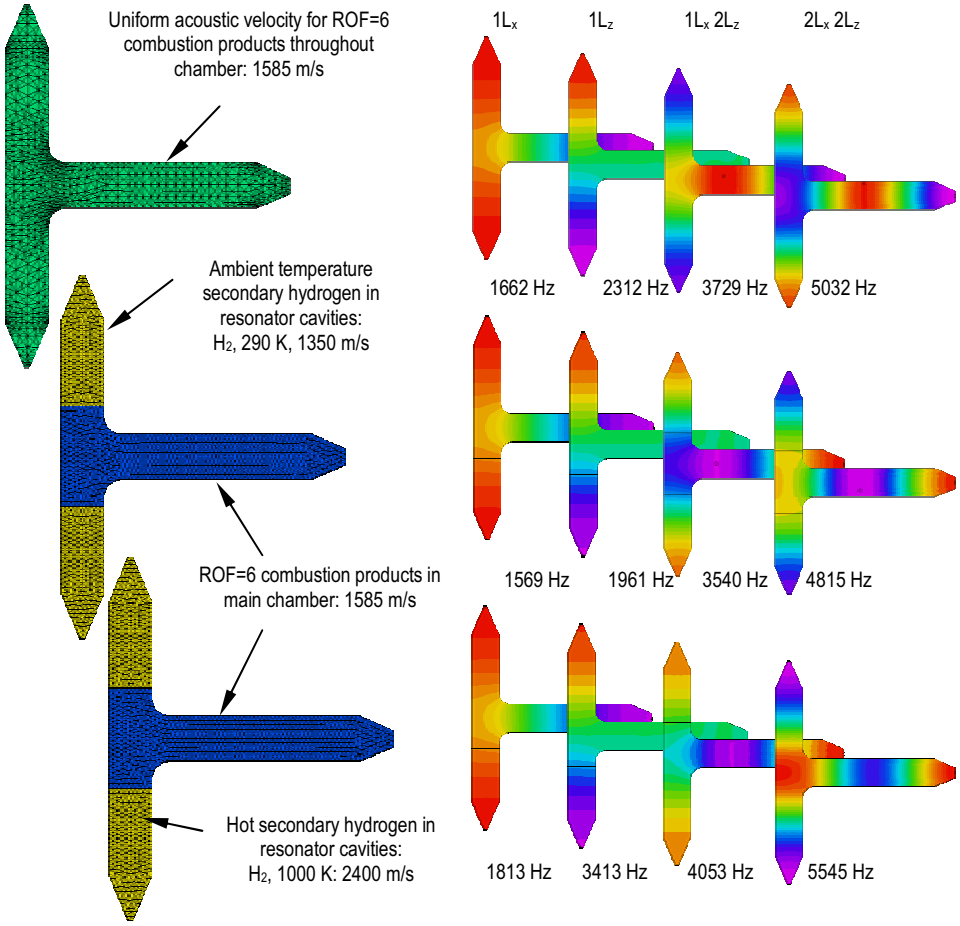

Figure A.14: Acoustic mode comparison for TRS with and without secondary H_2.

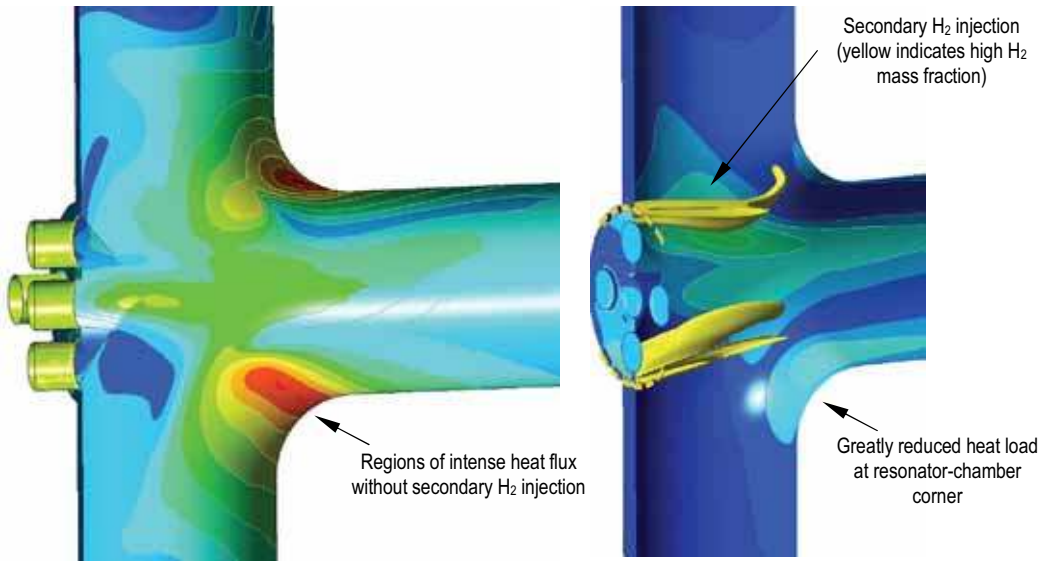

Figure A.15: TRS heat load with and without secondary H_2 injection.

As an aside, the use of nitrogen purge in the secondary nozzle for cooling purposes was briefly considered. The acoustic model was also run with a region of nitrogen gas in the secondary nozzle of sound speed c = 340 m/s, and ROF = 6 combustion gases of c = 1585 m/s elsewhere. Example results in Figure A.16 show extreme disruption to the desired mode shapes and frequencies. A similar example of this kind of disruption to the acoustic field was described by Kawashima et al. (2010). Their sub-scale combustor had a similar configuration to the TRS, with twin, recessed cavities near the injection plane housing optical windows. The cavities were purged with helium gas to protect the windows from thermal loads, however the mixture of acoustic properties in the chamber complicated the identification of acoustic modes. This highlights the importance of trying to establish sound speed conditions which are symmetrical about the axis of the combustion chamber.

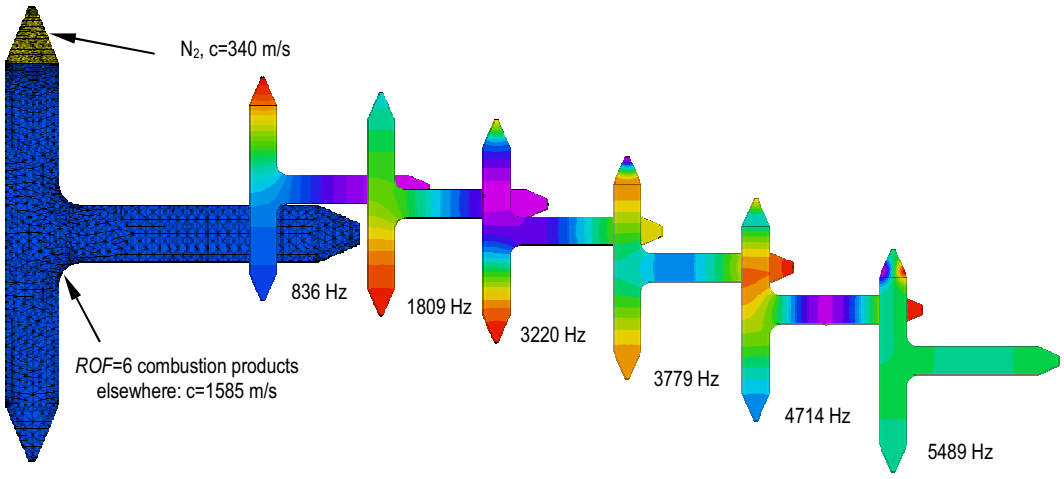

Figure A.16: Acoustic mode shapes with nitrogen injection.

A.4 Water condensation

A common issue observed in experimental LOx/H_2 combustion chambers is that of water condensation. The maximum operational wall temperature of combustion chambers, dictated by the chamber material properties, is quite often below the coexistence temperature for water. Windowed combustion chambers have allowed water condensate to be observed forming on the walls of combustion chambers during operation, in some cases forming ice on the injector face plate and in others even pooling at the bottom of the chamber.

The issue of water condensation and how it may affect the acoustic properties of the chamber was considered for the TRS concept. At the intended maximum operating pressure of 60 bar, the coexistence temperature for water is approximately 550 K, which is unlikely to be exceeded in many areas of the combustion chamber wall surface. If water condenses in sufficient quantities, it could pool at the bottom of the lower resonator cavity.

The potential impact of such pooling on chamber acoustics was checked using a numerical modal analysis with FlexPDE. Pooling water was modelled simply by taking the rising water level as decreasing depth of the lower resonator. The acoustic pressure distributions, examples of which are given in Figure A.17, show noticeable changes in the mode structure at the injector face when compared to an undisturbed geometry. Hence, depending on how significant the amount of pooling condensate becomes, the acoustic field uniformity may be adversely affected.

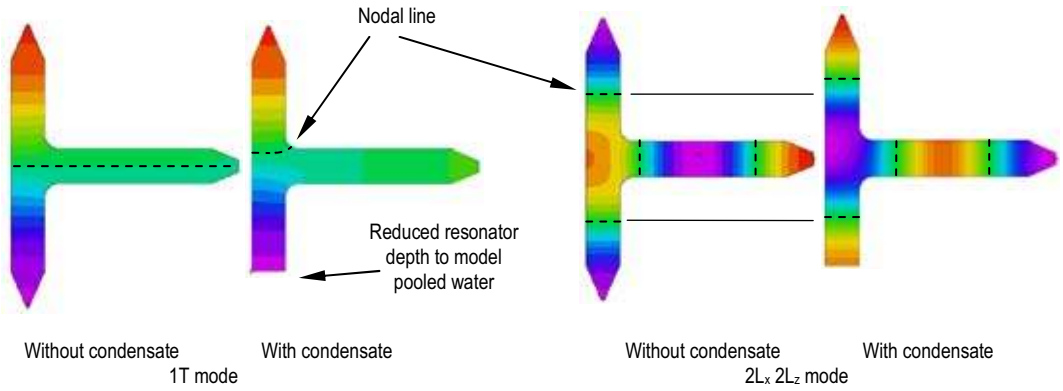

Figure A.17: Example numerical acoustic pressure distributions for the TRS, with and without pooled water condensate.

A.5 Manufacture feasibility study

While the TRS is conceptually simple, in practice the geometry would not be so simple to realise. Significant efforts were expended in investigating the feasibility of manufacturing the TRS, the outcome of which eventually led to the cancellation of TRS development.

The geometry at the intersection of the resonator and main combustion chamber would be particularly difficult to manufacture. The difficulty arises from the need for machine access to create the rounded internal profile of the resonator-chamber corner. The rounded geometry would also make the milling of cooling channels on the outside of the corner extremely difficult.

Space constraints and the complex geometry in the vicinity of the injector meant the exclusion of optical access from the design. The installation of dynamic pressure sensors in this region would also present difficulties. Without optical access or the ability to measure the acoustic pressure distribution in the near injector region the research value of the system would be greatly reduced.

One of the initial motivations for developing the TRS which integrates with the BKB combustion chamber was the ability to re-use an existing BKB penta-injector head. The resonator cavities extending above and below the primary injector face would not be accommodated by the original BKB injector head, requiring either extensive modifications or production of an entirely new injector head. This meant the effort of developing a new injector head would not be spared.

Various further issues with compatibility of existing hardware components introduced an increasing number of difficulties to the practical realisation of the design. These complications eventually outweighed the perceived benefits of utilising existing BKB hardware, and the TRS concept was subsequently abandoned in favour of a clean-slate design.

Appendix B. BKH dimensions

B.1 Combustor drawings

This Section contains drawings which provide more geometrical detail of the internal volumes of BKH. Fluid supply lines and test bench interfaces are again excluded due to their scale and complexity.

Figure B.1 is an overview of BKH, naming the various features of the system for reference. Figure B.2 contains dimensions of the internal volumes of the combustor, including the combustion chamber and injection system. Figure B.3 provides detailed dimensions of the injector. Figure B.4 provides the locations of conventional sensors for temperature and pressure measurements, as well as dynamic pressure sensors for acoustic measurements.

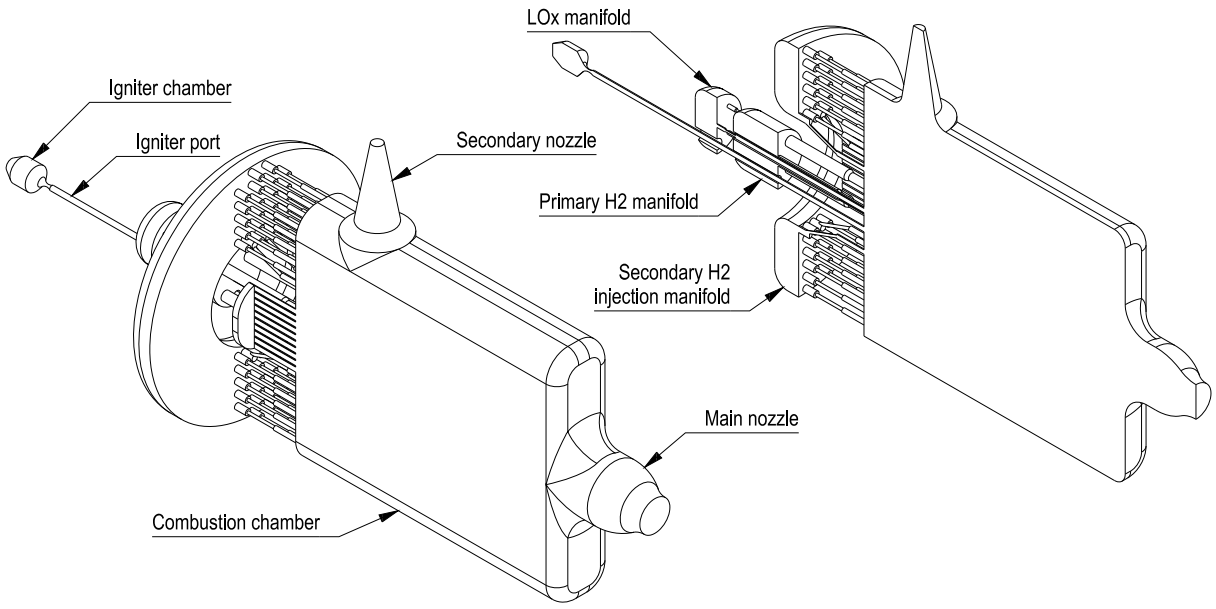

Figure B.1: Overview of the internal volumes of BKH.

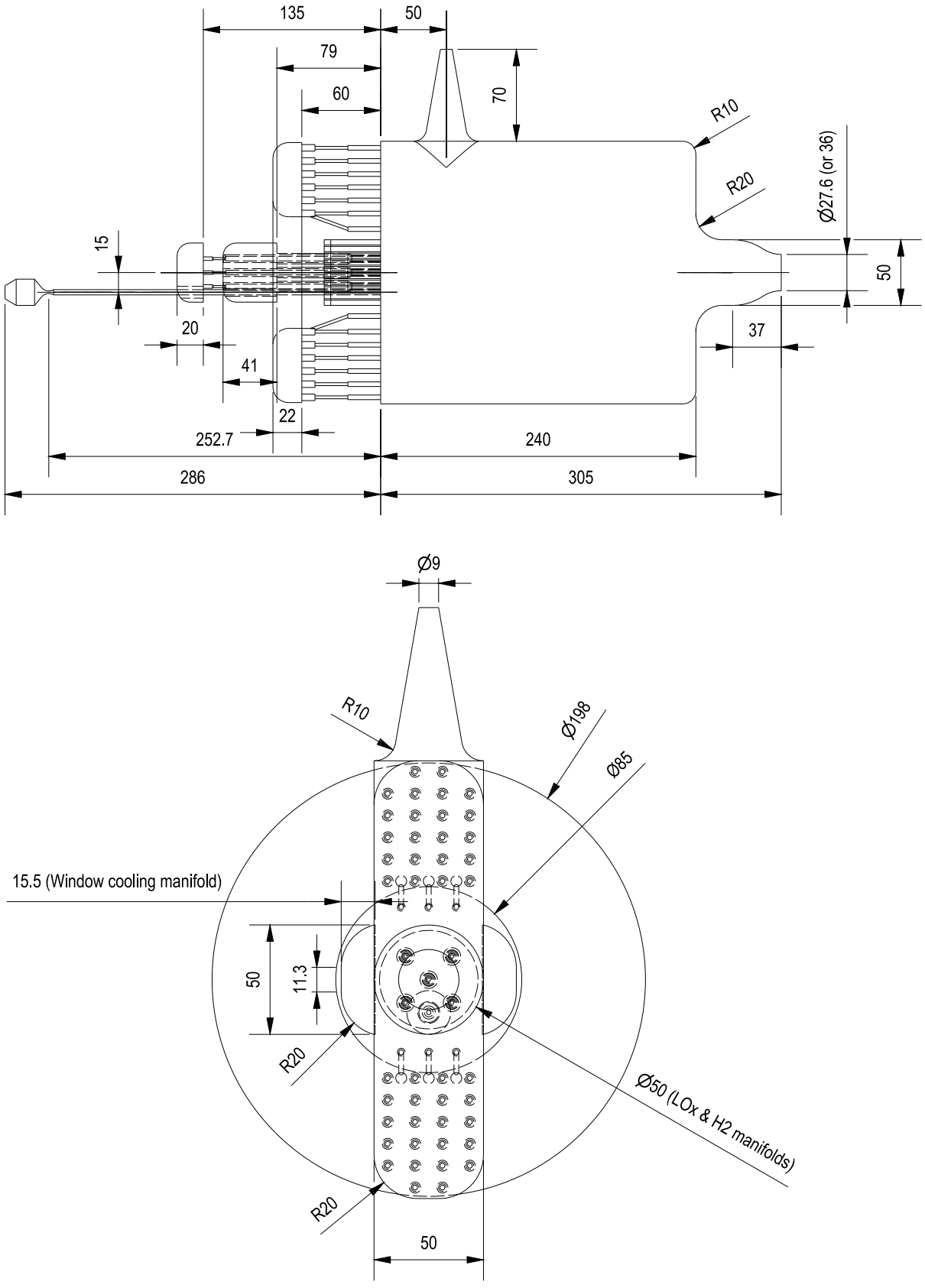

Figure B.2: Dimensions of the internal volumes of BKH.

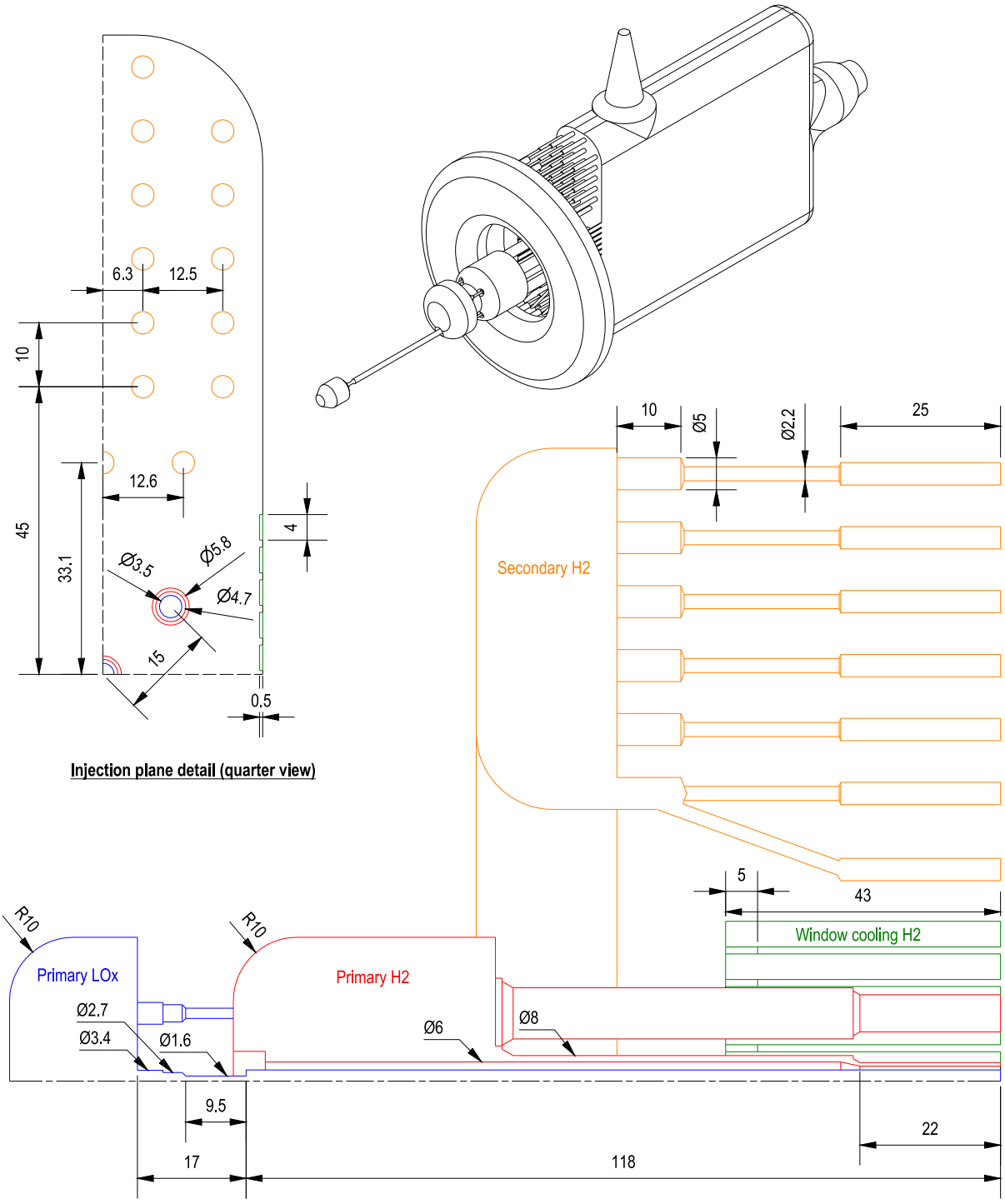

Figure B.3: Detailed BKH injector dimensions.

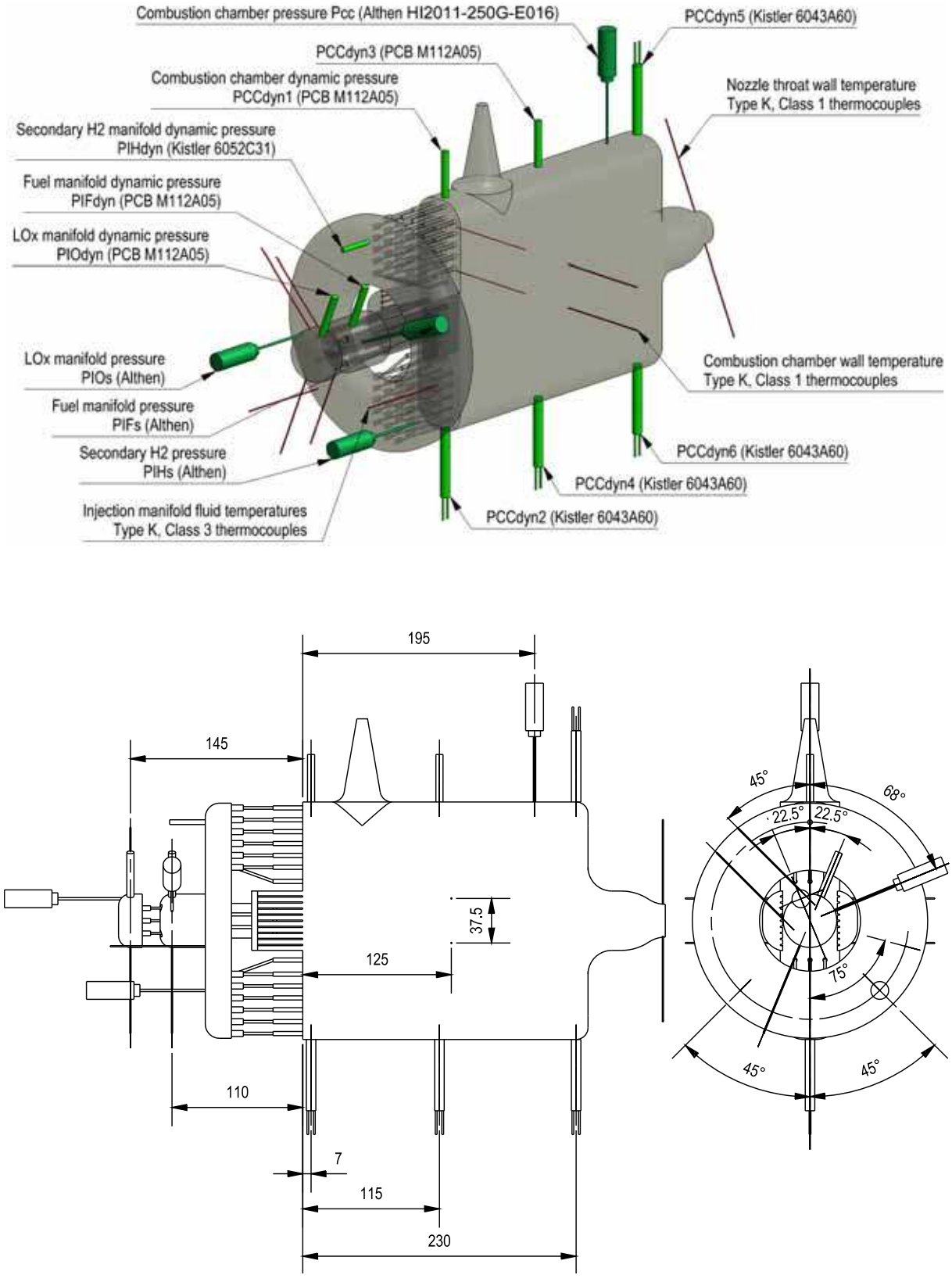

Figure B.4: Locations of sensors in BKH.

Appendix C. Modified secondary nozzle

C.1 Round nozzle

Clearly identifiable overtones of the excitation frequency are present in the spectra of all acoustic measurements from the combustion chamber, for both on- and off-resonance conditions. At least nine overtones of the excitation signal are visible in the spectrogram in Figure 6.13, for example. These overtones are present because the excitation signal is not purely sinusoidal. In cases of natural instability in real engines, the pressure oscillations are driven to large amplitudes and the waveforms typically become steep-fronted, resulting in a nonlinear signal and the presence of overtones. In the case of BKH, non-linearity in the forced excitation signal is believed to arise from the dynamics of modulation of the mass flow through the secondary nozzle.

The variation of nozzle exit area for one period of excitation was considered. Figure C.1a is a photograph of the secondary nozzle with the exciter wheel installed above it. Figure C.1b plots the exit area as the round nozzle exit is closed by the square exciter wheel tooth passing over it and then opened again. Compared to a sinusoidal variation in area, the nozzle exit closes more quickly during the first four degrees of exciter wheel rotation, followed by a short period of slower closure between four and six degrees, where at the six degree position the tooth covers the nozzle completely.

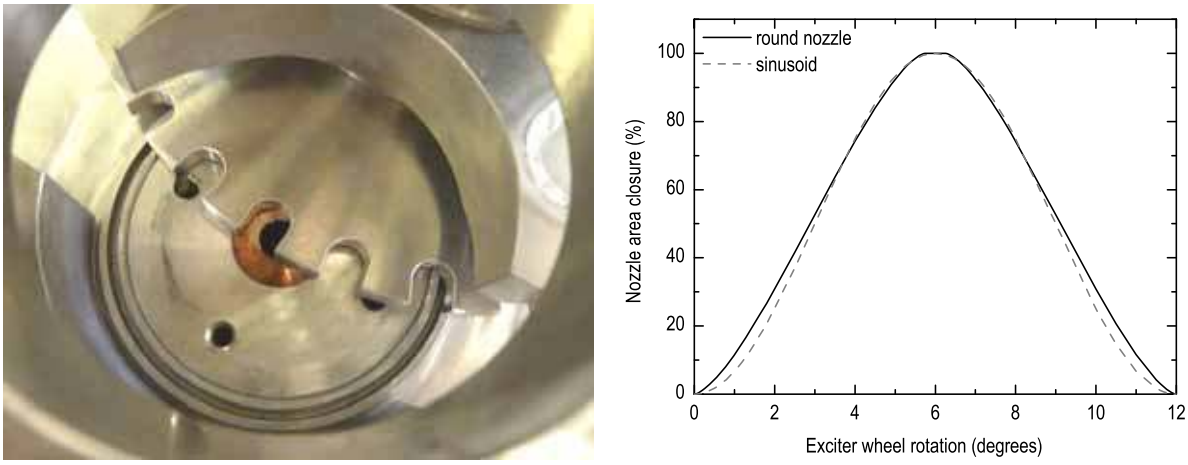

(a) (b)

Figure C.1: A photograph of the round secondary nozzle (a), and the corresponding excitation profile (b).

C.2 Double sine nozzle

The overtones of excitation are observed to excite higher acoustic modes aside from the three of interest; the 1L, 1T and 1L1T. It would be desirable to excite with a pure monotone signal in order to simplify analysis of acoustic response. In an attempt to eliminate the excitation overtones, a modified secondary nozzle was installed in campaigns 4 and 5. The modification consisted of introducing a 'double sine' profile into the nozzle throat (exit plane), as pictured in Figure C.2a. As the tooth of the exciter wheel passes over the nozzle throat, the change in exit area follows a nearly sinusoidal profile. Theoretically, the variation in mass flow rate passing through the nozzle should also be sinusoidal, resulting in a pure tone excitation signal inside the combustion chamber. The idea originates from an experiment operated at the Technical University of Munich, where pressurised air is injected into a model chamber via a siren wheel modulating the flow through a double sine-profiled orifice (Kathan et al. 2010). Figure C.2b plots the exit area as the double sine-profiled nozzle exit is closed by the square exciter wheel tooth passing over it and then opened again.

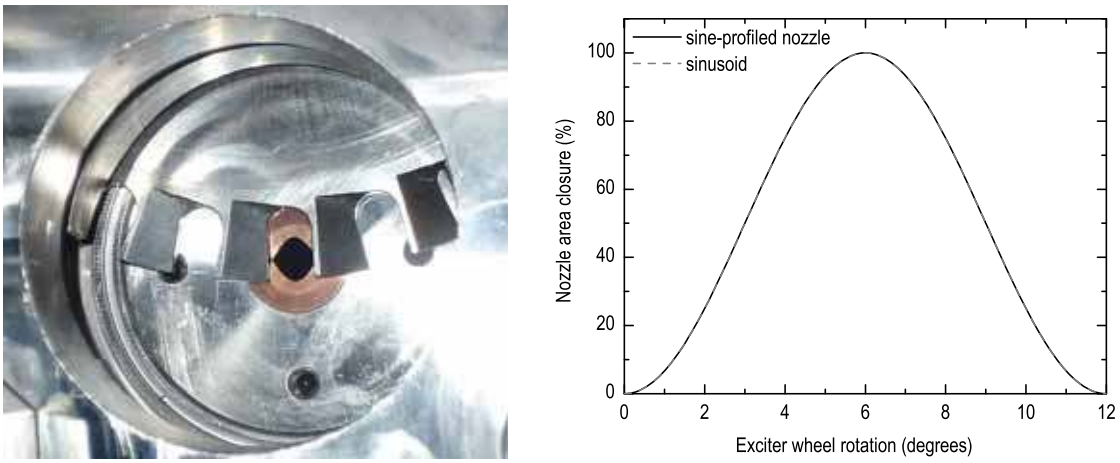

Figure C.2: A photograph of the secondary nozzle with double sine profile (a), and the corresponding excitation profile (b).

Figure C.3 compares BKH spectra for a test with the original, round secondary nozzle and the modified sine profiled-nozzle, with the sample taken from an off-resonance excitation condition. Although the exit area variation is nearly sinusoidal, there is no apparent reduction in the amplitude of the overtones compared to the primary excitation signal. The reason is unknown. The variation of mass flow through the secondary nozzle may not adhere solely to the instantaneous nozzle exit area, perhaps due to the transient nature of the flow, or perhaps due to inhomogeneous mass flux across the exit area. Alternatively, the mass flux variation may indeed be sinusoidal, but the production of the resulting acoustic pressure disturbance results from a more complex process. Either way, this exercise shows that the production of the acoustic excitation signal in the combustion chamber through nozzle modulation does not behave according to simple theoretical constructs. This issue is not addressed further in this work as excitation conditions with or without the modified nozzle are indistinguishable.

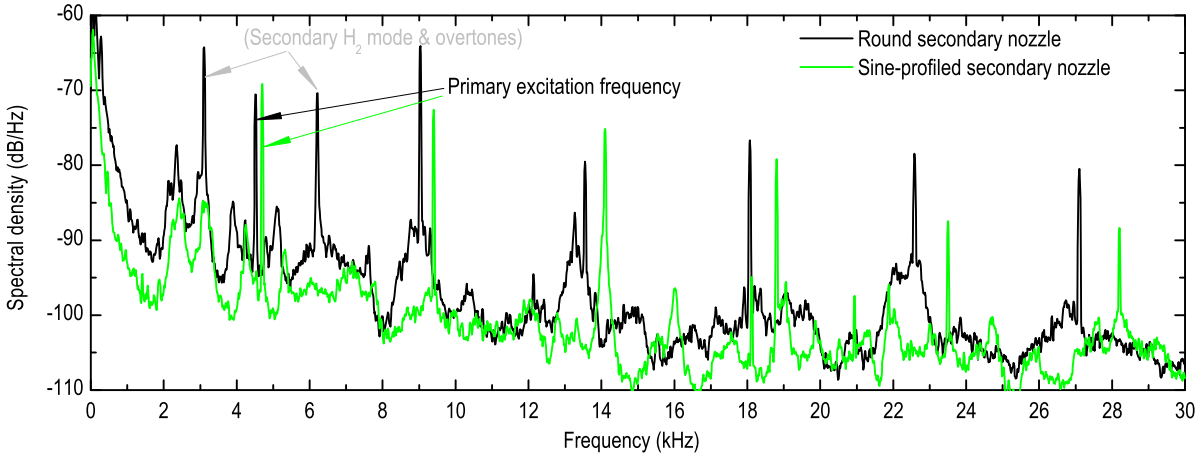

(a) Stationary, off-resonance excitation

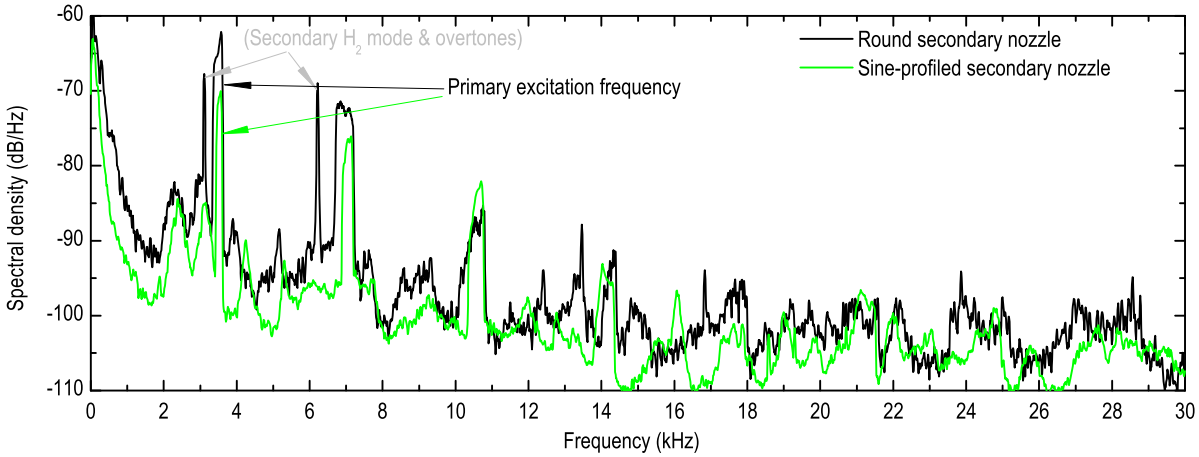

(b) Ramped, off-resonance excitation

Figure C.3: Comparison of acoustic pressure spectra in the combustion chamber for excitation with the round and sine-profiled secondary nozzles. Spectra are shown for stationary, off-resonance excitation (a), and for ramped, off-resonance excitation (b).

Appendix D. List of articles resulting from this work

The following is a list of articles that have resulted from this work.

D.1 Journal articles

Hardi, J. S., Oschwald, M. and Dally, B. (2011) 'Flame response to acoustic excitation in a rectangular rocket combustor with LOx/H_2 propellants', *CEAS Space Journal*, vol. 2, pp. 41–49.

Hardi, J. S., Oschwald, M. and Dally, B. (2012) 'Acoustic characterisation of a rectangular rocket combustor with liquid oxygen and hydrogen propellants', *Proceedings of the Institution of Mechanical Engineers, Part G: Journal of Aerospace Engineering*, Published online before print March 2, 2012, dio: 10.1177/0954410012437511.

D.2 Conference papers

Hardi, J. S., Beinke, S. K., Oschwald, M. and Dally, B. B. (2012) *Coupling behaviour of LOx/H_2 flames to longitudinal and transverse acoustic instabilities*, 48th AIAA/ASME/SAE/ASEE Joint Propulsion Conference and Exhibit, American Institute of Aeronautics and Astronautics, Atlanta, Georgia, 30 July -1 August 2012.

Hardi, J. S., Gomez Martinez, H. C., Oschwald, M. and Dally, B. (2012) *Response of a reacting LOx jet to a transverse acoustic oscillation*, Space Propulsion 2012, Bordeaux, France, 7-10 May 2012.

Hardi, J. S., Oschwald, M. and Dally, B. (2011) *Acoustic characterisation of a rectangular rocket combustor with LOx/H_2 propellants*, 4th European Conference for Aerospace Sciences, St. Petersburg, Russia, 4-8 July 2011.

Hardi, J. S., Oschwald, M. and Dally, B. (2011) *Cryogenic Oxygen/Hydrogen Flame Response to Acoustic Excitation in a Rectangular Rocket Combustor*, Proceedings of the Australian Combustion Symposium, The Combustion Institute/Australian & New Zealand Section, Shoal Bay, N.S.W., 29 November-1 December 2011.

Hardi, J. S., Oschwald, M. and Dally, B. (2011) *Flame Response to Acoustic Excitation in a Rectangular Rocket Combustor with LOx/H_2 Propellants*, 60th Deutscher Luft- und Raumfahrtkongress, Deutsche Gesellschaft für Luft- and Raumfahrt, Bremen, Germany, 27-29 September 2011.